**University of Alberta**

# The Effect of Surface Treatment on the High Temperature Oxidation of Ferritic Stainless Steels

by

Laurel Cooper

A thesis submitted to the Faculty of Graduate Studies and Research
in partial fulfillment of the requirements for the degree of

Master of Science

Chemical and Materials Engineering

Edmonton, Alberta
Fall 2007

Library and Archives Canada

Published Heritage Branch

395 Wellington Street
Ottawa ON K1A 0N4
Canada

Bibliothèque et Archives Canada

Direction du Patrimoine de l'édition

395, rue Wellington
Ottawa ON K1A 0N4
Canada

*Your file Votre référence*
*ISBN: 978-0-494-33225-2*
*Our file Notre référence*
*ISBN: 978-0-494-33225-2*

NOTICE:
The author has granted a non-exclusive license allowing Library and Archives Canada to reproduce, publish, archive, preserve, conserve, communicate to the public by telecommunication or on the Internet, loan, distribute and sell theses worldwide, for commercial or non-commercial purposes, in microform, paper, electronic and/or any other formats.

The author retains copyright ownership and moral rights in this thesis. Neither the thesis nor substantial extracts from it may be printed or otherwise reproduced without the author's permission.

AVIS:
L'auteur a accordé une licence non exclusive permettant à la Bibliothèque et Archives Canada de reproduire, publier, archiver, sauvegarder, conserver, transmettre au public par télécommunication ou par l'Internet, prêter, distribuer et vendre des thèses partout dans le monde, à des fins commerciales ou autres, sur support microforme, papier, électronique et/ou autres formats.

L'auteur conserve la propriété du droit d'auteur et des droits moraux qui protège cette thèse. Ni la thèse ni des extraits substantiels de celle-ci ne doivent être imprimés ou autrement reproduits sans son autorisation.

---

In compliance with the Canadian Privacy Act some supporting forms may have been removed from this thesis.

While these forms may be included in the document page count, their removal does not represent any loss of content from the thesis.

Conformément à la loi canadienne sur la protection de la vie privée, quelques formulaires secondaires ont été enlevés de cette thèse.

Bien que ces formulaires aient inclus dans la pagination, il n'y aura aucun contenu manquant.

Canada

# Abstract

Solid Oxide Fuel Cells (SOFCs) show promise as an alternative means of energy generation. However, a number of problems must be solved before SOFC commercialization is possible. The interconnect is an important fuel cell component as it allows single cells to be joined in series in order to achieve voltages required for practical applications. Ferritic stainless steel interconnects are promising; however, their oxidation resistance at SOFC operating temperatures is insufficient. This study examined the effect of cold rolling and sandblasting on the oxidation behaviour of three different ferritic stainless steels (430, 434, and ZMG 232) in air at 800°C. Both short term and long term oxidation studies were conducted. Various characterization techniques were used to analyze the oxide scales and to determine the oxide phases that were present. In addition, the carbides present in 434 steel prior to oxidation were characterized.

# Acknowledgements

I would like to express my gratitude to Dr. Douglas Ivey for his supervision of this work. I would not have been able to complete this work without the time, patience, encouragement, and guidance that Dr. Ivey generously provided.

I am grateful for the contributions provided by several individuals to this work. I would like to thank Ms. Tina Barker and Ms. Laura Gill for their assistance with the SEM analysis. I would especially like to acknowledge Tina for providing me with SEM training. I would also like to thank Ms. Diane Caird for performing the XRD analysis, as well as Dr. Anqiang He and Dr. Dimitre Karpuzov for performing the SIMS and XPS analysis and for assisting me with the analysis and interpretation of the data. Finally, I would like to thank Dr Jian Chen for conducting the jet polishing for my thin foil TEM samples.

I would also like to thank the many fellow graduate students who provided me with helpful suggestions and advice. In particular, I would like to thank Nima Shaigan, Weifeng Wei, and Junfang Lu for assisting me with sample preparation.

Funding for this research was provided by the Natural Sciences and Engineering Research Council of Canada (NSERC) and by Versa Power Systems (VPS). VPS also provided the steel specimens used in this research and carried out the sandblasting. I would paticularily like to thank Sofianne Benhaddad and Anthony Wood at VPS for their involvement with this research

Finally, I would like to acknowledge the encouragement I received from my family and friends over the past two years. Without the support of my parents Herman and Judy, my sister Joanna, and my boyfriend John, I would not have been able to complete this degree.

# Table of Contents


1 Introduction ..... 1
2 Literature Review ..... 4
2.1 Fuel Cells ..... 4
2.1.1 Advantages of Fuel Cells ..... 5
2.1.2 Disadvantages of Fuel Cells ..... 6
2.1.3 Types of Fuel Cells ..... 6
2.1.4 Applications of Fuel Cells ..... 8
2.2 Solid Oxide Fuel Cells ..... 9
2.2.1 Advantages of Solid Oxide Fuel Cells ..... 13
2.2.2 Disadvantages of Solid Oxide Fuel Cells ..... 14
2.2.3 Applications of Solid Oxide Fuel Cells ..... 15
2.3 Interconnects ..... 15
2.3.1 Interconnect Materials ..... 19
2.4 Oxidation of Metals ..... 40
2.4.1 Thermodynamics of Oxidation ..... 41
2.4.2 Kinetics of Oxidation ..... 44
2.4.3 Wagner's Theory of Oxidation ..... 48
2.4.4 Pilling-Bedworth Ratio ..... 49
2.5 Oxidation of Stainless Steel ..... 50
2.5.1 Effect of Environment ..... 56
2.6 Types of Surface Treatments ..... 65
2.6.1 Residual Stress ..... 65
2.6.2 Mechanical Surface Treatments ..... 67
2.7 Effect of Surface Roughness on Oxidation ..... 80
2.8 Effect of Surface Treatment on Oxidation ..... 83
3 Experimental Methods ..... 90
3.1 Steels ..... 90
3.2 Surface Treatments ..... 91
3.3 Surface Area Measurement ..... 91
3.4 Long Term Oxidation Experiments ..... 91
3.5 X-Ray Diffraction (XRD) Analysis ..... 93
3.6 Oxidized Cross Section Preparation ..... 93
3.7 Etched Cross Section Preparation ..... 94
3.8 Scanning Electron Microscopy (SEM) ..... 95
3.9 Short Term Oxidation Experiments ..... 95

3.10 Secondary Ion Mass Spectrometry (SIMS) Analysis ..... 96
3.11 X-Ray Photoelectron Spectroscopy (XPS) Analysis ..... 96
3.12 Thin Foil Specimen Preparation ..... 97
3.13 Carbon Extraction Replica Preparation ..... 97
3.14 Transmission Electron Microscopy (TEM) ..... 98
4 Results ..... 99
4.1 Unoxidized Specimens ..... 99
4.1.1 Plan View SEM Images ..... 99
4.1.2 Etched Cross Section SEM Images ..... 101
4.1.3 434 Carbides ..... 104
4.2 Long Term Oxidation Experiments ..... 113
4.2.1 Specific Mass Gain Results ..... 113
4.2.2 Parabolic Rate Constants ..... 122
4.3 430 Results ..... 123
4.3.1 XRD Results ..... 123
4.3.2 SEM Plan View Results ..... 128
4.3.3 SEM Cross Section Results ..... 133
4.3.4 SIMS Results ..... 143
4.3.5 XPS Analysis ..... 147
4.3.6 Summary of 430 Results ..... 153
4.4 434 Results ..... 156
4.4.1 XRD Results ..... 156
4.4.2 SEM Plan View Results ..... 159
4.4.3 SEM Cross Section Results ..... 162
4.4.4 SIMS Results ..... 167
4.4.5 XPS Analysis ..... 172
4.4.6 Summary of 434 Results ..... 181
4.5 ZMG 232 Results ..... 184
4.5.1 XRD Results ..... 184
4.5.2 SEM Plan View Results ..... 187
4.5.3 SEM Cross Section Results ..... 190
4.5.4 SIMS Results ..... 197
4.5.5 XPS Analysis ..... 201
4.5.6 Summary of ZMG 232 Results ..... 209
5 Discussion ..... 211
5.1 Specific Mass Gain ..... 211
5.2 Chromium Depletion ..... 229

5.3 Oxide Thickness ..... 233
5.4 Oxide Scale ..... 235
5.4.1 Spinel ..... 235
5.4.2 Insulating Oxides ..... 238
5.5 Oxidation Model ..... 239
6 Conclusions ..... 245
7 Recommendations ..... 247

# List of Tables

Table 1-1. Emissions Comparison (Pounds of Emissions Per 1650 MWh From One Year of Operation) (Kendall. 2005)..... 2
Table 2-1. Types of Fuel Cells (Boudghene Stambouli & Traversa. 2002, Fuel Cells 2000. 2006, Johnson Matthey. 2006, Smithstonian Institution. 2005, Thomas & Zalbowitz. 2000)..... 7
Table 2-3. Parabolic Rate Constants for the Oxidation of Ferritic Stainless Steels at 800°C (Yang, et al. 2004a)..... 54
Table 2-4. Categories of Surface Treatment Methods (Burakowski & Wierzchon. 1999). ..... 65
Table 3-1. Composition of Ferritic Stainless Steels (Garcia Vargas, et al. 2005b, Metal Suppliers Online. 2006)..... 90
Table 4-1. R and d Values from Carbide Diffraction Pattern..... 107
Table 4-2. R and d Values from Carbide Diffraction Pattern..... 109
Table 4-3. Multiplication Factors for Selected Specimens and Treatment Conditions.. 117
Table 4-4. Parabolic Rate Constants ($x10^{-14} g^2/cm^4 \cdot s$)..... 122
Table 4-5. Literature Values of Parabolic Rate Constants for Oxidation in Air at 800°C (Antepara, et al. 2005, Brylewski, et al. 1999, Yang, et al. 2003b)..... 123
Table 4-6. Relative Intensities of Chromia X-Ray Peaks for 430 Specimens..... 126
Table 4-7. Relative Intensities of Spinel X-Ray Peaks for 430 Specimens..... 126
Table 4-8. Spinel to Chromia Peak Area Ratios for 430 Specimens..... 127
Table 4-9. Cr:Mn and Cr:Fe Ratios from Quantitative EDX Analysis of the Oxide Scale for 430 Specimens..... 132
Table 4-10. Oxide Layer Thickness for 430 Specimens..... 138
Table 4-11. Cr:Mn and Cr:Fe Ratios From Quantitative EDX Analysis of the Spinel for 430 Specimens..... 139
Table 4-12. Estimated Scale Thicknesses Corresponding to 430 SIMS Depth Profiles. 146
Table 4-13. Relative Intensities of Chromia X-Ray Peaks for 434 Specimens..... 157
Table 4-14. Relative Intensities of Spinel X-Ray Peaks for 434 Specimens..... 158
Table 4-14. Spinel to Chromia Peak Area Ratios for 434 Specimens..... 158
Table 4-16. Cr:Mn and Cr:Fe Ratios from Quantitative EDX Analysis of the Oxide Scale for 434 Specimens..... 162
Table 4-17. Oxide Layer Thickness for 434 Specimens..... 164
Table 4-18. Cr:Mn and Cr:Fe Ratios From Quantitative EDX Analysis of the Spinel for 434 Specimens..... 164
Table 4-19. Estimated Scale Thicknesses Corresponding to 434 SIMS Depth Profiles. 172

Table 4-20. Relative Intensities of Chromia X-Ray Peaks for ZMG 232 Specimens. ... 186
Table 4-21. Relative Intensities of Spinel X-Ray Peaks for ZMG 232 Specimens. ..... 186
Table 4-22. Spinel to Chromia Peak Area Ratios for ZMG 232 Specimens. ..... 187
Table 4-23. Cr:Mn and Cr:Fe Ratios from Quantitative EDX Analysis of the Oxide Scale for ZMG 232 Specimens. ..... 189
Table 4-24. Oxide Layer Thickness for ZMG 232 Specimens. ..... 192
Table 4-25. Cr:Mn and Cr:Fe Ratios From Quantitative EDX Analysis of the Spinel for ZMG 232 Specimens. ..... 193
Table 4-26. Estimated Scale Thicknesses Corresponding to ZMG 232 SIMS Depth Profiles. ..... 200
Table 5-1. Data Used In First Diffusion Calculation (Cermak, et al. 1996). ..... 218
Table 5-2. Data Used in Second Diffusion Calculation *(Brandes & Brook. 1998). ..... 219
Table 5-3. Order of Magnitude Diffusion Distance Calculation. ..... 230
Table 5-4. Chromia Thickness Comparison. ..... 234

# List of Figures

Figure 2-1. Solid Oxide Fuel Cell (Smithstonian Institution. 2005)..... 9
Figure 2-2. Planar Configuration of an SOFC (Kee & Goodwin. 2004)..... 11
Figure 2-3. Two Possible Tubular Configurations for SOFCs (Kee & Goodwin. 2004). 12
Figure 2-4. Ellingham Diagram (Shifler. 2003)..... 43
Figure 2-6. Residual Stress Distribution Following Shot Peening (Hammersly. 1993)... 71
Figure 4-1. SEM SE Images of Unoxidized Steel Specimens..... 99
Figure 4-2. SEM SE Image and EDX Spectrum of 434 steel subjected to 10 Sandblasting Passes. a) Image of Specimen with Alumina Particle Circled; b) EDX Spectrum of Alumina Particle..... 100
Figure 4-3. SEM SE Images of Etched Cross Sections of Unoxidized Specimens. a) 430 As-is; b) 434 As-is, c) ZMG 232 As-is..... 102
Figure 4-4. Fe-Cr Phase Diagram for a C Content of 0.1 wt% (Smith. 1993)..... 103
Figure 4-5. Carbides in 434 Steel. a) TEM BF Image; b) EDX Spectrum from Precipitate 1; c) EDX Spectrum from Precipitate 2..... 105
Figure 4-6. Reference Diffraction Pattern From Steel Substrate..... 106
Figure 4-7. Fe-Cr-Nb-Mo Carbide Diffraction Pattern. a) TEM BF Image; b) SAD Pattern; c) Simulated Pattern for $Cr_7C_3$ (orthorhombic); d) Simulated Pattern for $Fe_3Nb_3C$ (cubic)..... 108
Figure 4-8. Fe-Cr-Nb-Mo carbide. a) TEM BF Image; b) SAD Pattern; c) Simulated Pattern for $Cr_7C_3$ (orthorhombic)..... 109
Figure 4-9. Two Types of Carbides From 434 Extraction Replica. a) TEM BF Image of Two Types of Precipitates; b) EDX Spectrum from Nb-Fe Carbide; c) EDX Spectrum from Nb-Ti Carbide..... 111
Figure 4-10. Carbide Diffraction Patterns. a) Nb-Fe SAD Pattern; b) Simulated Pattern for $Cr_7C_3$ (orthorhombic); c) Nb-Ti SAD Pattern; d) Simulated Pattern for NbC (cubic). ..... 112
Figure 4-11. Mass Gain Due to Oxidation for 430 Specimens..... 113
Figure 4-12. Mass Gain Due to Oxidation for 434 Specimens..... 114
Figure 4-13. Mass Gain Due to Oxidation for ZMG 232 Specimens..... 114
Figure 4-14. Schematic of Surface Profile..... 116
Figure 4-15. XRD Spectra from 430 6% Cold Rolled Specimens After Oxidation..... 124
Figure 4-16. Comparison of the 430 XRD Spectra After 502 h of Oxidation..... 125
Figure 4-17. SEM SE Plan View Images for 430 Specimens After 50 h and 502 h of Oxidation..... 129

Figure 4-19. 430 Thin As-Is Specimen. a) SEM Image; b) Chromia EDX Spectrum; c) Spinel EDX Spectrum. 134
Figure 4-20. SEM Cross Section Images of 430 Specimens After 502 h of Oxidation. 135
Figure 4-21. Two Distinct Regions of the Oxide Scale on the 430 Thin As-Is Specimen. a) Protective Oxide; b) Evidence of Spalling. 137
Figure 4-22. EDX Linescans for 430 Thin As-Is Cross Section After 502 h. a) Protective Oxide; b) Spalled Region. 140
Figure 4-23. EDX Linescan for 430 As-Is Cross Section After 502 h. 141
Figure 4-24. EDX Linescan for 430 Rolled 15% Cross Section After 502 h. 141
Figure 4-25. EDX Linescan for 430 Sandblasted 10 Passes Cross Section After 502 h. 142
Figure 4-26. SIMS Depth Profile of 430 Native Oxide. 143
Figure 4-27. SIMS Depth Profiles of 430 Specimens Oxidized for 15 Minutes at 800°C. a) As-Is; b) Rolled 15%; c) Sandblasted 10 Passes 145
Figure 4-28. XPS 2p Peak Plots for 430 Native Oxide. a) Cr; b) Fe; c) Mn; d) Si. 149
Figure 4-29. XPS 2p Peak Plots for 430 As-Is Specimen Oxidized for 15 Minutes at 800°C. a) Cr; b) Fe; c) Mn; d) Si. 152
Figure 4-30. Comparison of the 434 XRD Spectra After 502 h of Oxidation. 156
Figure 4-31. SEM Plan View Images of 434 Specimens After 50 h and 502 h of Oxidation. 160
Figure 4-32. SEM Cross Section Images of 434 Specimens After 502 h of Oxidation. 163
Figure 4-33. EDX Linescan for 434 Thin As-Is Cross Section After 502 h. 165
Figure 4-34. EDX Linescan for 434 Rolled 15% Cross Section After 502 h. 166
Figure 4-35. EDX Linescan for 434 Sandblasted 10 Passes Cross Section After 502 h. 166
Figure 4-36. SIMS Depth Profile of 434 Native Oxide. a) Si and Mn; b) Mo and Nb... 168
Figure 4-37. SIMS Depth Profile of 434 Specimens Oxidized for 15 Minutes at 800°C. a) As-Is; b) Rolled 15%; c) Sandblasted 10 Passes. 171
Figure 4-38. XPS Peak Plots for 434 Native Oxide. a) Cr 2p; b) Fe 2p; c) Mn 2p; d) Si 2p; e) Mo 3d; f) Nb 3d. 176
d) 179
Figure 4-39. XPS Peak Plots for 434 As-Is Specimens Oxidized for 15 Minutes at 800°C. a) Cr 2p; b) Fe 2p; c) Mn 2p; d) Si 2p; e) Mo 3d; f) Nb 3d. 180
Figure 4-40. Comparison of the ZMG 232 XRD Spectra After 502 h of Oxidation. 185
Figure 4-41. SEM Plan View Images of ZMG 232 Specimens After 50 h and 502 h of Oxidation. 188
Figure 4-42. SEM Cross Section Images of ZMG 232 Specimens After 502 h of Oxidation. 191
Figure 4-43. EDX Linescan for ZMG 232 As-Is Cross Section After 502 h. 194

Figure 4-44. EDX Linescan for ZMG 232 Rolled 21% Cross Section After 502 h. ..... 195
Figure 4-45. EDX Linescan for ZMG 232 Sandblasted 10 Passes Cross Section After 502 h. ..... 196
Figure 4-46. SIMS Depth Profile of ZMG 232 Native Oxide. ..... 197
Figure 4-47. SIMS Depth Profile of ZMG 232 Specimens Oxidized for 15 Minutes at 800°C. a) As-Is; b) Rolled 15%; c) Sandblasted 10 Passes. ..... 199
Figure 4-48. XPS Peak Plots for ZMG 232 Native Oxide. a) Cr 2p; b) Fe 2p; c) Mn 2p; d) Si 2p; e) Al 2s. ..... 204
Figure 4-49. XPS Peak Plots for ZMG 232 As-Is Specimen Oxidized for 15 Minutes at 800°C. a) Cr 2p; b) Fe 2p; c) Mn 2p; d) Si 2p; e) Al 2s. ..... 208
Figure 5-1. Isothermal Section of the Fe-Mo-Nb Phase Diagram at 900°C (ASM International. 2002b). ..... 212
Figure 5-2. Geometry for Combining Grain Boundary and Lattice Diffusion). ..... 217
Figure 5-3. Relative Contributions of Bulk and Grain Boundary Diffusion as a Function of Temperature Based on Data in Table 5-1. a) 430; b) 434. ..... 220
Figure 5-4. Relative Contributions of Bulk and Grain Boundary Diffusion as a Function of Temperature Based on Data in Table 5-2. a) 430; b) 434. ..... 222
Figure 5-5. Grain Structure of 434 Specimens Oxidized for 15 Minutes at 800°C. As-Is Centre (a) and Surface (b) of Specimen; Rolled 15% Centre (c) and Surface (d) of Specimen. ..... 223
Figure 5-6. Cr Concentration Profile Through the Steel for 430 As-Is Thick and Thin Specimens After 502 h of Oxidation at 800°C. ..... 231
Figure 5-7. Cr Concentration Below The Oxide Scale at Regions Where Spalling Was Observed. ..... 232
Figure 5-8. Comparison of Oxide Scale Thickness and Specific Mass Gain. ..... 233
Figure 5-9. Model of Oxidation for 430, 434, and ZMG 232 at 800°C in Air. a) Formation of Chromia Nuclei; b) Continuous Chromia Layer and Formation of Spinel and Insulating Oxides; c) Inner Chromia, Outer Spinel, and Insulating Oxides at Metal/Oxide Interface. ..... 242

# 1 Introduction

In recent years, there has been a growing concern that our society may be facing an energy crisis. The demand for energy has been continually increasing due to increases in both economic development and world population (Boudghene Stambouli & Traversa. 2002). Currently, the majority of the world's power is generated from fossil fuels such as natural gas, coal, and crude oil, all of which are non-renewable resources (Boudghene Stambouli & Traversa. 2002). In addition to this, a large part of the world's fossil fuel reserves is concentrated in only a few countries, many of which are controlled by unstable political regimes (Thomas & Zalbowitz. 2000). The net result is growing attention towards the need to develop practical alternative methods of power generation.

Environmental concerns about traditional power generation involving fossil fuel combustion have been recently discussed at length. A major problem is the emission of noxious gases such as $SO_x$ and $NO_x$ in addition to $CO_2$, which is considered to be a greenhouse gas (Thomas & Zalbowitz. 2000). Increasing amounts of greenhouse gases in the atmosphere are thought to be linked to climate change, particularly global warming and "more frequent winter events" (Government of Canada. 2001). A growing public concern over climate change has prompted the governments of many developed countries to take measures to reduce greenhouse gas emissions. In 1997, the Kyoto Protocol was established in a meeting of over 160 countries, including Canada. This agreement established Canada's target to reduce greenhouse gas emissions to 6 percent below 1990 emissions by 2012. However, despite all the attention being paid to climate change, some scientists dispute the validity of the claim that the recent increase in global temperatures is a direct result of human activity. What cannot be disputed is the global concern for air pollution. The World Bank estimates that over 1 billion people in urban areas are exposed to severe air pollution, which results in over 700 000 deaths each year (Thomas & Zalbowitz. 2000).

Alternative energy generation approaches have been proposed as a solution to the environmental problems associated with fossil fuel combustion. One such technology is the fuel cell. Fuel cells convert the energy of a hydrogen-containing fuel to electrical energy through an electrochemical reaction. There are several advantages of fuel cells compared to traditional thermo-mechanical energy generation. The efficiency of fuel

cells can reach 70%, and efficiencies as high as 90% are thought to be possible if heat recovery is used (Boudghene Stambouli & Traversa. 2002). In comparison, thermo-mechanical power generation has an efficiency of 30-40% (Boudghene Stambouli & Traversa. 2002). Emissions of noxious gases, dust, and noise can be significantly reduced if fuel cells are used to generate energy. Table 1-1 is a comparison of the emissions of a fuel cell with those of a fossil fuel power plant.

Table 1-1. Emissions Comparison (Pounds of Emissions Per 1650 MWh From One Year of Operation) (Kendall. 2005).

| Air Emissions | $SO_x$ | $NO_x$ | CO | Particles | Organic Compounds | $CO_2$ |
|---|---|---|---|---|---|---|
| Fossil Fuel Plant | 28000 | 41427 | 28125 | 500 | 468 | 4044000 |
| Fuel Cell | 0 | 0 | 72 | 0 | 0 | 1860000 |

In the future, fuel cells offer the possibility of generating "zero emissions" power if hydrogen can be obtained through solar or wind powered electrolysis of water (Geyer. 2001).

Solid Oxide Fuel Cells (SOFCs) are a type of fuel cell containing a solid ceramic electrolyte that operates at high temperatures. SOFCs are a promising type of fuel cell due to their ability to tolerate a wide variety of fuels (natural gas, gasoline, diesel, and others) in addition to pure hydrogen, their ability to tolerate fuel impurities such as sulphur, and their high efficiency compared to other types of fuel cells. A single cell consists of an anode and cathode separated by an oxygen ion-conducting ceramic electrolyte. In order to achieve voltages required for industrial applications, cells are connected in series by interconnects to form a fuel cell stack. Recent developments in SOFC technology have enabled operating temperatures to be reduced to the range of 700 to 800°C, allowing material costs, particularly those of the interconnect, to be reduced. The use of metallic interconnects has been proposed due to their high thermal and electrical conductivity and low material and fabrication costs compared to ceramic alternatives. In particular, ferritic stainless steels containing 16-26 wt% Cr are promising due to their low cost, machinability and thermal expansion compatibility with the other stack materials. However, the oxidation resistance of ferritic stainless steel interconnects at the operating temperature is insufficient due to the formation of a poorly conductive

oxide layer which increases the electrical resistance of the interconnect and decreases fuel cell performance.

In this research, the effect of cold rolling and sandblasting on the oxidation behaviour of three ferritic stainless steels (430, 434, and ZMG 232) in air at 800°C was studied. The motivation for this study was an observation made by Vera Power Systems during testing of SOFC stacks that reused stainless steel interconnects oxidized less than new interconnects. The major difference between new and reused interconnects was that the reused interconnects were sandblasted prior to testing in order to remove oxide scales formed in the previous test. A temperature of 800°C was selected for this research because it is the upper range of SOFC operating temperatures and thus would represent a worst case scenario for oxidation. Also, even if the nominal operating temperature of the stack was 750°C, the temperature distribution is not uniform and it is possible that some areas, particularly in the middle of the stack, would be exposed to higher temperatures.

A number of different characterization techniques, including scanning electron microscopy (SEM), transmission electron microscopy (TEM), energy-dispersive x-ray analysis (EDX), x-ray diffraction (XRD), x-ray photoelectron spectroscopy (XPS) and secondary ion mass spectrometry (SIMS), were used to analyze the oxide layers that formed on the ferritic stainless steels at 800°C in air after both short term and long tem exposure.

# 2 Literature Review

## 2.1 Fuel Cells

A common definition of a fuel cell is an "energy conversion device," one that converts chemical energy of a fuel into electrical energy (Boudghene Stambouli & Traversa. 2002). Fuel cells are similar to batteries, except that fuel cells operate continuously (Boudghene Stambouli & Traversa. 2002). As long as they are supplied with fuel, fuel cells do not run down as batteries do, nor do they require recharging (Boudghene Stambouli & Traversa. 2002). In order to produce electricity, a fuel cell electrochemically combines a hydrogen-containing fuel with an oxidant, typically air (Minh & Takahashi. 1995).

Fuel cells have three main components: the electrodes (anode and cathode), the electrolyte, and the interconnect (Boudghene Stambouli & Traversa. 2002). A single cell consists of an anode and cathode separated by the electrolyte (Boudghene Stambouli & Traversa. 2002). The electrodes serve two main purposes: they provide a surface where electrochemical reactions take place, and they physically separate the reactant gasses from the electrolyte (Boudghene Stambouli & Traversa. 2002). Porous electrodes are used in order to increase the area available for the electrochemical reaction to take place, thus increasing the current density produced by the cell (EG&G Services, et al. 2000). The electrolyte also has two main functions: to conduct ions (either hydrogen or oxygen, depending on the type of fuel cell) between the anode and cathode, and to physically separate the two electrodes (Boudghene Stambouli & Traversa. 2002). In order to increase output voltages, single cells are combined in series to form a fuel cell stack (Boudghene Stambouli & Traversa. 2002). The interconnect electrically connects the anode of one cell to the cathode of an adjacent cell (Boudghene Stambouli & Traversa. 2002). The electricity produced by fuel cells is DC; therefore, an inverter is needed in order to obtain the AC power that is required by many applications (Smithstonian Institution. 2005).

### 2.1.1 Advantages of Fuel Cells

There are several advantages of using fuel cells to generate electricity. First, fuel cells involve electrochemical reactions rather than the combustion reactions used in traditional thermo-mechanical power generation; because of this, much less pollution is generated (Boudghene Stambouli & Traversa. 2002, Thomas & Zalbowitz. 2000). If pure hydrogen is used as a fuel, the only waste products are heat and water vapour (Boudghene Stambouli & Traversa. 2002). Currently, hydrogen is extracted from a variety of different fuels including natural gas, propane, butane, and diesel (Boudghene Stambouli & Traversa. 2002). In the future, there is the possibility of generating "zero emissions" power by obtaining hydrogen through solar or wind power-driven electrolysis of water (Geyer. 2001, Government of Canada, et al. 2003).

A second advantage of fuel cells is their high efficiency. Traditional thermo-mechanical methods of power generation first convert the chemical energy of a fuel into thermal energy through a combustion reaction, and then convert the thermal energy into mechanical energy and finally electrical energy (Thomas & Zalbowitz. 2000). This places an upper limit on the efficiency of the process as heat is always lost in the conversion of thermal energy to mechanical energy (Thomas & Zalbowitz. 2000). This efficiency limit is known as the Carnot limit and is described by the following equation:

$$\varepsilon = 1 - \frac{T_l}{T_h} \qquad (2\text{-}1)$$

where $\varepsilon$ is the efficiency of the thermo-mechanical process (a value between 0 and 1), $T_l$ (K) is the low temperature heat sink, and $T_h$ (K) is the high temperature heat sink (Minh & Takahashi. 1995). According to Equation 2-1, in order to maximize the efficiency, $T_h$ should be as high as possible and $T_l$ as low as possible (Minh & Takahashi. 1995). However, in reality $T_h$ is constrained by material limitations and $T_l$ by room temperature (Minh & Takahashi. 1995). Because fuel cells convert chemical energy directly to electrical energy, they are not restricted by the Carnot limit and thus the efficiency is much higher (Thomas & Zalbowitz. 2000).

A third advantage of fuel cells is that they contain no moving parts. Because of this, noise pollution is significantly reduced (Boudghene Stambouli & Traversa. 2002). Also, maintenance costs are significantly reduced as fuel cells do not suffer the same wear and lubrication problems as mechanical systems (Kendall. 2005). As a result, fuel cells have the potential for longer lifetimes than traditional thermo-mechanical generators (Government of Canada, et al. 2003).

A final advantage of fuel cells is that they are extremely versatile (EG&G Services, et al. 2000, Fuel Cells 2000. 2006). Currently, power generation relies on a centralized power grid distribution system where electricity is generated in remote locations and transmitted to consumers using power lines (Geyer. 2001). With fuel cells, electricity could be generated in appropriate amounts at locations where it is required (Werner. 2000). This would result in reduced capital costs since large power plants and transmission lines would no longer be necessary (Werner. 2000).

### 2.1.2 Disadvantages of Fuel Cells

There are several problems with fuel cells that can limit their usefulness. First, some types of fuel cells have liquid electrolytes. These electrolytes are typically corrosive and can be difficult to handle. Second, many types of fuel cells require extremely expensive materials or catalysts, for example, platinum. Finally, some types of fuel cells operate at high temperatures which limit the range of potential applications.

### 2.1.3 Types of Fuel Cells

Fuel cells are typically classified according to the type of electrolyte used; however, they can also be grouped by type of fuel and oxidant used, whether the fuel is processed inside or outside the fuel cell (internal or external reforming), or by operating temperature (Boudghene Stambouli & Traversa. 2002, EG&G Services, et al. 2000). Table 2-1 lists the common types of fuel cells and some of their operating characteristics. Of all the fuel cell types listed, PEMFCs and SOFCs currently show the most promise for commercialization (Government of Canada, et al. 2003).

Table 2-1. Types of Fuel Cells (Boudghene Stambouli & Traversa. 2002, Fuel Cells 2000. 2006, Johnson Matthey. 2006, Smithstonian Institution. 2005, Thomas & Zalbowitz. 2000).

| Type | Electrolyte | Operating Temperature (°C) | Fuel | Efficiency (%) | Typical Electric Power (kW) |
|---|---|---|---|---|---|
| Alkaline (AFC) | potassium hydroxide | 50 - 200 | pure hydrogen, hydrazine | up to 70 | 0.3 - 500 |
| Direct Methanol (DMFC) | polymer | 60 - 200 | liquid methanol | 40 | <10 |
| Phosphoric Acid (PAFC) | phosphoric acid | 160 - 210 | hydrocarbons, alcohol, impure hydrogen | 40 - 80 | up to 200 |
| Sulphuric Acid (SAFC) | sulphuric acid | 80 - 90 | alcohol, impure hydrogen | - | - |
| Proton Exchange Membrane or Polymer Electrolyte Membrane (PEMFC) | polymer, proton exchange membrane | 50 - 80 | hydrocarbons, methanol | 40 - 50 | 50 - 250 |
| Molten Carbonate (MCFC) | moten salt (nitrate, sulphate, carbonate, etc.) | 630 - 650 | hydrogen, carbon monoxide, natural gas, propane, marine diesel, landfill gas, simulated coal gasification products | 60 - 80 | 10 - 2000 |
| Solid Oxide (SOFC) | stabilized zirconia and doped perovskite | 600 - 1000 | natural gas, propane | up to 90 | >200 |
| Solid Polymer (SPFC) | solid sulphonated polystyrene | 90 | hydrogen | - | - |

There are several other fuel cells under various stages of development that are not listed in Table 2-1, including regenerative fuel cells, the Metal Air Fuel Cell (MAFC), and the

Protonic Ceramic Fuel Cell (PCFC) (Fuel Cells 2000. 2006, Johnson Matthey. 2006). Regenerative fuel cells rely on the electrolysis of water to obtain $H_2$ and $O_2$, thus eliminating the need for a hydrogen infrastructure (Thomas & Zalbowitz. 2000). This technology requires further development, because in order to reduce overall greenhouse gas emissions, the electricity used for electrolysis must come from renewable sources such as wind and solar power (Thomas & Zalbowitz. 2000). Metal Air Fuel Cells have more in common with batteries than other types of fuel cells as they do require recharging; however, this process is more rapid and the fuel cell has a higher specific energy than batteries (Fuel Cells 2000. 2006). One type of MAFC under development is the Zinc Air Fuel Cell (ZAFC) (Johnson Matthey. 2006). The Protonic Ceramic Fuel Cell is similar to a SOFC as they both operate at high temperatures; however, for a PCFC, the electrolyte conducts protons as opposed to oxygen ions in SOFCs (Fuel Cells 2000. 2006). Other novel fuel cell types in the early stages of development are the blue energy fuel cell and various types of biological fuel cells (Wikimedia Foundation. 2006a).

### 2.1.4 Applications of Fuel Cells

There are many possible areas where fuel cells could potentially be used. Stationary applications of fuel cells include residential or commercial power and heating, or backup power applications such as emergency generators (Geyer. 2001, Government of Canada, et al. 2003). Since fuel cells continue to operate as long as both fuel and air are supplied, they are extremely reliable (Geyer. 2001). Fuel cells also show promise in the transportation sector, where they can be used as a replacement for the traditional thermal combustion engine in buses, cars, locomotives, boats, large trucks, industrial vehicles, and military vehicles (Geyer. 2001, Government of Canada, et al. 2003). Portable applications of fuel cells include electronic devices such as cellular phones and laptops (Geyer. 2001). Fuel cells operating at high temperatures tend to be used for stationary applications, while portable applications use fuel cells operating at lower temperatures (Geyer. 2001).

## 2.2 Solid Oxide Fuel Cells

The operation of a typical Solid Oxide Fuel Cell (SOFC) is illustrated in Figure 2-1.

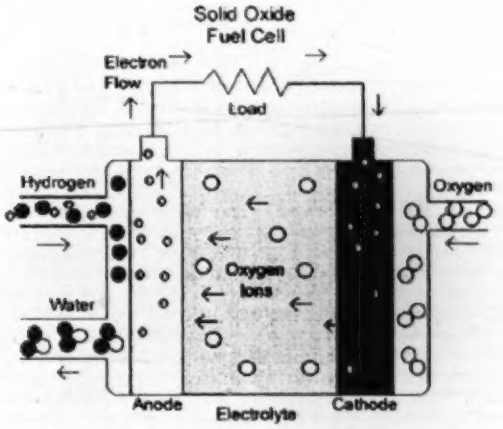


Figure 2-1. Solid Oxide Fuel Cell (Smithstonian Institution. 2005).

Oxygen enters the fuel cell at the cathode, where it combines with electrons returning from the external circuit, and is ionized (Smithstonian Institution. 2005). The oxygen ions then travel through the electrolyte towards the anode, where they combine with hydrogen ions from the fuel to form water (Government of Canada, et al. 2003). The exact overall electrochemical reaction depends on the type of fuel that is used, but it is essentially the following (Kendall. 2005):

$$H_2 + CO + O_2 \rightarrow H_2O + CO_2 \qquad (2\text{-}2)$$

Theoretically, a single cell can produce 1 V of electricity; however, the actual cell voltage is lower due to several factors, including activation polarization (related to the kinetics of the electrochemical reaction), concentration polarization (associated with the diffusion of reactants and products), and ohmic polarization (due to the resistance to ion flow in the electrolyte and to the resistance to electron flow in the electrodes) (Zhu & Deevi. 2003a). Single cell voltages under SOFC operating conditions typically range from 0.5 to 0.9 V (Alman & Jablonski. 2004).

There are two main classifications of SOFCs: high temperature, i.e., those that operate at approximately 1000°C, and reduced temperature or intermediate temperature, with operating temperatures ranging from 600 to 800°C (Grabke, et al. 1997). There are several advantages to operating at high temperatures, including increased mass transfer, faster reaction kinetics, and lower electrical resistance of cell materials, all of which result in a high power density (Minh & Takahashi. 1995). However, as in other high temperature applications there are materials problems; in this case, electrode sintering, interdiffusion at the interface between the electrodes and the electrolyte, mechanical stresses due to differences in the thermal expansion coefficients of individual cell components, and other interaction and degradation issues (Minh & Takahashi. 1995, de Souza, et al. 1997). In order to achieve a similar power density in low temperature fuel cells, electrolytes with improved oxygen conductivity are selected and the electrolyte thickness is also reduced (Grabke, et al. 1997, Huang, et al. 2000). Electrolytes in reduced temperature SOFCs typically have a thickness of 10-20μm, compared to a thickness of 150μm for high temperature SOFCs (Zhu & Deevi. 2003b). Because of the reduced electrolyte thickness, intermediate temperature SOFCs can no longer be electrolyte-supported as is the case for high temperature fuel cells; instead, an anode-supported design is used (Zhu & Deevi. 2003b). Although many of the materials problems no longer exist at lower temperatures, disadvantages of operating at low temperatures include slower reaction kinetics, increased resistive losses across the electrolyte, and increased overpotentials at the electrodes (de Souza, et al. 1997). It is difficult to reduce the operating temperature of SOFCs below approximately 600°C for several reasons: extremely thin electrolytes would be needed, demanding special fabrication techniques, power density would be reduced, and internal reforming of the fuel would no longer be possible (Wincewicz & Cooper. 2005).

A common electrolyte material in SOFCs is $Y_2O_3$-stabilized $ZrO_2$ (yttria-stabilized zirconia (YSZ)) (EG&G Services, et al. 2000, Quadakkers, et al. 2003). Scandia-stabilized zirconia (SSZ) is also used (Kendall. 2005). For intermediate temperature fuel cells, doped ceria ($CeO_2$) is also possible. Dopants include $La_2O_3$, $Y_2O_3$, $Sm_2O_3$, $Gd_2O_3$, other rare earth oxides, $Gd_2O_3$+$Pr_2O_3$, CaO, and SrO (Minh & Takahashi. 1995). Other candidate electrolyte materials include stabilized bismuthsesquioxides ($Bi_2O_3$), pyrochlore oxides ($A_2B_2O_7$), and perovskite oxides ($ABO_3$) (Minh & Takahashi. 1995).

Traditional anode materials are cermets: Ca-$ZrO_2$ (calcium-doped zirconia), Ni-$ZrO_2$ (Ni-YSZ), Ni-SDC (samaria-doped ceria), and Ru-YSZ (EG&G Services, et al. 2000, Kee & Goodwin. 2004, Minh & Takahashi. 1995, Quadakkers, et al. 1994). Other promising anode materials are a $ZrO_2$-$Y_2O_3$-$TiO_2$ solid solutions and transition metal (Cr, Mn, Fe) perovskites (Kendall. 2005, Minh & Takahashi. 1995).

Initially, SOFC cathodes were made of doped lanthanum cobaltites, but this material reacted with YSZ, a common electrolyte, and also had a significant thermal expansion coefficient mismatch with other cell components (Kendall. 2005). Most current cathode materials are mixed ionic-electronic conductors such as LSCF (a four component oxide consisting of La, Sr, Co, and Fe oxides) or LSM ($LaMnO_3$ doped with SrO, CaO, NiO, $ZrO_2$, or $SrO/Cr_2O_3$) (Ceram Research. 2006, Kee & Goodwin. 2004, Minh & Takahashi. 1995, Quadakkers, et al. 1994). Other possible cathode materials are CGO (gadolinium oxide), doped $LaCoO_3$, and other doped oxides (Minh & Takahashi. 1995).

Unlike other types of fuel cells, there are several possible geometries for the SOFC, the most popular being the planar configuration and the tubular configuration (Minh & Takahashi. 1995, Wikimedia Foundation. 2006a). The planar configuration is displayed below in Figure 2-2, and the tubular configuration is shown in Figure 2-3.

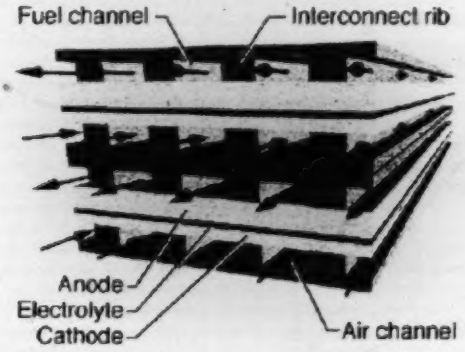


Figure 2-2. Planar Configuration of an SOFC (Kee & Goodwin. 2004).

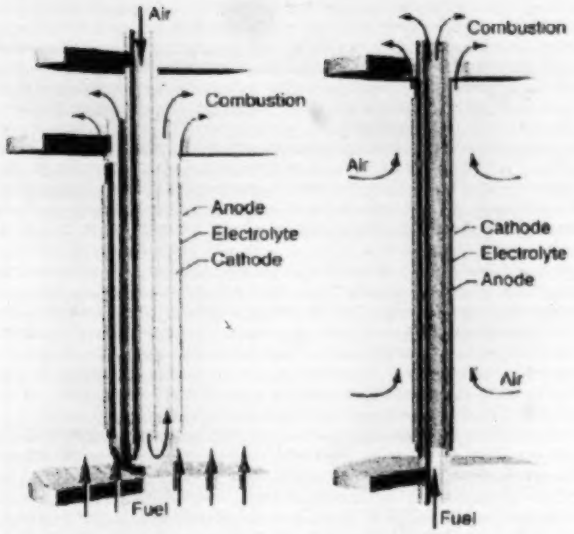


Figure 2-3. Two Possible Tubular Configurations for SOFCs (Kee & Goodwin. 2004).

The planar configuration can be described as a "sandwich" of the electrolyte between the two electrodes (Wikimedia Foundation. 2006a). The stack can be made up of either circular or rectangular plates (Wincewicz & Cooper. 2005). There are several advantages of the planar design. It has a higher power density than the tubular configuration because of the higher electrical resistance and more difficult mass and heat transfer characteristics of the tubular design (Wincewicz & Cooper. 2005). The planar design is also easier to fabricate, reducing the manufacturing costs of the fuel cell (Wincewicz & Cooper. 2005).

The tubular SOFC geometry consists of a tube with either air or fuel flowing on the outside of the tube and the other on the inside (Wikimedia Foundation. 2006a). Both configurations are shown in Figure 2-3. The stack is made up of a series of either circular, as shown in the figure, or flattened tubes which are joined in parallel or in series (Wincewicz & Cooper. 2005). Using the tubular design, it is easier to maintain the separation of the fuel and air than with the planar configuration (Wikimedia Foundation. 2006a). Also, the tubular SOFC has been proven for longer operating periods than planar stacks (Wincewicz & Cooper. 2005).

### 2.2.1 Advantages of Solid Oxide Fuel Cells

One major advantage of SOFCs is their ability to tolerate a wide variety of fuels in addition to hydrogen. Natural gas, gasoline, diesel, alcohol fuels, synthesis gas from biomass, and industrial waste are all possible sources of fuel (National Energy Technology Laboratory. 2006). Because of the high operating temperatures, the SOFC is able to internally reform these fuels to hydrogen, meaning that an external reformer is not necessary (Government of Canada, et al. 2003, Smithstonian Institution. 2005). This makes the fuel cell more compact (Grabke, et al. 1997).

A second advantage of SOFCs is that they are one of the most efficient types of fuel cells. Overall efficiency of a fuel cell is defined as the electrical power output divided by the energy input of the fuel (Kendall. 2005). Typically, the electrochemical efficiency of an SOFC is 70% (Kendall. 2005). However, not all of the fuel that enters the fuel cell at the anode is reacted – approximately 20% is lost (Kendall. 2005). Therefore, the overall efficiency of a typical SOFC is 0.8 x 0.7 = 0.56 or 56% (Kendall. 2005). In reality, the efficiency is reduced to 50% due to losses in auxiliary systems, such as air pumps, fuel reforming, and power conversion (Kendall. 2005). However, there is the possibility of further increasing the efficiency of the fuel cell by cogeneration, which means that the waste heat generated by the fuel cell is recovered and used to generate additional electric power using a turbine (Fuel Cells 2000. 2006, Government of Canada, et al. 2003). Cogeneration is made possible by the high operating temperature of the SOFC which allows for high quality heat as a byproduct (Minh & Takahashi. 1995). If cogeneration is carried out by a pressurized hybrid SOFC, the efficiency can reach 75% and even as high as 80% if the power output of the SOFC is decreased in order to reduce ohmic and catalyst losses (Kendall. 2005).

Due to the high operating temperature of the SOFC, catalysts may not be required (Minh & Takahashi. 1995). For intermediate temperature SOFCs, typical catalysts are perovskites and nickel-based compounds (Government of Canada, et al. 2003). The cost of these catalysts is much lower than those used in other types of fuel cells, such as platinum (Williams, et al. 2005).

The electrolyte material in SOFCs also offers several advantages. First, there are no handling or corrosion problems that occur with liquid electrolytes (EG&G Services, et al.

2000). Also, there are more possible cell configurations if a solid electrolyte is used (Minh & Takahashi. 1995). In general, cells with a solid electrolyte tend to be lighter and more compact than cells that use a liquid electrolyte (Minh & Takahashi. 1995). Finally, the electrolyte materials used in SOFCs are mixed ionic and electronic conductors, helping to increase the overall fuel cell efficiency; electronic conduction is not possible with liquid electrolytes (Minh & Takahashi. 1995).

A final advantage of SOFCs is their high tolerance to impurities in the fuel relative to other types of fuel cells. The SOFC is the most resistant to sulphur of all of the types of fuel cells; it can tolerate sulphur levels of several orders of magnitude higher than other types are capable of handling (U.S. Department of Energy. 2006). In addition to this, since SOFCs can use CO itself as a fuel, they are resistant to CO poisoning and thus can use coal-based fuels, such as synthesis gas from coal gasification (33 CO + 1 $CO_2$ + 66 $H_2$) (Alman & Jablonski. 2004, Williams, et al. 2005).

### 2.2.2 Disadvantages of Solid Oxide Fuel Cells

One major disadvantage of SOFCs is that their high operating temperature requires the use of expensive materials, in particular for the interconnect (Boudghene Stambouli & Traversa. 2002). In addition to this, at high temperatures the degradation of cell materials is more rapid and thus the operating lifetime of the fuel cell is reduced (Thomas & Zalbowitz. 2000). By lowering the operating temperature, as in the case of intermediate temperature SOFCs, material costs can be reduced. However, the cell voltage is reduced at lower temperatures due to decreased electrolyte conductivity, diffusion, and reaction kinetics (EG&G Services, et al. 2000).

A second problem with SOFCs is the relatively high thermal expansion coefficient (TEC) of typical electrolyte materials (Kendall. 2005). In addition to this, there can be a TEC mismatch between different cell components depending on the materials used (Kendall. 2005). Because of this, the brittle electrolyte is susceptible to cracking during both start-up and shut-down, when large temperature gradients can develop in the stack (Kendall. 2005). Therefore, long warm-up times are needed for SOFC operation, up to 3 hours can be required for the planar stack configuration (Kendall. 2005). This is a disadvantage compared to most other fuel cell types which have much shorter warm-up times (Kendall. 2005). In order to minimize problems associated with thermal expansion of the stack,

TEC mismatch could be minimized through material selection and processing of the ceramic electrolyte could be improved in order to reduce the defect size and correspondingly increase the fracture resistance (Kendall. 2005).

An additional problem with SOFCs is the difficulty in fabricating thin cell components. It is important that the components be as thin as possible in order to decrease the electrical resistance of the cell, but this presents some manufacturing challenges and thus increases the overall cell cost (Minh & Takahashi. 1995).

### 2.2.3 Applications of Solid Oxide Fuel Cells

One of the major applications of SOFCs is in the area of stationary power generation, potentially both on the large and small scale (Government of Canada, et al. 2003). SOFCs could also be used in the transporation sector in applications such as commercial trucks, military vehicles, aircrafts, and ships (Ceram Research. 2006, Williams, et al. 2005). The ability of SOFCs to tolerate a wide variety of fuels would be an advantage for portable applications as well as in the transportation sector; however, the high operating temperature of SOFCs could be an obstacle to commercialization (Wikimedia Foundation. 2006a).

## 2.3 Interconnects

As mentioned earlier, the interconnect is the component of a fuel cell stack that electrically connects adjacent cells in series (EG&G Services, et al. 2000, Grabke, et al. 1997). The interconnect allows the electrons produced at the anode of one cell to be transferred to the cathode of the adjacent cell in the stack, and it also transports electrons to the external circuit (Wincewicz & Cooper. 2005). Evidently, it is important that the interconnect be electronically conductive (or have a low electrical resistance) at the SOFC operating temperature (EG&G Services, et al. 2000). An accepted minimum electrical conductivity for candidate interconnect materials is 1 S/cm (Zhu & Deevi. 2003a). The electrical properties are usually measured in terms of an area specific resistance (ASR), defined as the ratio of thickness to conductivity (Huang, et al. 2001). The maximum ASR of a candidate interconnect material should not exceed 0.1 $\Omega \cdot cm^2$

(Zhu & Deevi. 2003b). Some authors state an even lower ASR requirement of less than 0.05 $\Omega \cdot cm^2$ or 0.025 $\Omega \cdot cm^2$ (Antepara, et al. 2005, Linderoth, et al. 1996).

In a planar stack, the interconnect also contains channels that distribute the reactant gases to the cell in co-, cross-, or counterflow directions depending on the specific design (Quadakkers, et al. 1996). These channels separate the fuel and oxidant gas from adjacent cells and prevent the gases from directly mixing (EG&G Services, et al. 2000). This is important because if direct combination of the reactant gases does occur, the operating voltage will drop with respect to the ideal cell voltage and the overall efficiency will decrease as a result (Zhu & Deevi. 2003a). Therefore, only a minimum amount of interconnect porosity can be tolerated, and it is especially important that there be no linked or open porosity (Brylewski, et al. 2001). The presence of the interconnect in the stack also ensures that the anode is only contacted by the fuel environment and the cathode is exposed only to the air environment (Zhu & Deevi. 2003a).

In some designs, the interconnect also helps maintain the structural integrity of the stack (Yang, et al. 2003b). Especially for SOFCs operating at reduced temperatures, the interconnect may act as a support for the thin cell components (Quadakkers, et al. 1996). Therefore, one important requirement is that the interconnect have sufficient mechanical strength and creep resistance at the relatively high SOFC operating temperature (Quadakkers, et al. 1994, Wincewicz & Cooper. 2005).

Additionally, the interconnect must satisfy the requirement that its coefficient of thermal expansion (TEC) be compatible with that of the other stack components (EG&G Services, et al. 2000, Grabke, et al. 1997). Thermal stress can be described by the following equation:

$$\sigma = E\Delta\alpha\Delta T \quad (2\text{-}3)$$

where $E$ is the elastic modulus of the interconnect, $\Delta\alpha$ is the difference in coefficient of thermal expansion between the interconnect and adjacent stack components, and $\Delta T$ is the change in temperature that the stack experiences (Yang, et al. 2003b). From Equation 2-3, it is evident that in order to reduce thermal stress, the TEC of the interconnect must be as close as possible to that of the anode, cathode, and electrolyte materials. The TEC of these components typically ranges between 10.5 and 12.5 x $10^{-6}$/°C (Yang, et al.

2003c, Yang, et al. 2003b, Zhu & Deevi. 2003a). TEC compatibility is especially important for brittle interconnect materials as they are less capable of accommodating thermal stress than interconnect materials that are more ductile (Zhu & Deevi. 2003a).

Another important interconnect requirement is high thermal conductivity (Wincewicz & Cooper. 2005). This enables the heat generated at the cathode of one cell to be transferred to the anode of the adjacent cell where it can be used to drive the endothermic fuel reforming reaction (Zhu & Deevi. 2003a). As was mentioned earlier, if internal reforming is possible, there is no need for an external fuel reformer and thus the cost of the fuel cell is reduced (Zhu & Deevi. 2003a). A minimum thermal conductivity limit that candidate interconnect materials must satisfy is 5 W/m·K (Zhu & Deevi. 2003a).

During fuel cell operation, interconnects are simultaneously exposed to two distinctly different environments: an oxidizing gas on the cathode side and a reducing fuel gas on the anode side (Kofstad. 1992). Not only does the interconnect need to be chemically stable in both of these environments, it must also be chemically compatible with other cell materials, in particular with the anode and cathode that it directly contacts (Köck, et al. 1995). If reaction or interdiffusion occurs between the interconnect and electrodes, the formation of intermediate layers is possible, which can increase resistive losses and thus is a detriment to cell performance (Köck, et al. 1995). In addition to this, the interconnect must be chemically compatible with sealing materials and with electrical contact materials, which are used to reduce the contact resistance at the interface between the interconnect and the electrodes (Chen, et al. 2006). Stability of the interconnect involves high temperature oxidation, reduction, sulphidation, and carburization resistance over the projected 40 000 h SOFC lifetime (Wincewicz & Cooper. 2005, Zhu & Deevi. 2003a). It is also important that the interconnect be able to withstand the numerous temperature cycles that will occur within the operating period (Grabke, et al. 1997).

In addition to these requirements, it is important that the cost of the interconnect be as low as possible. Especially for reduced temperature SOFC designs, the interconnect is the bulkiest stack component and thus typically makes up a significant portion of the overall cost (Zhu & Deevi. 2003a). In order for SOFC commercialization to be feasible, both the interconnect raw material cost and fabrication cost must be reduced significantly (Wincewicz & Cooper. 2005).

Over the years, many candidate interconnect materials have been proposed. Despite this, the interconnect remains a critical area that must be addressed before SOFC commercialization becomes a reality (Grabke, et al. 1997). The main interconnect problems that have yet to be solved are low cost and long-term reliability (Elangovan, et al. 2004). Table 2-2 summarizes some important properties of several candidate interconnect materials.

Table 2-2. Properties of Candidate Interconnect Materials (ASM International. 2002a, England & Virkar. 1999, Kofstad. 1992, Köck, et al. 1995, Mankins & Lamb. 2002, Meadowcroft. 1969, Paulik, et al. 1998, Quadakkers, et al. 1994, Yamamoto, et al. 2002, Yang, et al. 2003b, Zhu & Deevi. 2003a).

| Type | | Material | Electrical Conductivity (S/cm) | Tensile Strength (MPa) | Coefficient of Thermal Expansion ($\times 10^{-6}$/°C) | Thermal Conductivity (W/m·K) |
|---|---|---|---|---|---|---|
| Ceramics | | $LaCrO_3$ | 0.34 (700°C)<br>1 (1000°C) | 35 - 65*<br>(800°C)<br>20 - 60*<br>(1000°C) | 9.5 | 5.1<br>(827 - 1127°C) |
| Metals | Cr-Based | Cr-5Fe-1$Y_2O_3$ | $3.4 \times 10^6$<br>(20°C) | 260 - 370<br>(800°C)<br>140 - 200<br>(1000°C) | 11.8<br>(20 - 1000°C) | 35 (20°C)<br>50 (1000°C) |
| | Superalloys | Ni-Base | 8800<br>(800°C) | 750 - 950<br>(700°C) | 14.0 - 19.0<br>(20 - 800°C) | 9 - 11 (20°C)<br>24.4 (800°C)<br>28.4 (1000°C) |
| | Stainless Steels | Austenitic | $1.4 \times 10^5$<br>(20°C)<br>8600<br>(650°C) | 620 - 930<br>(24°C)<br>325 - 580<br>(650°C) | 18.0 - 20.0<br>(20 - 800°C) | 16.3 (100°C)<br>21.5 (500°C) |
| | | Ferritic | $1.7 \times 10^5$<br>(20°C)<br>8700<br>(800°C) | 450 - 590<br>(24°C)<br>160 - 215<br>(650°C) | 11.5 - 14.0<br>(20 - 800°C) | 26.1 (100°C)<br>26.3 (500°C) |

*Flexural Strength (MPa)

### 2.3.1 Interconnect Materials

#### *2.3.1.1 Ceramics*

An early candidate ceramic interconnect material was $Nb_2O_5$-doped $TiO_2$ (Steele. 2000). This material possessed good thermodynamic and electric properties, but had a lower TEC than other cell components (Steele. 2000). During thermal cycling, thermal stresses were generated as a result of the TEC mismatch, resulting in cracking of the brittle ceramic interconnect (Steele. 2000).

Currently, the ceramic interconnect material that is most often used in high temperature SOFCs is a complex perovskite ceramic oxide, doped lanthanum chromite ($LaCrO_3$) (Ceram Research. 2006, EG&G Services, et al. 2000). Many possible dopants have been used, including Co, Fe, Ni, Mg, Cu, S, and V (Wincewicz & Cooper. 2005). Other possible dopants that show promise are alkaline earth oxides: oxides of Be, Mg, Ca, Sr, and Ba (Kofstad. 1992, Wikimedia Foundation. 2006b). Noble metals, such as Au, Pd, Ag, and Pt, have also been tried as dopants for lanthanum chromite; however, they were found to cause volatility above 800°C, which is a concern for long-term fuel cell operation (Wincewicz & Cooper. 2005). Other possible ceramic interconnect materials under development for high temperature SOFCs include a system of $(La,Sr,Ca)(Cr,Mg)O_3$ and $(Y,Ca)CrO_3$ (Kendall. 2005, Minh & Takahashi. 1995).

There are several advantages of using a lanthanum chromite interconnect. It has high electronic conductivity as well as low ionic conductivity, chemical stability in both fuel and air environments at high temperatures, high oxidation resistance, adequate high temperature strength, and finally chemical and TEC compatibility with other cell components (Brylewski, et al. 2001, Kadowaki, et al. 1993, Kendall. 2005, Minh & Takahashi. 1995, Quadakkers, et al. 1994). The long-term reliability of this interconnect material does not seem to be a concern as the lifetime of lanthanum chromite interconnects in tubular SOFCs has been demonstrated for up to 70 000 h with hydrogen as a fuel (Kendall. 2005).

There are several disadvantages of using lanthanum chromite as an interconnect material. First, in the high SOFC operating temperature range, chromium is volatile; evaporation of Cr and its subsequent redeposition on other cell components results in contamination and deteriorates the performance of the fuel cell (Ceram Research. 2006). There are also

difficulties in the manufacturing of lanthanum chromite interconnects. The poor workability of the ceramic limits the size, shape, and complexity of interconnect that can be produced (Brylewski, et al. 2001, Quadakkers, et al. 1994). The sintering process itself is difficult as low pressures and extremely high temperatures can be required. If the lanthanum chromite is undoped, the sintering process must be done at $10^{-7}$ Pa at 1720°C; however, with B doping, sintering can be done in air at 1300°C and with Ca doping, in air at 1600°C (Kendall. 2005). Despite the high sintering temperatures involved, full densification of the lanthanum chromite is extremely difficult to achieve; therefore, the interconnect is not completely gas-tight (Brylewski, et al. 2001, Kadowaki, et al. 1993, Yang, et al. 2003b). Lanthanum chromite is brittle, and because of this it cannot tolerate sudden temperature changes or mechanical impacts (Brylewski, et al. 2001, Horita, et al. 2003, Jian, et al. 2005, Wincewicz & Cooper. 2005). The lack of ductility of ceramic interconnects becomes a major concern for long-term commercial applications (Quadakkers, et al. 1994). The dependence of both the electrical conductivity and mechanical strength of lanthanum chromite on oxygen partial pressure is also a concern. The conductivity of this type of interconnect is high in environments with a high oxygen partial pressure; however, the conductivity is reduced in environments with a low oxygen partial pressure such as in the fuel gas (Quadakkers, et al. 1994, Zhu & Deevi. 2003a). The mechanical strength of lanthanum chromite is also reduced with a decrease in oxygen partial pressure, and the mechanical strength drops more rapidly as doping content is increased (Quadakkers, et al. 1994, Zhu & Deevi. 2003a). An additional problem with lanthanum chromite is its expansion by up to 3% in length when it is exposed to the fuel gas (Kendall. 2005). The result of the expansion is warping, distortion, and possible cracking of the interconnect (Jian, et al. 2005, Kendall. 2005, Yang, et al. 2003b). A final disadvantage of using lanthanum chromite interconnects is its cost. As was mentioned above, the manufacturing of these interconnects is very difficult; therefore, the cost is high. In addition to this, the raw material cost is high because La is a rare earth element (Linderoth, et al. 1996). The material cost for lanthanum chromite interconnects is much higher than that for metallic interconnects, since the base elements of high temperature alloys are transition metals (Ni, Fe, Co, and Cr), which are much cheaper than rare earth elements (Linderoth, et al. 1996).

#### *2.3.1.2 Metals*

The use of metallic interconnects both with and without coatings becomes a possibility for reduced temperature SOFCs, which operate below 800°C (Grabke, et al. 1997, Wincewicz & Cooper. 2005). There are several advantages to using metallic interconnects as an alternative to ceramic materials. First, metallic interconnects are stronger and more ductile than lanthanum chromite (Jian, et al. 2005, Wincewicz & Cooper. 2005). Also, the electrical conductivity of metallic materials is higher than that of ceramics (Jian, et al. 2005, Wincewicz & Cooper. 2005). A typical metallic interconnect will have an electrical conductivity at least 2 orders of magnitude higher than that of doped lanthanum chromite (Kofstad. 1992). Metals also have higher thermal conductivities than ceramics (Jian, et al. 2005, Wincewicz & Cooper. 2005). Therefore, by using a metallic interconnect, more of the heat generated at the cathode can be transferred to the anode where it can be consumed in the endothermic fuel reforming reaction (Quadakkers, et al. 1994). Also, high thermal conductivity reduces stresses generated in the stack due to temperature gradients and reduces the air cooling requirement of the fuel cell (Elangovan, et al. 2003, Linderoth, et al. 1996). The material and fabrication costs of metallic interconnects are much lower than for lanthanum chromite (Jian, et al. 2005, Wincewicz & Cooper. 2005). It is estimated that replacing ceramic interconnects with metallic materials could reduce material costs by approximately 85% (Alman & Jablonski. 2004). Manufacturing metallic interconnects is much simpler than ceramics and greater control over interconnect dimensions is possible (Elangovan, et al. 2003, Yang, et al. 2003b).

There are problems with using metallic interconnects as opposed to ceramic materials. First, the thermal expansion coefficient of metals tends to be higher than that of the other stack components. This results in the generation of thermal stresses in the stack as was discussed previously. A more significant problem with metallic interconnects is that even at the reduced SOFC operating temperatures, they can react with the service environment on both the anode and cathode sides, resulting in the formation of a surface oxide scale on the interconnect (Quadakkers, et al. 2003). This oxide layer is susceptible to cracking and spalling when exposed to temperature cycles occurring during normal fuel cell operation (Jian, et al. 2005). Oxidation of metallic interconnects can cause dimensional changes and thus reduce the load bearing ability of the component (Quadakkers, et al. 2003). The scales could also block the flow of gas, either fuel or air,

through the interconnect channels (Quadakkers, et al. 2003). In addition to this, the formation of a surface oxide greatly reduces the electrical conductivity of the interconnect as these scales tend to be semi-conducting or even insulating (Quadakkers, et al. 2003, Zhu & Deevi. 2003b). As mentioned previously, the area specific resistance (ASR) of an interconnect material should be as low as possible. The electrical resistance of the oxide scale is proportional to its thickness, and increases with cracking and porosity of the layer (Zhu & Deevi. 2003b). There are several requirements for an oxide scale forming on an SOFC interconnect. It should have a low growth rate in both oxidising and reducing environments, good scale adhesion in order to resist cracking and spalling during thermal cycling, a homogeneous microstructure, a uniform thickness, little or no porosity, and be electrically conductive (Zhu & Deevi. 2003b). Unfortunately, the properties of a low growth rate and a high electronic conductivity are mutually exclusive and a compromise must be made between them (Zhu & Deevi. 2003b). A possible solution would be to use a noble metal interconnect that does not oxidize in the fuel cell environment; however, the limited availability and high cost of these materials makes noble metal interconnects unsuitable for commercial application (Quadakkers, et al. 2003).

Candidate metallic interconnect materials are divided into three main groups: chromium-based alloys, superalloys (Ni-, Fe- and Co-based), and stainless steels. The composition of all alloys in all subsequent text is given in wt% unless otherwise stated.

#### 2.3.1.2.1 High Temperature Alloys

In general, high temperature alloys contain chromium and/or aluminum (Kofstad. 1992). The oxidation resistance of these alloys comes from the formation of a protective scale on the surface of the metal through the preferential oxidation of Cr to $Cr_2O_3$ (chromia), or Al to $Al_2O_3$ (alumina), or a combination of the two (Kofstad. 1992). Alloys that form a protective scale consisting predominately of chromia are referred to as "chromia formers"; similarly, those with an oxide scale consisting mainly of alumina are called "alumina formers" (Kofstad. 1992). As was mentioned in the previous section, the conductivity of the oxide scales that form on candidate interconnect materials must be as high as possible for SOFC applications. The conductivity of chromia is much higher than that of alumina; the former is considered a semi-conductor while the latter is an insulator (Yang, et al. 2003b). In the literature, a large range of conductivity values are listed for

both chromia and alumina; however, it is generally accepted that the conductivity of alumina is up to a factor of $10^5$ to $10^6$ lower than that for chromia (Kofstad. 1992, Yang, et al. 2003b). At 900°C, the conductivity of chromia is $10^{-2}$ to $10^{-1}$ S/cm while that for alumina ranges from $10^{-8}$ to $10^{-6}$ S/cm (Kofstad. 1992, Quadakkers, et al. 1994). Therefore, only chromia formers are typically considered as candidate interconnect materials (Kofstad. 1992).

Although it may seem advantageous to use chromia formers for SOFC interconnects, there is one disadvantage of selecting this group of high temperature alloys instead of the alumina formers. The oxidation rates of alumina forming alloys are much lower than those of chromia forming alloys (Quadakkers, et al. 1994). One author states that the growth rate of chromia is "usually 4 orders of magnitude higher than alumina (Zhu & Deevi. 2003a). Another source reports that the growth rate of alumina "is 10 times slower" than that of chromia (Huang, et al. 2001). The main reason for the more rapid oxidation kinetics of chromia forming alloys is that diffusion of both metal and oxygen ions through alumina is much slower than ion transport through chromia scales (Kane. 2003).

The oxide scales that form on the surface of high temperature alloys are susceptible to cracking and spalling over long periods of time due to stresses in the scale generated by heating and cooling (Quadakkers, et al. 1994). Breakdown of the protective scales can also generated by mechanical action such as erosion, wear, and impact among others (Kane. 2003). Repeated oxide growth, damage, and repair can result in depletion of the scale-forming elements in the alloy (Quadakkers, et al. 1994). Once the amount of scale-forming element in the alloy drops below a certain level, a protective oxide is no longer formed (Quadakkers, et al. 1994). In some types of high temperature alloys, oxidation of the base element, typically Fe or Ni, will then occur, resulting in the formation of a scale that grows rapidly and is non-protective (Quadakkers, et al. 1994).

Some high temperature alloys contain large amounts of silicon and form a protective silica layer instead of chromia or alumina; these alloys are known as "silica formers" (Ostwald & Grabke. 2004). These alloys are not usually considered to be candidate SOFC interconnect materials for two reasons. First, in order to form a protective silica layer, the silica content must be fairly high and embrittlement of the alloy tends to occur

as a result (Ostwald & Grabke. 2004). Also, like alumina, silica is a poor electronic conductor (Ostwald & Grabke. 2004).

*2.3.1.2.1.1 Cr-Based Alloys*

Cr-based alloys are a group of high temperature alloys with a bcc crystal structure (Yang, et al. 2003b). These alloys contain reactive element (RE) alloying additions (Y, Ce, La, or Zr) either as metals or as oxides (Zhu & Deevi. 2003a). The purpose of the RE addition is to reduce the rate of oxidation, to improve scale adhesion and reduce spalling, and to refine the grain size of the oxide scale (Quadakkers, et al. 1994, Zhu & Deevi. 2003a). The parabolic rate constant of Cr-based alloys is reduced by a factor of 10 to 100 from that of pure Cr due to the RE alloying additions (Zhu & Deevi. 2003a). Although it is known that RE additions improve oxidation behaviour, the exact mechanism has not been established. It is thought that that the reactive elements segregate to the oxide grain boundaries where they are able to reduce outward Cr diffusion (Zhu & Deevi. 2003a). Oxidation then occurs predominately through inward oxygen diffusion, which reduces the oxidation rate (Zhu & Deevi. 2003a). Also, fewer cavities and pores are formed in the oxide scale as a result of the change in oxidation mechanism, improving scale adherence (Zhu & Deevi. 2003a).

There are several commercially available Cr-based high temperature alloys. These include Durcopur CR (Cr), Ducrolloy CRL (Cr-$La_2O_3$ or Cr-0.4$La_2O_3$), Ducrolloy CRF (Cr-5Fe-1$Y_2O_3$), and $Cr_3Co$ (Köck, et al. 1995, Zhu & Deevi. 2003a). $Cr_3Co$ is not usually considered as a candidate interconnect material because it has a much higher oxidation rate than other Cr-based alloys as well as reduced scale adherence, which results in spallation of the protective oxide at temperatures above 950°C (Zhu & Deevi. 2003a). The reason for this is that $Cr_3Co$ lacks the RE additions of the other Cr-based alloys (Zhu & Deevi. 2003a).

Ducrolloy CRF, or Cr-5Fe-1$Y_2O_3$ (this notation indicates that the alloy is primarily composed of Cr and contains additions of 5 wt% Fe and 1 wt% $Y_2O_3$), has the best properties of the Cr-based alloys and is thus a possible SOFC interconnect material for high temperature SOFCs (Köck, et al. 1995). Cr-5Fe-1$Y_2O_3$ is known as an oxide dispersion strengthened (ODS) alloy because the RE addition is in the form of fine, uniformly distributed oxide particles (particle size range of 0.03 to 1μm) which, in

addition to improving the oxidation behaviour of the alloy, also provide high temperature strength (Köck, et al. 1995). For Ducrolloy CRF, the Fe addition provides additional solid solution strengthening (Köck, et al. 1995). Cr-5Fe-1$Y_2O_3$ is produced using powder metallurgy (PM) processing operations (Köck, et al. 1995).

There are several advantages to using Ducrolloy CRF as an interconnect material. This alloy has high electrical and thermal conductivity, limited ionic conductivity, and is non-permeable to gases (Köck, et al. 1995). It has good high temperature oxidation resistance, strength, and creep resistance (Quadakkers, et al. 1994). Cr-5Fe-1$Y_2O_3$ also has good corrosion resistance in high temperature carburizing and nitriding environments, and it is not susceptible to embrittlement in environments containing hydrogen (Köck, et al. 1995). Although Cr-based alloys are fairly brittle compared to other metallic materials and have a ductile to brittle transition temperature (DBTT) above room temperature due to their bcc crystal structure, these alloys are significantly more ductile at the SOFC operating temperature range than ceramic alternatives (Köck, et al. 1995). Finally, the thermal expansion coefficient of Cr-5Fe-1$Y_2O_3$ (11.8 x $10^{-6}$/°C in the range of 20 – 1000°C) is very similar to that of the other stack components (Grabke, et al. 1997, Yang, et al. 2003b, Zhu & Deevi. 2003a). By varying the Fe content, the TEC of Ducrolloy CRF can be adjusted to match that of the other cell materials (Köck, et al. 1995).

Compared to other commercially available high temperature alloys, Ducrolloy CRF has much better oxidation resistance. During oxidation for 100 h at 1000°C, Cr-5Fe-1$Y_2O_3$ had significantly lower weight gain than two Ni-based superalloys: Inconel 601 and Inconel 657 (Linderoth, et al. 1996). The oxide layer on the Ni-based superalloys spalled significantly, while that on the Cr-based alloy buckled significantly but did not spall (Linderoth, et al. 1996). Also, internal oxidation was observed in the Ni-based alloys but not in Cr-5Fe-1$Y_2O_3$ (Linderoth, et al. 1996).

One major disadvantage of using Cr-based alloys at high temperatures is the formation of volatile Cr species (Zhu & Deevi. 2003a). There are several possible reactions (Kofstad. 1992, Zhu & Deevi. 2003a):

$$\frac{1}{2}Cr_2O_3(s) + \frac{3}{4}O_2(g) \Leftrightarrow CrO_3(g) \quad (2\text{-}4)$$

$$\frac{1}{2}Cr_2O_3(s)+\frac{3}{4}O_2(g)+H_2O(g)\Leftrightarrow CrO_2(OH)_2(g) \qquad (2\text{-}5)$$

$$\frac{1}{2}Cr_2O_3(s)+\frac{1}{2}O_2(g)+\frac{1}{2}H_2O(g)\Leftrightarrow CrO_2OH(g) \qquad (2\text{-}6)$$

As the above reactions are dependent on the oxygen partial pressure, they are significant at the cathode (Kofstad. 1992). Once the volatile Cr vapour species are formed, they can deposit as chromia at the cathode/electrolyte interface, where they can then react with the cathode to form additional spinel phases (Köck, et al. 1995, Yang, et al. 2003b). The first problem with this is that the number of active sites on the cathode available for reaction decreases (Yang, et al. 2003b). Also, the deposits increase both diffusion and charge transfer resistances (Simner, et al. 2005, Yang, et al. 2003b). The overall effect is electrochemical degradation and a reduction in cell performance, the extent of which depends on the type of cathode material in the stack (Quadakkers, et al. 2003). Another problem with the vaporisation of chromium from the oxide layer is that the oxidation rate is increased (Huang, et al. 2000). Below temperatures of 900°C, the amount of material lost to the formation of volatile vapour species is not significant; however, even in the reduced operating temperature range of 700 – 850°C, formation of the oxyhydroxide species, as in Equations 2-5 and 2-6, is not negligible and can result in cell degradation (Kofstad. 1992, Köck, et al. 1995, Quadakkers, et al. 2003, Yang, et al. 2003b). The presence of water vapour in the air stream enhances the formation of oxyhydroxides and thus degradation is more likely (Zhu & Deevi. 2003a). In order to prevent the vaporisation of chromium from occurring, it is possible to apply a protective coating to the cathode side of the Cr-based alloy interconnect (Batawi, et al. 1999). Types of possible coatings include lanthanum chromite, lanthanum magnetite ($La_{0.8}Sr_{0.2}MnO_3$), Sr-doped lanthanum cobalt oxide ($LaCoO_3$, or LSC), Sr-doped lanthanum iron cobalt (LSFeCo), metallic layers, or oxide layers (Batawi, et al. 1999, Minh & Takahashi. 1995, Quadakkers, et al. 2003, Zhu & Deevi. 2003b). The advantage of using perovskite oxide or metallic coatings is that these materials are highly conductive and thus interconnect resistance would be reduced (Batawi, et al. 1999). However, both material and production costs of the interconnect increase substantially when a coating is required (Zhu & Deevi. 2003b).

There are several other disadvantages of using Cr-based high temperature alloys as an SOFC interconnect material. First, the processing cost is quite high. Initially, extensive machining was required to fabricate Cr-5Fe-1$Y_2O_3$ interconnects. Following the development of powder metallurgy methods such as near-net-shaping, manufacturing costs were reduced; however, manufacturing of Cr-based alloy interconnects is more expensive and difficult than for other types of metallic interconnects (Batawi, et al. 1999, Kendall. 2005, Yang, et al. 2003c). Also, after long-term oxidation studies, it was determined that Cr-based alloys are unsuitable for application in high temperature SOFCs. One study predicted that at 900°C, the oxide layer formed on Cr-5Fe-1$Y_2O_3$ would be 10μm thick after 1 year and 23μm after 5 years (close to the projected SOFC operating lifetime of 40 000 h) (Zhu & Deevi. 2003a). At 1000°C, the ASR of Ducrolloy CRF was found to be greater than the maximum value of 0.1 $\Omega \cdot cm^2$ after only 75 h (Zhu & Deevi. 2003b). Both authors concluded that the application of Cr-based alloys as SOFC interconnects should be limited to reduced operating temperatures (Zhu & Deevi. 2003a, Zhu & Deevi. 2003b). However, other types of alloys, such as Fe- or Ni-based Cr-containing alloys, would be better suited for reduced temperature SOFC interconnect applications than Cr-based alloys, because they are less expensive, more ductile, and easier to manufacture (Zhu & Deevi. 2003b).

*2.3.1.2.1.2 Superalloys*

Superalloys are a group of alloys designed for high temperature applications where both mechanical strength and corrosion resistance are required (Yang, et al. 2003b). The base metal is a group VIII element, typically Fe, Ni, or Co (Yang, et al. 2003b). Superalloys have a γ-austenitic fcc matrix containing second phase particles that provide strengthening (Yang, et al. 2003b). The most important second phase particles are carbides of the form MC, $M_{23}C_6$, $M_6C$, or more rarely $M_7C_3$, where M is a carbide-forming element such as Mo, W, Ti, Nb, Ta, and/or Cr (Yang, et al. 2003b). In Ni- and Fe-(Ni)-based superalloys, second phase γ' fcc ordered intermetallic compounds of the form $Ni_3(Al,Ti)$ are also present (Yang, et al. 2003b). Three groups of superalloys are considered for high temperature SOFC interconnect applications: Fe-based, Ni-based, and Co-based superalloys.

#### 2.3.1.2.1.2.1 Fe-Based Superalloys

Fe-based superalloys considered as candidate interconnect materials are chromia formers. In order to form a continuous, protective chromia scale, a minimum of 18% Cr is required (Yang, et al. 2003c). However, in order to ensure that no significant Cr depletion of the alloy occurs over long-term operation and to prevent significant scale rupture, a Cr content in the range of 20 to 25% is needed (Yang, et al. 2003b). If alloying additions such as Al, La, Ce, Y, or other reactive elements are present, the minimum chromium content can be reduced to approximately 18%, depending on the exact alloy composition (Yang, et al. 2003b). The Al content of the alloy should be kept below 3% to prevent the formation of an insulating alumina scale on the interconnect surface (Yang, et al. 2003b). One advantage of using Fe-based superalloys as interconnect materials is that they are typically less expensive than Cr-based alloys or Ni-based superalloys (Yang, et al. 2003c). However, their thermal expansion coefficient is typically between 15.0 and 20.0 x $10^{-6}$/°C within the range of room temperature to 800°C, which is much higher than that of the other fuel cell components (Yang, et al. 2003b).

#### 2.3.1.2.1.2.2 Ni-Based Superalloys

Ni-based superalloys are widely used in industry for their high temperature strength and corrosion resistance in aggressive environments (Vázquez-Navarro, et al. 1999). Ni-based superalloys can be either chromia formers or alumina formers; however, only the chromia formers are considered as candidate SOFC interconnect materials (Kadowaki, et al. 1993). Similar to Fe-based superalloys, a minimum Cr content of 18% is required to ensure the formation of a protective chromia scale, and additions of 20 to 25% are recommended to prevent depletion of the base metal over long periods of exposure (Yang, et al. 2003c, Yang, et al. 2003b). Again, additions of reactive elements can lower the Cr requirement to 18%, and Al content should be kept below 3% to avoid the formation of an insulating oxide layer (Yang, et al. 2003b). Commercially available Ni-based superalloys typically contain between 15 and 30% Cr (Quadakkers, et al. 1994)

One study of the oxidation of a commercial Ni-based superalloy containing 22% Cr in pure $O_2$ at 800°C found that in the initial stages of oxidation, both NiO and $Cr_2O_3$ are formed (Vázquez-Navarro, et al. 1999). Subsequently, a Cr-based spinel ($NiCr_2O_4$)

forms in the NiO layer, impeding the outward diffusion of Ni through the oxide scale (Vázquez-Navarro, et al. 1999). The resulting oxide consists of a NiO layer at the surface of the base alloy with an external chromia scale (Vázquez-Navarro, et al. 1999). Growth of the oxide is then controlled by the outward diffusion of chromium ions (Vázquez-Navarro, et al. 1999). Although the Cr content of the superalloy was not high enough to result in the formation of an oxide scale consisting solely of chromia, the protective layer was found to be stable and adherent with no spalling for up to 27 days of oxidation (Vázquez-Navarro, et al. 1999).

Slightly different results were found in a study of the oxidation of Ni-Cr alloys in 0.1 atm $O_2$ at temperatures from 800 to 1200°C. If the Cr content of the alloy was below 5%, internal chromium oxidation was found to occur below the outer NiO scale covering the alloy surface (Giggins & Petit. 1969). The oxidation rate was controlled by outward diffusion of Ni through the oxide layer. NiO is not considered to be a protective oxide as its growth rate is too high (Wasielewski & Rapp. 1972). When a higher amount of Cr was added, between 5 and 30%, the oxide layer formed was found to consist of chromia at the alloy grain boundaries while a base layer of chromia with a NiO external scale was observed to cover the grain surfaces (Giggins & Petit. 1969). Lateral diffusion occurred between the outer chromia and the internal chromia subscale, in some cases resulting in the formation of an outer protective chromia layer depending on the oxidation time and the initial alloy grain size (Giggins & Petit. 1969). For Ni-Cr alloys with a Cr content above 30%, an external protective chromia scale was formed on the surface of the alloy and the oxidation rate depended on the outward diffusion of Cr through the oxide scale (Giggins & Petit. 1969).

As mentioned above, additions of reactive elements such as La, Zr, and Y improve the oxidation resistance of Ni-based superalloys and allow the Cr content of the alloy to be reduced. One study of the oxidation of ASL528, an Ni-based alloy containing 16% Cr and additions of La and Zr, at 1000°C for 100 h, found that the oxidation rate was much lower than that of Inconel 600, a Ni-based alloy that also contains 16% Cr but without RE additions (Uehara, et al. 2003). The oxide layer that formed on ASL528 had much better adhesion and, as a result, significantly less spalling than in the case of Inconel 600 (Uehara, et al. 2003). In a study of the effect of RE additions on Inconel 600, it was found that the addition of La resulted in a reduction in the area specific resistance (ASR)

of the interconnect by one order of magnitude during oxidation at 900°C for 200 h in both air and a $H_2/H_2O$ reducing atmosphere (Zhu & Deevi. 2003b).

Several commercially available Ni-based superalloys have been considered as candidate materials for SOFC interconnect applications. One study compared the oxidation behaviour of thin foils (approximately 113μm thick) of various Ni-based superalloys over a range of temperatures between 800 and 1000°C for up to 10 000 h (England & Virkar. 1999). The oxidation rate of Haynes 230 (22% Cr, 5max% Co, 2% Mo, 14% W, 0.35% Al, 3 max% Fe, 0.1% C, 0.02% La) was the slowest of the superalloys studied, followed by Hastelloy X (22% Cr, 18% Fe, 9% Mo, 1.5% Co, 0.1% C, 0.6% W), Inconel 718 (50 – 55% Ni, 17 – 21% Cr, 2.8 – 3.3% Mo, 4.75 – 5.5% Nb, 0.65 – 1.15% Ti, 0.2 – 0.8% Al, balance Fe) , and finally Inconel 625 (20 – 23% Cr, 5% Fe, 8 – 10% Mo, 0.4% Ti, 3.15 - 4.15% (Nb + Ta), 0.4% Al), which had the fastest oxidation rate (England & Virkar. 1999). ASR measurements of the foils agreed with the oxidation results. Inconel 625, with the thickest oxide scale, had the highest ASR while Haynes 230 had the lowest ASR (England & Virkar. 1999). Despite this result, the study concluded that Haynes 230 thin foils are unsuitable as high temperature SOFC interconnects since the ASR of this alloy was found to be 1.1 $\Omega \cdot cm^2$ after 10,000 h of oxidation in air at 800°C, which is at least one order of magnitude higher than the upper limit for SOFC applications (England & Virkar. 1999).

There are several advantages of using Ni-based superalloys as SOFC interconnect materials. Both gas tightness and machinability are significantly better than for ceramic alternatives (Kadowaki, et al. 1993). Also, Ni-based superalloys have better oxidation resistance than many other metallic materials proposed for interconnect applications, in particular stainless steels (England & Virkar. 1999). In the case of Haynes 230, an oxidation study at 850°C for 100 h found that this promising Ni-based superalloy had a lower weight gain than Cr-5Fe-1$Y_2O_3$ (Linderoth, et al. 1996).

One of the disadvantages of using Ni-based alloys is shared with Cr-based alloys, i.e., the formation of volatile Cr species, which results in the degradation of cell performance (Zhu & Deevi. 2003b). Also, the oxidation rate of these alloys over long periods of exposure to high temperature SOFC operating conditions is too high, due in part to spallation of the oxide under thermal cycling conditions (Zhu & Deevi. 2003b). In addition to this, the material cost of Ni-based superalloys is significantly higher than

other candidate interconnect materials such as stainless steels (Yang, et al. 2003c). However, the most significant problem with Ni-based alloys is their thermal expansion coefficient mismatch with other cell components (Quadakkers, et al. 2003). The TEC of Ni-based superalloys typically ranges between 14.0 and 19.0 x $10^{-6}$/°C, which is significantly higher than the TEC range for the other stack components (10.5 to 12.5 x $10^{-6}$/°C) (England & Virkar. 1999, Ostwald & Grabke. 2004, Yang, et al. 2003c, Zhu & Deevi. 2003a). One way of minimizing this problem is to use thin foil Ni-based superalloy interconnects, which are more flexible and should be able to better accommodate the thermal stresses generated by the TEC mismatch (Zhu & Deevi. 2003b). Alternately, the TEC of Ni-based alloys can be modified through alloying additions (Yang, et al. 2006c). Additions of Mn, Fe, Co, and Cr cause the TEC of Ni-based alloys to increase, while additions of Mo, W, C, Al, and Ti result in a decrease in the TEC (Alman & Jablonski. 2004, Yang, et al. 2006c). The following relation has been proposed for estimating the TEC of Ni-based alloys that do not contain Fe in the temperature range of room temperature to 700°C (Alman & Jablonski. 2004):

$$CTE = 13.8732 + 7.2764 \times 10^{-2}[Cr] + 3.751 \times 10^{-2}([Ta] + 1.95[Nb]) + 1.9774 \times 10^{-2}[Co] + 7.3 \times 10^{-5}[Co]^2 + 1.835 \times 10^{-2}[Al] - 7.9532 \times 10^{-2}[W] - 8.2385 \times 10^{-2}[Mo] - 1.63381 \times 10^{-1}[Ti] \quad (2\text{-}7)$$

In Equation 2-7, each term in square brackets represents the concentration of the specific element in wt%. The calculated CTE value represents the mean thermal expansion coefficient of the alloy with units of $10^{-6}$/°C. A recent study focused on developing a Ni-based superalloy with a low TEC that would be suitable for use in intermediate temperature SOFCs, with operating temperatures in the range of 700 to 800°C (Alman & Jablonski. 2004). Alloys based on the composition Ni-(18–22)Mo-12Cr-1Ti were developed with a TEC ranging between 12.9 and 15.4 x $10^{-6}$/°C, depending on the exact concentration of alloying elements such as W, Mn, and Y (Alman & Jablonski. 2004). During oxidation at 750 and 800°C in dry air for 3300 h; oxide scales consisting primarily of $Cr_2O_3$ and $(Mn,Cr,Ni)_3O_4$ spinel were formed on the alloys (Alman & Jablonski. 2004). Two different low TEC Ni-based superalloys had a lower specific mass gain than Crofer 22 APU, a ferritic stainless steel containing 22% Cr, despite the lower Cr content of the Ni-based alloys (Alman & Jablonski. 2004). When the oxidation results were extrapolated to the projected SOFC operating life of 40 000 h, the specific mass gain of

the low TEC Ni-based alloys was calculated to be 1.25 and 2 times lower than that of Crofer 22 APU (Alman & Jablonski. 2004).

Another solution to the TEC mismatch problem, recently proposed, is the use of cladding or a similar process in order to fabricate a composite interconnect structure consisting of a thick plate of ferritic stainless steel with a thin plate of Ni-based superalloy on either side (Chen, et al. 2006, Yang, et al. 2006a). An advantage of this type of interconnect structure is that it would be cheaper than an interconnect made entirely of a Ni-based superalloy (Chen, et al. 2006, Yang, et al. 2006a).

2.3.1.2.1.2.3 Co-Based Superalloys

As with the other groups of superalloys, Co-based superalloys that are considered as candidate SOFC interconnect materials are chromia formers. In order for a protective, adherent chromia layer to form, a minimum of 25% Cr should be added (Yang, et al. 2003b). If Cr is added to Co in an amount less than 10%, the oxidation rate of the alloy actually increases by a factor of 3 from that of pure Co; in this case the oxide scale is composed predominately of CoO with some $CoCr_2O_4$ spinel (Yang, et al. 2003b). The oxidation rate decreases as more Cr is added, and reaches a minimum in the range of 20 to 30% Cr. In this Cr content range, a protective chromia scale is formed on the surface of the alloy (Kofstad & Hed. 1969). In order to improve the oxidation resistance of Co-based superalloys, additions of Al, B, Ca, and Zr can be used (Yang, et al. 2003b). If Mo or Nb is present, the oxidation resistance of Co-based alloys is reduced and in some cases, catastrophic oxidation is possible (Wasielewski & Rapp. 1972).

Of all the groups of superalloys, the Co-based alloys are the least promising candidates for SOFC interconnect application. The TEC range of the Co-based alloys is typically 14.0 to 17.0 x $10^{-6}$/°C between room temperature and 800°C. Although this range is slightly lower than that of the Ni-based superalloys, it is still significantly higher than that of other stack components (Yang, et al. 2003b). The high temperature mechanical properties of the Co-based superalloys are not as good as those of the Ni-based superalloys. Also, the oxidation resistance of the Co-based alloys is not as good as other high temperature alloys (Wasielewski & Rapp. 1972, Yang, et al. 2003b).

2.3.1.2.2 Stainless Steels

Stainless steels are a group of Fe-C based alloys that contain Cr and additional alloying elements (Smith. 1993, Yang, et al. 2003b). Stainless steels are typically used in industry in applications where corrosion resistance is required (Smith. 1993). In order for a steel to be considered a stainless steel, it must contain at least 12% Cr (Smith. 1993). In order to obtain adequate oxidation resistance under SOFC operating conditions, chromium additions of a minimum of 18% and preferably greater than 20% are required (Yang, et al. 2003c). However, too much Cr can deteriorate the performance of the fuel cell (Kung, et al. 2000). Stainless steels are divided into four main groups: austenitic stainless steels, ferritic stainless steels, martensitic stainless steels, and precipitation hardening stainless steels (Smith. 1993). Two groups of stainless steels have been considered for SOFC interconnect application: austenitic stainless steels and ferritic stainless steels.

*2.3.1.2.2.1 Austenitic Stainless Steels*

Austenitic stainless steels have an fcc crystal structure in the temperature range from room temperature to the melting point (Yang, et al. 2003b). In order to stabilize the austenite phase at lower temperatures, alloying additions such as Ni, Mn, or a combination of the two are added (Yang, et al. 2003b). A major problem with using austenitic stainless steels as a SOFC interconnect material is that these steels have a higher thermal expansion coffecient than the other stack materials (Grabke, et al. 1997). The TEC range of austenitic stainless steels is typically 18 to 20 x $10^{-6}$/°C from room temperature to 800°C, compared to 10 to 12 x $10^{-6}$/°C for the other cell components (Yang, et al. 2003b). Although austenitic stainless steels are significantly cheaper than the high temperature alloys, they are typically more expensive than ferritic stainless steels (Garcia-Vargas, et al. 2005a).

*2.3.1.2.2.2 Ferritic Stainless Steels*

Ferritic stainless steels have a body centered cubic (bcc) ferritic (α-Fe) microstructure under most heat treatment conditions (Smith. 1993). The Cr content of commercial ferritic stainless steels typically ranges from 11 to 30%, and the carbon content is usually

less than 0.12% (Smith. 1993). Ferritic stainless steels can be used in applications requiring corrosion resistance as well as high temperature resistance (Smith. 1993). The corrosion resistance of ferritic stainless steels is similar to that of austenitic stainless steels; however, ferritic stainless steels are cheaper as they lack the Ni alloying additions of austenitic stainless steels (Smith. 1993). Ferritic stainless steels can be divided into two groups based on microstructure: group 1, containing 15 to 18% Cr and approximately 0.06% C, and group 2, containing 25 to 30% Cr and approximately 0.08% C. Group 1 steels have a ferritic microstructure below 900°C consisting of a Cr-rich solid solution of α-Fe and (Fe,Cr)-C intergranular precipitates (Smith. 1993). The microstructure of group 2 steels is similar to that of group 1 steels, except that the (Fe,Cr)-C precipitates are typically coarser (Smith. 1993). In order to reduce the amount of Cr consumed in the formation of carbide precipitates, small amounts of carbide forming elements, such as Nb or Ti, are added (Smith. 1993).

Commercially available ferritic stainless steels typically have chromium contents in the range of 7 to 28%, with larger chromium additions providing increased oxidation resistance (Quadakkers, et al. 2003). In order to ensure the formation of a protective chromia layer on the surface of the steel under intermediate temperature SOFC operating conditions, a minimum of 17% Cr is required; however, at least 20% Cr should be added in order to prevent Cr depletion in the alloy (Yang, et al. 2003c, Yang, et al. 2003b). In many SOFC stacks, a contact paste is applied to the interconnect in order to improve its electrical conductivity. Cr can also be consumed in the interaction between the stainless steel interconnect and this contact material; therefore, up to 22% Cr may be required to prevent depletion of Cr below the metal/oxide interface (Yang, et al. 2003b). There is also an upper limit on the Cr content of stainless steels suitable for SOFC interconnect applications. If the alloy contains too much chromium, there is a possibility of sigma phase formation (Yang, et al. 2003b). Sigma phase is an intermetallic (Fe,Cr) precipitate that forms at the stainless steel grain boundaries during prolonged exposure to temperatures between 550 and 870°C (Smith. 1993, Yang, et al. 2003b). The precipitates are hard and brittle and thus cause reduced ductility of the stainless steel known as sigma phase embrittlement (Smith. 1993, Yang, et al. 2003b). Another problem with the formation of sigma phase precipitates is that Cr from the alloy is consumed, meaning that less Cr is available for the formation of a protective chromia layer (Yang, et al. 2003b). The formation of sigma phase precipitates is enhanced by the presence of various alloying additions such as Mo (Yang, et al. 2003b). In order to avoid the formation of

sigma phase at SOFC operating temperatures, the Cr content of the stainless steel should be kept well below 29% (Elangovan, et al. 2006). Another problem with using stainless steels with high chromium contents for interconnect materials is that thermal expansion mismatch becomes a problem; this typically occurs for chromium contents above 26% (Yang, et al. 2003c, Yang, et al. 2003b). In terms of TEC constraints, stainless steels containing 20% Cr would be ideal, whereas in order to maximize the electrical conductivity of the interconnect, 22% Cr should be added (Antepara, et al. 2005, Mikkelsen & Linderoth. 2003).

In order to improve the properties of Fe-Cr stainless steel alloys, to make them more suitable for interconnect applications, various alloying additions have been examined. Additions of Al and Si improve the oxidation behaviour of stainless steels (Uehara, et al. 2003, Yang, et al. 2003c). However, these additions are typically kept below 1% in order to avoid the formation of an insulating alumina or silica scale on the surface of the alloy (Yang, et al. 2003c, Zhu & Deevi. 2003a). In addition, the Al and Si contents should be kept at low levels to maintain good fabricability of the steel (Jablonski, et al. 2005). At low alloying contents, the Al and Si react with oxygen diffusing inward through the oxide scale to form internal oxides at the metal/oxide interface which improve the adhesion of the oxide scale (Yang, et al. 2004a).

Additions of Ti have also been found to improve the oxidation behaviour of ferritic stainless steels under SOFC operating conditions. In an oxidation study at 1000°C for 100 h, increasing Ti additions up to a maximum of 0.54% reduced the weight gain of stainless steels containing between 16 and 25% Cr (Uehara, et al. 2003). Similar to Al and Si, Ti has a high affinity for oxygen and thus it reacts with inward diffusing oxygen to form titania precipitates below the metal/oxide layer which strengthen the interface (Quadakkers, et al. 2003). Titanium is also a strong carbide former; therefore, it can also form Ti carbides below the metal/oxide interface and prevent the formation of Cr carbides, thus effectively increasing the amount of Cr that is available to form a protective oxide. Titanium decreases the electrical resistance of the oxide layer, as it can diffuse into the chromia and increase its conductivity through defect conduction (Meulenberg, et al. 2003). Although small alloying additions of Ti are beneficial, there is an upper limit on the amount of Ti that should be added. In an oxidation study at 800°C in air for 1000 h, the weight gain of Fe-25Cr-0.1Y-2.5Ti was significantly higher than that for similar steels containing no Ti (Zhu & Deevi. 2003a). Niobium and Mo are also

added to ferritic stainless steels as carbide formers. A ferritic Ti-Nb stabilized 17% Cr steel had adequate oxidation resistance at 700°C for 5000 h (Steele. 2000). For oxidation of Fe-26Cr-1Mo at 800°C, the ASR of the steel was 0.015 Ω·cm after 48 h, which is well below the maximum acceptable level; however, the ASR increased to 0.2 Ω·cm after 1000 h, meaning that this alloy is not suitable for use as an interconnect material at an operating temperature of 800°C (Zhu & Deevi. 2003b).

Manganese is an alloying element commonly present in stainless steels. In a study at 800°C in air for 1000 h, Fe-25Cr-0.2Y-0.6Mn and Fe-17Cr-0.2Y-1Mn steels had higher weight gains than steels of similar composition that did not contain Mn (Zhu & Deevi. 2003a). Another study of the oxidation at 800 and 900°C for 24 h of 446 stainless steel (23 – 27% Cr) and Ebrite (25 – 27.5% Cr) had similar findings. The oxidation rate of Ebrite was lower than that of 446; the authors attributed this finding to the higher Mn content of 446, which was 1.5% maximum as opposed to 0.1% in Ebrite (Huang, et al. 2001). The presence of Mn results in the formation of (Cr, Mn) spinel on the surface of the protective chromia layer (Zhu & Deevi. 2003a). The thickness of the outer spinel layer depends on the Mn content in the alloy; the more Mn present, the thicker the layer of spinel (Honneger, et al. 2001). The presence of spinel in the oxide layer is advantageous due to its high electrical conductivity; therefore, even though oxide scales that form on Mn-containing steels are thicker than those formed on steels of a similar composition lacking Mn, the electrical resistance of the scales is lower (Zhu & Deevi. 2003a). Also, the outer spinel layer reduces the formation of volatile Cr species from the chromia (Quadakkers, et al. 2003). This is because the vapour pressure of these volatile species is directly related to the activity of $Cr_2O_3$, which is reduced by Mn substituting for Cr in $Cr_2O_3$ or by the formation of a Mn-containing spinel (Holcomb & Alman. 2006). Ideally, enough Mn should be added to allow the formation of a continuous layer of spinel on the surface of the chromia; however, in addition to increasing the oxidation rate of the steel, too much Mn can adversely affect the mechanical properties of the interconnect (Holcomb & Alman. 2006). In the early stages of oxidation, the spinel layer is not continuous and the formation of volatile Cr vapour species from regions of chromia that are not covered with spinel is a problem regardless of the Mn content (Yang, et al. 2006b). Finally, a study at 800°C in moist air containing 3 vol% $H_2O$ found that the volatility of Cr from Mn-containing spinels was only a factor of 2 to 3 lower than the volatility from $Cr_2O_3$ (Yang, et al. 2006b).

The conductivity of the oxide scale can also be increased by adding Ni to stainless steels (Zhu & Deevi. 2003b). Additions of Ni can reduce the formation of volatile Cr species as Ni is able to reduce the activity of chromia by substituting for Cr in $Cr_2O_3$ (Holcomb & Alman. 2006). However, if too much Ni is added, the oxidation resistance of the alloy decreases due to the formation of NiO, a relatively fast growing, non-protective oxide. In a study of oxidation in air at 800°C for 100h, for Fe-17Cr-0.4Y-2Ni, the Ni addition prevented the formation of a protective chromia layer, resulting in much larger weight gains than steels of a similar composition that did not contain Ni (Zhu & Deevi. 2003a). Another disadvantage of adding too much Ni is that Ni increases the thermal expansion coefficient of the stainless steel, resulting in a TEC mismatch of the steel interconnect with other stack components (Zhu & Deevi. 2003b).

Fe-Cr-W alloys are a group of stainless steels that have been evaluated for SOFC interconnect applications. The addition of W reduces the thermal expansion coefficient of the steel, resulting in a good match with the TEC of other stack components (Zhu & Deevi. 2003a). Unfortunately, the oxidation behaviour of W-containing stainless steels is not as good as that of other ferritic stainless steels. In a study at 800°C for 288 h in a simulated fuel atmosphere ($CH_4$-Ar mixture saturated with $H_2O$), the weight gain of Fe-20Cr-7W was much higher than either 430 (16 – 18% Cr) or ZMG 232 (22% Cr, also contains Ni, Al, La, and Zr), neither of which contain W (Horita, et al. 2004). Also, no spinel formed on the Fe-Cr-W alloy, whereas an outer spinel layer was present on the oxides of both the 430 and ZMG 232 (Horita, et al. 2004). Due to the lack of spinel, the increased thickness of the oxide scale, and the formation of pores at the metal/oxide interface, the conductivity of the Fe-Cr-W alloy was much lower than that of the other two stainless steels (Horita, et al. 2004).

A final group of elements that are extremely beneficial to the oxidation behaviour of stainless steels are the reactive elements (RE). These elements include Y, Ce, La, and Hf, and are added in relatively small amounts: 0.1 to 0.2% in elemental form or 1 to 2 vol% as an oxide dispersion (Huang, et al. 2001). Adding more than this amount is not recommended, not only because these elements are relatively expensive, but because scale adhesion can be reduced (Huang, et al. 2001). It is important that the RE are uniformly distributed in the alloy; for this reason, La is more beneficial than either Y or Ce (Quadakkers, et al. 2003). Lanthanum does not form intermetallic compounds with Fe and can, thus, be uniformly distributed in the steel, whereas both Y and Ce tend to

form intermetallic precipitates along the ferrite grain boundaries (Quadakkers, et al. 2003). One advantage of RE additions is that the Cr content required to ensure the formation of a protective chromia layer is reduced since RE additions are able to promote selective Cr oxidation (Quadakkers, et al. 2003). In RE doped steels, only 16 to 18% Cr is required, compared to a minimum of 18% and preferably greater than 20% for steels that do not contain RE (Quadakkers, et al. 2003, Yang, et al. 2003c, Yang, et al. 2003b). However, due to the possibility of Cr losses through spalling of the oxide and interaction with other stack materials, a higher Cr content in steels containing RE is still beneficial (Quadakkers, et al. 2003). Other advantages of adding RE to stainless steels are that the oxidation rate is reduced and scale adhesion is improved, especially under thermal cycling conditions (Huang, et al. 2001, Riffard, et al. 2002, Zhu & Deevi. 2003b). In a study of ferritic stainless steels at 1000°C for 100 h, ZMG 232, a 22% Cr steel containing 0.22% Zr and 0.04% La, had the lowest oxidation rate. In addition to this, no spalling of the oxide was observed (Uehara, et al. 2003). Another study found that for 1000 h of oxidation at 800°C in air, Fe-25Cr-0.2Y and Fe-17Cr-0.2Y had the lowest weight gains compared to other ferritic stainless steels containing either 17 or 25% Cr with no RE additions (Zhu & Deevi. 2003a). Another promising RE-containing ferritic stainless steel is Crofer 22 APU, a 22% Cr steel containing 0.04 to 0.2% La in addition to 0.03 to 0.2% Ti. In a study of oxidation at 800°C in air for 1000 h, the weight gain of Crofer 22 APU was lower than that of ZMG 232, which also contains 22% Cr (Antepara, et al. 2005). A final advantage of RE-containing stainless steels is that the electrical resistance of the oxide is reduced (Kendall. 2005). This is due to the reduction of scale thickness and also to the improvement in scale adhesion (Zhu & Deevi. 2003b). One study compared the oxidation behaviour of ZMG 232 and 430 stainless steel in air at 750°C for 1000 h and found that, although the weight gain for the two alloys was similar, with that for the ZMG 232 being slightly lower, the contact resistance for the ZMG 232 was significantly lower than that for the 430 (Uehara, et al. 2003). The low electrical resistance for the ZMG 232 was attributed to its denser, more adherent oxide owing to the presence of RE in the steel (Uehara, et al. 2003). Another study on the oxidation of commercial ferritic stainless steels in air at 800°C for 600 h found that FeCrMnLaTi steels formed oxide scales with the lowest contact resistance (Quadakkers, et al. 2003). A similar study of the oxidation behaviour of FeCrMnLaTi steels at 800°C for 500 h in Ar, containing 4 vol% $H_2$ and 3 vol% $H_2O$, determined that the contact resistance of the oxide scale formed on these alloys did not increase despite the fact that the thickness of the oxide was increasing during this time (Meulenberg, et al. 2003). This observation was attributed to the

diffusion of La into the scale and the subsequent increase in defect conduction (Meulenberg, et al. 2003). A final RE-containing ferritic stainless steel that shows promise for interconnect applications contains alloying additions of Mo, Ti, and $Y_2O_3$, and was produced using powder metallurgy (PM) techniques (Honneger, et al. 2001). The oxidation behaviour of two different compositions, Fe-22Cr-2Mo-0.29Ti-0.37Y and Fe-26Cr-2Mo-0.31Ti-0.25Y, was studied in air for 500 h at 700, 800, and 900°C (Honneger, et al. 2001). At 700 and 800°C, the oxidation rate of the stainless steels was comparable to that of two high temperature alloys: Haynes 230 (Ni-based superalloy) and Ducrolloy CRF (Cr-based alloy) (Honneger, et al. 2001). The oxidation rate of the PM stainless steels was much lower at all three temperatures than that of commercial stainless steels Fe-18Cr-0.62Nb-0.27Ti (DIN 1.4509), Fe-26Cr (446), and Fe-18Cr-Al-Si (DIN 1.4742) (Honneger, et al. 2001).

There are several advantages of using ferritic stainless steels for interconnect materials in intermediate temperature SOFCs. The typical TEC range of commercial ferritic stainless steels is 9 to 13 x $10^{-6}$/°C from room temperature to 800°C, depending on the alloying additions (Brylewski, et al. 2001, Uehara, et al. 2003, Yang, et al. 2003b). This range is similar to that of the other stack components. Within the operating temperature range of 600 to 800°C, stainless steels are able to form a protective chromia layer in air, oxygen, $H_2$-$H_2O$, and $H_2$-$H_2O$-$H_2S$ gas mixtures (Brylewski, et al. 2001). Machinability of stainless steels is good, and they are significantly cheaper than the high temperature alloys (Yang, et al. 2003c).

The main problem with stainless steel interconnects in intermediate temperature SOFC applications is their oxidation resistance, which is much worse than that of the high temperature alloys. The scale growth rate and electrical resistance are too high to satisfy requirements for SOFC commercialization, and the adhesion of the oxide is insufficient to prevent scale spalling over long periods of time, especially under thermal cycling conditions (Huang, et al. 2001). Also, thick oxide scales make it difficult to achieve a good seal at the interconnect, which prevents direct mixing of the air and fuel (Deng, et al. 2006). Commercially available stainless steels may be suitable for SOFC interconnect application without modification if the operating temperature can be further reduced to below 700 or even as low as 600°C (Zhu & Deevi. 2003b).

One way to improve the oxidation behaviour of stainless steels is to apply a coating to the surface. There has been a significant amount of research on different types of coatings suitable for SOFC interconnect applications; however, a major disadvantage of coatings is they increase both the material and fabrication cost when compared to an uncoated interconnect (Kendall. 2005).

## 2.4 Oxidation of Metals

Oxidation is a process that occurs when a metal reacts with oxygen in the environment to form an oxide. The overall chemical reaction for this process can be written as follows (Kofstad. 1998):

$$aM(s) + \left(\frac{b}{2}\right)O_2(g) \rightarrow M_aO_b(s) \qquad (2\text{-}8)$$

The oxidation half reaction consists of the formation of metal ions and occurs at the metal/oxide interface (Kofstad. 1998). The reduction half reaction consists of the formation of oxygen ions and occurs at the oxide/gas interface (Kofstad. 1998).

Although the overall chemical reaction that describes the oxidation process appears quite simple, the actual oxidation reaction mechanism is much more involved (Kofstad. 1998). First, the oxygen from the environment adsorbs on the surface of the metal (Kofstad. 1998). This process continues until a 2-D layer of adsorbed oxygen, that completely covers the metal surface, is formed (Bradford. 2002). The formation of 3-D oxide nuclei then occurs at defects on the metal surface such as grain boundaries, impurities, dislocations, and surface flaws (Bradford. 2002). Growth of the nuclei results in the formation of a continuous oxide film covering the metal surface (Kofstad. 1998). At this point, further oxide growth relies on the solid state transport of metal and oxide ions across the scale (Kofstad. 1998). If the oxide layer is not completely dense, but instead is porous, transport of reactants is much easier as they are able to travel through cavities and pores (Kofstad. 1998). The exact oxidation reaction mechanism depends on many factors such as surface treatment, gas composition, and gas pressure (Kofstad. 1998).

There are several characteristics that define a protective oxide layer. First, the oxide must be thermodynamically stable so that it forms preferentially over other, less protective oxides (Kane. 2003). Also, the vapour pressure of the oxide must be low so that it remains as a solid layer and does not vaporize, which would result in accelerated oxide growth (Kane. 2003). The oxide scale should completely cover the metal surface, and the diffusion rates of the scale-forming species should be relatively low so that the overall oxide growth rate is reduced (Kane. 2003). It is also important that the oxide scale has good adherence to the underlying alloy, especially under thermal cycling conditions (Kane. 2003). In order for this to be possible, the TEC difference between the oxide and the alloy should be as low as possible (Kane. 2003). Finally, the oxide should have adequate plasticity at high temperatures so that cracking and spalling do not occur if the alloy is subjected to a stress (Kane. 2003).

### 2.4.1 Thermodynamics of Oxidation

The thermodynamics of the oxidation process provides information about whether or not an oxidation process will occur under certain environmental conditions. As with any process, the driving force for oxidation is a reduction in Gibbs free energy arising in this case from the formation of an oxide (Kofstad. 1998). This free energy change can be described by the following equation (Bradford. 2002):

$$\Delta G = \Delta G^{\circ} + RT \ln\left(\frac{a_{products}}{a_{reactants}}\right) \qquad (2\text{-}9)$$

where $\Delta G$ is the change in Gibbs free energy, $\Delta G^{\circ}$ is the Gibbs free energy change under standard conditions, $R$ is the universal gas constant (8.134 J/mol·K), $T$ is the absolute temperature (K), and $a$ is the activity (Bradford. 2002). Equation 2-9 can be simplified by assuming that the metal and the oxide are both pure, which means they both have an activity of 1 (Bradford. 2002). Also, it can be assumed that the oxygen behaves as an ideal gas, meaning that the activity of oxygen can be approximated as the oxygen partial pressure in the environment (Bradford. 2002). The simplified expression for 1 mole of oxygen reacting is as follows (Bradford. 2002):

$$\Delta G = \Delta G^{\circ} + RT \ln\left(\frac{1}{p_{o_2}}\right) \qquad (2\text{-}10)$$

where $p_{o_2}$ is the oxygen partial pressure in atmospheres (Bradford. 2002). If it is assumed that the oxidation process reaches equilibrium, then $\Delta G$ is equal to 0, and the equation becomes the following (Bradford. 2002):

$$\Delta G^{\circ} = RT \ln p'_{o_2} \qquad (2\text{-}11)$$

where $p'_{o_2}$ is the equilibrium partial pressure of oxygen (Bradford. 2002). By substituting Equation 2-11 into Equation 2-10, the following relationship is obtained for $\Delta G$, the driving force for the oxidation process (Bradford. 2002):

$$\Delta G = RT \ln\left(\frac{p'_{O_2}}{p_{O_2}}\right) \qquad (2\text{-}12)$$

where $p_{O_2}$ is the partial pressure of oxygen in the environment (Bradford. 2002). From the above expression, it can be seen that oxidation will occur spontaneously (the value of $\Delta G$ is negative) when the partial pressure of oxygen in the environment is larger than the equilibrium value (Bradford. 2002, Khanna. 2002).

In order to concisely represent thermodynamic information about the formation of a variety of oxides, an Ellingham Diagram is used. Figure 2-4, displayed below, shows an Ellingham diagram, which is a plot of the standard free energy of formation of various oxides per mole of oxygen vs. temperature (Shifler. 2003).

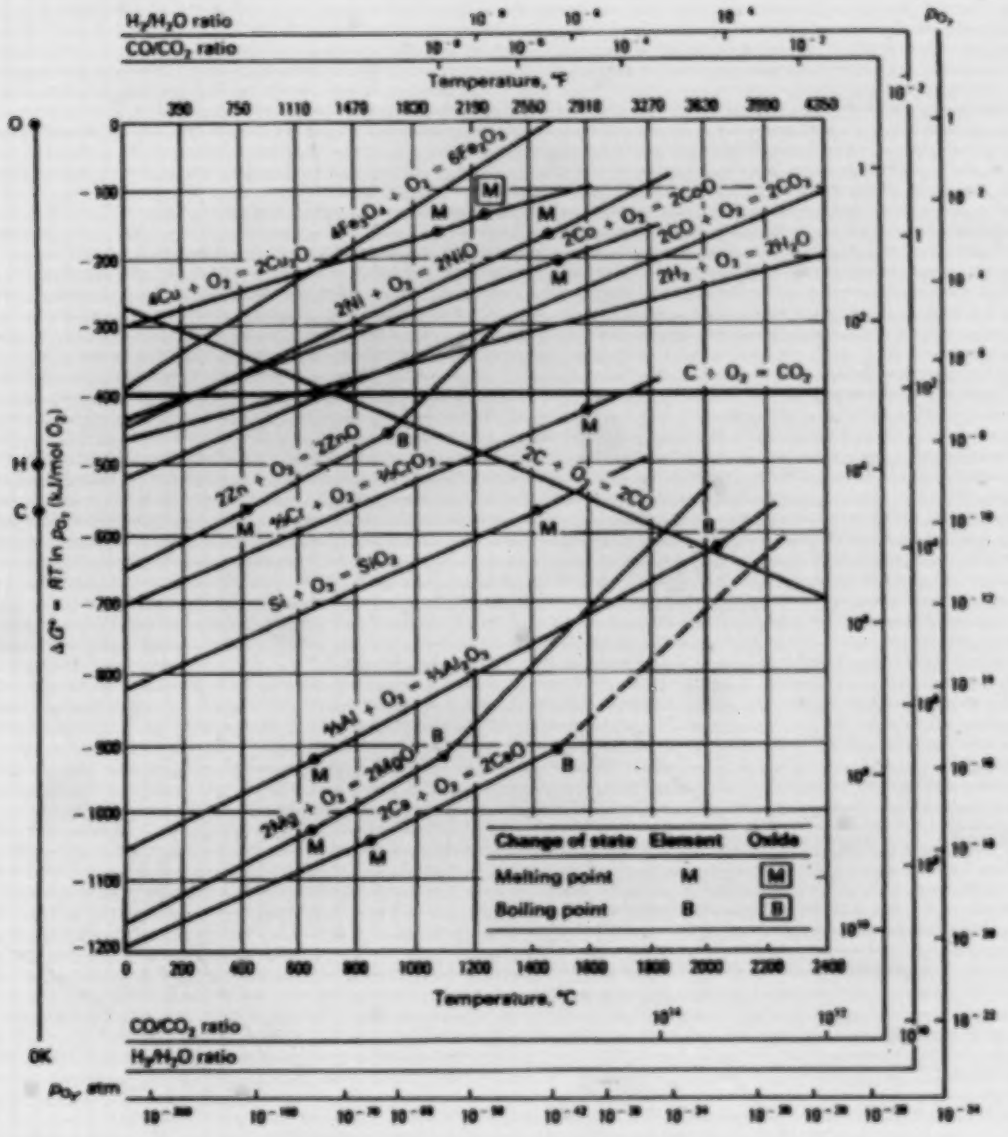


Figure 2-4. Ellingham Diagram (Shifler. 2003).

In order to construct an Ellingham diagram, the free energy of formation of each oxide as a function of absolute temperature must first be experimentally determined (Khanna

2002). Then, the data is fit to an expression of the form $\Delta G^\circ = A + BT + \frac{C}{T} + DT^2$ (Khanna. 2002). The last two terms of the equation are dropped since they are generally small in magnitude and the remaining expression, $\Delta G^\circ = A + BT$, is plotted on the Ellingham diagram (Khanna. 2002). Since $\Delta G^\circ = \Delta H^\circ - T\Delta S^\circ$, the slope of the Ellingham diagram is $-\Delta S^\circ$ and the y-intercept is $\Delta H^\circ$ (Khanna. 2002).

The Ellingham diagram provides useful thermodynamic information about the formation of oxides. The most stable oxides will have the largest negative values of $\Delta G^\circ$; therefore, on the Ellingham diagram, the most stable oxides are located near the bottom and the least stable at the top (Shifler. 2003). In a given environment, more stable oxides will form preferentially over those that are less stable; therefore, with the help of an Ellingham diagram it is possible to predict the type of oxide that is thermodynamically inclined to form at a specific temperature and oxygen partial pressure (Wasielewski & Rapp. 1972). Also, by examining an Ellingham diagram, it is possible to predict a temperature range for which oxidation will occur in a given environment (Shifler. 2003).

There are several limitations to using only thermodynamic information to understand an oxidation process. Thermodynamics is not able to accurately predict the composition or morphology of oxide scales as these are dependent on both the environment and the alloy composition (Wasielewski & Rapp. 1972). Also, even though the formation of a particular oxide may be thermodynamically favourable, the kinetics of the reaction may be so slow that in reality, a negligible amount of oxide formation occurs (Khanna. 2002). Therefore, it is also important to consider the kinetics of oxidation.

### 2.4.2 Kinetics of Oxidation

It is important to study the kinetics of oxidation for several reasons. First, kinetic information is useful in understanding the oxidation reaction mechanism and in determining the rate-limiting step of an oxidation process (Kofstad. 1998). Also, kinetics gives information about the rate at which oxidation is occurring, and can be used to predict the thickness of the oxide layer after a given oxidation time (Kofstad. 1998). Spalling of the oxide scale becomes more likely as the oxide thickness increases; therefore, kinetic information can be used to predict whether or not a protective layer will

remain adherent after a given oxidation time (Quadakkers, et al. 2003). Oxidation chemical reaction rates increase exponentially with temperature; therefore, oxidation becomes a more severe problem at high temperatures (Bradford. 2002).

#### *2.4.2.1 Logarithmic Oxidation*

Logarithmic rate equations are typically used to describe the formation of thin oxides (1 to 100 nm) at low temperatures (300 to 400°C) (Bradford. 2002, Kofstad. 1998). Logarithmic oxidation can also apply to the early stages of oxidation of metals at high temperatures, when the protective film is still thin (Bradford. 2002, Khanna. 2002). For logarithmic kinetics, the initial reaction rate is high, but the rate drops rapidly to a low or even negligible value (Kofstad. 1998). The two equations used to describe logarithmic kinetics are shown below (Kofstad. 1998):

$$x = k_{\log} \log(t + t_0) + A \qquad (2\text{-}13)$$

$$\frac{1}{x} = B - k_{il} \log t \qquad (2\text{-}14)$$

where $k$ is the oxidation rate constant, $x$ is either mass gain or oxide thickness, $t$ is time, and A and B are constants (Kofstad. 1998). Equation 2-13 describes direct logarithmic kinetics, while Equation 2-14 corresponds to inverse logarithmic kinetics (Kofstad. 1998). For very short periods of time, the two equations are similar; however, they differ from each other after longer oxidation times (Bradford. 2002). The rate-limiting step for logarithmic kinetics is not as well understood as that for the other kinetic models, and several theories have been proposed (Kofstad. 1998). At a thickness of less than 100 nm, the film is too thin for the rate-limiting step to be solid-state diffusion of reactants through the oxide scale (Bradford. 2002). Rate-limiting processes that have been proposed include chemisorption, cavity formation in the film, or transport of electrons or ions across the oxide layer in the presence of an electric field in or around the oxide (Kofstad. 1998). The oxide electric field is due to the potential difference between the alloy and the adsorbed layer of oxygen anions on the outer surface of the film (Bradford. 2002).

Logarithmic kinetics can also apply to thicker oxide films containing a significant amount of porosity or cracks running parallel to the metal surface (Bradford. 2002). In this case, the formation of pores or cavities decreases the effective cross section for solid-state diffusion, and thus the diffusion rate is reduced (Bradford. 2002). Although the logarithmic rate equations used in this case are the same as for thin films, the oxidation mechanism is obviously completely different (Bradford. 2002).

#### *2.4.2.2 Linear Oxidation*

Linear oxidation applies to situations where the oxidation rate is constant (Kofstad. 1998). In reality, this occurs when the oxide scale does not protect the underlying metal (Bradford. 2002). The scale can be porous, or it can crack, spall, or flake off (Bradford. 2002, Callister Jr. 2000). Linear oxidation is described by the following equations (Kofstad. 1998):

$$\frac{dx}{dt} = k_l t \qquad (2\text{-}15)$$

or alternately,

$$x = k_l t + C \qquad (2\text{-}16)$$

There are several possible rate-limiting steps: adsorption of reactants on the surface of the oxide, steady-state oxide formation at the metal/oxide interface, or solid state diffusion of reactants through an oxide of constant thickness (Khanna. 2002). Linear oxidation kinetics is sometimes referred to as "interface controlled" or "reaction controlled" since the rate-limiting process is either the oxide formation reaction or a process occurring at a surface or phase boundary (Bradford. 2002, Khanna. 2002, Kofstad. 1998).

#### *2.4.2.3 Parabolic Oxidation*

Parabolic oxidation occurs when the oxide scale is able to protect the underlying metal from further oxidation (Bradford. 2002). It is known to describe the oxidation of most

metals at high temperatures (Kofstad. 1998). As with logarithmic oxidation, the reaction rate is initially high but it decreases with time (Kofstad. 1998). Parabolic oxidation is described by the following equations (Kofstad. 1998):

$$\frac{dx}{dt} = \frac{k_p}{x} \qquad (2\text{-}17)$$

or alternately,

$$x^2 = 2k_p t + C \qquad (2\text{-}18)$$

where C is a constant (Kofstad. 1998).

The rate-limiting step for parabolic oxidation is diffusion; therefore, parabolic oxidation can also be referred to as "diffusion limited" (Kofstad. 1998). Either the diffusion of oxygen or metal ions can be the rate-limiting process (Kofstad. 1998). Initially, the oxidation rate is fairly high because the diffusion distance, equal to the thickness of the oxide scale, is small. As the oxidation proceeds, the diffusion distance becomes larger as the scale grows and thus the oxidation rate is reduced (Bradford. 2002).

#### *2.4.2.4 Paralinear Oxidation*

Paralinear oxidation represents the more complicated situation where the oxidation process initially follows parabolic kinetics, but then a transition to linear oxidation is observed (Bradford. 2002, Kofstad. 1998). There are several situations where paralinear kinetics applies. In some cases, in the early stages of oxidation, a protective oxide is formed on the alloy surface; however, the oxide later becomes non-protective due to sublimation of the oxide, porosity generation, or cracking of the scale (Bradford. 2002). At the metal/oxide interface, the newly-formed oxide is protective; however, its growth rate is linear and equal to its transition rate from protective to non-protective (Bradford. 2002). Another situation that can be described by paralinear kinetics is periodic cracking of the oxide scale (Bradford. 2002). In this case, a protective oxide initially forms, cracking or spalling occurs, and a new protective oxide then forms (Bradford. 2002). The result is a series of "steps" of parabolic oxidation, typically spaced at regular time

intervals, which can be approximated as slow linear oxidation (Bradford. 2002). A final case of paralinear oxidation occurs when a protective oxide initially forms on an alloy; however, following the formation of the scale, the region of the alloy below the metal/oxide interface is depleted of scale-forming elements (Bradford. 2002). If the depletion is severe enough, upon cracking or spalling of the oxide, the alloy will no longer be able to form a protective scale, and the oxidation rate becomes linear and rapid (Bradford. 2002). This situation is also known as "breakaway oxidation" (Bradford. 2002).

### 2.4.3 Wagner's Theory of Oxidation

Wagner's theory of oxidation describes the oxidation behaviour of metals at high temperatures (Kofstad. 1998). There are several assumptions in the theory. First, the oxide scale must be compact and adherent (Bradford. 2002). Equilibrium conditions are assumed to exist at both the metal/oxide and oxide/gas interface as well as throughout the oxide scale (Bradford. 2002). Also, the oxide must not deviate significantly form stoichiometry; therefore, it is assumed that there is adequate oxygen in the environment for this condition to be met (Bradford. 2002, Kofstad. 1998). Finally, the oxide scale must cover the entire surface of the alloy (Kofstad. 1998).

During the initial stages of oxidation, a thin oxide film is rapidly formed on the surface of the alloy (Wasielewski & Rapp. 1972). The composition of this film differs from that of the protective oxide that will form later; it typically contains oxides of every scale-forming element in the alloy in an amount proportional to the overall composition of the alloy (Wasielewski & Rapp. 1972). Many of these oxides are of lower thermodynamic stability than the protective oxide (Wasielewski & Rapp. 1972). This initial stage of oxidation is referred to as "transient oxidation" (Wasielewski & Rapp. 1972).

Following the formation of a thin oxide film, nucleation of the protective oxide begins to occur under the film (Wasielewski & Rapp. 1972). The oxide nuclei then grow laterally until they impinge on one another and a continuous, protective oxide is formed (Wasielewski & Rapp. 1972). Growth of the protective oxide is favoured at grain boundaries where rapid diffusion of the scale-forming elements occurs (Wasielewski & Rapp. 1972). At this stage, oxidation of the protective scale follows parabolic kinetics (Wasielewski & Rapp. 1972).

Once a protective film is established on the surface of the alloy, many factors can cause the oxidation kinetics to differ to varying degrees from the parabolic model (Wasielewski & Rapp. 1972). These factors include cracking and spalling of the oxide, which occurs more easily at the edges and corners of the metal, blistering of the scale, internal oxidation (oxidation that occurs at the metal/oxide interface below the protective scale), evaporation of elements in the protective oxide, formation of pores and voids at the metal/oxide interface due to vacancy coalescence, spinel formation, depletion of scale-forming elements in the alloy below the metal/oxide interface, chemical doping of the oxide by non scale-forming elements, and preferential oxidation at alloy grain boundaries (Wasielewski & Rapp. 1972).

The oxidation rate of metals has a strong dependence on temperature. The oxidation rate constant $k$ can be described using the Arrhenius equation (Kofstad. 1998):

$$k = k_0 \exp(-\frac{Q}{RT}) \qquad (2\text{-}19)$$

where $k_0$ is a constant, $Q$ is the activation energy for oxidation (J/mol·K), $R$ is the universal gas constant, and $T$ is the absolute temperature (K) (Kofstad. 1998).

### 2.4.4 Pilling-Bedworth Ratio

The Pilling-Bedworth Ratio (PBR) is a rule of thumb for determining whether or not an oxide will be protective. It assumes that the oxidation mechanism is the inward diffusion of oxygen ions through the oxide scale, meaning that oxide formation occurs at the metal/oxide interface (Kofstad. 1998). The PBR is defined as the ratio of the volume of oxide to the volume of metal from which the oxide was formed (Kofstad. 1998). It can be calculated using the following equation (Callister Jr. 2000):

$$PBR = \frac{A_O \rho_M}{A_M \rho_O} \qquad (2\text{-}20)$$

where $A_O$ and $A_M$ are the molecular weight of the oxide and metal, respectively, and $\rho_O$ and $\rho_M$ are the densities of the oxide and metal, respectively (Callister Jr. 2000).

If the PBR is less than 1, the scale is porous and unprotective because the volume of oxide formed is not sufficient to completely cover the alloy surface (Bradford. 2002, Callister Jr. 2000). In this case, the oxide is under tensile stress (Kofstad. 1998). If the PBR is greater than 1, the scale completely covers the metal surface and is thus able to protect the alloy from further oxidation (Bradford. 2002). In this case, in order for further oxidation to occur, soild-state diffusion of the reactants through the oxide scale is required (Bradford. 2002). If the PBR is greater than 1, the oxide is under compressive stress (Kofstad. 1998). However, if the PBR is significantly higher than one, in the range of 2 to 3, the oxide is under a significant amount of compressive stress and if the thickness becomes large, buckling and spalling of the oxide scale will likely result (Bradford. 2002, Callister Jr. 2000). The ideal protective oxide has a PBR as close to 1 as possible (Callister Jr. 2000).

There are several limitations of using the PBR to predict oxidation behaviour. Some metals with a PBR less than 1, for example the alkali and alkaline earth metals, are able to form a thin protective oxide (Kofstad. 1998). Some metals that have a PBR greater than 1, for example Nb and Ta, form thick oxides that are non-protective (Kofstad. 1998). However, since it is easy to calculate, the PBR is useful as starting point for understanding the oxidation behaviour of a particular metal (Bradford. 2002).

## 2.5 Oxidation of Stainless Steel

According to Wagner, the theoretical minimum content of a scale-forming element in an alloy in order to ensure that a protective oxide scale is formed can be calculated using the following equation (Danielewski, et al. 2005):

$$N_M = \left( \frac{\pi g N_0 D_0 V_m}{3 D_M V_{ox}} \right)^{\frac{1}{2}} \qquad (2\text{-}21)$$

where $g$ is a constant, $N_0$ is the oxygen concentration, $D_0$ is the diffusivity of oxygen in the alloy, $V_m$ is the molar volume of the alloy, $D_M$ is the diffusivity of the scale-forming element in the alloy, and $V_{ox}$ is the molar volume of the oxide (Danielewski, et al. 2005). According to the above relationship, for ferritic stainless steels, the minimum

chromium content required in order to form a protective chromia scale is 6.3% (Danielewski, et al. 2005). However, the minimum requirement calculated with Equation 21 refers to the amount of scale-forming element in the region just below the metal/oxide interface; therefore, the bulk alloy requirement should be higher to account for depletion of chromium in the alloy due to scale formation, especially if oxide spalling occurs (Danielewski, et al. 2005). Also, the amount of Cr available for oxide formation is typically less than the amount of Cr present in the alloy due to the precipitation of Cr carbides (Grabke, et al. 1997). For ferritic stainless steels, more than 11% Cr is required to form a protective chromia layer whereas for austenitic stainless steels, at least 18% Cr is required (Grabke & Müller-Lorenz. 1998, Grabke, et al. 1997, Ostwald & Grabke. 2004). If Cr contents are below this level, the formation of non-protective, Fe-rich oxides such as $Fe_3O_4$, $Fe_2O_3$, and $(Fe,Cr)_3O_4$ spinels will occur (Grabke, et al. 2004). Scales containing iron-rich oxides typically contain pores and channels that allow corrosive environmental species such as C and S to attack the underlying metal (Ostwald & Grabke. 2004). The minimum scale-forming element requirement decreases as alloy grain size decreases (Danielewski, et al. 2005). This is because grain boundaries act as fast diffusion paths, making the transport of the scale-forming element to the alloy surface more rapid in the case of fine-grained alloys (Danielewski, et al. 2005). The amount of scale-forming element required to form a protective layer also depends on factors such as oxidation temperature, impurity content in the alloy, alloying additions, and surface treatment (Quadakkers, et al. 2003). As the oxidation temperature increases, the critical Cr content above which the formation of a protective chromia layer is possible decreases (Zurek, et al. 2004). This is due to increased Cr diffusion rates as well as increased carbide solubility at higher temperatures (Zurek, et al. 2004). Alloying additions such as Si and Co are known to reduce the amount of Cr required for the formation of a protective oxide, whereas Mn increases the Cr requirement (Zurek, et al. 2004). Alloying elements affect the critical Cr content by influencing the activity of Cr, the diffusion rate of Cr, and the solubility of chromium carbides in the stainless steel (Zurek, et al. 2004). Some alloying elements, such as Si and Mn, can also affect the critical Cr content through their incorporation into the protective oxide layer (Zurek, et al. 2004).

The oxidation rate of stainless steels is dependent on their Cr content. For alloys containing less than the minimum amount of Cr required to form a protective oxide layer, the oxidation rate is high (Quadakkers, et al. 2003). With increasing Cr content, the

oxidation rate decreases until the formation of a protective chromia layer is possible (Quadakkers, et al. 2003). For Fe-Cr alloys containing between 28 and 68% Cr, as the Cr content increases, the oxidation rate increases slowly up to a Cr content of 37.4% (Whittle & Wood. 1968). With higher Cr contents, up to 59.5% and 68.0%, the oxidation rate increases more rapidly (Whittle & Wood. 1968). It is also known that cracking and spalling of the oxide scale is more likely in stainless steels with higher Cr contents. As the Cr content of the steel increases, its plasticity decreases, reducing the ability of the alloy to accommodate stresses in the oxide layer (Whittle & Wood. 1968). The porosity of the oxide layer is also dependent on the Cr content in the stainless steel. In a study of stainless steels containing 2 to 50% Cr, it was observed that scale porosity decreased with increasing Cr content up to 12.5%, and reached a minimum level at Cr contents in the range of 12.5% to 17% (Leistikow, et al. 1987). Above 17% Cr, the porosity of the oxide layer was found to increase (Leistikow, et al. 1987). All these factors suggest that the oxidation behaviour of stainless steels can be optimized by a Cr content in the range of 20 to 40% (Leistikow, et al. 1987, Whittle & Wood. 1968).

The oxide scale formed on stainless steels is not pure chromia; in fact, it is usually composed of two distinct layers: an inner layer of $Cr_2O_3$, typically containing some Fe, and an outer $(Mn,Cr)_3O_4$ spinel layer, which can also contain Fe (Grabke, et al. 2004, Ostwald & Grabke. 2004, Yang, et al. 2003b). The presence of spinel on the surface of the protective chromia layer is beneficial for SOFC interconnect applications as the spinel has a lower electrical resistance than chromia, and thus increases the overall conductivity of the oxide layer (Zhu & Deevi. 2003b). The spinel also reduces the loss of Cr from the oxide due to the vaporisation of volatile Cr species (Brylewski, et al. 2004, Franco, et al. 2003). The formation of a distinct Mn-containing spinel layer is due to the fact that Mn has a low solubility in chromia (Quadakkers, et al. 2003). The spinel forms on the outer surface of the chromia because of the fast diffusion of Mn ions in $Cr_2O_3$ (Brylewski, et al. 2004). The diffusivity of various metal ions in chromia, assuming substitutional diffusion through cation lattice sites in the chromia, increases in the following order: $D_{Cr} < D_{Ni} < D_{Fe} < D_{Mn}$ (Kurokawa, et al. 2004). In fact, the diffusivity of Mn ions in chromia is two orders of magnitude larger than that of Cr ions in chromia (Kurokawa, et al. 2004). In a study of the oxidation of Fe-Cr steels in air at 800°C for 500h, it was found that the thickness of the spinel layer is dependent on the amount of Mn present in the stainless steel, with a thicker layer corresponding to a higher Mn content (Honneger, et al. 2001).

A spinel has a structure of the form $AB_2O_4$, where A and B are both metals (Sakai, et al. 2005). In the case of stainless steels, A is typically Mn and B is Cr (Sakai, et al. 2005). Iron can substitute for either Mn on the A-site or Cr on the B-site (Sakai, et al. 2005). If Fe substitutes for Cr, forming a spinel of the form $Mn(Cr,Fe)_2O_4$, the conductivity of the spinel phase increases (Sakai, et al. 2005). In $MnCr_2O_4$ spinels, the only charge carriers are $Mn^{2+}$ and $Mn^{3+}$, whereas in $Mn(Cr,Fe)_2O_4$ spinels, $Fe^{2+}$ and $Fe^{3+}$ are able to act as additional charge carriers (Sakai, et al. 2005). The conductivity of the oxide layer formed on the ferritic stainless steel ZMG 232 is higher than that of the oxide formed on 430 stainless steel; this is because the former steel forms a $Mn(Cr,Fe)_2O_4$ spinel while the latter has an oxide scale containing $MnCr_2O_4$ spinel (Sakai, et al. 2005). Fe-Cr-W alloys, a group of ferritic stainless steels, form oxide scales with relatively low conductivity compared with other steels since the oxide consists solely of chromia and no spinel layer is present (Sakai, et al. 2005).

As mentioned earlier, the oxidation of most metals at high temperatures can be described by parabolic kinetics. In this model, the rate-limiting step is the diffusion of ions through the oxide scale. For stainless steels, the outward grain boundary diffusion of chromium through the chromia scale is rate-limiting (Huang, et al. 2001). However, the oxidation of stainless steels is more complicated than the parabolic kinetics model. For the oxidation of ferritic stainless steels containing 9-12% Cr at 600°C, for the first 15 minutes of oxidation, the supply of oxygen from the atmosphere was rate-limiting (Grabke, et al. 2004). For the following 1 to 2 hours, oxide growth faster than that predicted by the parabolic model was observed due to the rapid diffusion of Cr along fast diffusion paths such as alloy grain boundaries (Grabke, et al. 2004). After this period of time, depletion of Cr below the metal/oxide interface was observed and the rate-limiting step was bulk diffusion of Cr until an equilibrium Cr concentration at the metal/oxide interface was established (Grabke, et al. 2004). As the thickness of the oxide scale increased, diffusion of Cr through the oxide scale became rate-limiting and the Cr concentration at the metal/oxide interface subsequently increased (Grabke, et al. 2004). After 100 h of oxidation, the oxidation rate was limited by both bulk Cr diffusion and diffusion of Cr through the oxide scale (Grabke, et al. 2004).

A wide range of parabolic rate constants has been reported in the literature for the oxidation of stainless steels (Brylewski, et al. 2004, Huang, et al. 2001, Mikkelsen & Linderoth. 2003). Typically, $k_p$ values for oxidation temperatures between 750 and

900°C are between $10^{-14}$ and $10^{-12}$ $g^2cm^{-4}s^{-1}$ (Brylewski, et al. 2004). Parabolic rate constants for several commercially available ferritic stainless steels are listed in Table 2-3.

Table 2-3. Parabolic Rate Constants for the Oxidation of Ferritic Stainless Steels at 800°C (Yang, et al. 2004a).

| Steel | $k_p$ (x $10^{-14}$ $g^2cm^{-4}s^{-1}$) |
|---|---|
| Crofer22 APU | 7.96 |
| E-Brite | 3.53 |
| AISI446 | 13.32 |
| AL453 | 19.84 |
| AISI430 | 35.00 |

In order for ferritic stainless steels to be suitable for SOFC interconnect applications, a parabolic rate constant below $10^{-14}$ $g^2cm^{-4}s^{-1}$ is required, and a $k_p$ value of less than $10^{-15}$ $g^2cm^{-4}s^{-1}$ would be ideal (Antepara, et al. 2005).

In environments containing high oxygen partial pressures, such as air, synthetic air, or oxygen, many oxides are thermodynamically stable (Ostwald & Grabke. 2004). In the initial stages of oxidation, referred to as transient oxidation, nucleation of all these stable oxides is observed (Mikkelsen & Linderoth. 2003). Depending on the composition of the steel, the formation of $Cr_2O_3$, $Fe_2O_3$, $Fe_3O_4$, NiO, and various spinels is possible (Ostwald & Grabke. 2004). Transient oxidation proceeds until a continuous layer of chromia forms on the surface of the alloy (Mikkelsen & Linderoth. 2003). At first, nucleation of chromia occurs predominately in regions where alloy grain boundaries intersect the metal surface since diffusion of Cr along the grain boundaries is faster than diffusion through the grains (Grabke, et al. 2004). However, after a relatively short time, growth of the oxide nuclei results in the formation of a continuous chromia layer covering the alloy surface (Grabke, et al. 2004). At this point, the growth of the other, less stable, oxides is stopped in favour of the growth of the chromia (Leistikow, et al. 1987). The least stable oxides decompose, and the others are later converted to spinels (Leistikow, et al. 1987). This process is referred to as chromia "undercutting", and it is dependent on an adequate supply of Cr (Leistikow, et al. 1987).

As a chromia layer is established on the surface of the stainless steel, depletion of Cr in the region of the alloy below the metal/oxide interface is observed (Ostwald & Grabke. 2004). In order for further oxidation to occur, diffusion of Cr from the bulk alloy to the metal/oxide interface is required (Ostwald & Grabke. 2004). The formation of a protective chromia layer is easier at higher temperatures since the diffusion of Cr is more rapid (Grabke, et al. 1997). Ferritic stainless steels are able to more easily form a protective chromia layer than austenitic steels because the Cr diffusivity is 1 to 2 orders of magnitude larger in the ferritic lattice due to its more open structure (Grabke & Müller-Lorenz. 1998, Grabke, et al. 1997, Grabke, et al. 2004).

For stainless steels, although there is some inward diffusion of oxygen ions through the protective scale, oxide growth occurs predominantly by outward diffusion of Cr from the alloy through the oxide towards the oxide/gas interface (Kofstad. 1992, Quadakkers, et al. 2003). Because of this, oxide formation occurs for the most part at grain boundaries within the scale close to the oxide/gas interface (Kofstad. 1992, Minh & Takahashi. 1995). As a result, the oxide scale grows not only outward from the metal/oxide interface but also laterally, creating large compressive growth stresses in the oxide (Kofstad. 1992, Minh & Takahashi. 1995). The oxide stresses are accommodated either by plastic deformation, which is easier at lower oxygen partial pressures, or by cracking of the scale (Kofstad. 1992, Minh & Takahashi. 1995). Another result of scale growth occurring mainly through outward diffusion of Cr is the formation of pores, voids, or cavities at the metal/oxide interface which reduce scale adhesion (Brylewski, et al. 2004, Minh & Takahashi. 1995, Quadakkers, et al. 2003). The end result is that chromia scales that form on stainless steels at high temperatures are typically not ideally flat but are buckled and may form localized intrusions or protrusions (Kofstad. 1998, Quadakkers, et al. 2003). The protective chromia layer is susceptible to both cracking and spalling under thermal cycling conditions or during cooling as there is a large TEC mismatch between the chromia scale and the underlying stainless steel (the TEC of the stainless steel is approximately twice that of the chromia) (Bradford. 2002).

As mentioned earlier, the oxidation behaviour of stainless steels can be improved by adding small amounts of reactive elements (RE). There are many benefits of RE additions. RE are known to enhance the selective oxidation of chromium, thus reducing the amount of Cr required for the formation of a protective chromia scale (Huang, et al. 2001). The scale growth rate is also reduced through RE additions, and scale adhesion is

improved (Huang, et al. 2001). RE additions have also been shown to reduce the porosity of the oxide layer (Riffard, et al. 2002).

Many theories or mechanisms have been proposed to explain the effect of RE on the oxidation behaviour of metals; however, no single explanation completely describes the RE effect (Huang, et al. 2001, Riffard, et al. 2002). One theory is that RE segregate to the metal/oxide interface where they are able to improve scale adhesion and resistance to spalling by preventing void formation due to the coalescence of vacancies at the interface (Huang, et al. 2001, Riffard, et al. 2002). A similar theory proposes that the presence of reactive elements at the metal/oxide interface results in a "pegging" of the oxide scale to the alloy, again improving scale adhesion (Riffard, et al. 2002). The presence of RE at the metal/oxide interface is also thought to promote the accumulation of Si, which forms a Si rich layer below the chromia that is able to act as a diffusion barrier and thus to both improve scale adhesion and reduce scale growth (Riffard, et al. 2002). Alternately, it has been proposed that reactive elements segregate to oxide grain boundaries, where they are thought to either remain in elemental form or to form $YCrO_4$ or $YCrO_3$ mixed oxides (Riffard, et al. 2002). The RE elements or particles at the grain boundaries are thought to modify the diffusion rates of metal and oxygen ions, indirectly reducing the oxidation rate (Riffard, et al. 2002). Also, the scale growth mechanism in the presence of REs is changed to the inward diffusion of oxygen ions, resulting in the elimination of lateral growth of the oxide and a corresponding reduction in oxide growth stresses (Huang, et al. 2001). RE oxide particles at the oxide grain boundaries are thought to have a pinning effect on the oxide grains; therefore, oxide grain growth is reduced (Riffard, et al. 2002). A uniform, fine-grained oxide is promoted by the presence of RE at the grain boundaries as they are able to act as nucleation sites for oxide formation (Huang, et al. 2001). Finally, RE at the grain boundaries of the oxide scale are thought to prevent the passage of adsorbed gas atoms such as C or N through the oxide scale, thus improving the resistance of the alloy to gaseous corrosion (Zheng & Young. 1998).

### 2.5.1 Effect of Environment

Under SOFC operating conditions, at an operating temperature of 800°C, the oxygen partial pressure on the cathode (air) side of the interconnect is 21 kPa, while the anode (fuel) side of the interconnect experiences an oxygen partial pressure that is typically as

low as $10^{-16}$ Pa (England & Virkar. 2001). Therefore, it is important to understand the oxidation behaviour of stainless steels in both of these environments.

#### *2.5.1.1 Air (Cathode) Side*

Commercial SOFCs use air as a source of oxygen. In addition to oxygen, air also contains nitrogen and water vapour, both of which have an effect on the oxidation behaviour of stainless steels. Nitrogen is known to accelerate the growth of chromia (Grabke, et al. 2004). If nitrogen is present in the atmosphere, it adsorbs onto the surface of the stainless steel (Grabke, et al. 2004). The formation of an intermediate nitride at the surface, $Cr_2N$, results in the segregation of Cr to the alloy surface (Grabke, et al. 2004). The end result is an increase in the nucleation of chromia, causing the formation of a fine-grained oxide layer (Grabke, et al. 2004, Ostwald & Grabke. 2004). Oxide scales with fine grains grow faster than those with coarse grains due to the rapid transport of Cr along the oxide grain boundaries (Grabke, et al. 2004). Nitrogen is also a concern if it is able to penetrate the oxide scale, as it can cause high temperature embrittlement of the stainless steel (Quadakkers, et al. 2003). Nitrogen can be transported as a single gas molecule through porosity or defects in the oxide scale (Zheng & Young. 1998). As the thickness of the chromia scale increases, it tends to become more permeable to gases (Quadakkers, et al. 2003). Embrittlement can be caused both by nitrogen dissolved in the steel or by the formation of nitrides below the oxide scale (Quadakkers, et al. 2003).

The presence of water vapour in the oxidising environment, either air or oxygen, has a detrimental effect on the oxidation behaviour of stainless steels. The oxidation rate of stainless steels is increased in the presence of water vapour, and scale porosity is also increased (Garcia-Vargas, et al. 2005a, Mikkelsen & Linderoth. 2003). The presence of water vapour in the environment reduces the stability of chromia by enhancing the formation of volatile Cr oxide and oxyhydroxide species (Danielewski, et al. 2005, Quadakkers, et al. 2003). Also, the Fe content of chromia scales formed on stainless steels in humid air is higher than that of chromia scales formed in the presence of dry air (Kofstad. 1998). This is due to the fact that water vapour enhances the transport of Fe in the oxide scale (Yang, et al. 2004b). For Fe-13Cr alloys, as the water vapour content in oxygen was increased from 0.03 to 2 vol% for oxidation at 980°C, the oxide composition changed from $Cr_2O_3$, $Fe_2O_3$, and $(Fe,Cr)_2O_3$ at low water vapour contents to a thicker $Fe_2O_3/Fe_3O_4/Fe$ and chromia multilayered scale (Kofstad. 1998). The Fe enrichment of

oxide scales in the presence of water vapour is not observed if the Cr content of the stainless steel is high enough; this was found to be the case for Fe-28Cr alloys (Yang, et al. 2004b). Therefore, in order to selectively form a protective chomia layer in humid air or oxygen, a higher Cr alloy content is required (Kofstad. 1998). Also, in a study of 9-12% Cr stainless steels, a more rapid depletion of Cr in the alloy below the metal/oxide interface at a given oxidation temperature was observed in the presence of water vapour than for dry air (Danielewski, et al. 2005).

In summary, as compared with the oxide scale formed on stainless steels in dry oxygen or air, the oxide layer formed in a moist environment is thicker, more porous, and less homogeneous (Garcia-Vargas, et al. 2005a). The net result is a reduction in the operating lifetime of the stainless steel interconnect as the oxide is more susceptible to cracking and spalling than the thinner, more dense oxide formed in the absence of moisture (Garcia-Vargas, et al. 2005a).

#### *2.5.1.2 Fuel (Anode) Side*

##### 2.5.1.2.1 $H_2/H_2O$

One difference between oxidation in a fuel environment compared to an air environment is the morphology of the oxide scale. In a study of the oxidation of a 22% Cr steel at 900°C for 70 h, the oxide scale that formed in a 7% $H_2$/93% Ar by volume environment had a fine grain size and contained ridges and whiskers (Mikkelsen & Linderoth. 2003). In contrast, the oxide formed on the same steel in air was composed of larger nodules of oxide made up of many smaller grains (Mikkelsen & Linderoth. 2003). It was noted that the morphology difference only existed close to the oxide/gas interface and did not extend through the entire oxide scale; close to the metal/oxide interface, the grain size of the scales formed in fuel and air environments was similar (Mikkelsen & Linderoth. 2003). The observed morphology difference was not affected by varying the amount of water vapour present in the environment from 1 vol% to 12 vol% (Mikkelsen & Linderoth. 2003). A study of the oxidation of Ducrolloy CRF, a Cr-based ODS high-temperature alloy, between 950 and 1050°C in an $Ar/H_2/H_2O$ mixture with an oxygen partial pressure of $10^{-10}$ Pa, also noted the presence of oxide whiskers, which are due to

enhanced outward diffusion of scale-forming cations (Quadakkers, et al. 2003, Tomlinson & Blick. 1990).

The adhesion of oxide scales formed in fuel environments has been found to be better than that of scales formed in air. For a 22% Cr steel oxidized at 900°C for 70 h, the presence of voids and cavities at the metal/oxide interface was noted for scales formed in air; however, in a 7% $H_2$/93% Ar by volume environment containing either 1 or 12 vol% $H_2O$, no voids or pores were found (Mikkelsen & Linderoth. 2003). In a study on the cyclic oxidation of Ducrolloy CRF at 950°C in an Ar/$H_2$/$H_2O$ mixture with an oxygen partial pressure of $10^{-10}$ Pa for several thousands of hours, reduced oxide spalling was found compared to that observed in air (Quadakkers, et al. 2003). This was due to reduced scale buckling during growth in the fuel environment (Quadakkers, et al. 2003). The reduced void formation in fuel environments has been attributed to the presence of "$H_2$/$H_2O$ bridges" in cation vacancies at the metal/oxide interface which prevent their growth and coalescence into pores and cavities (Quadakkers, et al. 2003). It is also thought that the ability of chromia to undergo creep deformation is improved with decreasing oxygen activity in the environment (Mikkelsen & Linderoth. 2003). Finally, improved scale adhesion in fuel environments may be due to the ability of hydrogen to scavenge impurities such as S at the metal/oxide interface according to the following reaction (Park & Speigel. 2005):

$$H_2(g) + \dot{S}_{surf} \rightarrow H_2S(g) \qquad (2\text{-}22)$$

Impurities such as S have a negative affect on scale adhesion (Mikkelsen & Linderoth. 2003).

The composition of oxide scales formed in $H_2$/$H_2O$ environments differs from that of scales formed in air. For 8 – 11% Cr stainless steels in $H_2$/$H_2O$ at 800°C for 100 h, the oxide scale formed was enriched in Cr, Mn, and Si relative to oxides formed under similar conditions in air (Ostwald & Grabke. 2004). For stainless steels containing 14% Cr, in $N_2$/$H_2$ mixtures at 800°C, the amount of Cr enrichment in the oxide scale increased as the amount of $H_2$ in the gas mixture increased (Park & Speigel. 2005). Hydrogen enhances the diffusion of scale-forming elements by bonding to oxygen ions at the metal/oxide interface or within the oxide scale, resulting in the formation of substitutional hydroxide point defects and, more importantly, cation vacancies (Yang, et al. 2004b).

Hydrogen is also able to enhance the dissolution of Cr carbides, particularly in the vicinity of grain boundaries, making more Cr available for scale formation (Park & Speigel. 2005). Finally, as the amount of hydrogen in the environment increases, the oxygen partial pressure decreases. This enhances the selective oxidation of Cr as the formation of other, less stable oxides is thermodynamically unfavourable (Park & Speigel. 2005, Quadakkers, et al. 2003).

The influence of oxidation in $H_2/H_2O$ on the thickness of the oxide scale has also been studied. For the oxidation of 430 stainless steel at temperatures between 750 and 900°C for 300 h, it was found that the parabolic rate constant was the same magnitude in $H_2/H_2O$ as in air (Brylewski, et al. 2001). A similar study of the oxidation of 430 stainless steel at 750, 800, 850, and 900°C for 300 h in $H_2/H_2O$ environments with a ratio of 94/6 or 97/3 vol% and in air found that the parabolic rate constant was independent of oxygen partial pressure within the studied range of $5.2 \times 10^{-22}$ to 0.21 atm (Brylewski, et al. 1999). Another study of 430 stainless steel under the same conditions found that the thickness of the oxide scales was similar to that of scales formed in air at the same oxidation temperatures (Kurokawa, et al. 2004). A study of the oxidation of a 22% Cr stainless steel at 900°C for 70 h found that the thickness of the oxide scale formed in 7%$H_2$/93% Ar by volume was slightly larger than that formed in air (Mikkelsen & Linderoth. 2003). For the oxidation of Crofer 22 APU at 800°C in hydrogen containing 3 vol% $H_2O$, the oxide scale was thinner than the scale formed in air at the same temperature; however, the porosity of the oxide was increased relative to that of the scale formed in air (Yang, et al. 2004a).

#### 2.5.1.2.2 $CH_4/H_2O$

In a study of the oxidation of 430 stainless steel at 800°C in an $Ar/CH_4$ mixture with $p_{Ar}$ = 85 kPa, $p_{CH_4}$ = 5 kPa, and $p_{H_2O}$ = 10 kPa, the parabolic rate constant was the same magnitude as that for oxidation in air (Horita, et al. 2004). Under the same conditions, the composition of the oxide formed on 430 stainless steel and ZMG 232 was similar to that formed in air (Horita, et al. 2004).

One difference between the oxidation of stainless steel in a hydrogen-containing fuel environment and that in $CH_4$, CO, or other carbon-containing fuels is the possibility of

carbon deposition. Due to the presence of porosity, the chromia scale is not completely impermeable to gases and thus the transfer of C from the gas through the oxide to the underlying metal is possible (Zheng & Young. 1998). Carbon in the alloy is able to react with Cr, resulting in the precipitation of fine Cr carbides such as $Cr_{23}C_6$ or $Cr_7C_3$ (Quadakkers, et al. 2003). This results in a depletion of Cr in the region of the alloy close to the metal/oxide interface and a reduction in the amount of Cr that is available for oxide formation (Quadakkers, et al. 2003). If the Cr content of the alloy is low (<20%), the exposure of the stainless steel to carbon-containing gases can significantly reduce its oxidation resistance (Quadakkers, et al. 2003). If the formation of Cr carbides occurs predominately along the ferrite grain boundaries, embrittlement of the stainless steel results (Jian, et al. 2003). The formation of Cr carbides can be prevented by alloying additions of carbide formers such as Si, Nb, Ti, W, and rare earth elements (Kane. 2003). In this case, the alloying element will preferentially form carbides, meaning that more Cr is available for protective scale formation (Kane. 2003). In a study of 430 stainless steel at 750°C in a simulated reformed fuel environment containing 53.09% $N_2$, 25.19% $H_2$, 18.26% CO, 3.27% $CO_2$, and 0.17% $CH_4$ by volume, no significant carburization was observed as the chromia scale was an adequate diffusion barrier against C transfer from the gas (Jian, et al. 2003).

#### *2.5.1.3 Simultaneous Air/Fuel*

The majority of studies on the oxidation of stainless steel under SOFC operating conditions have been carried out either in air or in a fuel environment; however, in service, the interconnect is simultaneously exposed to both environments (Yang, et al. 2003a). A study of the oxidation of 430 stainless steel at 800°C for 300 h, under simultaneous exposure to air and $H_2$ containing approximately 3 vol% $H_2O$, found that the oxidation behaviour differed from that in air or wet hydrogen fuel alone (Yang, et al. 2003a). The oxidation behaviour observed under simultaneous exposure conditions is referred to in the literature as "anomalous oxidation" (Yang, et al. 2004b, Yang, et al. 2005). The oxide scale formed on the fuel side of the interconnect under simultaneous air/fuel exposure was similar to the protective scale formed during exposure to fuel alone; both scales consisted of outer MnO crystals and inner $(Mn, Cr, Fe)_3O_4$ spinel (Yang, et al. 2003a). However, there was a significant difference between the oxide layer formed on the air side of the stainless steel interconnect and that which formed on the stainless steel during exposure to air alone (Yang, et al. 2003a). For the oxide scale formed in air alone,

the protective layer consisted of inner chromia and outer $(Mn,Cr,Fe)_3O_4$ spinel (Yang, et al. 2003a). The scale was fairly homogeneous, and in some cases, a thin layer of silica formed between the oxide layer and the stainless steel interconnect (Yang, et al. 2003a). For the air side of the interconnect under simultaneous exposure conditions, in addition to chromia and spinel, $Fe_2O_3$ was also present in the oxide layer (Yang, et al. 2003a). Porous Fe-rich nodules randomly distributed across the surface of the scale were also observed (Yang, et al. 2003a). The nodules were found to contain Cr and Mn; therefore, they could consist of either a mixture of $Fe_2O_3$ and (Cr,Mn) spinel or a $Fe_2O_3$-based Fe-Cr-Mn solid solution (Yang, et al. 2003a). In the regions of the oxide scale adjacent to the Fe-rich nodules, localized metal loss was observed, although the composition of the scale in these regions was the same as the rest of the scale (Yang, et al. 2003a).

The presence of Fe-enriched nodules on the air side of the interconnect under simultaneous air/fuel exposure is attributed to the ability of hydrogen to enhance the transport of Fe through the oxide scale, as well as to increase its solubility in the scale (Yang, et al. 2003a, Yang, et al. 2005). Before a protective oxide has formed on the fuel side of the interconnect, hydrogen from the environment adsorbs onto the stainless steel surface (Yang, et al. 2004b). Then, the adsorbed hydrogen dissolves as atomic H in the alloy (Yang, et al. 2004b). Due to the difference in the chemical potential of hydrogen between the air and fuel sides of the interconnect, H then rapidly diffuses to the air side of the interconnect (Yang, et al. 2004b). The presence of H on the stainless steel surface, before a protective oxide is formed, results in the formation of defects in the oxide scale, allowing the transport of Fe through the protective layer on the air side of the interconnect (Yang, et al. 2003a). Defects in the oxide scale also increase the solubility of Fe in the scale on the air side of the interconnect (Xia, et al. 2004). Once a protective layer forms on the fuel side of the interconnect, hydrogen transport to the air side is more difficult as it must occur through the oxide scale (Yang, et al. 2004b). However, the oxide scale formed in the hydrogen-containing fuel environment likely contains defects and is thus not an effective barrier against hydrogen transport (Yang, et al. 2004b).

Another study of anomalous oxidation examined the behaviour of 316 stainless steel tubes that were preoxidized at 700°C in dry air for 100h and then exposed to one of four different environments at 700°C for 100h: $H_2$-air, $H_2$-Ar, air, or Ar (Holcomb, et al. 2006). For the $H_2$-air dual environment, the air side scale was discontinuous and consisted of two distinct layers: an inner Cr-Fe-Ni spinel and an outer, flaky, $Fe_2O_3$ layer

(Holcomb, et al. 2006). For the specimen exposed to air only, the oxide scale was thicker and continuous, consisting of an inner $Cr_2O_3$ and Cr-Fe-Ni spinel layer and an outer layer of $Fe_3O_4$ (Holcomb, et al. 2006). For the $H_2$-Ar dual environment, no anomalous oxidation behaviour was observed as the scale that formed on the side of the steel that was exposed to Ar was relatively thin and continuous, consisting of $Cr_2O_3$ and Cr-Fe-Ni spinel (Holcomb, et al. 2006). The oxide scale on the steel exposed to Ar alone had a similar composition to that on the Ar side of the dual exposure; however, in the former case, the scale was detatched from the metal (Holcomb, et al. 2006). The authors of the study proposed a different mechanism to explain the anomalous oxidation behaviour in the $H_2$-air dual environment (Holcomb, et al. 2006). They suggested that H from the fuel side of the interconnect is able to diffuse to the air side of the interconnect, where it reacts with oxygen, that had diffused into the scale, to form water vapour (Holcomb, et al. 2006). Once the vapour pressure of the water reaches a critical level, the formation of pores in the protective oxide layer occurs (Holcomb, et al. 2006). The presence of pores in the oxide scale would allow oxygen to be transported through the scale as a gas rather than as an anion, resulting in an increase in the oxidation rate of the alloy (Holcomb, et al. 2006). In addition to this, the presence of water vapour in the scale is known to account for the formation of less protective oxides containing Fe enrichment (Holcomb, et al. 2006).

The anomalous oxidation behaviour observed under simultaneous air/fuel exposure depends on the Cr content of the stainless steel. A study of the oxidation behaviour of Crofer 22 APU, containing 22% Cr, and E-brite, containing 27% Cr, under simultaneous air/fuel exposure conditions did not find the presence of $Fe_2O_3$ in the air side oxide scale that was observed for the 430 stainless steel, containing 17% Cr (Yang, et al. 2005). However, the Fe-rich nodules that were present on the air side scale for 430 were also observed for Crofer 22 APU and E-brite (Yang, et al. 2005).

The presence of water vapour on the air side of the interconnect was found to enhance the anomalous oxidation behaviour. In an oxidation study of Crofer 22 APU at 800°C for 300 h under simultaneous exposure to moist air and moist hydrogen, each containing 3 vol% water vapour, the thickness of the oxide scale formed on the air side of the interconnect was larger than the oxide scale formed in moist air alone (Yang, et al. 2005). Also, the spinel to chromia ratio was smaller under the simultaneous exposure conditions (Yang, et al. 2005). The air side scales formed under simultaneous moist air/ moist fuel

exposure, similar to those formed under simultaneous dry air/moist fuel conditions, contained $Fe_2O_3$ and Fe-rich nodules (Yang, et al. 2005). However, with the presence of water vapour on the air side of the interconnect, the nodule growth was more significant. The nodules were 3 to 4 times thicker than the rest of the oxide scale, and the regions of the oxide scale adjacent to the nodules were also thicker than the rest of the scale (Yang, et al. 2005). Also, the entire oxide scale formed on the moist air side of the interconnect was found to be enriched with Fe compared to the oxide scale formed in moist air alone (Yang, et al. 2005). This is in contrast to the case of simultaneous exposure to dry air/moist fuel, where Fe enrichment was only observed in the nodules (Yang, et al. 2005).

Thermal cycling was found to increase the amount of anomalous oxidation under simultaneous exposure conditions. A study of Crofer 22 APU exposed simultaneously to ambient air and moist hydrogen, containing approximately 3 vol% $H_2O$, studied the effect of thermal cycling on oxidation behaviour at 800 and 850°C (Xia, et al. 2004). Three thermal cycles were performed, in which the stainless steel was heated to the oxidation temperature at a rate of 10°C/minute, held at the oxidation temperature for 100 h, and cooled to room temperature (Xia, et al. 2004). For thermal cycling at 800°C, no significant difference was found between the anomalous oxidation behaviour under isothermal conditions (Xia, et al. 2004). However, at 850°C, the oxide scale that formed on the air side of the stainless steel consisted mainly of hematite (Xia, et al. 2004). Porous, Fe-rich nodules were randomly distributed over the surface of the scale and, with thicknesses ranging from a few μm to over 20 μm, were significantly thicker than the rest of the scale (Xia, et al. 2004). Adjacent to the nodules, severe metal consumption was observed (Xia, et al. 2004). It was also noted that the composition of the scale in regions below the Fe-rich nodules was different than that of the rest of the scale; it was enriched in Mn and Cr and also contained a significant amount of porosity (Xia, et al. 2004). In contrast, the oxide layer in areas where no nodules were present consisted of an upper layer of $Fe_2O_3$ and a lower layer comprised of both chromia and spinel (Xia, et al. 2004). The reason that thermal cycling was found to increase the anomalous oxidation behaviour is because of the thermal stresses generated during the temperature changes (Xia, et al. 2004). Thermal stresses cause deformation of the oxide scale and, as a result, the formation of defects in the oxide layer (Xia, et al. 2004). As mentioned earlier, a higher concentration of defects in the oxide increases the transport of Fe through the oxide layer as well as increases the solubility of Fe in the oxide.

## 2.6 Types of Surface Treatments

A surface treatment can be defined as a technique that is used in the formation of a layer on the surface of a material (Burakowski & Wierzchon. 1999). Surface treatments can be divided into six categories: mechanical, thermo-mechanical, thermal, thermo-chemical, electrochemical and chemical, and physical (Burakowski & Wierzchon. 1999). These categories are described in Table 2-4. Each category of surface treatments results in the formation of a surface layer with a distinct depth and specific properties (Burakowski & Wierzchon. 1999).

Table 2-4. Categories of Surface Treatment Methods (Burakowski & Wierzchon. 1999).

| Technique | Mechanical | Thermo-mechanical | Thermal | Thermo-chemical | Electro-chemical and Chemical | Physical |
|---|---|---|---|---|---|---|
| **Layer Depth** | fractions of mm to several mm | several tens of mm to several mm | fractions of mm to several mm | several tens of μm to several mm | several μm to several hundred μm | tenths of μm to several tens of μm |
| **Examples** | •Burnishing<br>•Detonation Spraying<br>•Machining<br>•Cold Deformation | •Thermal Spraying<br>•Spray Melt Coating<br>•Plating<br>•Hardening<br>•Detonation<br>•Hot Reduction | •Hardening, Tempering, Annealing<br>•Surface Remelting<br>•Cladding<br>•Melt Coating<br>•Melting<br>•Hot Dip Processes | •Saturation by Unassisted Diffusion<br>•Saturation by Assisted Diffusion<br>•Alloying<br>•Thermo-chemical Setting | •Deposition<br>•Polishing<br>•Etching<br>•Chemical Setting<br>•Sol-Gel Techniques | •Physical Setting<br>•Vapor Deposition<br>•Ion Implantation |

### 2.6.1 Residual Stress

Residual stresses can be defined as stresses that exist in a material when no external loads are being applied (Karabelchtchikova & Rivero. 2005). When an external load is applied to a material, both elastic and plastic deformation of the material can occur if the magnitude of the load is greater than the elastic limit of the material (Althaus. 1985,

Burakowski & Wierzchon. 1999). When the load is removed, the elastic deformation is recovered; however, the plastic deformation remains (Burakowski & Wierzchon. 1999). The stresses in the material resulting from the irreversible plastic deformation are residual stresses ($\sigma_w$) (Burakowski & Wierzchon. 1999). The sign of the residual stress is opposite to that of the external load (Althaus. 1985). In order to fully characterize the residual stress state of a material, it is important to know the sign of the residual stress (a negative residual stress indicates compression while a positive value indicates tension), the numerical value, distribution, depth of penetration, and gradient (Burakowski & Wierzchon. 1999). There are three categories of residual stresses: mechanical, thermal, and structural (Burakowski & Wierzchon. 1999).

Mechanical residual stresses usually result from non-uniform deformation of the surface layer of a material during cold work (Burakowski & Wierzchon. 1999). Plastic deformation resulting from cold work causes a reduction in the surface material density and therefore results in compressive residual stresses (Burakowski & Wierzchon. 1999).

Thermal residual stresses result from non-uniform heating or cooling of different layers of the material (Burakowski & Wierzchon. 1999). When a material is heated in a surface treatment process, the temperature at the surface of the material is typically higher than the temperature of the core of the material (Karabelchtchikova & Rivero. 2005). Because of this, the thermal expansion of the core of the material will be smaller than that of the surface of the material, resulting in tensile stress in the core material and compressive stress at the surface (Burakowski & Wierzchon. 1999). When the material is cooled to room temperature, the contraction of the surface will be greater than that of the core, resulting in the establishment of compressive stresses in the core and tensile stresses at the surface of the material at room temperature (Althaus. 1985, Burakowski & Wierzchon. 1999). The magnitude of thermal residual stresses increases if the temperature gradient between the surface and the core of the material increases and decreases if the yield strength of the material is higher (Burakowski & Wierzchon. 1999).

Structural residual stresses result from phase transformations in the material (Burakowski & Wierzchon. 1999). Phase transformations can result in a volume change which typically ranges from 0.5 to 1.5%, but can be as high as 3% (Burakowski & Wierzchon. 1999). The volume change in the material is accommodated by the formation of residual stresses: compressive if the material volume increases, and tensile if the volume is

reduced (Burakowski & Wierzchon. 1999). The magnitude of structural residual stresses is typically larger than that of thermal residual stresses (Burakowski & Wierzchon. 1999)

For surface treatments, there is typically no simple mathematical expression to correlate the material, surface treatment parameters, and the resulting residual stress state (Burakowski & Wierzchon. 1999). Several measurement techniques exist for determining the magnitude of residual stresses in a given material; however, the results obtained usually depend on the measurement technique that is used (Burakowski & Wierzchon. 1999).

### 2.6.2 Mechanical Surface Treatments

In mechanical surface treatments, the pressure of a tool or the kinetic energy of a tool or of particles is used to plastically deform the surface layer of a material at room temperature (Burakowski & Wierzchon. 1999). The greater the degree of plastic deformation, the higher the magnitude of the resulting residual stress (Burakowski & Wierzchon. 1999). Common types of mechanical surface treatments include machining, cold rolling, shot peening, sandblasting, and grinding (Leistikow. 1981).

#### *2.6.2.1 Machining*

The main purpose of machining operations such as milling or turning is to create a part with specified dimensions while maintaining a good surface finish (Burakowski & Wierzchon. 1999, Scholtes & Vöhringer. 2001). Machining involves the removal of the outer layer of material of the part being machined, thus exposing the underlying metal to the environment, which is typically either air or a coolant (Burakowski & Wierzchon. 1999). As a result, reactions occur between the metal and the environment, producing a thin surface layer, approximately 2μm in depth, containing oxides, sulphides, nitrides, and other reaction products as well as contaminants from the environment such as dust, grease, and condensed vapours (Burakowski & Wierzchon. 1999).

A consequence of machining is the establishment of residual stresses in the surface layer of the machined part (Burakowski & Wierzchon. 1999). During a typical machining operation, both cutting forces (mechanical effects) and frictional forces (thermal effects)

are important (Burakowski & Wierzchon. 1999, Jacobus, et al. 2000). Cutting forces result in chip formation and thus cause plastic deformation and subsequent hardening of the surface layer (Burakowski & Wierzchon. 1999, Scholtes & Vöhringer. 2001). Due to the action of cutting forces alone, compressive residual stresses are established in the surface layer (Burakowski & Wierzchon. 1999). However, the overall residual stress distribution is strongly affected by frictional forces. At the point of contact between the machining tool and the part, frictional heating increases the temperature of the surface of the workpiece relative to that of the underlying metal (Burakowski & Wierzchon. 1999). After the tool passes, rapid cooling occurs and tensile residual stresses form in the surface layer of the machined part (Burakowski & Wierzchon. 1999, Jacobus, et al. 2000). Compressive stresses develop in the subsurface layer where only mechanical effects are significant (Jacobus, et al. 2000). A typical residual stress distribution resulting from a machining process is displayed in Figure 2-5.

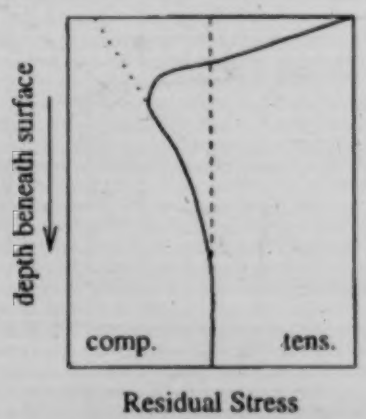


Figure 2-5. Residual Stress Distribution in a Machined Part (Jacobus, et al. 2000).

In Figure 2-5, the dotted line represents the residual stresses resulting from mechanical effects alone, while the solid line represents the residual stress distribution resulting from the combination of thermal and mechanical effects produced by the machining process (Jacobus, et al. 2000).

The type of machining operation has an influence on the residual stress distribution in the machined part. For rough machining, the amount of material deformation is large; therefore, the magnitude of the resulting residual stresses is higher and the depth of

material affected by residual stresses is greater (Burakowski & Wierzchon. 1999). In contrast, finish machining operations involve much smaller deformations and, as a result, both the depth and magnitude of residual stresses in the finished part are reduced (Burakowski & Wierzchon. 1999). Other factors also influence the residual stresses resulting from machining processes, including the material properties of the part as well as process variables such as cutting speed, type of cutting tool, and type of coolant used, if any (Burakowski & Wierzchon. 1999). In machining processes where the tool passes over the workpiece more than once, such as milling, the increase in temperature at the surface of the material is typically lower, and as a result, thermal effects are reduced (Scholtes & Vöhringer. 2001). In some cases, it is possible to form compressive residual stresses in the surface layer of the machined part, and the resulting residual stress distribution would approach that represented by the dotted line in Figure 2-5 (Jacobus, et al. 2000).

#### *2.6.2.2 Cold Rolling*

The process of cold rolling involves placing a piece of metal between two metal rolls that rotate in opposite directions and apply pressure to the metal workpiece at room temperature in order to reduce its thickness (Callister Jr. 2000, Ross. 1988). Several changes in the microstructure and the resulting properties of a metal occur as a result of cold rolling. The grains of the metal are elongated in the direction of rolling, producing a microstructure with preferred orientation and thus one with anisotropic properties (Burakowski & Wierzchon. 1999, Ross. 1988). Plastic deformation of the rolled metal is accommodated by an increase in the dislocation density of the metal; as a result, the hardness and tensile strength of the metal increase and a reduction in ductility is observed (Ross. 1988). Due to mechanical deformation, compressive residual stresses are established at the surface of a cold rolled metal (Burakowski & Wierzchon. 1999, Callister Jr. 2000). In a rolling process, the resulting residual stress distribution depends on several rolling parameters including roll design, temperature distribution, cooling rate, initial thickness, material properties, and material composition (Amin & Ganesh. 1981). The depth of the deformed region increases with increasing percent reduction (Sun, et al. 2004). In a cold rolling study of eutectoid steel, containing 0.73% C, 0.27% Si, and 0.75% Mn, the relationship between the magnitude of compressive residual stress and the amount of reduction was linear and could be described by the following equation (Sun, et al. 2004):

$$\sigma_{RS} = -1135\Delta t - 366 \qquad (2\text{-}23)$$

where $\Delta t$ represents the amount of reduction due to cold rolling (Sun, et al. 2004). However, in a similar study of the low carbon steel JIS S25C, the magnitude of the residual stress due to cold rolling was much smaller than for the eutectoid steel, and the magnitude increased much more gradually with an increase in the amount of cold rolling reduction (Sun, et al. 2004). Therefore, it was proposed that the effect of residual stress is more significant as the carbon content of the steel increases (Sun, et al. 2004). A study of copper-2% beryllium alloys determined that for large cold rolling reductions, there is a possibility of forming tensile residual stresses at the surface of the deformed metal (Amin & Ganesh. 1981). The study found that for 11% reduction, the residual stresses at the surface were compressive and the magnitude remained constant through a depth of 0.127 mm below the surface (Amin & Ganesh. 1981). However, for 22% reduction and 37% reduction, the residual stresses at the surface were tensile, and they decreased rapidly in magnitude with increasing depth to become compressive below the metal surface at a depth of 0.025 mm and 0.127 mm, respectively (Amin & Ganesh. 1981). The magnitude of the residual stresses increased with an increase in the amount of cold reduction, and varied from 20% to 40% of the alloy yield strength as the amount of deformation increased from 11% to 37% (Amin & Ganesh. 1981). The formation of tensile residual stresses in materials that have been heavily cold worked is due to the difference in the amount of deformation of the surface compared to the core of the material (Amin & Ganesh. 1981). For less severe deformations, the surface of the metal is more heavily deformed than the core of the metal and, as a result, the metal strip is concave shaped (Amin & Ganesh. 1981). However, for more severe deformations, the core of the metal undergoes more deformation than the surface and the metal strip is convex shaped (Amin & Ganesh. 1981).

#### *2.6.2.3 Shot Peening*

Shot peening is a process in which small hard particles, called shots, are projected at high velocities towards the surface of a metal part (Callister Jr. 2000). Shots are typically spherical in shape and have a diameter ranging between 0.1 and 2 mm (Burakowski & Wierzchon. 1999, Callister Jr. 2000, Kruger, et al. 2000, Ross. 1988). Typical shot

velocities are between 10 and 120 m/s (Kruger, et al. 2000). Either air pressure or the centrifugal force of an impellor is used to project the shots (Ross. 1988).

Upon impact, the kinetic energy of the shot is transferred to the metal, producing deformation of the surface layer of the metal (Burakowski & Wierzchon. 1999). The impact of a shot on the metal surface produces an indentation known as a dimple (Hammersly. 1993). The depth of the dimple formed on the metal surface depends on the blast speed, shot hardness, and shot diameter (Parent Simonin & Flavenot. 1987). Following the impact of many shots, the indentations overlap and eventually, a deformed layer of constant depth is produced on the metal surface (Hammersly. 1993). The depth of the plastically deformed layer is typically between 0.2 and 0.4 mm (Scholtes & Vöhringer. 2001).

As a result of the surface deformation induced by shot peening, compressive residual stresses develop in the surface layer of the peened metal (Kruger, et al. 2000). The depth of the residual stresses is the same as the diameter of the dimple formed on the metal surface by the impact of the shot, typically 0.25 to 0.5 times the diameter of the shot (Callister Jr. 2000, Hammersly. 1993). The maximum magnitude of the compressive residual stress is typically 60% of the ultimate tensile strength (UTS) of the material; however, in some cases it can be as high as 80 to 85% of the UTS or even of the same order as the UTS (Hammersly. 1993, Parent Simonin & Flavenot. 1987). A typical residual stress distribution resulting from a shot peening process is shown below in Figure 2-6.

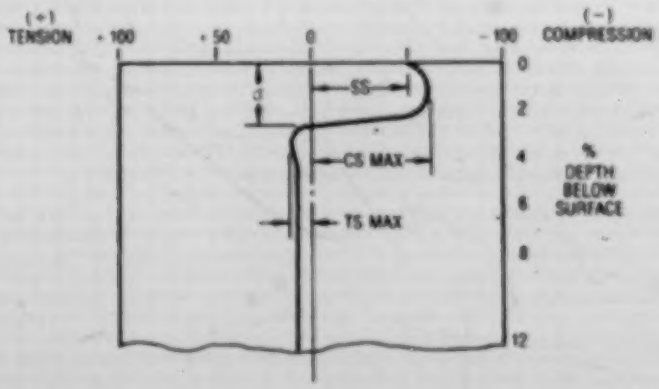


Figure 2-6. Residual Stress Distribution Following Shot Peening (Hammersly. 1993).

The compressive residual stress at the surface of the metal is balanced by tensile residual stresses in the core of the material (Hammersly. 1993). As shown in the figure, the tensile residual stress is of relatively small magnitude and extends throughout the entire core region (Menig, et al. 2001).

The magnitude and depth of the compressive residual stresses resulting from a shot peening process depend on several process parameters: shape of shot, shot material, shot hardness, shot density, workpiece hardness, angle of impingement of shot, shot impact velocity, size of shot, and shot peening time (Hammersly. 1993). The last three parameters are often considered together as shot intensity, which is empirically determined. Shot peening intensity is represented by the following relationship (Vöhringer. 1987):

$$i \propto vdt \qquad (2\text{-}24)$$

where $i$ represents shot intensity, $v$ is shot velocity, $d$ is shot diameter, and $t$ represents shot peening time (Vöhringer. 1987). Increasing the shot intensity increases the magnitude of the maximum compressive residual stress and also increases the depth of its location below the surface (Was, et al. 1981). The overall penetration depth of the residual stresses is increased with increasing shot intensity; however, the magnitude of the compressive residual stress at the surface is decreased (Parent Simonin & Flavenot. 1987, Was, et al. 1981).

The effect of several shot peening process parameters on the resulting residual stress distribution is summarized in Figure 2-7 (Scholtes & Vöhringer. 2001). In Figure 2-7, $HV_w$ represents the hardness of the workpiece, $HV_s$ represents the hardness of the shot, $\dot{m}$ represents the mass flow rate of shots impinging on the workpiece, $d$ represents the shot diameter, $p$ is the shot pressure, $v$ is the shot velocity, and $t$ is the exposure or shot peening time (Scholtes & Vöhringer. 2001). Each arrow represents the change in the residual stress distribution resulting from an increase in the shot peening parameters indicated beside the arrow.

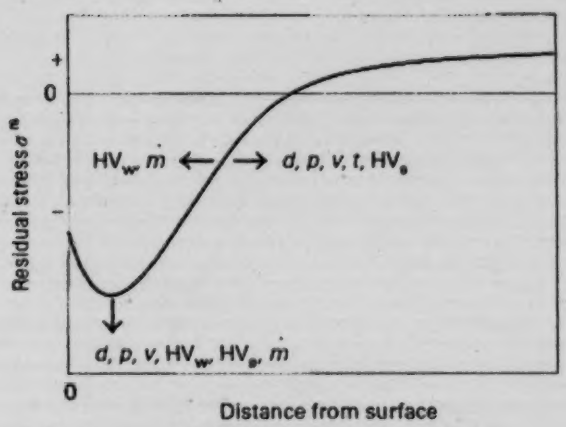


Figure 2-7. Effect of Shot Peening Process Parameters on the Residual Stress Distribution (Scholtes & Vöhringer. 2001).

Various types of shot are used depending on the purpose of the shot peening treatment (Ross. 1988). Cast iron, carbon steel, and glass shots are all commonly used (Ross. 1988). As shown in Figure 2-7, using a softer shot decreases the maximum magnitude of the compressive residual stress and also decreases the depth of the stressed layer (Was, et al. 1981).

One of the most important mechanical properties affecting the residual stress distribution resulting from a shot peening process is the hardness of the metal being treated (Vöhringer. 1987). Figure 2-7 demonstrates that by increasing the hardness of the workpiece metal, the magnitude of the maximum compressive residual is increased (Scholtes & Vöhringer. 2001). As the hardness of the shot peened metal increases, the magnitude of the residual stress at the surface is also increased (Vöhringer. 1987). For a harder workpiece metal, the maximum compressive residual stress is located closer to the surface of the metal (Scholtes & Vöhringer. 2001). The residual stress state of a shot peened metal is also affected by other material properties such as strength. Since the hardness and the strength of a metal are related to one another, the magnitude of the residual stresses resulting from shot peening also increases as the strength of the metal increases (Parent Simonin & Flavenot. 1987).

The impact angle between the shot and the metal surface can also have an effect on the resulting residual stress distribution. In studies of plain carbon steel, increasing the impact angle of the shot in the range of 45° to 90° resulted in an increase in the magnitude of both the compressive residual stress at the metal surface and the maxiumum residual stress (Ebenau, et al. 1987, Vöhringer. 1987). In addition, by increasing the impact angle, the penetration depth of the residual stresses into the metal was also increased (Vöhringer. 1987).

The size of the shot used in the shot peening process can also affect the residual stress state of the workpiece metal. If the shot diameter is increased, the magnitude of the compressive residual stress at the metal surface and the maximum compressive residual stress is increased (Was, et al. 1981). The maximum compressive residual stress is located farther away from the metal surface if a larger shot is used (Was, et al. 1981). Also, a larger shot causes the resulting residual stresses to extend deeper into the metal (Was, et al. 1981). In contrast, peening with a smaller shot reduces the depth of material containing residual stress and causes the maximum residual stress to be located closer to the metal surface (Woelfel. 1987).

The degree of coverage is also an important parameter of the shot peening process. In order to obtain a residual stress profile that is relatively constant across the metal surface, 100% coverage is required (Hammersly. 1993). In some cases, 200% or even 400% coverage is used in order to obtain additional benefits such as increased surface hardness and grain refinement of the surface layer (Hammersly. 1993).

Another surface property that is changed by shot peening is roughness, although the amount of surface roughening produced by shot peening is much less than that produced by a sandblasting treatment (Ross. 1988). The surface roughness of a shot peened metal is increased by increasing shot hardness, blast speed, shot diameter, and shot intensity (Parent Simonin & Flavenot. 1987, Was, et al. 1981).

#### *2.6.2.4 Sandblasting*

Sandblasting, also referred to as abrasive blasting or grit blasting, is typically used to clean the surface of a metal by removing oxide scale or surface contaminants (Ross. 1988). Both sandblasting and shot peening are processes that involve particles impacting

the surface of a metal; however, for sandblasting, the particles also cut the metal surface (Ross. 1988). Shot peening does not typically result in the removal of material from the metal surface (Ross. 1988). Finally, sandblasting processes are not typically as controlled as shot peening processes (Ross. 1988).

There are three different types of sandblasting commonly used. Air blasting uses air pressure to project the particles towards the surface of the metal being treated (Ross. 1988). For airless blasting, the particles are directed towards the center of an impellor, which is a rotating-vane type wheel, and are propelled by the centrifugal force resulting from the impellor rotation (Murphy. 1971, Ross. 1988). Liquid blasting is similar to air blasting except that the pressure of a liquid stream, typically water, is used instead of air (Ross. 1988).

Many different types of particles are used for sandblasting, including alumina, silicon carbide, quartz, fractured chilled iron, and blast furnace slag (Murphy. 1971, Ross. 1988). Unlike shot peening, which typically uses spherical shots, grit particles are typically sharp edged, and the particle shape is not usually controlled (Murphy. 1971). Because of this, the metal surface produced by sandblasting is non-oriented and isotropic, and is not as uniform as a surface resulting from shot peening (Bačová & Draganovská. 2004). The size of grit particles is usually described by mesh size, and the amount of control over particle size depends on the purpose of the sandblasting process (Ross. 1988). Particles used in sandblasting are usually much smaller than those used in shot peening. As mentioned earlier, shot diameters generally range between 0.1 and 2 mm. In contrast, one study of sandblasting used quartz particles that were 40μm, 100μm, and 160μm in size (Rhouma, et al. 2001). Because of the smaller particle size, the amount of surface deformation produced in a sandblasting process is usually smaller than for shot peening (Rhouma, et al. 2001).

A typical residual stress profile resulting from a sandblasting process is displayed in Figure 2-8 (Badawi, et al. 1986). The residual stress profile in Figure 2-8 was obtained by averaging the results of 18 different test specimens obtained by air blasting 1010 steel with alumina particles with a size of 423μm, 282μm, or 169μm at a blasting angle of 0°, 30°, or 60°, measured between the stream of grit particles and the normal to the metal surface, and with a distance of 100 mm or 25 mm between the nozzle and the metal surface (Badawi, et al. 1986). The residual stress profile is similar in shape to that

obtained from a shot peening process. Although they are not shown in Figure 2-8, tensile residual stresses are present in the core of the material to maintain equilibrium.

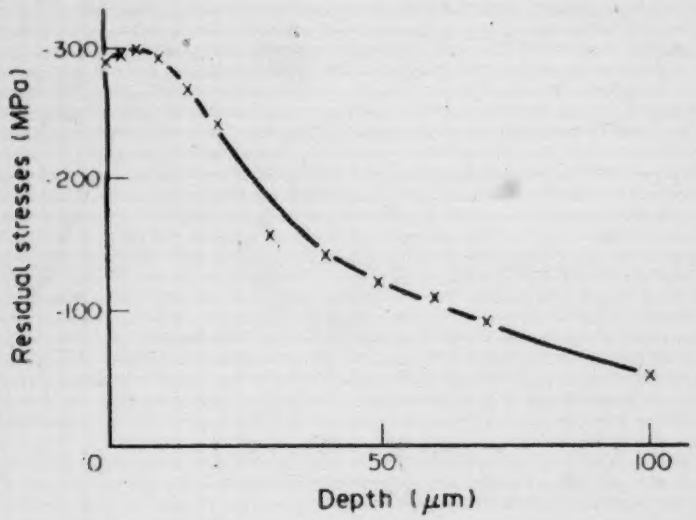


Figure 2-8. Residual Stress Profile Resulting from Sandblasting (Badawi, et al. 1986).

Several sandblasting parameters, such as grit size, blasting angle, and blasting distance, can have an effect on the resulting residual stress distribution. It was found that for 1010 steel, the magnitude of the compressive residual stresses increased as the alumina particle size decreased (Badawi, et al. 1986). This trend is opposite to that for shot peening. The same study also found that the magnitude of the residual stresses decreased slightly as the blasting angle increased, and that the distance between the nozzle and the metal surface had very little effect on the magnitude of the resulting residual stresses (Badawi, et al. 1986).

Sandblasting processes increase the surface roughness of the treated metal much more significantly than for shot peening due to the angularity of the grit particles used in the former process (Bačová & Draganovská. 2004). The degree of roughening produced by a particular sandblasting treatment can depend on process parameters such as grit size, particle velocity, blasting angle, and blasting distance. Surface roughness increases with

increasing grit size and particle velocity, and decreases as the hardness of the blasted metal increases (Badawi, et al. 1986, Bačová & Draganovská. 2004). The blasting distance and blasting angle have little effect on the resulting roughness of the treated metal surface (Badawi, et al. 1986).

#### *2.6.2.5 Grinding*

There are many different methods of grinding the surface of a metal. Rotating grinding wheels, hand-held emery papers or cloths, and lapping techniques, in which a flat band of emery paper rotates against the metal, are commonly used for small-scale operations (Ross. 1988). Large-scale operations often employ automated grinding processes (Ross. 1988). The effect of a grinding process is to produce a series of parallel scratches on the surface of the metal which have a depth that is approximately equal to the size of the abrasive particles used in the process (Ross. 1988). The material located below the scratches produced by grinding is work hardened (Ross. 1988). Grinding is similar to machining in that the resulting residual stress state of the ground material depends on both thermal and mechanical effects (Brinksmeier. 1987). During grinding, mechanical deformation of the metal results in the formation of compressive residual stresses in the surface layer of the metal (Brinksmeier. 1987). However, the generation of thermal energy during the grinding process generates tensile residual stresses in the surface of the ground metal (Brinksmeier. 1987). In most grinding processes, thermal effects dominate and the resulting residual stresses in the metal surface are tensile (Notoya, et al. 1986). Figure 2-9 displays a residual stress profile resulting from the grinding of 316L stainless steel (Rhouma, et al. 2001). In the figure, $\Phi = 0^\circ$ represents the grinding direction and $\Phi = 90^\circ$ represents the direction perpendicular to the grinding direction (Rhouma, et al. 2001). From Figure 2-9, it can be seen that tensile residual stresses are generated both in the grinding direction and also perpendicular to the grinding direction (Rhouma, et al. 2001). Typically, the magnitude of the tensile residual stress is smaller in the direction perpendicular to the grinding direction (Rowe, et al. 2001, Yamamoto, et al. 2004). Similar to shot peening, the maximum residual stress value is located below the surface of the metal (Notoya, et al. 1986, Rhouma, et al. 2001).

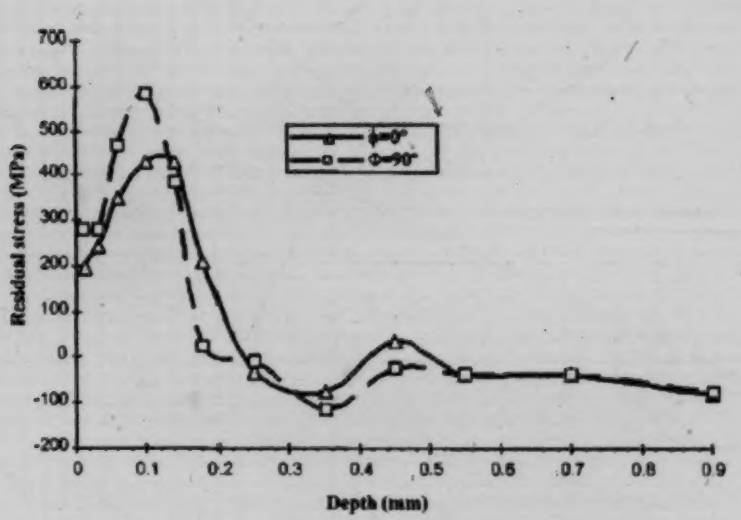


Figure 2-9. Residual Stress Profile Resulting From a Grinding Process (Rhouma, et al. 2001).

As mentioned earlier, thermal effects typically are more important than mechanical effects in determining the residual stress profile resulting from a grinding process. In a study of the grinding of En31, a bearing steel, a direct relationship between work piece temperature and the magnitude of the resulting tensile residual stresses was found (Rowe, et al. 2001). It was also observed for a given material, that there is a critical temperature corresponding to the onset of tensile residual stresses that depends on factors such as material heat treatment, yield strength, temperature dependence of yield strength, and various grinding parameters (Rowe, et al. 2001). In order to reduce the temperature attained by the work piece during a grinding process, the amount of thermal energy generated during grinding that is transferred to the work piece must be reduced.

Several grinding parameters have been found to affect the resulting residual stress profile in a ground metal. First, as work speed is increased, the resulting magnitude of the tensile residual stresses is also increased (Hamdi, et al. 2004, Notoya, et al. 1986). This is due to the increase in work piece temperature resulting from an increase in grinding speed (Hamdi, et al. 2004). An exception to this trend is in the process of high speed grinding (HSG), where compressive residual stresses are generated at the surface of the ground work piece despite high grinding speeds (Hamdi, et al. 2004). A possible

explanation for this is that the temperature rise in HSG processes may be high enough to result in austenitization of the surface of the work piece. During the rapid cooling following the grinding process, martenisite may form, resulting in compressive residual stresses due to the increase in volume (Hamdi, et al. 2004). Increasing the work speed also results in the location of the maximum tensile residual stress moving closer to the surface of the metal (Notoya, et al. 1986). The depth of the metal surface layer containing residual stresses is reduced as grinding speed increases (Notoya, et al. 1986).

Another grinding parameter that affects the resulting residual stress is depth of cut, which itself is dependent on the size of abrasive used in the grinding process. At low work speeds of 0.05 m/s, the depth of cut had little effect on the residual stresses generated during grinding of S45C carbon steel (Notoya, et al. 1986). However, at higher work speeds of 0.1, 0.15, and 0.2 m/s, the magnitude of the maximum tensile residual stress increased with increasing depth of cut (Notoya, et al. 1986). Increasing the depth of cut also increased the grinding force, and thus the increase in work piece temperature was larger (Notoya, et al. 1986). An increase in the depth of cut also resulted in the maximum residual stress location moving closer to the surface of the ground metal (Notoya, et al. 1986). Both the magnitude of the residual stresses and the location of the maximum residual stress were more strongly affected by depth of cut than by grinding speed (Notoya, et al. 1986).

The type of abrasive particles used in a grinding process also affects the resulting residual stress profile in the ground metal. In studies of grinding En31 bearing steel, alumina abrasive particles result in the generation of tensile residual stresses, whereas under the same grinding conditions, cubic boron nitride (CBN) abrasive particles generate compressive residual stresses in the ground metal (Brinksmeier. 1987, Rowe, et al. 2001). One explanation for the difference is that the hardness of CBN is approximately twice that of alumina (Brinksmeier. 1987). Because of this, the grinding forces in the case of CBN are lower and thus less heat is generated in the grinding process (Brinksmeier. 1987). The grinding forces for alumina abrasive particles are twice as large, resulting in 2 to 3 times more heat being generated at the surface of the work piece than for grinding with CBN (Brinksmeier. 1987). Also, the thermal conductivity of CBN is 40 times larger than that of alumina (Brinksmeier. 1987). This allows for more of the heat generated during grinding to be transferred away from the work piece surface, and thus a lower temperature rise occurs in the ground metal (Rowe, et al. 2001).

The surface roughness of a ground metal is also affected by several grinding parameters. In a study of stainless steels, increasing grinding speed resulted in greater surface roughness as the contact time between the workpiece and the grinding surface was reduced (Mũnoz-Escalona, et al. 2001). Increasing the depth of cut results in increased surface roughness since the contact area between the grinding surface and the work piece is increased and thus more material is removed (Mũnoz-Escalona, et al. 2001). Finally, as work piece hardness is increased, the resulting surface roughness initially increases but then decreases at high hardness values (Mũnoz-Escalona, et al. 2001).

## 2.7 Effect of Surface Roughness on Oxidation

Surface roughness has been found to have an effect on several different aspects of oxidation: oxidation rate and resulting scale thickness, scale composition, scale adhesion, and oxide grain size. A study of the oxidation of Fe-5Cr-16Al at 900°C for 2 h in air and an alloy of the same composition, also containing 0.2Zr-0.015B, at 1100°C for 30 min in air, examined the effect of surface roughness using polishing grits of 1, 3, 9, and 30μm (Uran, et al. 2000). The study found that the oxide layer on the smoothest specimens was almost twice as thick as that formed on the roughest specimens (Uran, et al. 2000). The thinnest scales were observed on samples with a 3μm finish (Uran, et al. 2000). It was also observed that the oxides formed on rough surfaces were Fe-rich and were found to contain $Fe_2O_3$, whereas the scales formed on smooth surfaces consisted mainly of alumina with almost no Fe (Uran, et al. 2000).

A study of the oxidation in air for up to 27 h of Ni at 700, 800, and 900°C and Ni-20Cr at 800, 900, and 1000°C examined the effect of erosion and the resulting surface finish on subsequent oxidation (Roy, et al. 1999). For Ni, increasing surface roughness resulted in a significant increase in weight gain during oxidation (Roy, et al. 1999). However, for Ni-20Cr, the oxidation rate decreased with increasing surface roughness (Roy, et al. 1999). The difference between the two metals was attributed to a difference in oxide grain size (Roy, et al. 1999). For Ni, which forms NiO, the oxide scales formed on rough surfaces had smaller grains than oxide scales formed on smooth surfaces (Roy, et al. 1999). Because of this, there was a higher concentration of grain boundaries in the oxide scale formed on the rough surface, providing more diffusion paths through the oxide layer and thus an increased oxidation rate (Roy, et al. 1999). For Ni-20Cr, larger $Cr_2O_3$

grains formed on rough surfaces, meaning that fewer diffusion paths existed through the oxide scale and thus the oxidation rate was reduced (Roy, et al. 1999).

A study of the two-step oxidation of $UO_2$ to $U_3O_8$ at 250°C in air for up to 200 h examined the effect of different polished surface finishes: 100, 45, 23, 17, 15, 7.5, 1.0, and 0.05μm (Taylor, et al. 1998). This study found that the oxidation rate increased as surface roughness increased; however, oxidation rate was independent of surface finish for extremely smooth (≤1μm) or extremely rough surfaces (18 to 100μm) (Taylor, et al. 1998). The increase in oxidation kinetics corresponding to an increase in surface roughness was attributed to an increase in nucleation rate on rough surfaces (Taylor, et al. 1998). Rougher surfaces have a larger surface area than smooth surfaces, thus providing an increased number of oxide nucleation sites (Roy, et al. 1999, Taylor, et al. 1998). In addition to this, rough surfaces have more sharp edges and points which are preferred sites for nuclei formation (Taylor, et al. 1998). For extremely rough surfaces, when the grinding media are larger than the $UO_2$ grain size, the surface state is essentially the same and roughness no longer affects oxidation rate (Taylor, et al. 1998). For extremely smooth surfaces, nucleation occurs predominately at surface irregularities and areas of locally high porosity, and thus the oxidation rate is dependent on the number of surface defects rather than the surface roughness (Taylor, et al. 1998). Another factor affecting oxide nucleation on smooth surfaces is preferred orientation. For rough surfaces, the surface facets are typically randomly oriented and it is unlikely that preferred orientation exists (Taylor, et al. 1998). However, for smooth surfaces, preferred orientation is possible (Taylor, et al. 1998). Preferred orientation can result in an increased oxidation rate if the preferred orientation corresponds to a favourable orientation for oxide nucleation (Taylor, et al. 1998).

The adhesion of an oxide scale to the underlying alloy is dependent on the initial surface roughness. In a study of the oxidation of 99.7% pure Cr containing Fe as the major impurity in dry oxygen at 900°C for 1 h, four different surface finishes ranging from 60μm to 1μm were examined (Mougin, et al. 2001). The average compressive residual stresses in the oxide scale formed on a rough surface were lower in magnitude than for a smooth surface; however, the residual stresses in the scale formed on the rough surface were less uniform across the scale (Mougin, et al. 2001). For an initially smooth surface, uniform compressive residual stresses exist in the oxide scale (Mougin, et al. 2001). For an initially rough surface, tensile stresses are present in the crests and compressive

stresses in the troughs (Mougin, et al. 2001). This difference in oxide residual stresses is shown in Figure 2-10 (Mougin, et al. 2001).

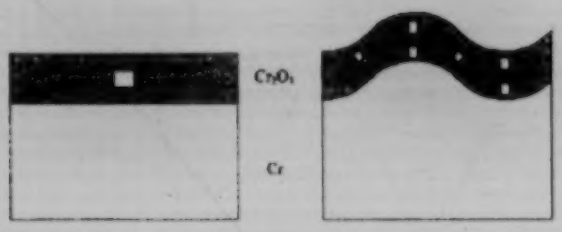


Figure 2-10. Residual Stress in an Oxide Scale Formed on a Smooth Surface (Left) and on a Rough Surface (Right) (Mougin, et al. 2001).

Oxide scales that form on rough Cr surfaces tend to spall, while oxides that form on smooth Cr surfaces do not (Mougin, et al. 2001). The reduced adhesion of the oxide scales formed on rough surfaces was attributed to the presence of tensile residual stresses in the oxide crests (Mougin, et al. 2001). When thermal stresses develop in the oxide scale, notably on cooling, the magnitude of the tensile stresses in the oxide crests will increase, resulting in cracking of the oxide at these locations and subsequent spalling extending from one or both sides of the crest (Mougin, et al. 2001). This process is illustrated in Figure 2-11 (Mougin, et al. 2001).

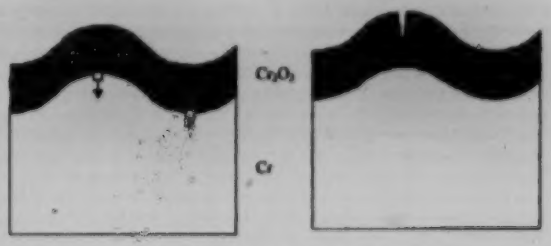


Figure 2-11. Spalling of the Oxide Scale Formed on a Rough Surface (Mougin, et al. 2001).

## 2.8 Effect of Surface Treatment on Oxidation

In the literature, the effect of surface treatments such as etching, electropolishing, polishing, grinding, shot peening, sandblasting, machining, and cold rolling on oxidation has been studied. Several studies have observed a difference in composition between the oxide scales formed on deformed metals and those on untreated metals. In particular, metals that have undergone surface treatment form oxides that are enriched in Cr and Mn and contain a reduced amount of Fe (Grabke, et al. 1997, Grabke, et al. 2004, Leistikow, et al. 1987, Rao, et al. 1986). One study looked at the effect of various surface treatments, including electropolishing, polishing, grinding, and sandblasting with coarse and fine grains, on the oxidation of 9 – 20% Cr steels for up to 100 h at 600°C. In reducing environments ($H_2$-2.5 vol% $H_2O$ and $N_2$-20 vol% $H_2$-0.49 vol% $H_2O$), the oxide layer formed on strongly deformed specimens (ground and sandblasted) was enriched in Cr relative to specimens that experienced weaker deformation (electropolished and polished) (Ostwald & Grabke. 2004). The same study found that in air, strong surface deformation again resulted in the formation of an oxide layer rich in Cr, while specimens that were weakly deformed formed an oxide scale rich in Fe (Ostwald & Grabke. 2004). Similar results were found in a study of ferritic and austenitic Cr-containing steels at 600°C for up to 100 h in $H_2$-2.5%$H_2O$, in which the oxide scales formed on sandblasted specimens were found to be enriched in Cr relative to the oxide scales formed on electropolished specimens (Piehl, et al. 2000). However, a study of 9%Cr-Mo and 12%Cr-Mo-V steels at 600°C in air and reducing environments ($H_2$-2.5%$H_2O$ and $N_2$-20%$H_2$-0.49%$H_2O$) found that although initially a Cr and Mn-rich scale formed on sandblasted specimens, after 100 h of oxidation in air, the sandblasted specimens had formed Fe-rich oxide scales containing $Fe_3O_4$, $(Fe,Cr)_3O_4$, and $(Fe,Cr)_2O_3$ (Grabke, et al. 2004). The Fe-enrichment of oxide scales on the sandblasted specimens was attributed to the increased surface roughness and surface activity resulting from the sandblasting treatment (Grabke, et al. 2004).

Another study examined the effect of surface treatment on the composition of the oxide scale formed during the early stages of oxidation using Auger electron spectroscopy (AES) (Grabke, et al. 1997). This study of 2.25-20% Cr ferritic and austenitic steels compared specimens ground with 600 grit SiC paper and specimens etched with a mixture of 64% $H_3PO_4$, 15% $H_2SO_4$, and 21% $H_2O$ by volume for 1 min during oxidation at various temperatures between 525 and 650°C in flowing 24.4% CO-$H_2$-2.4% $H_2O$

(Grabke, et al. 1997). For the ground ferritic steel P91, containing 9% Cr, Si and Mn peaks at short oxidation times indicated that Si and Mn-containing oxides formed initially, followed by the formation of $Cr_2O_3$ (Grabke, et al. 1997). The Fe peaks decreased in height as oxidation proceeded, indicating that Fe-containing oxides did not form (Grabke, et al. 1997). After 240 h of oxidation, the oxide scale on the ground specimen consisted of an inner $Cr_2O_3$ layer and an outer $MnCr_2O_4$ spinel layer (Grabke, et al. 1997). For the etched P91 specimen, Si and Mn peaks were not observed and the Fe peaks did not decrease in height as oxidation proceeded, indicating the formation of an Fe-rich oxide layer (Grabke, et al. 1997). After 240 h of oxidation, the etched specimen was found to have an oxide scale consisting of $FeCr_2O_4$ spinel (Grabke, et al. 1997). It has also been observed that an increase in the degree of surface deformation results in an increase in the amount of Cr and Mn enrichment of the oxide scale (Leistikow, et al. 1987). In a study of the oxidation of Incoloy 800 in superheated steam between 600 and 800°C, increasing the degree of cold work due to cold rolling between 10% and 90% resulted in an increase in the content of Cr, Mn, and Si in the oxide layer (Leistikow. 1981).

The effect of surface treatment on the rate of oxide formation has also been studied. Many studies have found that an increasing degree of surface deformation results in a larger weight gain during oxidation. In a study of 9 to 20% Cr steels at 600°C for 100 h, in both air and reducing environments, ($H_2$-2.5 vol% $H_2O$ and $N_2$-20 vol% $H_2$-0.49 vol% $H_2O$), the oxide thickness was found to increase with surface treatment as follows: electropolished ($H_3PO_4$-15% $H_2SO_4$ – 21% $H_2O$) < polished (1μm diamond) < ground (600 grit) < sandblasted with fine grains (25 μm diameter) < sandblasted with coarse grains (150 μm diameter) (Ostwald & Grabke. 2004). Similar results were found in a study of 9%CrMo and 12%CrMoV steels in air and reducing environments at 600°C for 100 h (Grabke, et al. 2004). A study of ferritic and austenitic stainless steels containing Cr (9 to 16% for the ferritic steels, 18 to 21% for the austenitic steels) at 600°C, for up to 100 h in $H_2$-2.5%$H_2O$, also found that the oxide thickness increased with the degree of surface deformation (Piehl, et al. 2000). However, a study of the oxidation of an Fe-based oxide dispersion strengthened (ODS) Fe-Cr-Al alloy at 1000°C, for up to 100 h, found that the thickness of the oxide scale formed on specimens sandblasted with alumina for 30 min was smaller than the oxide thickness of specimens that were polished with 1μm alumina paste (García-Alonso, et al. 2001). A study of the oxidation of ferritic and austenitic Cr-containing steels at 600°C in 24%CO-74%$H_2$-2% $H_2O$ for up to 250 h

found that specimens that were ground to a 600 grit finish experienced lower weight gains than etched specimens (Grabke, et al. 1998). This was because of reduced carbon uptake from the environment for the ground specimens (Grabke, et al. 1998). Two studies of the effect of the degree of cold rolling on oxidation found that the weight gain during oxidation decreased as the amount of rolling reduction increased. In a study of the oxidation of Alloy 800, a Ni-Cr-Fe alloy, in superheated steam at 600°C for 1000 h, it was found that as the amount of cold work increased from 10% to 90%, the weight gain decreased (Leistikow, et al. 1987). The kinetics of the oxidation process changed from parabolic to cubic to logarithmic as the reduction due to cold rolling was increased (Leistikow, et al. 1987). In a study of the oxidation of Inconel 625 in air at 1000°C for up to 36 h, the weight gain due to oxidation decreased as the cold rolling reduction was increased from 10% to 30% (Khalid & Benjamin. 2000).

The morphology of the oxide scales that form on metals that have experienced surface deformation is different from that of oxides that form on untreated metals. In a study of the cyclic oxidation of a (Ni,Pt)Al bond coated Ni-based superalloy at 1150°C in air, the oxide scale formed on the surface of a specimen that was sandblasted with <220 grit alumina had smaller oxide grains than the oxide scale formed on an untreated specimen (Tolpygo, et al. 2001). The smaller grains on the treated surface were attributed to increased nucleation at impurities and surface defects introduced by the sandblasting process (Tolpygo, et al. 2001). In a study of the effect of cold rolling on the oxidation behaviour of Alloy 800 at 600°C in a superheated steam environment, it was noted that the undeformed specimen formed a uniform oxide layer with relatively coarse grains (Leistikow, et al. 1987). Specimens that had between 10 and 50% reduction formed uneven scales with preferential oxidation at the grain boundaries (Leistikow, et al. 1987). Specimens that experienced 90% deformation formed a relatively uniform scale with fine oxide grains (Leistikow, et al. 1987). Similar results were found in a study of the oxidation behaviour of Inconel 625 at 1000°C for either 24 or 36 h, in which specimens were cold rolled to 10, 20, or 30% reduction (Khalid & Benjamin. 2000). In this case, the undeformed specimen again formed a relatively uniform oxide scale while the oxide scale formed on the rolled specimens nucleated preferentially at twin boundaries and grain boundaries (Khalid & Benjamin. 2000).

It has also been found that the oxide layers of specimens that have undergone surface treatment contain reduced amounts of porosity when compared to undeformed

specimens, making the oxide scales more protective. In a study of Alloy 800 at 1000°C in a carburizing environment containing $H_2$, $H_2O$, $CO_2$, and CO, the amount of carbon penetration through the oxide scale was reduced as the amount of cold work reduction due to cold rolling was increased from 30% to 65% (Leistikow, et al. 1987). Less carbon penetration occurred for deformed specimens because of the reduced porosity of the oxide layers formed on these specimens (Leistikow, et al. 1987). Similar results were found in a study of the oxidation of pure Fe in air at temperatures ranging from 400 to 650°C (Caplan & Cohen. 1966). In this study, specimens that were treated by polishing (8μm diamond), grinding (600 grit SiC) or cold rolling (5% reduction) formed oxide scales with reduced porosity compared to untreated specimens (Caplan & Cohen. 1966).

The effect of surface treatment on the adhesion of oxide scales is not fully understood. Some studies claim that specimens that have undergone surface deformation form oxide scales with improved adhesion to the underlying metal. In a study of the oxidation of pure iron in air at temperatures between 200 and 600°C, specimens that were treated with grinding (600 grit) or cold rolling (80% reduction) formed oxide scales that did not experience cracking or blistering at any oxidation temperature (Tomlinson & Blick. 1990). For specimens that were weakly deformed (electropolished or polished with 1μm diamond paste), the oxide scales showed signs of severe cracking and blistering at all temperatures (Tomlinson & Blick. 1990). Similar results were found in a study of the oxidation of Fe in air at temperatures between 400 and 650°C (Caplan & Cohen. 1966). However, other studies have found that the oxide scales formed on specimens that have experienced surface treatment are more susceptible to spalling than oxides formed on undeformed specimens. In a study of the cyclic oxidation of Fe-Cr-Ni alloys at 650, 700, and 750°C in $CO$-$CO_2$ gas mixtures, the weight gain due to oxidation was much larger for a chemically etched specimen than for a specimen ground with 800 grit SiC, due to spalling of the oxide scale on the ground specimen (Hänsel, et al. 2003). In a study of the oxidation of Inconel 625 in air at 1000°C for 24 or 36 h, the oxide scales formed on specimens that were cold rolled (10, 20, or 30% reduction) experienced cracking and spalling, which was not observed for undeformed specimens (Khalid & Benjamin. 2000). For cyclic oxidation of a (Ni,Pt)Al bond coated Ni-based superalloy at 1150°C in air, specimens that were sandblasted with <220 grit alumina formed oxide scales that spalled extensively. No spallation was observed for specimens that were not sandblasted (Tolpygo, et al. 2001). In a study of the oxidation of a FeCrAl oxide dispersion strengthened alloy at 1100°C in air for up to 100h, the oxide scales that formed on

samples sandblasted for 30 min with alumina spalled to a greater extent than oxide scales formed on specimens polished with 1μm alumina (García-Alonso, et al. 2001). The increased spallation of the oxide scales formed on the sandblasted specimens was attributed to increased residual stress in the oxide layer due to the rough, uneven surface produced by sandblasting (García-Alonso, et al. 2001).

The initial effect of surface deformation is to store deformation energy in the surface region of the metal in the form of dislocations (Ostwald & Grabke. 2004, Rakowski, et al. 1996). During the early stages of oxidation, these additional dislocations are able to act as "fast diffusion paths" for substitutional solute scale-forming atoms with a high affinity for oxygen, such as Cr, Mn, Si, and Al (Grabke, et al. 1998, Leistikow, et al. 1987). Recovery and recrystallization of the deformed surface material at the oxidation temperature subsequently occurs, resulting in the formation of a fine-grained surface microstructure (Ostwald & Grabke. 2004, Rakowski, et al. 1996, Stokes, et al. 1989). Grain boundaries and subgrain boundaries also act as short circuit diffusion paths, allowing for more rapid transport of scale forming elements to the metal/oxide interface (Rakowski, et al. 1996). The result is the preferential oxidation of these elements in regions adjacent to the grain boundaries and the rapid formation of an oxide scale that is more protective than that which forms over the surface of the grains (Leistikow, et al. 1987). Alloys with a small surface grain size are able to form Cr-rich, protective oxide scales over the entire metal surface because diffusion distances between grain boundaries are small (Grabke, et al. 1998). However, for alloys with a coarse grain structure at the surface, Cr-rich oxide scales are only able to form in regions adjacent to the grain boundaries while the grain surfaces are covered with a Fe-rich scale (Grabke, et al. 1998).

Surface deformation also affects the depletion of scale-forming elements in the alloy. For undeformed alloys, the ability to form a protective scale is limited by the depletion of scale-forming elements in the region directly below the metal/oxide interface (Grabke, et al. 2004, Ostwald & Grabke. 2004). However, if many fast diffusion paths exist, scale-forming elements are able to diffuse from regions deeper in the alloy (Ostwald & Grabke. 2004). The result is a reduced amount of depletion of scale-forming elements in a zone that extends deeper into the metal (Grabke, et al. 2004, Ostwald & Grabke. 2004). The advantage of the latter situation is that more scale-forming elements are present near the metal/oxide interface, allowing for repair of the protective oxide if cracking or spalling of the scale occurs, particularly under thermal cycling conditions (Grabke, et al. 2004).

As mentioned earlier, some studies have found that surface treatment can promote the formation of an oxide scale that has good adherence to the underlying alloy. For undeformed alloys, the incorporation of oxygen into the protective scale at the outer surface results in the formation of cation vacancies, which diffuse through the oxide scale and agglomerate to form pores and voids at the metal/oxide interface (Caplan & Cohen. 1966, Tomlinson & Blick. 1990). If the oxide layer is sufficiently plastic, deformation of the scale is able to collapse the pores; otherwise, separation of the oxide and the underlying alloy at the interface occurs (Caplan & Cohen. 1966). This separation between the metal and the oxide impedes the diffusion of scale-forming elements and thus reduces the scale growth rate (Tomlinson & Blick. 1990). For an alloy that has undergone surface treatment, vacancy sinks such as dislocations and lattice steps are present at the surface, thus preventing the formation of pores at the metal/oxide interface (Caplan & Cohen. 1966, Tomlinson & Blick. 1990).

It has been found that oxidation temperature has an influence on the effect of surface treatment on oxidation. In general, at lower oxidation temperatures, the effect of surface deformation on oxidation is fairly small as overall oxidation rates are low (Leistikow, et al. 1987). Also, diffusion rates are slow, and the formation of a protective oxide scale may not be possible (Leistikow, et al. 1987). At intermediate oxidation temperatures, surface treatment has a large effect on oxidation behaviour (Leistikow, et al. 1987). Because bulk diffusion rates are still relatively low, the contribution of fast diffusion paths arising from surface treatment is significant (Dudala, et al. 2005). At higher oxidation temperatures, the effect of surface treatment on oxidation is less significant as bulk diffusion rates are higher, meaning that the mobility of scale-forming elements such as Cr is relatively independent of grain boundary and dislocation density (Dudala, et al. 2005, Leistikow, et al. 1987). For the oxidation of Incolloy 800 in superheated steam, the beneficial effect of surface treatment on oxidation was present at temperatures between 600°C and 800°C (Leistikow. 1981). At oxidation temperatures as high as 900°C and above, severe surface deformation, between 70 and 90% cold work, had a detrimental effect on oxidation behaviour due to extensive grain growth (Leistikow. 1981). In addition to this, at oxidation temperatures between 900 and 1100°C, oxide scales rich in chromia are no longer protective due to the formation of volatile Cr-containing vapour species such as $CrO_3$ (g) and $CrO_2(OH)$ (g) (Leistikow. 1981). In a study of the oxidation of pure Fe in air, the difference in weight gain between specimens that had undergone surface treatment and those that had not was reduced as temperature was increased in the

range of 200 to 600°C (Tomlinson & Blick. 1990). At temperatures above 650°C, surface treatment no longer had an effect on the oxidation behaviour of pure Fe in air (Caplan & Cohen. 1966).

The effect of surface treatment on oxidation behaviour can also be influenced by the uniformity of the treatment as well as by the introduction of contaminants to the alloy surface. It is important that the surface treatment results in uniform deformation of the alloy surface in order that a oxide scale of uniform thickness and composition is formed (Van der Biest, O., et al. 1979). Depending on the particular surface treatment method used, this may or may not be easy to control. Also, the introduction of contaminant species through surface treatment can cause an unwanted increase in the oxidation rate of the alloy (Leistikow. 1981). This is particularly evident for sandblasting. In a study of the cyclic oxidation at 1150°C in air of a (Ni,Pt)Al bond coated Ni-based superalloy, sandblasting with <220 grit alumina particles for 30 minutes resulted in the introduction of impurities (alkali, alkaline-earth elements and titanium) into the alloy surface (Tolpygo, et al. 2001). Following oxidation, the impurity species were detected both in the surface and the subsurface regions of the oxide scale (Tolpygo, et al. 2001). The reason for the incorporation of these particular impurity species into the oxide scale was their high oxygen affinity (Tolpygo, et al. 2001). The authors of the study concluded that the presence of impurities in the protective scale caused an increase in the oxidation rate of the alloy (Tolpygo, et al. 2001).

# 3 Experimental Methods

## 3.1 Steels

Three different ferritic stainless steels were used in this study: AISI430 (or 430), AISI434 (or 434), and ZMG 232. The compositions of the three steels are listed in Table 3-1.

Table 3-1. Composition of Ferritic Stainless Steels (Garcia Vargas, et al. 2005b, Metal Suppliers Online. 2006).

| Composition (wt%) | Steel | | |
|---|---|---|---|
| | 430 | 434 | ZMG 232 |
| C | 0.12 max | 0.12 max | 0.02 |
| Cr | 16 - 18 | 19 | 22.0 |
| Fe | balance | balance | balance |
| Mn | 1 max | 1 max | 0.5 |
| P | 0.04 max | 0.04 max | - |
| Si | 1 max | 1 max | 0.4 |
| S | 0.03 max | 0.03 max | - |
| Mo | - | 2 | - |
| Nb | - | 0.35 | - |
| Ni | - | - | 0.26 |
| Al | - | - | 0.22 |
| La | - | - | 0.04 |
| Zr | - | - | 0.22 |

For each steel, specimens approximately 2.5 cm x 2.0 cm in size were cut from sheets that had been cold rolled and bright annealed. The thickness of the 430 and the 434 specimens was approximately 1 mm, while the thickness of the ZMG 232 specimens was approximately 0.25 mm. Additional 430 and 434 specimens, denoted as "thin" specimens, with a thickness of approximately 0.25 mm, were also prepared. In total, there were 5 different treatment conditions: as-is, 6% rolled (8% for ZMG 232), 15% rolled (21% for ZMG 232), 1 pass sandblasted, and 10 pass sandblasted.

## 3.2 Surface Treatments

Two different surface treatment methods were used in this study: sandblasting and cold rolling. Sandblasting was done on only one side of the steel and was performed on the sheet metal before it was cut into specimens. Alumina particles (100 grit) were used in the sandblasting process. The particles were projected towards the steel surface under 0.7 MPa pressure using a nozzle with an inside diameter of 2.3 cm that was held 8 to 10 cm above the steel sheet. Samples were subjected to either 1 pass or 10 passes, with each pass taking 3 seconds to cover a steel strip that was 13 cm in length and 2.5 cm in width. Cold rolling was carried out using a rolling mill and was performed on the individual specimens after cutting. The rolling direction was parallel to the length of the specimens. Two different thickness reductions were studied: 6% and 15% for the 430 and 434 specimens, and 8% and 21% for the ZMG 232 specimens.

## 3.3 Surface Area Measurement

In order to correct for the effect of the surface roughness, produced by the different treatment conditions, on the actual surface area of the specimens, an Alpha-Step 200 profilometer was used. A trace of 2 mm was performed on samples of each steel and treatment condition. The trace was oriented across the diagonal of the specimen in order to account for any anisotropic effects of the surface treatments, particularly cold rolling, producing an average surface roughness. The resulting profile had a depth resolution of approximately ±100 nm. For some specimens, it was difficult to obtain an accurate trace. The rolling and sandblasting treatments caused the samples to bend or twist slightly. As the stylus tip traced the surface, even slight bends or twists of the sample caused the sample to move slightly, and this movement was reflected in the resulting profile. In some cases, the trace had to be repeated several times before an accurate profile was obtained.

## 3.4 Long Term Oxidation Experiments

One option for measuring mass gain was to prepare a single specimen for each steel and treatment condition, remove it from the furnace at a selected time interval, cool it, weigh

it, return it to the furnace, and repeat the entire process at other time intervals. The above method was not used in this study because it incorporates the effects of thermal cycling at each measurement interval and makes the situation more complicated than oxidation under isothermal conditions. Instead, five identical specimens were prepared for each steel and treatment condition to be removed from the furnace at different time intervals.

Prior to oxidation, a Mitutiyo digital calliper was used to measure the length, width, and thickness of each steel specimen to the nearest 0.01 mm. Then, the treated specimens were cleaned with soap, rinsed with deionized water, rinsed with ethanol, and finally dried with a hand dryer. This cleaning process was designed to remove contaminants such as dust, oil, and fingerprints from the specimens. A more intensive cleaning process was not used in order to more closely replicate the conditions in industry, where no special cleaning of the steel interconnects is done before they are inserted into the fuel cell stack.

Alumina combustion boats (99.8%) were used to hold the specimens. Prior to oxidation, the alumina boats were cleaned with a blast of pressurized air to remove any contaminants from the inside surfaces that would be in contact with the steel specimens.

The initial mass of the steel specimens to the nearest 0.01 mg was determined using a Sartorius CP225D high precision balance. Then, specimens were placed in the alumina crucibles. Each crucible held the five identical specimens for each steel and treatment condition. The alumina crucibles were then placed inside Lindberg/Blue laboratory box furnaces. Oxidation was carried out at 800°C in air. Once the crucibles were inside the furnaces, the furnaces were switched on and heated to the setpoint of 800°C. Timing of the experiment began once the furnaces were switched on. This was done to simulate the conditions in industry where the fuel cell stack starts at room temperature and is heated to the operating temperature. The actual temperature of the furnace was determined using a thermocouple inserted at the top of the furnace.

At each of the specimen removal times (50 h, 98 h, 148 h, 244 h, and 502 h), one specimen for each steel and treatment condition was removed from the hot furnace using tongs and was placed on a piece of stainless steel sheet on a refractory brick to cool to room temperature. Once the specimens were completely cooled, the final mass of the steel specimens was determined to the nearest 0.01 mg using the high precision balance.

Long term oxidation experiments were also performed for 430 and 434 as-is thin specimens. These specimens had a thickness of approximately 0.25 mm, which was the same as the ZMG 232 specimens. The long term oxidation of the thin specimens followed the same procedure as for the other specimens, except that only two identical specimens were prepared for each steel, and the specimen removal times were 255 h and 502 h.

## 3.5 X-Ray Diffraction (XRD) Analysis

X-ray diffraction (XRD) analysis of the specimens, that were oxidized for 50 h and 502 h, was performed using a Rigaku Geigerflex 2173 system with a vertical goniometer. The X-ray source was Co, with an average wavelength of 0.179021 nm for K alpha 1 and K alpha 2 combined. Analysis of the data was carried out using Jade software. The purpose of this analysis was to identify the phases present in the oxide layer of each of the specimens.

## 3.6 Oxidized Cross Section Preparation

In order to examine the oxide layer formed on each of the specimens and to obtain an estimate of the thickness of the oxide scale, cross sections of the 502 h specimens for each steel and treatment condition were prepared, including the 430 and 434 thin specimens. The method used for cross section preparation differed from standard metallographic techniques because the brittle oxide tends to crack and pull away from the steel substrate if extreme care is not taken. In order to protect the oxide layer during grinding and polishing, a layer of Ni was plated on top of the scale prior to cold mounting. However, plating directly on the oxide scale resulted in the deposition of a layer of nickel that was discontinuous and poorly adherent to the steel, due to the reduced electrical conductivity of the oxide scale. In order to increase the conductivity of the oxide enough for successful deposition of Ni, a thin layer of gold (approximately 12 nm thick) was sputter coated on both sides of the oxidized steel specimens.

Following Au coating, a layer of Ni was deposited on the oxidized specimens using electroplating. A Watts nickel solution, containing 270 g/L $NiSO_4$, 45 g/L $NiCl_2$, 40 g/L

boric acid, 150 mg/L coumarin (levelling agent), and 100 mg/L SDS (surfactant), was used. Prior to deposition, the solution was heated to the temperature range of 40 to 60°C. The temperature of the solution was maintained within this range throughout the plating process by placing the plating cell containing the solution in a beaker containing water, and then placing the beaker on a hot plate. A Ni anode was used, and the cathode was the oxidized steel specimen upon which Ni was to be deposited. Plating was carried out at a current density of 60 $mA/cm^2$ for a total of 30 minutes. After plating, the Ni anode was cleaned for 2 minutes in deionized water to remove any small Ni particles from the surface. In addition, a magnetic stirring rod was dragged through the plating solution in order to remove any small Ni particles. It was found that if any small Ni particles remained either on the surface of the anode or in the plating solution, a rougher Ni deposit was produced.

After Ni plating, the oxidized specimens were cold mounted in epoxy using steel clips to hold the specimens in a vertical position. Grinding of the cross section specimens was carried out manually on a Buehler Handimet 2 roll grinder using a sequence of strips of 240 grit, 320 grit, 400 grit, and 600 grit SiC papers. Care was taken to ensure that grinding only occurred parallel to the oxide layer to prevent a gap developing between the oxide scale and the protective Ni layer. Following grinding, polishing was done on polishing wheels at a low speed using 6μm diamond paste followed by 0.05μm $Al_2O_3$ slurry. Again, the sample was positioned so that polishing only occurred parallel to the oxide layer. After polishing was completed, the cold mounted specimens were cleaned for 5 minutes in ethanol in an ultrasonic bath in order to remove any $Al_2O_3$ particles from the specimen surface. A thin layer of carbon (approximately 10 nm) was then evaporated on the surface of the cold mounted specimens in order to prevent charging of the epoxy during scanning electon microscope (SEM) analysis.

## 3.7 Etched Cross Section Preparation

In order to examine the microstructure of the different specimens and different treatments prior to oxidation, a series of etched specimens was prepared, one for each steel and treatment condition. The treated specimens were first cold mounted in epoxy using steel clips. Grinding and polishing were carried out in the same manner as for the oxidized

specimens. Following polishing, the cold mounted specimens were cleaned for 5 minutes in ethanol in an ultrasonic bath.

An etchant consisting of 1 part $HNO_3$, 1 part HCl, and 1 part $H_2O$ was prepared. This particular etchant was selected because it is able to reveal both the ferrite grain boundaries as well as the carbides, and it can be stored. Throughout the etching process, the etchant was stirred with a magnetic stirring rod to help produce uniform etching of the surface and to prevent staining. The etching was carried out at room temperature.

The etchant was applied to the cold mounted cross sections using a swab for 20 s intervals, after which the specimen was rinsed with deionized water followed by ethanol rinsing, drying, and examination in a light microscope. A total etching time of approximately 1.5 minutes was required. The samples were slightly overetched to ensure that there was adequate contrast in the SEM. Finally, a thin layer of carbon (approximately 10 nm) was evaporated onto the surface of the cold mounted samples to prevent the epoxy from charging during SEM analysis.

## 3.8 Scanning Electron Microscopy (SEM)

The SEM was used to examine three different types of specimens: plan view specimens of each steel and treatment condition oxidized for 50 h and 502 h, epoxy mounted cross sections of each steel and treatment condition oxidized for 502 h, and etched epoxy mounted cross sections of each steel and treatment condition prior to oxidation. SEM analysis of these specimens was carried out using a Hitachi S-2700 SEM with a Princeton Gamma Tech (PGT) PRISM IG (intrinsic germanium) detector for energy dispersive X-ray (EDX) analysis. The imaging and EDX collection were performed using PGT IMIX software.

## 3.9 Short Term Oxidation Experiments

Short term oxidation experiments for selected treatment conditions (as-is, 15% or 21% cold rolled, and 10 passes sandblasted) were performed in order to study the oxidation behaviour at short times using surface science analysis techniques. In this case, the

procedure was slightly different from that used in the long term oxidation experiments. First, the treated specimens were cleaned with soap, rinsed with deionized water followed by ethanol, and finally dried with a hand dryer. The alumina boats were then cleaned with a blast of pressurized air and the specimens were placed in the boats.

Short term oxidation experiments were carried out at 800°C in air in the Lindberg/Blue laboratory box furnaces. The furnace was switched on and heated to the setpoint of 800°C. Then, using tongs, the alumina boats containing the specimens were inserted into the hot furnace; timing of the experiment began at this point. The actual temperature of the furnace was determined using a thermocouple inserted through a hole in the top of the furnace.

Oxidation was carried out for a total of 15 minutes. After this time, each specimen was removed from the hot furnace using tongs and was placed on a piece of stainless steel sheet on a refractory brick to cool to room temperature.

## 3.10 Secondary Ion Mass Spectrometry (SIMS) Analysis

Secondary ion mass spectrometry (SIMS) depth profiling was used to determine the distribution of various elements in the oxide layers formed on the steel specimens oxidized for 15 minutes, as well as in the native oxide. SIMS analysis was carried out using an Ion-ToF SIMS IV. For sputtering, $Cs^+$ ions at 1 keV and 250 nA were used over an area 200 x 200μm. For analysis, $Ga^+$ ions at 15 keV and an area of 34 x 34μm were used, corresponding to 128 x 128 pixels.

## 3.11 X-Ray Photoelectron Spectroscopy (XPS) Analysis

X-ray photoelectron spectroscopy (XPS) depth profiling was used to determine the chemical state of various elements in the oxide layers formed on as-is and cold rolled steel specimens oxidized for 15 minutes, as well as in the native oxide. A Kratos Axis 165 XPS system was utilized, with a monochromatic Al X-ray beam with a $K_\alpha$ energy of 1486.6 eV. Sputtering was carried out with $Ar^+$ ions with an accelerating voltage of 4 kV. Analysis of the XPS results was carried out using Casa software.

## 3.12 Thin Foil Specimen Preparation

In order to determine the composition and structure of the precipitates formed in 434 steel, a thin foil specimen was prepared for examination in the transmission electron microscope (TEM). First, a 434 specimen approximately 2.5 cm x 2.0 cm in size and approximately 1 mm thick was glued to a stainless steel support. The specimen and disk were clamped together overnight to ensure that the superglue was dry. The starting thickness of the disk and sample was measured to the nearest 0.01 mm using a Mitutiyo digital calliper. Then, a 120 grit belt grinder was used to reduce the thickness of the 434 specimen to approximately 0.1 mm. Following this, grinding of the specimen was continued manually with a Buehler Handimet 2 Roll Grinder using a sequence of strips of 240 grit, 320 grit, 400 grit, and 600 grit SiC papers. Polishing was carried out on polishing wheels at a low speed using 6μm diamond paste followed by 0.05μm $Al_2O_3$ slurry. After polishing was completed, the disk and specimen were placed in a beaker of acetone overnight to dissolve the glue and remove the specimen from the disk. Once the specimen was separated from the disk, it was turned over and the freshly polished side was superglued to the stainless steel disk as before. The second side of the specimen was then ground manually and polished to a 0.05μm finish. The disk and specimen were again placed in a beaker of acetone overnight to separate the specimen and the disk. Several circular disks 3 mm in diameter were punched out of the thin sheet 434 specimen. Jet polishing with a solution containing 5% perchloric acid and 95% glacial acetic acid by volume was used to perforate three of the circular specimens. The jet polishing was done at room temperature with a voltage of 80 V and a current of 75 mA. The polishing time was approximately 2 minutes for each specimen.

## 3.13 Carbon Extraction Replica Preparation

Carbon extraction replicas were also prepared for studying the structure and composition of the carbides in the 434 steel in the transmission electron microscope (TEM). First, a 434 specimen was cold mounted in cross section in epoxy as described previously. Grinding and polishing were carried out in the same manner as for the other mounted specimens. Following polishing, the cold mounted specimens were cleaned for 5 minutes in ethanol in an ultrasonic bath. The specimens were then etched in Vilella's reagent (1 g picric acid, 5 mL HCl, and 100 mL ethanol) at room temperature.

The etchant was applied to the cold mounted cross section using a swab for 20 s intervals, after which the specimen was rinsed with deionized water followed by ethanol rinsing, drying, and examination in a light microscope. A total time of approximately 1.5 minutes of etching was required. The sample was slightly overetched in order to ensure that at least some of the carbides would be sitting on top of the steel matrix. The entire surface of the cold mount, except for the steel, was covered with transparent tape and then a thin layer of carbon (approximately 10 nm) was evaporated onto the surface of the cold mounted specimen. Following carbon deposition, the transparent tape was removed. Lines were scribed on the carbon coating in order to section it into small pieces. A circular enclosure to hold the etching solution on top of the cold mount was created by wrapping transparent tape around the surface of the mount in such a way that only the nonadhesive side of the tape would be in contact with the etchant. Vilella's reagent was poured into the enclosure on top of the cold mount. The cold mount was tapped against the lab bench to help the etchant lift the carbon replica from the 434 steel. Once a small piece of carbon was lifted from the steel, a coarse mesh Cu grid held with tweezers was used to catch the piece of carbon. The small piece of carbon was rinsed in a beaker, containing a mixture of equal parts by volume of ethanol and deionized water, to remove any traces of the etchant. Using the Cu grid, the small piece of carbon was recaptured and placed in deionized water to allow it to completely spread out. The carbon was again recaptured with the Cu grid, and the water was removed by touching the grid to a piece of filter paper.

## 3.14 Transmission Electron Microscopy (TEM)

A JEOL 2010 transmission electron microscope (TEM) was used to obtain both images and selected area diffraction (SAD) patterns from the carbides present in the 434 steel. The TEM was operated at 200 kV and was equipped with a Noran Instruments Explorer ultra thin window (UTW) X-ray detector (Si). Diffract software was used to index the diffraction patterns.

# 4 Results

## 4.1 Unoxidized Specimens

### 4.1.1 Plan View SEM Images

Prior to oxidation, SEM secondary electron (SE) images of specimens for each steel and treatment condition were taken. These images are displayed in Figure 4-1.

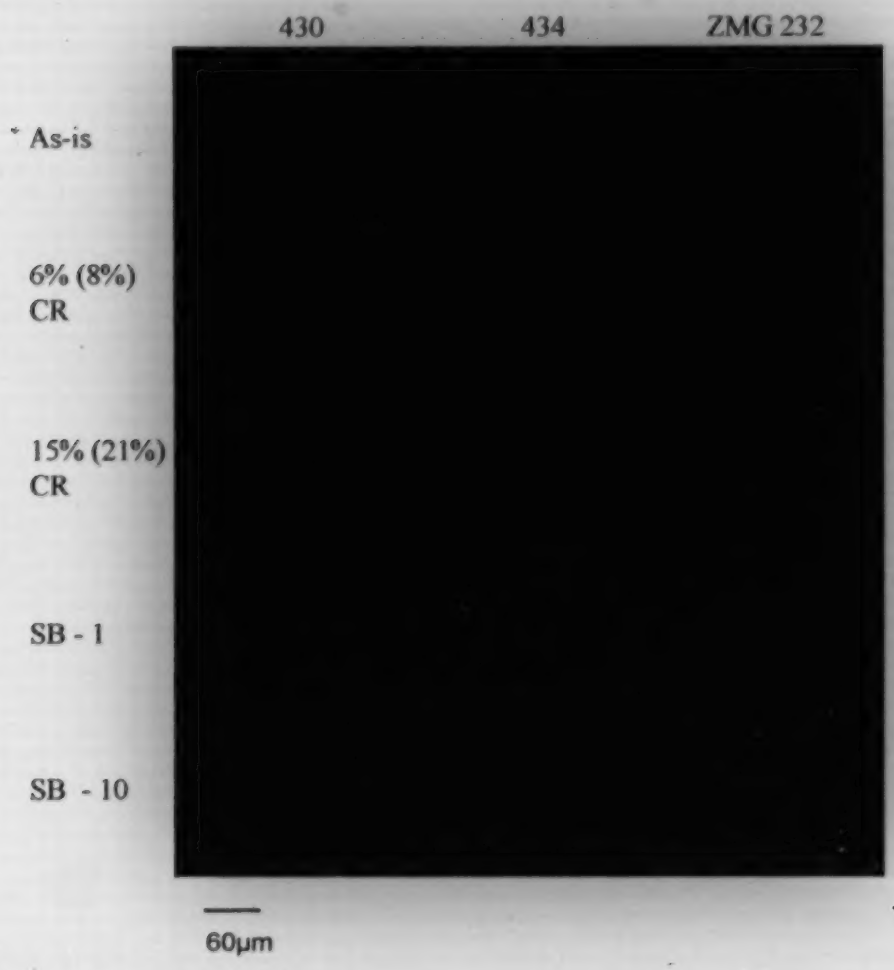


Figure 4-1. SEM SE Images of Unoxidized Steel Specimens.

From the images, it is clear that the roughness for the sandblasted specimens is much greater than that for the as-is or rolled specimens. The general appearance of the as-is and rolled specimens is similar, except that the number of surface flaws increases as the amount of rolling reduction increases.

For the sandblasted specimens, at higher magnifications, alumina particles embedded in the surface of the specimens were observed. Figure 4-2 is an image of one such particle in the 434 steel which had undergone 10 sandblasting passes.

a)

b)

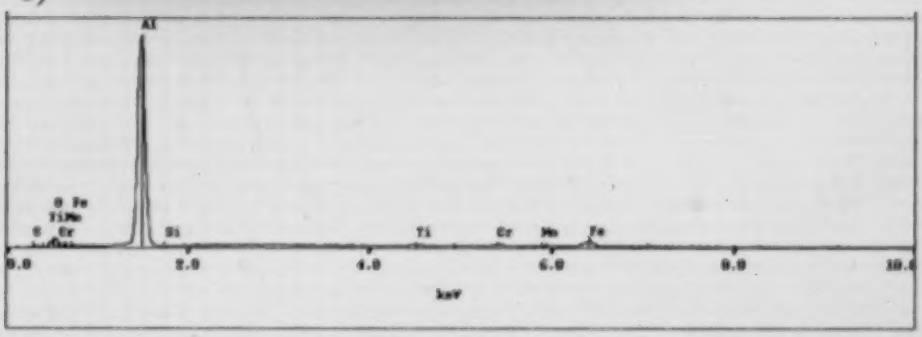


Figure 4-2. SEM SE Image and EDX Spectrum of 434 steel subjected to 10 Sandblasting Passes. a) Image of Specimen with Alumina Particle Circled; b) EDX Spectrum of Alumina Particle.

The EDX spectrum indicates that the particle is mainly composed of Al. The oxygen peak confirms that the particle is alumina. There is also a small Ti peak, indicating that the particles used in the sandblasting process are not pure alumina. The small Cr and Fe peaks are most likely from the surrounding steel.

### 4.1.2 Etched Cross Section SEM Images

Etched cross sections of each steel and treatment condition were prepared in order to examine the grain structure of the specimens prior to oxidation. SEM images of the as-is specimens for each steel are shown in Figure 4-3.

From Figure 4-3, some differences between the microstructures for the three steels are evident. The grain size of the 430 and ZMG 232 specimens is similar, in the range of 10 to 20μm. The grain size for the 434 steel is approximately twice as large, in the range of 25 to 35μm. EDX analysis of the small bright particles in Figure 4-3a indicated that they were Cr carbides. The small dark holes are places where Cr carbides have been pulled out of the steel during the grinding and polishing process. The Fe-Cr phase diagram for a C content of 0.1 wt% is shown in Figure 4-4 (Smith. 1993).

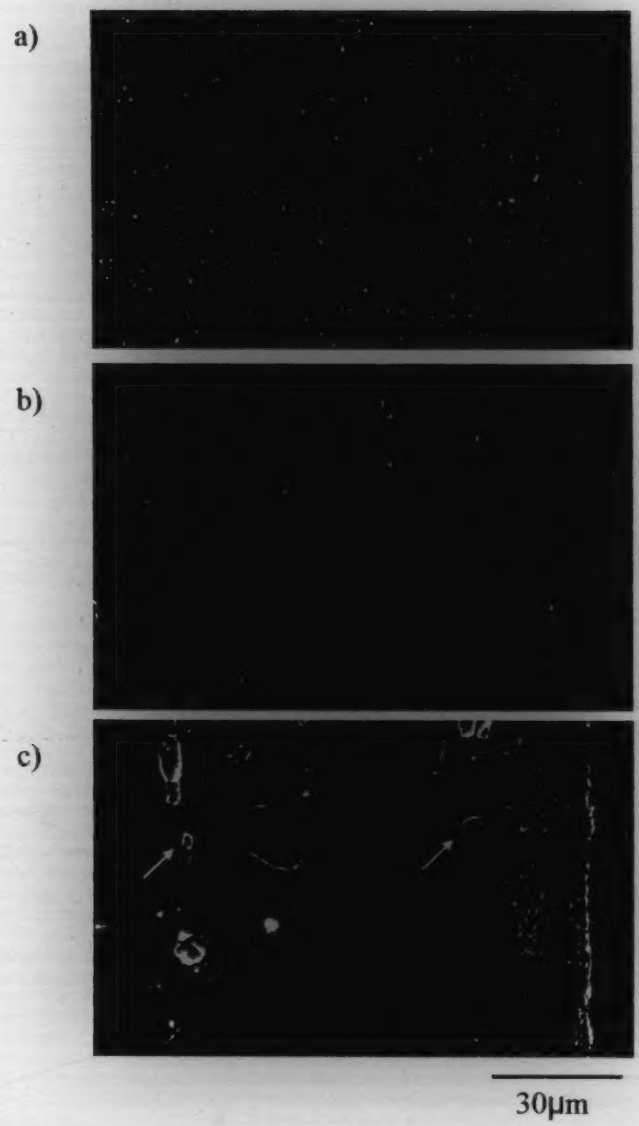


Figure 4-3. SEM SE Images of Etched Cross Sections of Unoxidized Specimens. a) 430 As-is; b) 434 As-is, c) ZMG 232 As-is.

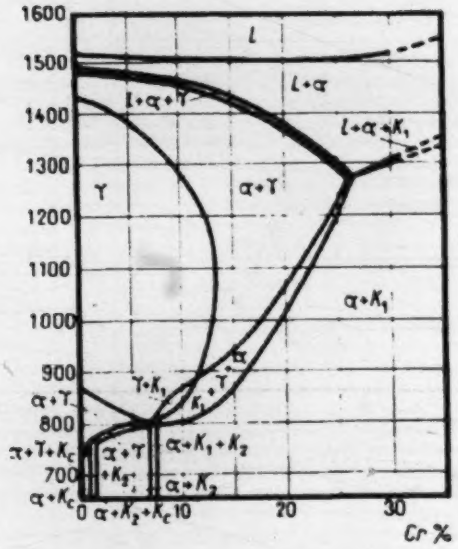


Figure 4-4. Fe-Cr Phase Diagram for a C Content of 0.1 wt% (Smith. 1993).

In Figure 4-4, $K_C$ is the cementite-type carbide $(Cr,Fe)_3C$, $K_1$ is $(Cr,Fe)_{23}C_6$, and $K_2$ is $(Cr,Fe)_7C_3$. Figure 4-4 indicates that for a Cr content of 16-18 wt%, the equilibrium carbide composition is $(Cr,Fe)_{23}C_6$. The presence of $(Cr,Fe)_{23}C_6$ carbides in ferritic stainless steels containing 16-18 wt% Cr has been previously confirmed by TEM analysis (Jian, et al. 2003).

In Figure 4-3b, the small bright particles are also carbides. Molybdenum and Nb have been added to the 434 steel; both are carbide formers. Of the three carbide forming elements present in 434 steel, Nb is the strongest carbide former, followed by Mo, and then Cr (Smith. 1993). Typically, Nb carbides are NbC and Mo carbides are $Mo_2C$ (Smith. 1993). If enough carbide-forming elements were added to form precipitates with all the carbon, more Cr would be available in the bulk of the steel for protective oxide formation. EDX analysis in the SEM of the carbides showed both Nb and Mo peaks, but there were also Cr and Fe peaks present, which could have come from either the particles or the surrounding steel matrix. Further analysis to determine the exact composition and structure of the carbides present in the 434 steel was carried out using TEM and is presented in section 4.1.3.

Larger carbides are present in the ZMG 232 steel (Figure 4-3c). These carbides, two of which are indicated by arrows, are not as round as those in the other two steels but are cuboidal in shape. EDX analysis in the SEM revealed that they are rich in Zr, but also contain Si and Fe. Zr is also a strong carbide former added to ZMG 232 to prevent the formation of Cr carbides. The Zr rich carbides in ZMG 232 steel have previously been identified as ZrC by TEM analysis (Ivey. 2003). Fewer carbides are present in ZMG 232 compared to the 430 and 434 steels due to both the larger size of the carbides and the lower carbon content of the ZMG 232 (Table 3-1).

SEM images of etched cross sections for the rolled and sandblasted specimens of each steel were also taken. These images are not shown as they were similar to those displayed in Figure 4-3. A slight elongation of the grains in the rolling direction was observed for the rolled specimens, and increased roughness of the surface was seen for the sandblasted specimens.

### 4.1.3 434 Carbides

#### *4.1.3.1 Thin Foil Results*

In order to study the composition and structure of the carbides in the 434 steel, a thin foil specimen was prepared for TEM analysis. Figure 4-5 shows a bright field (BF) image representative of the carbides, dispersed in the ferrite matrix, found in this specimen.

From the EDX spectra in Figure 4-5, it appears that the carbides are Fe-rich, with significant amounts of Cr and Nb as well as some Mo. It is difficult to tell whether the Cr and Fe peaks are coming from the precipitates themselves or from the surrounding steel. EDX analysis of a number of carbides was carried out and they all appeared to have a similar composition.

a)

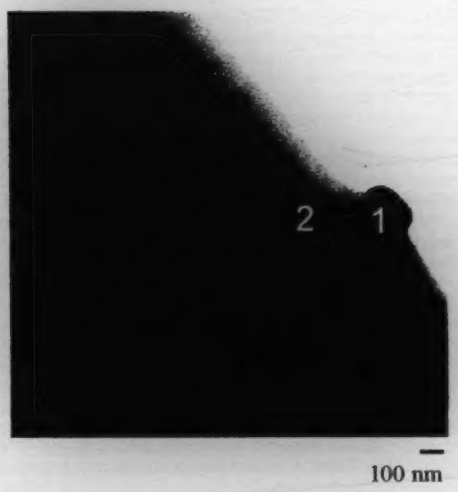


b)

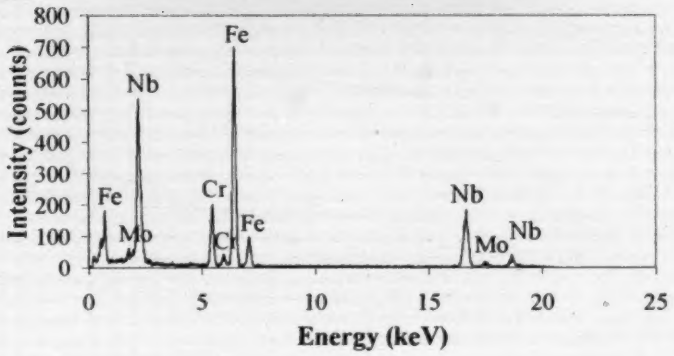


c)

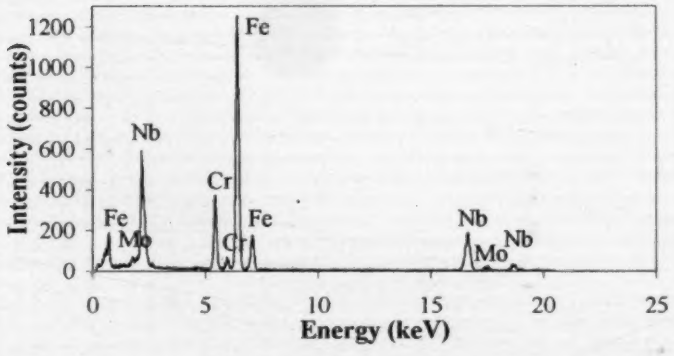


Figure 4-5. Carbides in 434 Steel. a) TEM BF Image; b) EDX Spectrum from Precipitate 1; c) EDX Spectrum from Precipitate 2.

In order to interpret selected area diffraction (SAD) patterns from the carbides, several patterns were taken from the steel substrate (ferrite) as a reference. One such pattern is displayed in Figure 4-6.

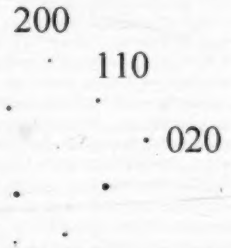


Figure 4-6. Reference Diffraction Pattern From Steel Substrate.

By comparing this pattern with reference patterns, it was determined that the zone axis was [001] (Beeston, et al. 1972). Three diffraction spots are indexed as indicated in the figure. The distances from the center spot to each of the diffraction spots, R, were then measured to be $R_{110}$ = 0.951 cm and $R_{200} = R_{020}$ = 1.34 cm. From the JCPDS diffraction card for bcc Fe, the d spacings corresponding to the 110 and 200 spots were $d_{110}$ = 0.20268 nm and $d_{200} = d_{020}$ = 0.14332 nm (International Center for Diffraction Data. 1996). Then, Equation 4-1 was used to determine the camera constant that was then used to solve the diffraction patterns from the carbides (Beeston, et al. 1972).

$$Rd = \lambda L \qquad (4\text{-}1)$$

In Equation 4-1, R is the distance from the center spot to a diffraction spot, d is the d-spacing of the set of lattice planes that give rise to the diffraction spot, λ is the wavelength of the incident electron beam, and L is the camera length, the distance between the specimen and the display screen (Beeston, et al. 1972). If the camera length L is kept constant for all diffraction patterns, the value of λL is a constant and is known as the camera constant. Using the known d spacings and the measured R values from Figure 4-6, an average value of the camera constant was calculated to be 0.193 nm·cm.

In order to solve a diffraction pattern from one of the Nb-rich carbides, Equation 4-1 can be rearranged as follows:

$$d = \frac{\lambda L}{R} \qquad (4\text{-}2)$$

The camera constant λL has been determined above and the R values for each diffraction spot on a carbide pattern can be measured.

Figure 4-7a shows an image of a carbide from the 434 thin foil specimen. A diffraction pattern from the particle indicated with a circle is shown in Figure 4-7b. From Figure 4-7b, R values were measured as shown on the figure. The R values and their corresponding d spacings, calculated using Equation 4-2 with a camera constant of 0.193 nm·cm, are listed in Table 4-1.

Table 4-1. R and d Values from Carbide Diffraction Pattern.

| n | $R_n$ Value (cm) | d Spacing (nm) |
|---|---|---|
| 1 | 0.96 | 0.402 |
| 2 | 1.11 | 0.348 |
| 3 | 1.48 | 0.261 |

In addition, the angles between $R_1$ and $R_3$ and $R_1$ and $R_2$ were measured from Figure 4-7b and were found to be $\theta_{13} \sim 48°$ and $\theta_{12} \sim 90°$.

As was mentioned in Section 4.1, Nb typically forms carbides of the form NbC and, therefore, it would be expected that the carbides would be of this type, with some Mo substituting for Nb. However, the d spacings in Table 4-1 do not match those of NbC, for which the largest d spacing, the (111) plane, is 0.25809 nm (International Center for Diffraction Data. 1996). Following this, the lattice parameters and d spacings for a number of carbide precipitates containing Fe, Cr, Mo, Nb, or a combination of these elements were obtained, and Diffract software was used to determine whether the diffraction pattern in Figure 4-7b would match any of these carbides. The following procedure was used for each potential carbide. First, the lattice parameters were entered into the software. Then, starting with $d_1$ and $d_2$, the software determined whether the potential carbide had d spacings with similar values that corresponded to planes separated by $\theta_{12}$. For each possible combination of planes, the zone axis was calculated by the software and the theoretical diffraction pattern corresponding to the calculated zone axis

was plotted. The d spacings for each spot and the angles between spots were calculated by the software and the values were compared with the measured values in Table 4-1. Two carbides were found that matched the diffraction pattern in Figure 4-7b: orthorhombic $Cr_7C_3$ (PDF # 00-036-1482) and cubic $Fe_3Nb_3C$ (PDF # 00-017-0128) (International Center for Diffraction Data. 1996). Figure 4-7c and 4-7d show the simulated patterns for the two possible carbides.

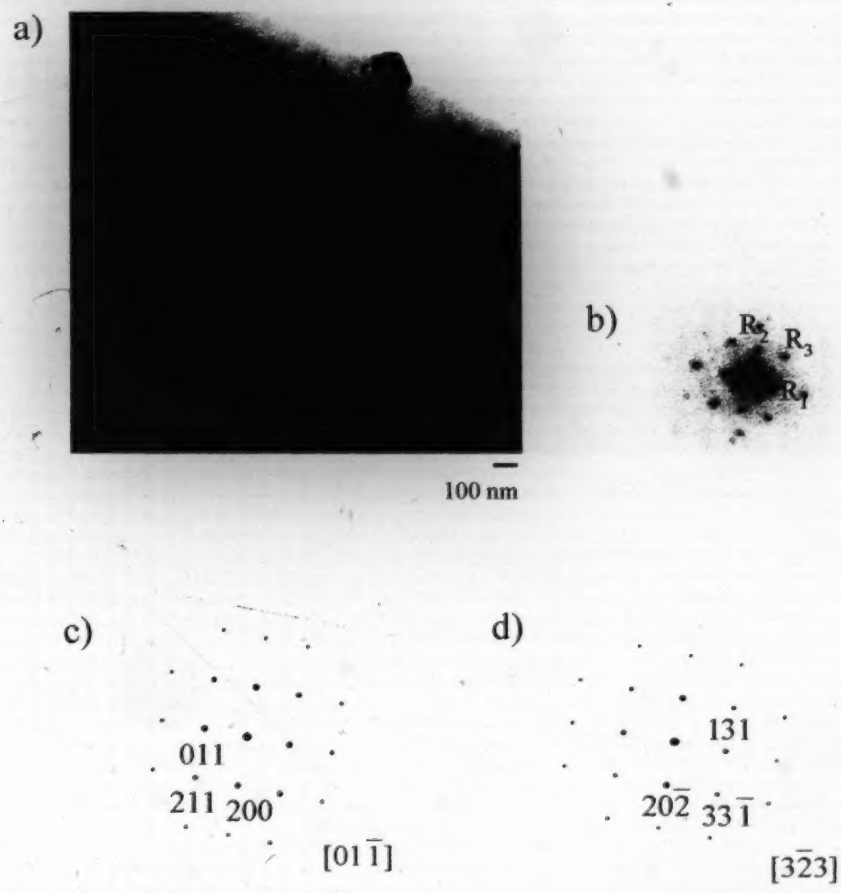


Figure 4-7. Fe-Cr-Nb-Mo Carbide Diffraction Pattern. a) TEM BF Image; b) SAD Pattern; c) Simulated Pattern for $Cr_7C_3$ (orthorhombic); d) Simulated Pattern for $Fe_3Nb_3C$ (cubic).

In order to positively identify the unknown carbides, other diffraction patterns were obtained. One such pattern is displayed in Figure 4-8.

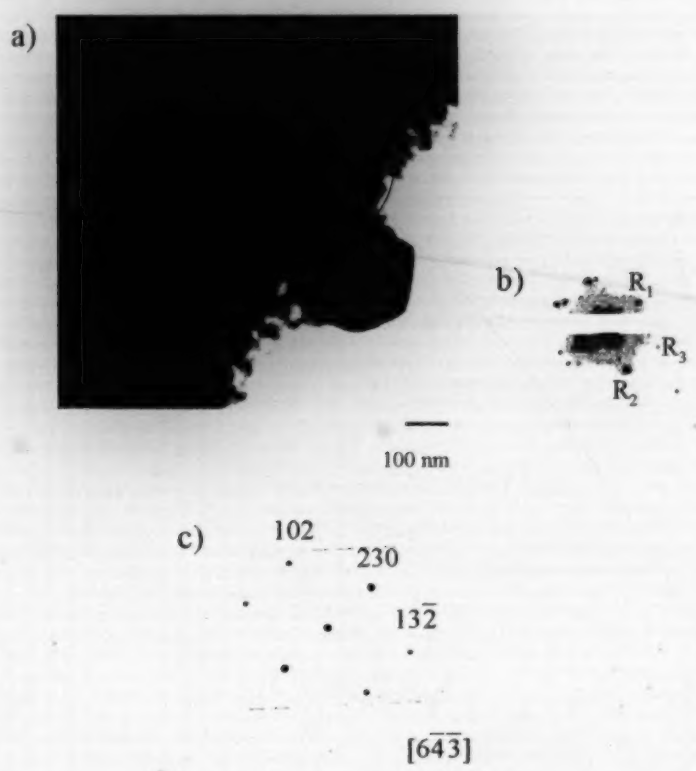


Figure 4-8. Fe-Cr-Nb-Mo carbide. a) TEM BF Image; b) SAD Pattern; c) Simulated Pattern for $Cr_7C_3$ (orthorhombic).

From Figure 4-8b, several R values were measured and their corresponding d spacings were calculated. The values are listed in Table 4-2.

Table 4-2. R and d Values from Carbide Diffraction Pattern.

| n | $R_n$ Value (cm) | d Spacing (nm) |
|---|---|---|
| 1 | 1.45 | 0.2655 |
| 2 | 1.85 | 0.2081 |
| 3 | 2.10 | 0.1833 |

In addition, the angles between R values were measured from Figure 4-8b and are as follows: $\theta_{13} \sim 60$, $\theta_{12} \sim 78°$, and $\theta_{23} \sim 45°$. The simulated pattern for the $Cr_7C_3$ orthorhombic structure is displayed adjacent to the measured diffraction pattern in Figure 4-8c. No match for the pattern was found for $Fe_3Nb_3C$, suggesting that the carbides were likely of the form $M_7C_3$, with M being mostly Fe, Cr, and Nb with some Mo. This was confirmed by solving a number of diffraction patterns from other carbides in the thin foil sample, which all matched the $M_7C_3$ orthorhombic structure.

#### *4.1.3.2 Carbon Replica Results*

In order to determine whether the Cr and Fe peaks detected by EDX were coming from the carbides themselves or from the steel matrix, a carbon replica specimen was prepared. In this type of sample, unlike the thin foil, the precipitates were extracted from the matrix, and therefore any Cr or Fe peaks detected by EDX analysis would only be coming from the carbides themselves. Figure 4-9 is a TEM BF image of a cluster of carbides from the replica. Two different types of carbides were identified: Nb-Fe rich carbides containing some Cr and Mo, and Nb-Ti carbides. The EDX spectra from the two types of carbides are displayed in Figure 4-9b and 4-9c, respectively.

From the EDX spectrum in Figure 4-9b, it appears that the Nb-Fe carbides are the same as those that were found in the thin foil sample. These carbides are Nb- and Fe-rich but also contain some Mo and Cr. Figure 4-9c indicates that a second type of carbide is also present in the 434 steel. This carbide is Nb-rich, but also contains some Ti. Ti is not specified in the 434 composition given in Table 3-1; however, a small amount of Ti must be present in the steel. In both EDX spectra, the Cu peak comes from the Cu grid used to support the specimen. The Nb-Ti carbides were most likely not seen in the thin foil sample due to the limited area of the foil that was examined. Only a small region surrounding the hole in the middle of the sample is electron transparent, and it is possible that none of the Nb-Ti carbides were present in this small region of the specimen. This is probably a sampling phenomenon as there were more Nb-Fe type carbides than Nb-Ti type carbides.

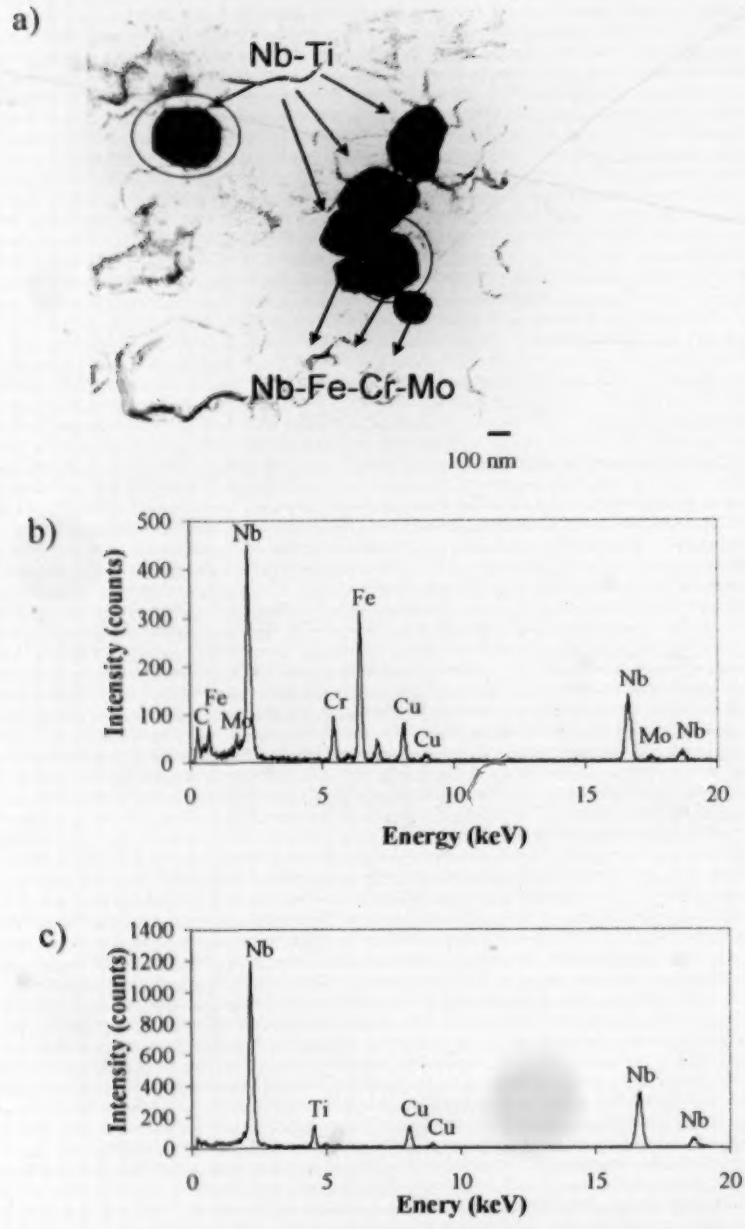


Figure 4-9. Two Types of Carbides From 434 Extraction Replica. a) TEM BF Image of Two Types of Precipitates; b) EDX Spectrum from Nb-Fe Carbide; c) EDX Spectrum from Nb-Ti Carbide.

Diffraction patterns were taken from both the Nb-Fe and Nb-Ti carbides. Indexing of the patterns was done using the procedure described previously. For the Nb-Fe carbides, the diffraction patterns were found to match the $M_7C_3$ orthorhombic structure, confirming that these carbides are the same as those that were detected in the thin foil specimen. Figure 4-10a and 4-10b, respectively, show a diffraction pattern taken from an Nb-Fe type carbide and the simulated pattern matching the $M_7C_3$ orthorhombic structure. For the Nb-Ti carbides, the diffraction patterns were found to match the NbC cubic structure (PDF # 00-038-1364) (International Center for Diffraction Data. 1996). Figure 4-10c and 4-10d display a diffraction pattern taken from a Nb-Ti type carbide and the simulated pattern matching the NbC cubic structure, respectively.

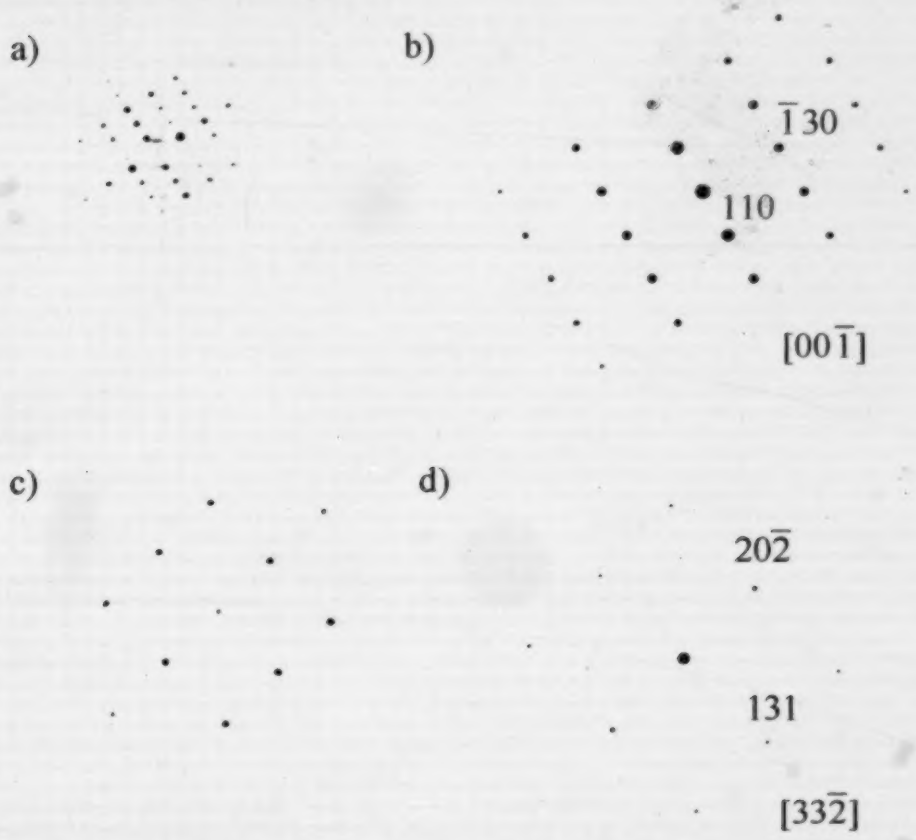


Figure 4-10. Carbide Diffraction Patterns. a) Nb-Fe SAD Pattern; b) Simulated Pattern for $Cr_7C_3$ (orthorhombic); c) Nb-Ti SAD Pattern; d) Simulated Pattern for NbC (cubic).

## 4.2 Long Term Oxidation Experiments

### 4.2.1 Specific Mass Gain Results

In order to compare the mass gain due to oxidation for the different steels, the mass gain data was plotted as $\left(\frac{\Delta m}{A}\right)^2$ vs t, where $\Delta m$ is mass gain in g, $A$ is specimen surface area in $cm^2$ calculated as two times the length of the specimen multiplied by the width of the specimen, and t is oxidation time in s. The results for the three steels are displayed in Figures 4-11 through 4-13. In all cases, the data points appear to follow a straight line, indicating that the oxidation process can be modeled using parabolic kinetics.

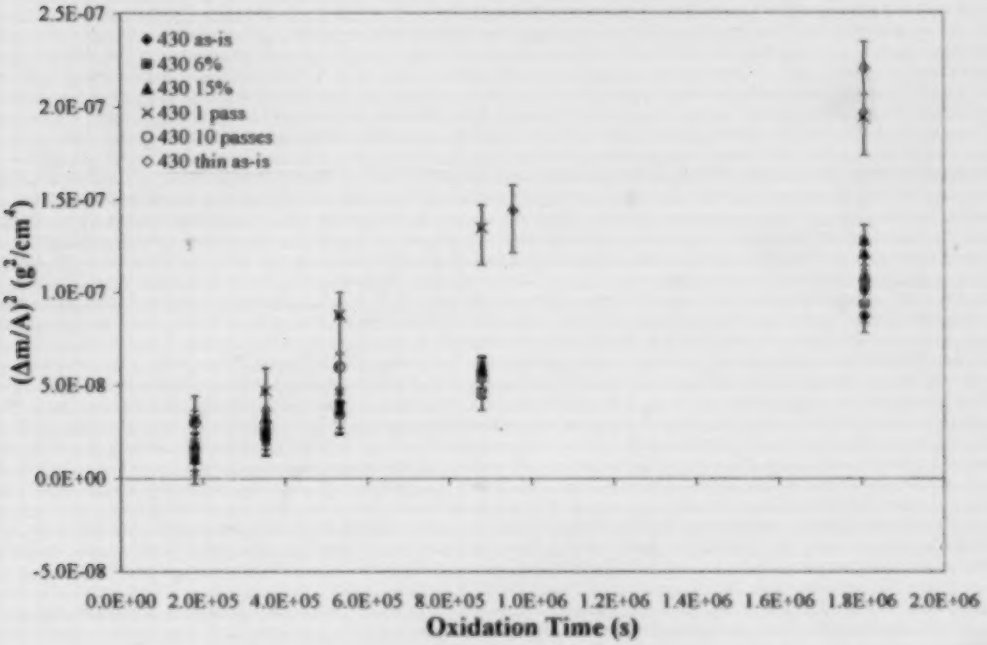


Figure 4-11. Mass Gain Due to Oxidation for 430 Specimens.

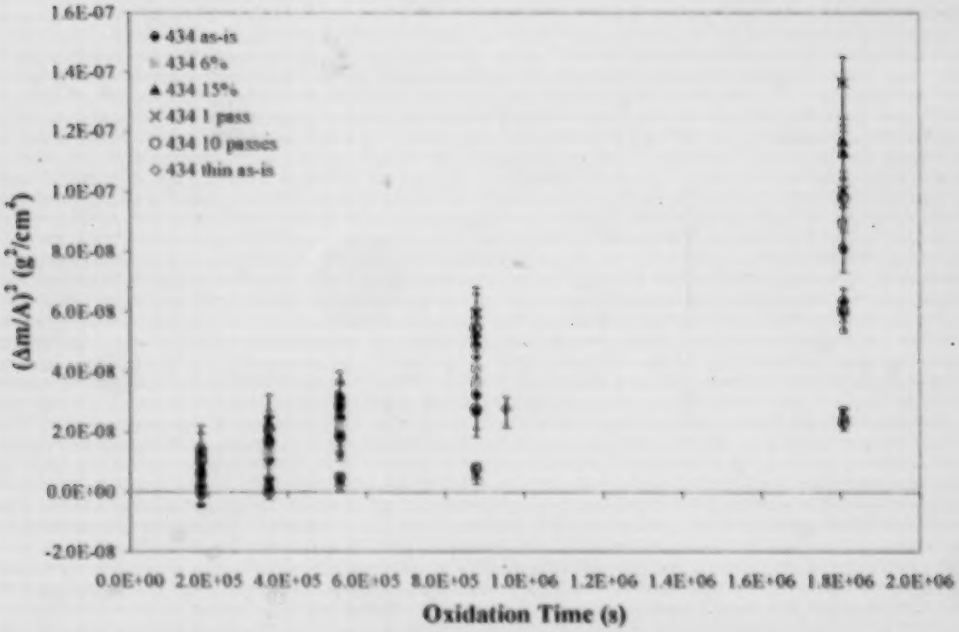


Figure 4-12. Mass Gain Due to Oxidation for 434 Specimens.

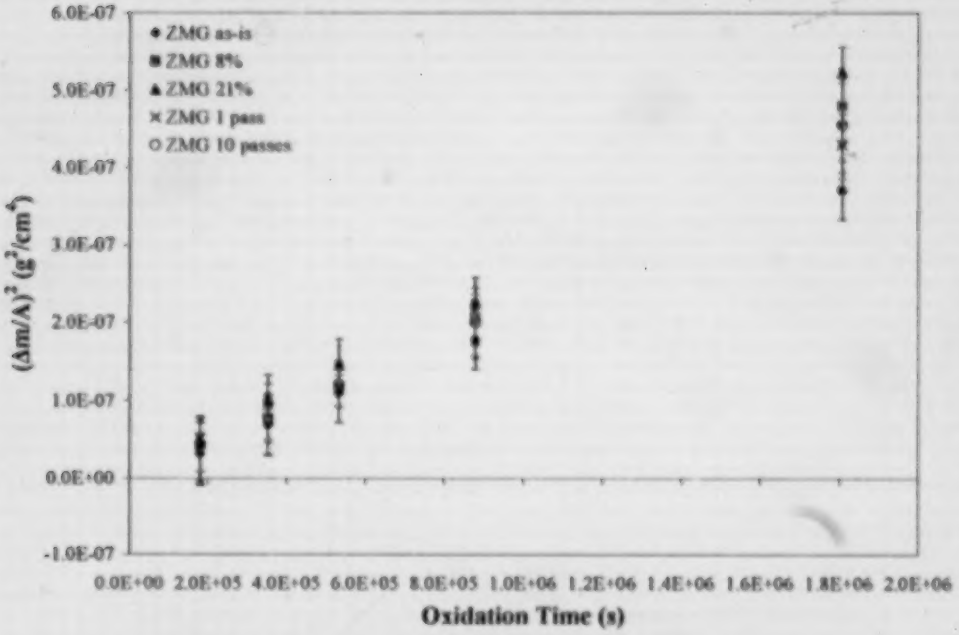


Figure 4-13. Mass Gain Due to Oxidation for ZMG 232 Specimens.

Comparing the data presented in Figures 4-11 through 4-13, it can be seen that the specific mass gains for the 430 and 434 specimens were fairly similar, with those for the 434 specimens being slightly lower. The ZMG 232 specimens had a much higher mass gain than the other two steels.

For all three steels, in general, the treated specimens had a higher specific mass gain than the as-is specimens. For the rolled specimens, for all three steels, the specimens with the higher rolling reduction (15% or 21% for ZMG 232) had a higher specific mass gain than the specimens with the lower rolling reduction (6% or 8% for ZMG 232). For the sandblasted 430 steel, the 1 pass specimen had a significantly higher specific mass gain than the 10 pass specimen. However, for the 434 and ZMG 232 steels, the 1 pass and 10 pass specimens had similar specific mass gains.

For the 430 and 434 specimens, as-is "thin" specimens were also tested. These "thin" specimens had a thickness of approximately 0.25 mm in comparison to the 1 mm thickness of the other 430 and 434 specimens. The ZMG 232 specimens also had a thickness of 0.25 mm. The reason for testing thin 430 and 434 specimens was to determine if the higher specific mass gain for the ZMG 232 specimens could be, at least in part, due to the specimens being thinner. In Figure 4-11, it can be seen that the 430 thin as-is specimen had a much higher mass gain than the thicker as-is specimen, although the mass gain for the 430 thin specimen was still lower than that for the ZMG 232 specimens. In Figure 4-12, it can be seen that the 434 thin as-is specimen had a similar mass gain to the thicker as-is specimen. Following 502 h of oxidation, significant spalling of the oxide from the 430 thin specimen was observed, as fairly large patches of bare metal were present on the specimen surface and a small amount of black powder at the bottom of the alumina crucible was observed. No evidence of significant spalling was observed for any of the other steels and treatment conditions, including the 434 thin as-is specimen.

#### *4.2.1.1 Surface Area Consideration*

From the SEM images of the unoxidized specimens in Figure 4-1, it is clear that the surface roughness of the sandblasted specimens is greater than that for the as-is and rolled specimens. As a result, the actual surface area of the sandblasted specimens taking into account the increase in surface area due to the roughness of these specimens should be

higher than that for the as-is or rolled specimens. If the surface roughness for each of the specimens is known, the increase in surface area due to roughness could be taken into account by a factor that would be multipled by the surface area. In this case, the corrected surface area can be determined from the following equation:

$$A_c = 2 \times [(f \cdot l) + (f \cdot w)] \qquad (4\text{-}3)$$

where $A_c$ is the corrected surface area of the specimen in $cm^2$, $f$ is the multiplication factor that would account for the surface roughness, $l$ is the length of the specimen, and $w$ is the width of the specimen.

In order to determine an estimate of the surface roughness, a profilometer was used to obtain a profile of the surface for each of the steels and treatment conditions. Figure 4-14 displays a schematic of a profile obtained by scanning the surface of a steel specimen. The curved profile can be approximated by a series of line segments. For each sample, 40 to 50 line segments were required.

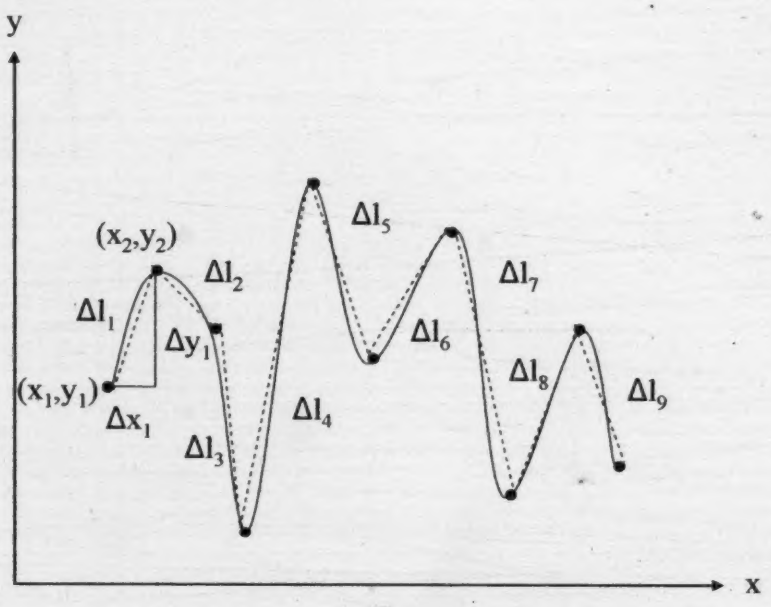


Figure 4-14. Schematic of Surface Profile.

The length of each line segment $\Delta l_i$ was determined using the following equations:

$$\Delta x_1 = x_2 - x_1 \qquad (4\text{-}4)$$

$$\Delta y_1 = y_2 - y_1 \qquad (4\text{-}5)$$

$$\Delta l_1 = \sqrt{\Delta x_1^2 + \Delta y_1^2} \qquad (4\text{-}6)$$

Finally, the total length of the profile L in μm was determined using Equation 4-7:

$$L = \sum l_i = l_1 + l_2 + \ldots + l_n \qquad (4\text{-}7)$$

Once the total length of the profile was determined, the multiplication factor f was determined using the following equation:

$$f = \frac{L}{2000} \qquad (4\text{-}8)$$

The nominal distance scanned by the stylus tip over the specimen surface was 2 mm or 2000 μm. Table 4-3 displays the actual distance travelled by the profilometer over the 2 mm trace for selected specimens and treatment conditions, and indicates the appropriate multiplication factor to two decimal places.

Table 4-3. Multiplication Factors for Selected Specimens and Treatment Conditions.

| Specimen | Distance Travelled by Profilometer (μm) | Multiplication Factor |
|---|---|---|
| 430 as-is | 2000.00 | 1.00 |
| 430 rolled 6% | 2000.05 | 1.00 |
| 430 rolled 15% | 2000.06 | 1.00 |
| 430 sandblasted 1 pass | 2001.70 | 1.00 |
| 430 sandblasted 10 passes | 2002.61 | 1.00 |
| 434 as-is | 2000.00 | 1.00 |
| ZMG 232 as-is | 2000.01 | 1.00 |
| ZMG 232 rolled 21% | 2000.12 | 1.00 |
| ZMG 232 sandblasted 1 pass | 2001.59 | 1.00 |
| ZMG 232 sandblasted 10 passes | 2003.30 | 1.00 |

From Table 4-3, as expected, the distance travelled by the profilometer and thus the surface roughness is largest for the 10 pass sandblasted specimens, and smallest for the as-is specimens. However, the roughness for all the specimens is not large enough to be significant, and the multiplication factor for all steels and treatment conditions is 1.00. Therefore, the effect of surface roughness for the different treatment conditions on the specific mass gain data plotted in Figures 4-11 to 4-13 can be considered to be negligible.

#### *4.2.1.2 Sandblasted Specimen Correction*

As was mentioned in the Experimental Methods section, the sandblasted specimens were only sandblasted on one side. Therefore, the measured specific weight gain for a nominally sandblasted specimen would be an average of the specific weight gain for a specimen with both sides in the as-is condition and the specific weight gain for a specimen with both sides in the sandblasted condition. In order to determine the experimental specific mass gain for a specimen with both sides in the sandblasted condition, the following correction was used:

$$\left(\frac{\Delta m}{A}\right)_{sb,2sides} = 2\times\left(\frac{\Delta m}{A}\right)_{sb,1side} - \left(\frac{\Delta m}{A}\right)_{as-is,2sides} \qquad (4\text{-}9)$$

The corrected results are displayed in the plots in Figures 4-11 through 4-13.

#### *4.2.1.3 Error Bar Calculation*

4.2.1.3.1 Error in the Abscissa Values

For the abscissa or x values of the data points, the only variable to consider is t. The first time related error that could have affected the results for the long term oxidation experiments was the precision of the watch that was used to time the experiment, which was ±0.5 s for each specimen. Also, once the specimens were removed from the furnace, they took approximately 5 min to cool to room temperature. Although the temperature of the specimens was continually decreasing during this time, for the purposes of the error bar calculation, a worst case scenario where the specimens remained at the oxidation temperature for an additional 5 min was assumed, which would give an error of +300 s

for each specimen. Also, since several specimens were removed from the furnace at the same time, the specimens did not begin to cool at the exact time specified for their removal. A conservative estimate of the time to remove all the specimens from the furnace at the removal time is 5 minutes. Therefore, an additional error of +300 s was assumed for each specimen. In addition, each instance a specimen was removed, the specimens inside would cool from the oxidation temperature for 5 minutes while the furnace door was open for specimen removal, and following this, it took approximately 15 minutes for the furnace temperature to return to the setpoint. Therefore, an error of -1200 s was assumed for each specimen removal time for the specimens remaining in the furnace. The worst case scenario would be for the 502 hour specimen, for which the error would be 4 x (-1200 s) = -4800 s. Finally, at the start of the long term oxidation experimens, after the specimens were placed in the box furnace, it took approximately 45 minutes for the furnace to heat to the oxidation temperature. Therefore, an error of -2700 s was assumed for each specimen.

Each of the individual positive and negative time related errors were added to give a maximum positive error and a maximum negative error for each annealing time. For the maximum positive error, the total was 0.5 s + 300 s + 300 s = 600.5 s. For the maximum negative error, the total was -0.5 s - 4800 s - 2700 s = -7500.5 s. Therefore, for each data point on the plots in Figures 4-11 through 4-13, error bars with a range of -7500.5 s to +600.5 s were plotted.

#### 4.2.1.3.2 Error in the Ordinate Values

##### *4.2.1.3.2.1 Error in Mass Gain*

In order to determine the mass of the specimens, a balance that measured to the nearest 0.01 mg was used. Therefore, the error in the measured masses would be equal to half of this value, ±0.005 mg or ±0.000005 g. In addition, it is possible that a small amount of oxide flaked off of the specimens when they were handled with tongs as they were removed from the furnace and placed on the stainless steel sheets. In order to account for this, an error of -2% of the total mass gain was assumed for each sample as a worst case estimate. Therefore, the maximum positive error in mass gain ($d\Delta m$) was equal to +0.000005 g for each specimen, and the maximum negative error in mass gain was equal to (-0.000005 – 0.02 x $\Delta m$) g for each specimen.

*4.2.1.3.2.2 Error in Area*

The digital calliper that was used to measure the dimensions of the specimens prior to oxidation was able to measure to the nearest 0.01 mm. The measurement error in the length and the width of each specimen was then equal to ±0.005 mm, or 0.0005 cm. In order to convert this error into an equivalent error for the measurement of the area of the specimen, the following procedure was used:

$$A = 2 \cdot l \cdot w \qquad (4\text{-}10)$$

$$\frac{dA_{meas}}{A} = 2 \cdot \left[ \left( \frac{dl}{l} \right) + \left( \frac{dw}{w} \right) \right]$$

$$dA_{meas} = 2A \cdot \left[ \left( \frac{dl}{l} \right) + \left( \frac{dw}{w} \right) \right] \qquad (4\text{-}11)$$

where $dA_{meas}$ is the error in the specimen area due to measuring instrument constraints and $dl$ and $dw$ are the measurement errors in length and width, respectively, both equal to ±0.0005 cm. Using Equation 4-11, a vaule of $dA_{meas}$ was determined for each specimen.

In addition to error in specimen area measurement, additional error was present due to the assumption in Equation 4-10 that the specimens were rectangular. Although the specimens were very close to being rectangular and this assumption was most likely a good one, a worst case scenario error $dA_{rect} = \pm 0.02 \cdot A$ was determined for each specimen.

Finally, the calculation of the specimen area using Equation 4-10 did not include the area of the sides of the specimen. In order to account for this, an error $dA_{sides} = +0.01 \cdot A$ was determined for each specimen.

In order to account for the worst case, a total error in the specimen area was determined as follows:

$$dA = |dA_{meas}| + |dA_{rect}| + |dA_{sides}|$$

$$dA = 2A \cdot \left[ \left( \frac{dl}{l} \right) + \left( \frac{dw}{w} \right) \right] + 0.02A + 0.01A$$

$$dA = \pm \left\{ 2A \cdot \left[ \left( \frac{dl}{l} \right) + \left( \frac{dw}{w} \right) \right] + 0.03A \right\} \qquad (4\text{-}12)$$

Using Equation 4-12, a value of $dA$ was calculated for each specimen.

*4.2.1.3.2.3 Error in Specific Mass Gain*

For the ordinate or y values in the plots of Figures 4-11 through 4-13, errors in both mass and area must be considered as $y = \left( \frac{\Delta m}{A} \right)^2$. In order to determine the maximum error for the specific mass gain values, the following procedure was used:

$$y = \left( \frac{\Delta m}{A} \right)^2$$

$$\frac{dy}{y} = \left[ 2 \cdot \left( \frac{d\Delta m}{m} \right) + 2 \cdot \left( \frac{dA}{A} \right) \right]$$

$$dy = y \cdot \left[ 2 \cdot \left( \frac{d\Delta m}{m} \right) + 2 \cdot \left( \frac{dA}{A} \right) \right]$$

$$dy = \left( \frac{\Delta m}{A} \right)^2 \cdot \left[ 2 \cdot \left( \frac{d\Delta m}{m} \right) + 2 \cdot \left( \frac{dA}{A} \right) \right] \qquad (4\text{-}13)$$

Using Equation 4-13, a value for the maximum positive and maximum negative error in the y values was calculated for each specimen.

For each steel and treatment type, the maximum value of the positive error in the y values $dy_{max}$ was determined as the largest positive $dy$ value for one of the five identical specimens that were removed from the furnace at different times. In the same way, the maximum value of the negative error in the y values was determined for each steel and treatment type.

### 4.2.2 Parabolic Rate Constants

From the experimental data presented in Figures 4-11 to 4-13, parabolic rate constants were determined for each steel and treatment condition from the slope of a best fit line passing through the data points as well as the origin. The parabolic rate constants are listed in Table 4-4. The numbers in brackets are the corresponding $R^2$ values.

Table 4-4. Parabolic Rate Constants ($x10^{-14} g^2/cm^4 \cdot s$)

| Surface Treatment | 430 | 434 | ZMG 232 |
|---|---|---|---|
| as-is | 5.62 (0.93) | 3.87 (0.98) | 20.5 (1.0) |
| as-is (thin) | 12.8 (0.80) | 3.20 (0.98) | - |
| rolled - 6% (8% ZMG) | 5.60 (0.97) | 4.73 (0.98) | 25.7 (0.99) |
| rolled - 15% (21% ZMG) | 6.85 (0.99) | 6.18 (0.99) | 28.3 (1.0) |
| sb - 1 pass | 12.0 (0.88) | 4.76 (0.94) | 24.0 (1.0) |
| sb - 10 passes | 6.34 (0.71) | 3.35 (0.96) | 24.5 (0.99) |

Similar to the specific mass gain data, the parabolic rate constants for the ZMG 232 specimens are much larger than those for the other two steels. Although the rate constants for the 430 and 434 steels are much closer to one another, the rate constants for the 434 specimens are slightly lower than those for the 430 specimens. In particular, the 434 as-is thin specimen has a much lower rate constant than the 430 as-is thin specimen. In general, the rate constants for the treated specimens are higher than for the as-is specimens. For the rolled specimens, the rate constant increases as the degree of rolling deformation increases. For the sandblasted specimens, the difference in parabolic rate constant between the two treatments is much smaller, with the exception of the 430 steel, and there is no trend that holds for all three steels.

Although no literature values of the parabolic rate constant for the oxidation of 434 steel in air at 800°C could be found, values for the other two steels are listed in Table 4-5.

Table 4-5. Literature Values of Parabolic Rate Constants for Oxidation in Air at 800°C (Antepara, et al. 2005, Brylewski, et al. 1999, Yang, et al. 2003b).

| Steel | Parabolic Rate Constant $x10^{-14}$ $g^2cm^{-4}s^{-1}$ |
|---|---|
| 430 | 35 |
| 430 | 8.5 |
| ZMG 232 | 27 |

The first value in the table for 430 steel was determined using an "isothermal oxidation study" (Yang, et al. 2003b). The second value for 430 steel was calculated from thermogravimetric meaurements of mass gain due to oxidation for 100 h (Brylewski, et al. 1999). The literature parabolic rate constant for ZMG 232 was determined using "weight gain measurements" for 1000 h of oxidation (Antepara, et al. 2005). The only study found in the literature that directly compared the oxidation behaviour of 430 and ZMG 232 determined that for oxidation in air at 750°C for 1000 h, the mass gain of ZMG 232 was slightly lower than that for 430; however, no parabolic rate constants were calculated (Uehara, et al. 2003).

In comparing the values in Table 4-5 with the parabolic rate constants determined in the long term oxidation experiments, it can be seen that the values obtained for the 430 and 434 steels are similar to, although slightly lower than, the second literature value for the 430 parabolic rate constant. The parabolic rate constants determined for ZMG 232 are comparable with the literature value in Table 4-5.

## 4.3 430 Results

### 4.3.1 XRD Results

#### *4.3.1.1 XRD Spectra*

In order to determine the oxide phases present on the 430 specimens after oxidation, XRD analysis was used. Figure 4-15 shows the XRD spectra obtained for the 6% cold rolled specimen after 50 h, 98 h, and 502 h of oxidation.

From Figure 4-15, there are two oxide phases present: $Cr_2O_3$ and $(Mn,Cr)_3O_4$ spinel. Both of the oxide phases are present after 50 h of oxidation and continue to be present after 502 h of oxidation. The peaks from the steel substrate are also present in each of the three spectra, which indicates that the entire oxide layer is being analyzed in each case. The height of the steel peaks decreases as oxidation time increases indicating that, as expected, the oxide layer is increasing in thickness. This is particularly clear with the (200) Fe peak. A decrease in the height of the steel peaks relative to the height of the oxide peaks from the 50 h spectrum to the 502 h spectrum was observed for all steels and treatment conditions.

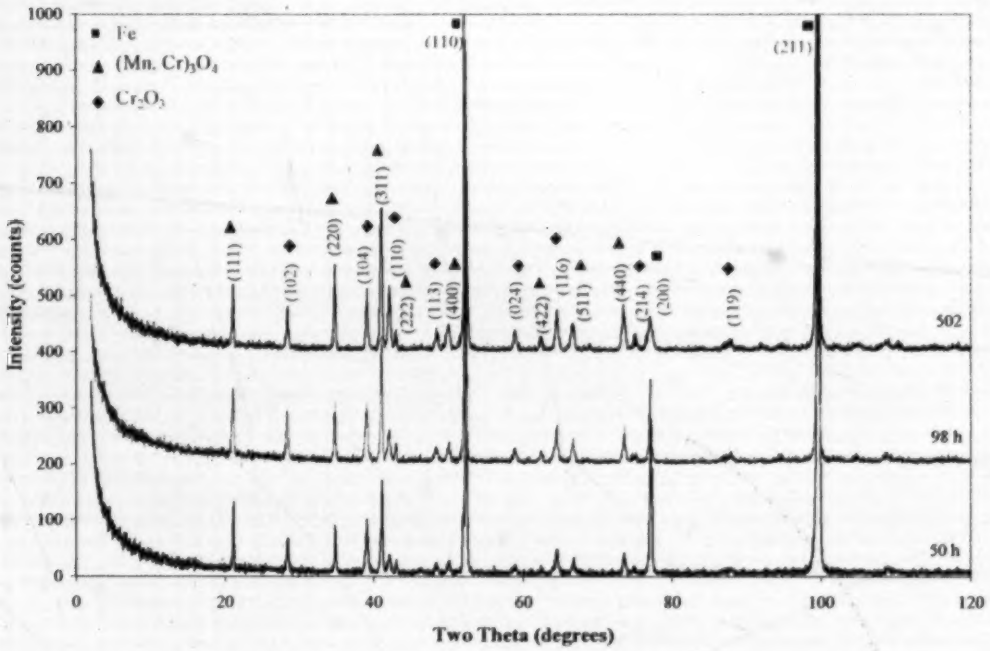


Figure 4-15. XRD Spectra from 430 6% Cold Rolled Specimens After Oxidation.

Figure 4-16 shows a comparison of the XRD spectra obtained after 502 h for the different treatments. From Figure 4-16, it is clear that although the same peaks are present in each spectrum, the relative heights of the peaks are different for the different treatment conditions. This indicates that the oxide phases are the same for all surface treatments,

but the type of surface treatment has affected the relative amount of the oxide phases present.

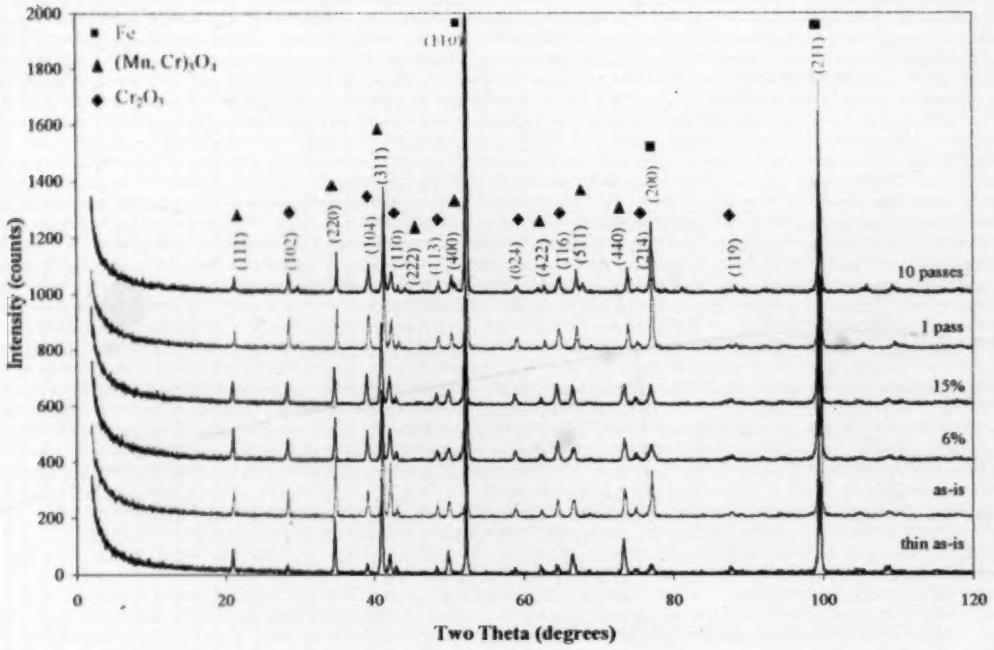


Figure 4-16. Comparison of the 430 XRD Spectra After 502 h of Oxidation.

#### *4.3.1.2 Relative Peak Intensities*

In order to analyze the XRD results, the first step was to determine the relative intensities of the five most intense peaks for each oxide phase and compare these values with the expected peak intensities from the JCPDS diffraction cards (International Center for Diffraction Data. 1996). A summary of this analysis is presented in Tables 4-6 and 4-7.

For the chromia phase, Table 4-6 indicates that a slight (012) preferred orientation exists for all treatments after 50 h. After 502 h, the (012) preferred orientation is still present for the sandblasted specimens. For the as-is and rolled specimens, the (012) preferred orientation is reduced after 502 h and a (110) preferred orientation is present for the as-is,

thin as-is, and rolled 6% specimens. For the spinel phase, Table 4-7 shows that a slight (111) preferred orientation is present for all treatments after 50 h and is reduced after 502 h.

Table 4-6. Relative Intensities of Chromia X-Ray Peaks for 430 Specimens.

| | | $Cr_2O_3$ (PDF#38-1479) | | | | | | | | | |
|---|---|---|---|---|---|---|---|---|---|---|---|
| | | 50 h | | | | | 502 h | | | | |
| | **Peak Order** | 1 | 2 | 3 | 4 | 5 | 1 | 2 | 3 | 4 | 5 |
| | **(hkl) Index** | (104) | (110) | (116) | (012) | (024) | (104) | (110) | (116) | (012) | (024) |
| | **Card Intensity (%)** | 100 | 93 | 87 | 73 | 38 | 100 | 93 | 87 | 73 | 38 |
| **Treatment** | As-is (thin) | - | - | - | - | - | 56 (2) | 100 (1) | 51 (3) | 43 (4) | 34 (5) |
| | As-is | 100 (1) | 84 (2) | 47 (4) | 79 (3) | 39 (5) | 50 (2) | 100 (1) | 35 (4) | 49 (3) | 23 (5) |
| | Rolled 6% | 100 (1) | 30 (4) | 43 (3) | 62 (2) | 14 (5) | 99 (2) | 100 (1) | 66 (4) | 70 (3) | 34 (5) |
| | Rolled 15% | 100 (1) | 45 (3) | 42 (4) | 58 (2) | 21 (5) | 100 (1) | 87 (2) | 63 (4) | 68 (3) | 33 (5) |
| | Sandblasted 1 pass | 100 (1) | 70 (2) | 46 (4) | 66 (3) | 24 (5) | 100 (1) | 85 (3) | 60 (4) | 91 (2) | 37 (5) |
| | Sandblasted 10 passes | 100 (1) | 55 (3) | 48 (4) | 79 (2) | 13 (5) | 100 (1) | 59 (3) | 50 (4) | 65 (2) | 26 (5) |

Table 4-7. Relative Intensities of Spinel X-Ray Peaks for 430 Specimens.

| | | $(Cr, Mn)_3O_4$ (PDF#33-0892) | | | | | | | | | |
|---|---|---|---|---|---|---|---|---|---|---|---|
| | | 50 h | | | | | 502 h | | | | |
| | **Peak Order** | 1 | 2 | 3 | 4 | 5 | 1 | 2 | 3 | 4 | 5 |
| | **(hkl) Index** | (311) | (220) | (440) | (511) | (111) | (311) | (220) | (440) | (511) | (111) |
| | **Card Intensity (%)** | 100 | 50 | 45 | 30 | 25 | 100 | 50 | 45 | 30 | 25 |
| **Treatment** | As-is (thin) | - | - | - | - | - | 100 (1) | 59 (2) | 37 (3) | 20 (5) | 22 (4) |
| | As-is | 100 (1) | 63 (2) | 27 (4) | 22 (5) | 48 (3) | 100 (1) | 54 (2) | 25 (3) | 15 (5) | 22 (4) |
| | Rolled 6% | 100 (1) | 51 (3) | 22 (4) | 17 (5) | 74 (2) | 100 (1) | 61 (2) | 32 (4) | 19 (5) | 44 (3) |
| | Rolled 15% | 100 (1) | 53 (3) | 23 (4) | 23 (5) | 65 (2) | 100 (1) | 46 (2) | 16 (5) | 21 (4) | 26 (3) |
| | Sandblasted 1 pass | 100 (1) | 40 (2) | 25 (3) | 15 (5) | 24 (4) | 100 (1) | 39 (2) | 23 (3) | 21 (4) | 16 (5) |
| | Sandblasted 10 passes | 100 (1) | 42 (2) | 19 (4) | 42 (2) | 26 (3) | 100 (1) | 39 (2) | 24 (3) | 21 (4) | 15 (5) |

#### *4.3.1.3 Peak Area Ratios*

In order to compare the relative amounts of the chromia and spinel phases between the different treatment conditions, the peak areas were determined using Jade software and the spinel to chromia peak area ratios were determined for each of the 430 specimens. The results of this analysis can be seen in Table 4-8.

Table 4-8. Spinel to Chromia Peak Area Ratios for 430 Specimens.

| | **Spinel to Chromia Peak Area Ratio** | | | |
|---|---|---|---|---|
| | **50 h** | | **502 h** | |
| **Treatment** | (311):(104) | (220):(104) | (311):(104) | (220):(104) |
| As-is (thin) | - | - | 13.3 | 5.6 |
| As-is | 1.4 | 0.5 | 4.3 | 1.8 |
| Rolled 6% | 1.6 | 0.6 | 2.8 | 1.2 |
| Rolled 15% | 1.3 | 0.6 | 2.4 | 1.0 |
| Sandblasted 1 pass | - | 0.3 | 2.1 | 0.7 |
| Sandblasted 10 passes | - | 0.4 | 3.3 | 1.0 |

The most intense peak for chromia is the (104) peak and for spinel the (311) peak. For the sandblasted specimens, after 50 h, peaks from the $Al_2O_3$ particles used in the sandblasting process were present in addition to the chromia and spinel peaks. The most intense alumuna peak, the (104) peak, overlaps with the (311) spinel peak, making the (311):(104) spinel to chromia ratio for these specimens meaningless. Therefore, the second most intense spinel peak, the (220) peak, was used to calculate a second spinel to chromia ratio. The alumina peaks were no longer detected after 502 h because growth of the oxide scale masked the weaker alumina peaks.

From Table 4-8, it is clear that the relative amounts of chromia and spinel phases vary with both treatment condition and oxidation time. For all specimens, the relative amount of spinel increased with increasing oxidation time. After 50 h of oxidation, the relative amount of spinel was similar for all the treatment conditions. However, after 502 h of oxidation, the relative amount of spinel was higher for the as-is specimen than for any of the specimens that were subjected to surface treatment. The relative amount of spinel was similar for the rolled and sandblasted specimens.

### 4.3.2 SEM Plan View Results

#### *4.3.2.1 SEM Images*

SEM plan view images for the 430 specimens after 50 h and 502 h of oxidation are displayed in Figure 4-17.

After 50 h, it can be seen that a continuous oxide scale has formed on the surface of all the specimens. For the as-is and rolled specimens, the oxide scale is fairly even except where bright clumps of fast growing oxide are visible, with the number of clumps increasing with the degree of rolling deformation. EDX analysis of a number of these oxide clumps was carried out for the as-is and rolled specimens. For the as-is specimen, the composition of the oxide clumps was similar to that of the surrounding oxide, implying that the rapid growth in these locations could be due to the presence of surface defects or flaws. For the rolled specimens, the bright oxide clumps were enriched in Fe compared with the surrounding oxide, with the degree of Fe enrichment more significant for the 15% rolled specimen than the 6% specimen. In this case, the rapid growth could be due to cracking or spalling of the protective oxide, allowing Fe-rich oxides to form.

For the sandblasted specimens, after 50 h the roughness resulting from the sandblasting treatment is still visible and the oxide scale is relatively uneven and consists of higher 'ridges' separated by lower 'depressions'. The appearance of the oxide scale on the sandblasted 1 pass and 10 passes specimens is similar.

After 502 h, the thickness of the oxide appears to have increased for all specimens. For the thin specimen, there are two distinct regions of oxide – one in the middle, referred to as 'low oxide', which contains circular regions referred to as 'holes', and one in the surrounding region, which has a similar appearance to the oxide on the thick as-is specimen. Figure 4-18 depicts EDX spectra taken from the low oxide, hole, and surrounding oxide regions of the sample.

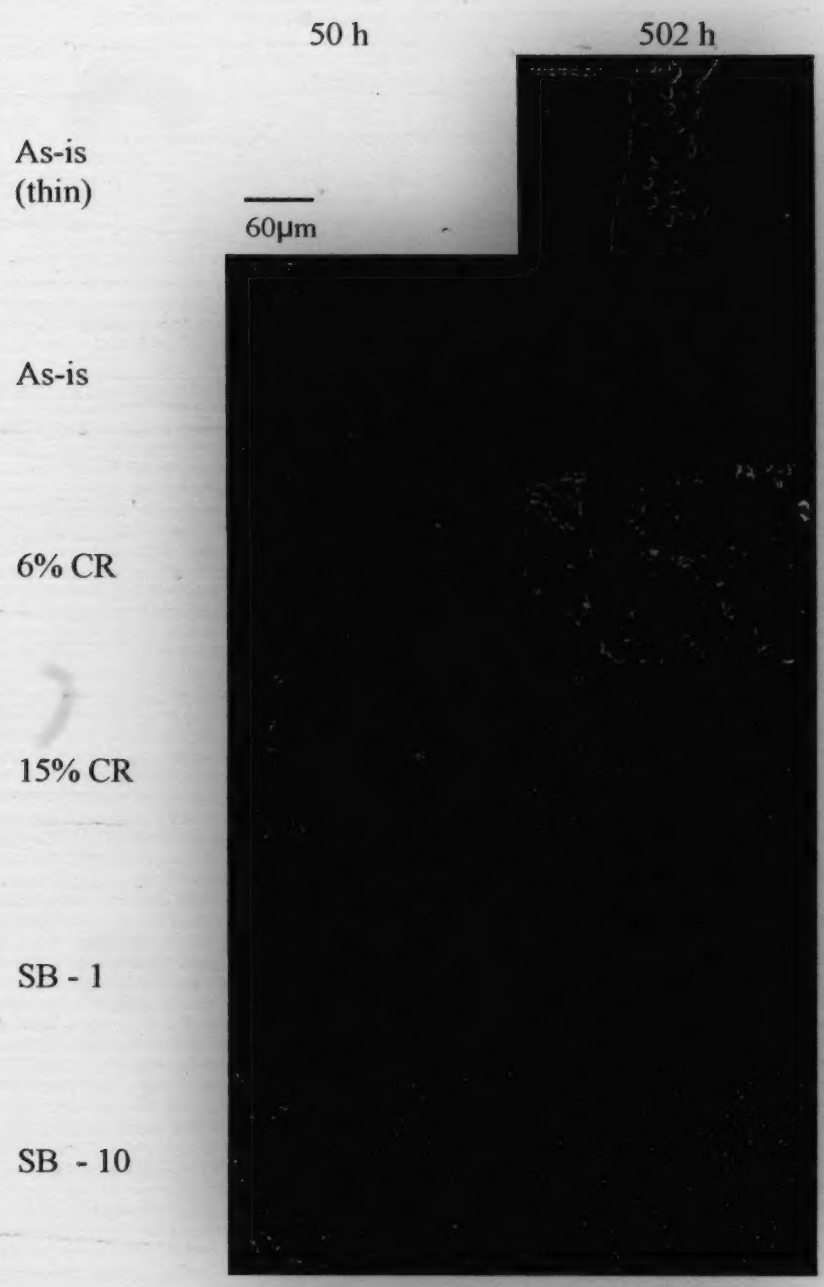


Figure 4-17. SEM SE Plan View Images for 430 Specimens After 50 h and 502 h of Oxidation.

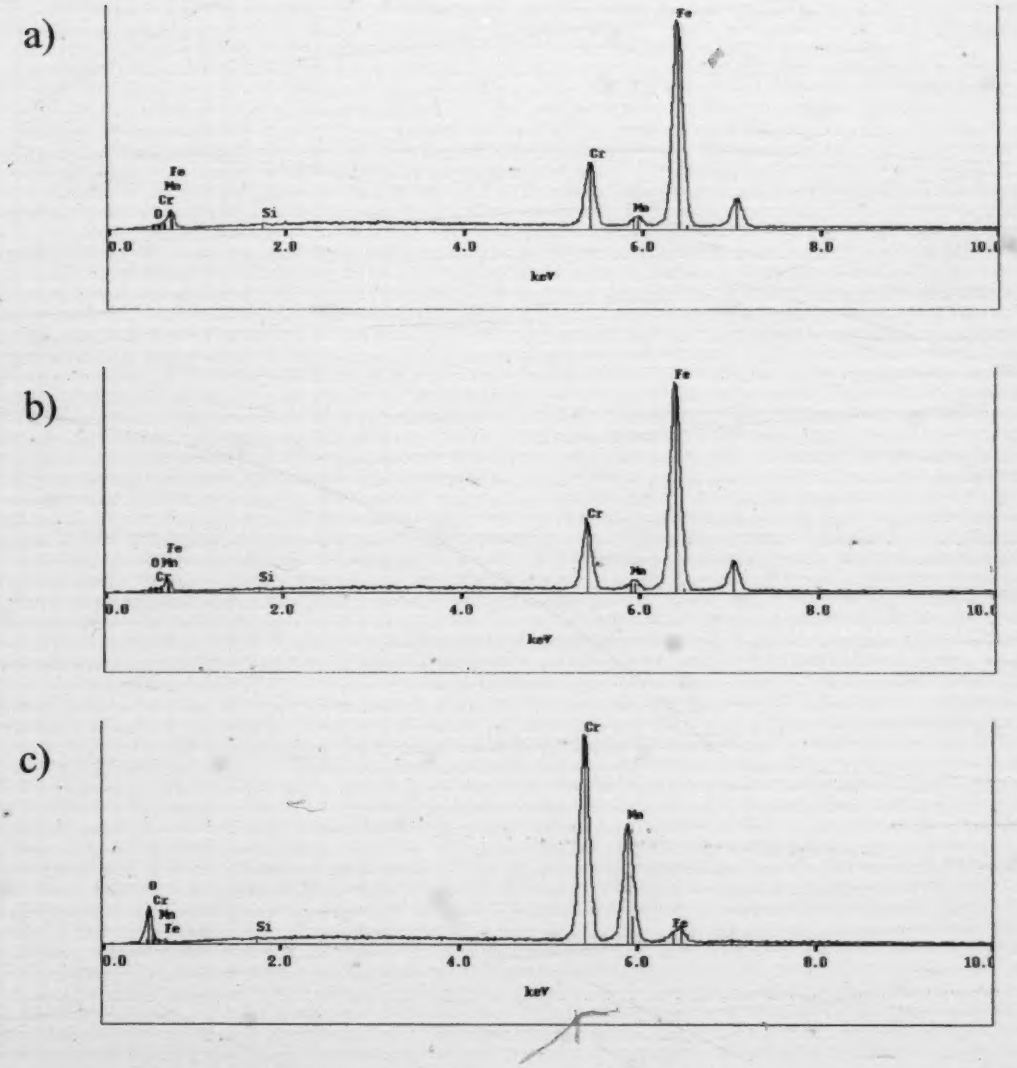


Figure 4-18. EDX Spectra from 430 as-is Specimen After 502 h of Oxidation. a) Low Oxide; b) Hole; c) Surrounding Oxide.

Figure 4-18 indicates that the low oxide and hole regions are similar in composition, and that these regions are significantly enriched in Fe when compared to the surrounding oxide. It is likely that the spalling of the oxide scale resulted in the formation of the low

oxide regions, as a small amount of black material was found in the bottom of the crucible containing the thin as-is specimen. Spalling could have occurred either during oxidation in the furnace or during rapid air cooling upon specimen removal. The mass gain results indicate that the oxide scale on the thin specimen was thicker than on the thick specimen, meaning that it would be more susceptible to cracking and spalling. However, the thin specimen would have cooled more rapidly than its thick counterpart, subjecting the oxide to a lower level of stress.

For the as-is and rolled specimens, bright clumps of fast growing oxide are still visible; however, after 502 h there are significantly more and larger clumps on the 6% rolled specimen than on the other two specimens. For the as-is specimens, EDX analysis showed that most of the bright oxide clumps contained slightly more Fe than the surrounding oxide, indicating that spalling or cracking of the oxide layer could have occurred at these sites. For the rolled specimens, the fast growing oxide was not enriched in Fe; however, various contaminants (Ni, Sn, Cu, P, Si, and Al) were detected. Not all the contaminants listed were present in a given clump. These contaminants were likely transferred to the rolled specimens from the rolling mill. They could have contributed to fast oxide growth either by acting as preferred sites for oxide nucleation or by themselves oxidizing. For the sandblasted specimens, there is little change in appearance from 50 h to 502 h, except that after 502 h the oxide scale is noticibly thicker and the surface roughness produced by the sandblasting treatment is less evident.

#### *4.3.2.2 EDX Analysis*

In order to approximate the overall composition of the oxide scale on each of the specimens, EDX spectra were collected from fairly large areas (~200μm x ~200μm). Chromium to Mn and Cr to Fe ratios were determined from quantitative analysis of the EDX spectra. These ratios are listed in Table 4-9.

Table 4-9. Cr:Mn and Cr:Fe Ratios from Quantitative EDX Analysis of the Oxide Scale for 430 Specimens.

| Surface Treatment | Cr:Mn | | Cr:Fe | |
|---|---|---|---|---|
| | 50 h | 502 h | 50 h | 502 h |
| As-Is (Thin) | - | 1.9 | - | 0.9 |
| As-Is | 6.1 | 2.5 | 1.5 | 19.0 |
| Rolled 6% | 4.6 | 2.4 | 1.3 | 15.3 |
| Rolled 15% | 4.8 | 2.4 | 1.2 | 13.7 |
| Sandblasted 1 Pass | 5.3 | 3.3 | 0.9 | 4.7 |
| Sandblasted 10 Passes | 6.0 | 3.6 | 0.8 | 4.4 |

From Table 4-9, it is noted that for all specimens, a decrease in the Cr:Mn ratio and an increase in the Cr:Fe ratio occured from 50 h to 502 h. A decrease in the Cr:Mn ratio indicates an increase in the amount of Mn enrichment relative to Cr in the oxide scale, while an increase in the Cr:Fe ratio indicates an increase in the amount of Cr relative to Fe in the oxide scale. One of the limitations of EDX analysis is that the depth of analysis is typically at least 1μm. After 50 h, the thicknesses of the oxide scales were less than 1μm; therefore, the analysis includes information from the steel substrate which accounts for the relatively low Cr:Fe ratio. After 502 h, the oxide scale was much thicker, and the Cr:Mn and Cr:Fe ratios are more meaningful.

After 502 h, the Cr:Mn ratio for the thin as-is specimen was much smaller than that for any of the other specimens. The ratios for the as-is (thicker) and rolled specimens were higher and similar to one another. The Cr:Mn ratio was highest for the two sandblasted specimens. This indicates that the highest amount of Mn enrichment in the oxide scale occured for the thin as-is specimen, followed by the as-is and rolled specimens, and the least amount of Mn enrichment occurred for the sandblasted specimens.

After 502 h, the Cr:Fe ratio was highest for the as-is and rolled specimens, lower for the sandblasted specimens, and still lower for the thin as-is specimen, which had a significantly lower Cr:Fe ratio than all the other specimens. As discussed above, the oxide scales were fairly thick after 502 h and, therefore, the Fe is mostly coming from the oxide and not from the underlying steel substrate. The ratios indicate that the amount of Fe in the oxide scale is lowest for the as-is and rolled specimens. There is more Fe present in the oxide scale of the sandblasted specimens compared with the as-is and

rolled specimens. This is likely not a result of spalling, as Figure 4-17 shows that the oxide scale on the sandblasted specimens is relatively continuous after 502 h. For the thin as-is specimen, Figure 4-18 shows that the Fe in the oxide scale is mainly due to cracking and spalling of the oxide scale, as the EDX spectrum in Figure 4-18c does not show Fe enrichment.

### 4.3.3 SEM Cross Section Results

#### *4.3.3.1 SEM Cross Section Images*

An SEM cross section image of the 430 thin as-is specimen is shown in Figure 4-19. Figure 4-19 indicates that the oxide scale consists of two distinct layers: inner chromia (brighter) and outer spinel (slightly darker). The same two phases were detected for all the steels and treatment conditions investigated in this work.

In Figure 4-19b, a Si peak is present in the chromia EDX spectrum. This is due to the presence of a thin layer of $SiO_2$ at the metal/oxide interface. In Figure 4-19c, Au and Al peaks are present in the spinel EDX spectrum. The Al peak is from $Al_2O_3$ particles used during the final polishing stage of cross section specimen preparation and the Au is from the thin sputtered layer deposited prior to Ni electrodeposition.

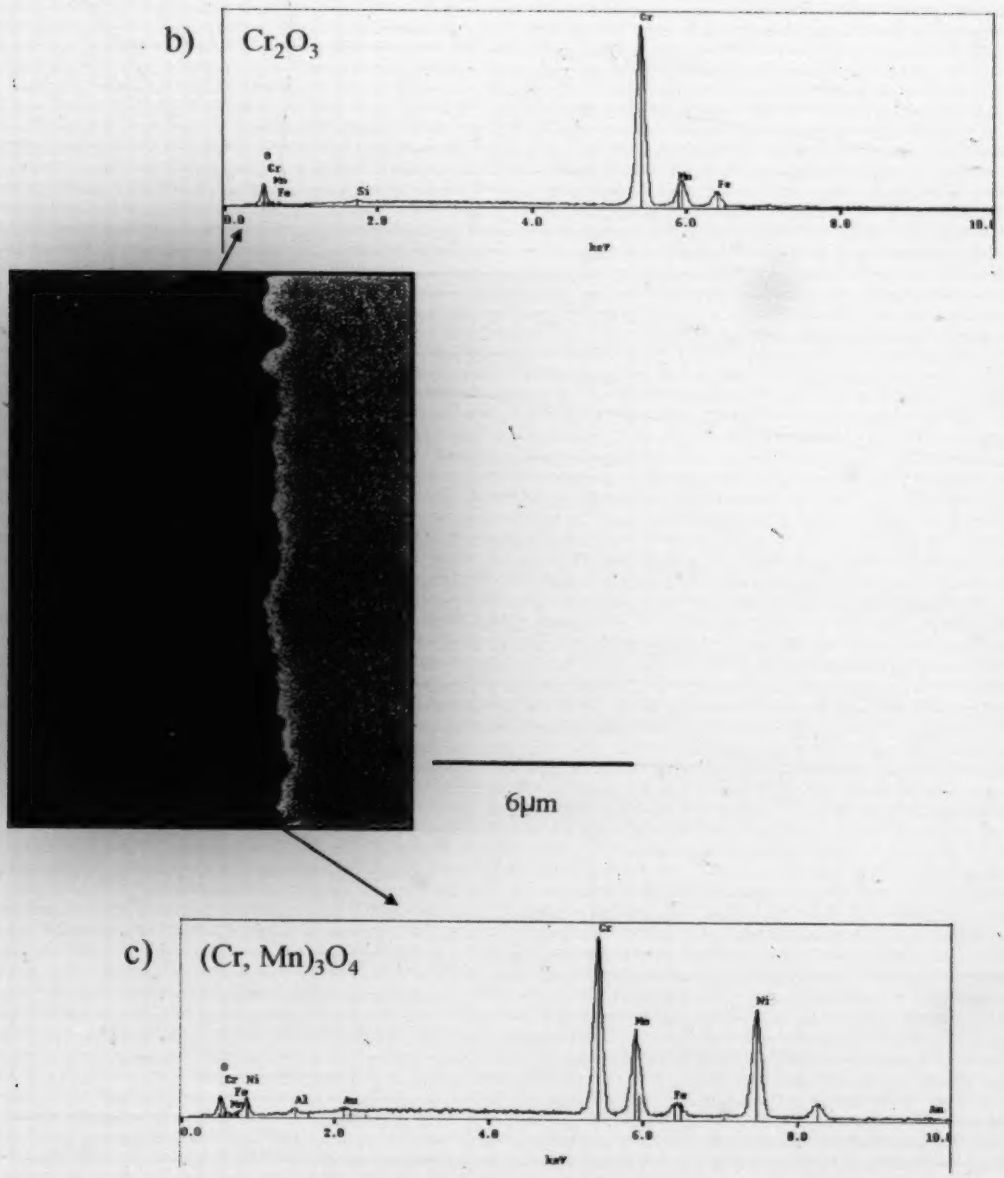


Figure 4-19. 430 Thin As-Is Specimen. a) SEM Image; b) Chromia EDX Spectrum; c) Spinel EDX Spectrum.

SEM cross section images of the 430 specimens after 502 h of oxidation are shown in Figure 4-20. As is the case for all of the SEM cross section images presented in this work, the steel is on the left, the oxide in the middle, and the Ni electroplayted layer is on the right.

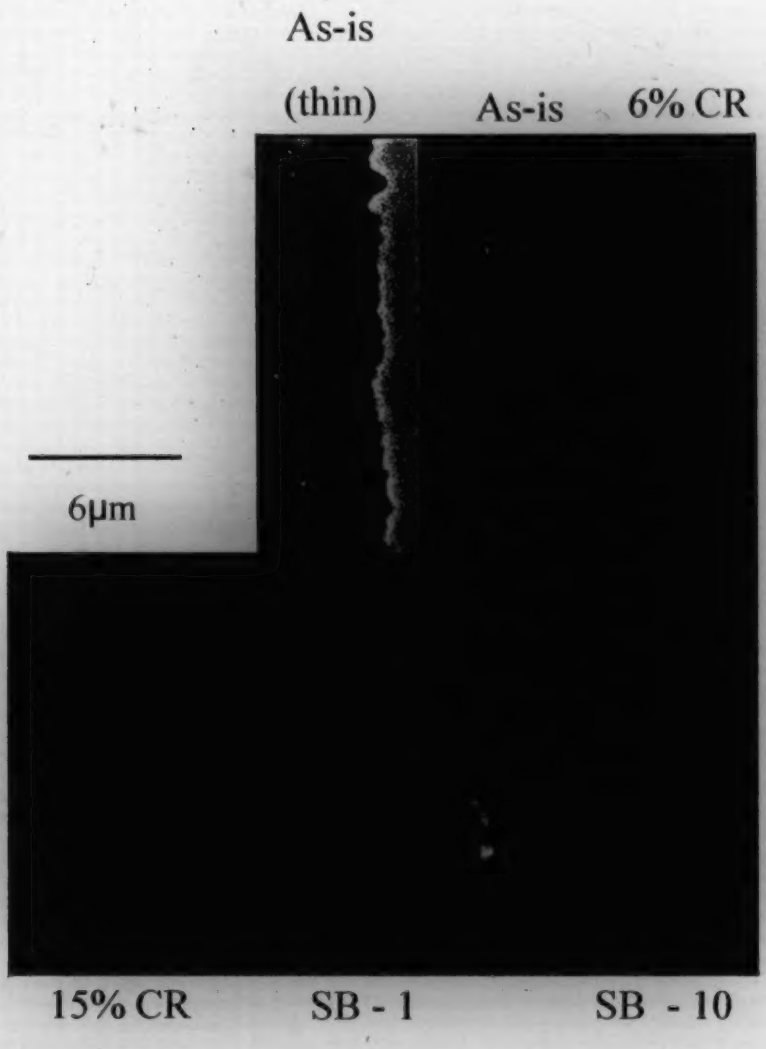


Figure 4-20. SEM Cross Section Images of 430 Specimens After 502 h of Oxidation.

For the sandblasted 1 pass specimen the bright Ni layer is quite thin and the epoxy surrounding the steel cross section, which is dark, is also visible. Several observations can be made from Figure 4-20. First, the appearance of the oxide scales for the as-is and rolled specimens are similar to one another, whereas the oxide scales on the sandblasted specimens, although continuous, are much less uniform due to the roughness of the sandblasted surface. Also, the amount of spinel, which is slightly darker than the chromia, varies depending on the surface treatment. The thin as-is specimen has significantly more spinel than the other samples, whereas for the sandblasted specimens, the spinel is less continuous and more difficult to distinguish from the chromia. The spinel on the thin as-is specimen also appears to be much more continuous than the spinel on the thick specimens.

For the thin as-is specimen, the entire oxide scale did not have the appearance of the image presented in Figure 4-20. In fact, for this specimen, there were two distinct oxide morphologies, illustrated in Figure 4-21, which alternated along the length of the specimen.

Figure 4-21. Two Distinct Regions of the Oxide Scale on the 430 Thin As-Is Specimen. a) Protective Oxide; b) Evidence of Spalling.

From the images presented in Figure 4-20, the oxide thickness was determined by taking measurements at 12 evenly spaced points, ignoring the largest and smallest values, and calculating the average of the remaining 10 measurements. The error for each thickness value was determined by taking the standard deviation of the 12 measured values. The results of this analysis are listed in Table 4-10.

Table 4-10. Oxide Layer Thickness for 430 Specimens.

| Surface Treatment | Oxide Layer Thickness (μm) | |
|---|---|---|
| | Mass Gain | SEM Image |
| As-is (thin) | 0.90 | 2.58 ± 0.15 |
| As-is | 0.57 | 1.62 ± 0.27 |
| Rolled 6% | 0.62 | 1.71 ± 0.18 |
| Rolled 15% | 0.69 | 2.12 ± 0.25 |
| Sandblasted 1 pass | 0.85 | 1.39 ± 0.73 |
| Sandblasted 10 passes | 0.62 | 2.31 ± 0.95 |

In Table 4-10, the oxide thickness from the mass gain data was determined by dividing the experimentally determined mass gain value by the measured surface area of the specimen, and then dividing the result by 5.21 g/cm$^3$, which is the density of chromia (Shackelford & Alexander. 2001). The density of chromia was used since it was difficult to determine accurately the thickness of chromia and spinel, especially for the sandblasted specimens. Also, the difference between the density of chromia and spinel is relatively small (the density of spinel is 4.93 g/cm$^3$) (International Center for Diffraction Data. 1996).

From Table 4-10, both the mass gain and SEM results indicate that, in general, the oxide layer on the treated specimens was thicker than on the as-is specimen, and that the oxide layer of the thin as-is specimen was much thicker than that on all the other specimens. The oxide layer thicknesses obtained from the SEM images were greater than those obtained from the weight gain results by a factor of 2 to 3. There are several reasons for this. First, the measurements of the oxide layer thickness were taken from the metal/oxide interface to the outer edge of the spinel particles, which were not continuous. Also, the density of spinel is lower than that of chromia, which would have resulted in an underestimate of the oxide layer thickness using the weight gain data. Finally, the value for the density of chromia is a bulk density value, and the oxide layer may not be compact. It is likely that the actual density of the chromia scale is lower than the bulk density value.

#### *4.3.3.2 EDX Analysis*

For all the cross section specimens, EDX spectra were collected from the outer region of the oxide layer. From quantitative analysis of the spectra, Cr:Mn and Cr:Fe ratios in the spinel phase were determined. The results are presented in Table 4-11.

Table 4-11. Cr:Mn and Cr:Fe Ratios From Quantitative EDX Analysis of the Spinel for 430 Specimens.

| Surface Treatment | Cr:Mn | Cr:Fe |
|---|---|---|
| As-Is | 2.3 | 13.3 |
| As-Is (Thin) | 1.8 | 18.2 |
| Rolled 6% | 2.3 | 16.5 |
| Rolled 15% | 1.7 | 10.9 |
| Sandblasted 1 Pass | 1.7 | 7.6 |
| Sandblasted 10 Passes | 1.8 | 10.3 |

Table 4-11 indicates that the relative amounts of Cr and Mn in the spinel phase were similar for all treatment conditions, with the relative amount of Mn slightly lower in the as-is and rolled 6% specimens. It is also clear that the relative amount of Fe in the spinel was highest for the sandblasted specimens and lowest for the thin as-is specimen.

#### *4.3.3.3 EDX Linescans*

EDX linescans were collected for the thin as-is, as-is, 15% rolled, and 10 pass sandblasted specimens and are shown in Figures 4-22 through 4-25, respectively.

In Figure 4-22a, the linescan shows that Fe was present in the steel but depleted in the oxide layer. Cr was present in the steel and enriched in the oxide layer, with the amount of Cr in the inner oxide higher than that in the outer oxide. Mn was present mainly in the outer oxide. Si had segregated to the metal/oxide interface, likely forming a thin layer of $SiO_2$.

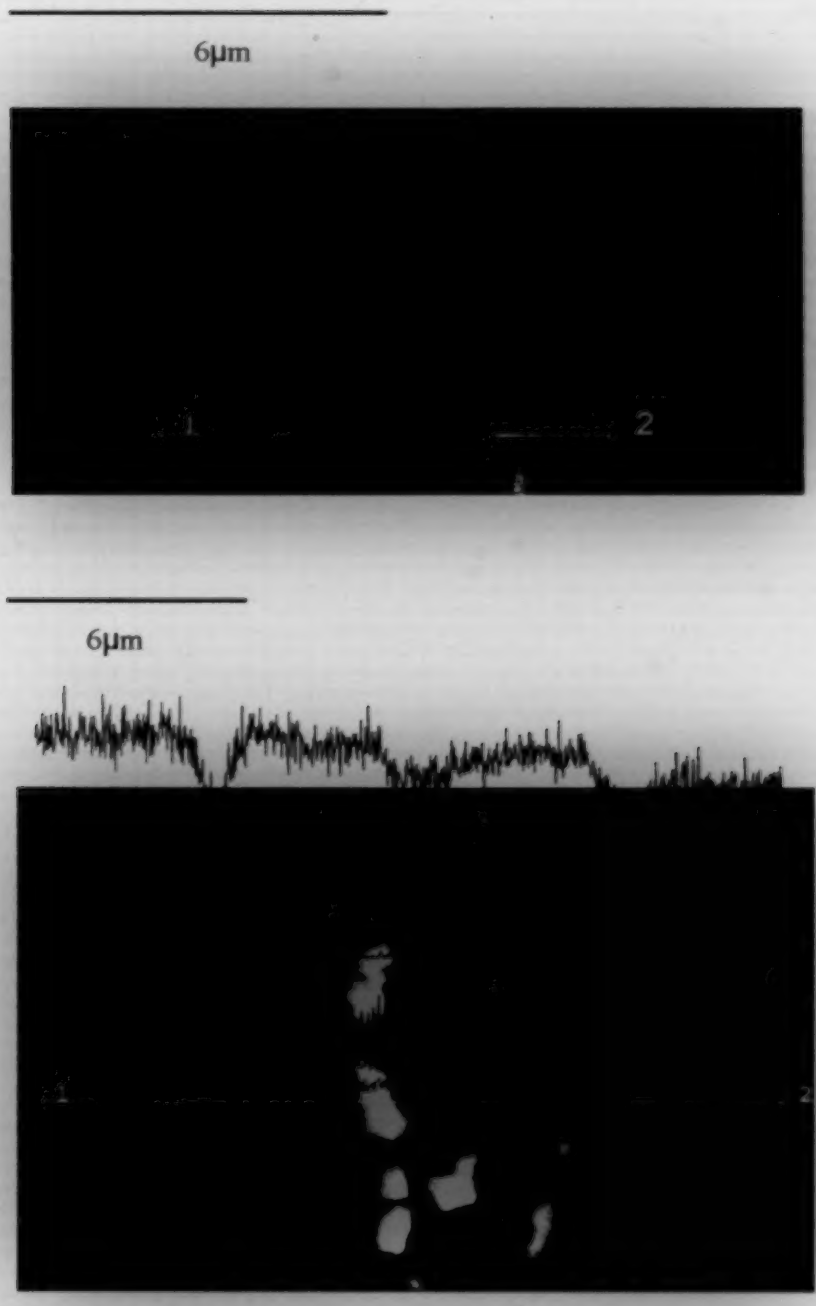


Figure 4-22. EDX Linescans for 430 Thin As-Is Cross Section After 502 h. a) Protective Oxide; b) Spalled Region.

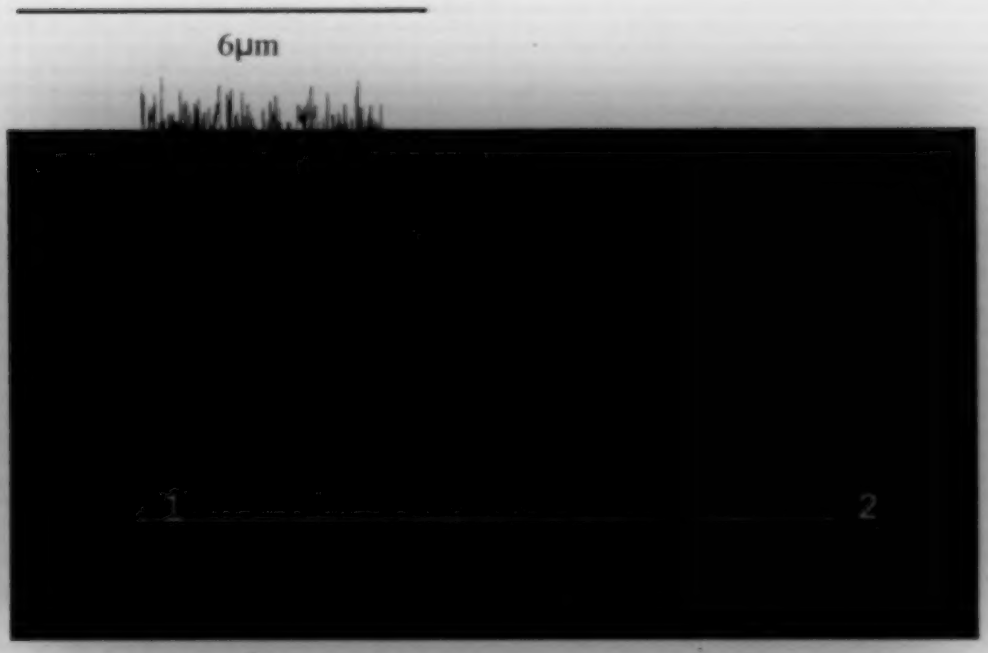


Figure 4-23. EDX Linescan for 430 As-Is Cross Section After 502 h.

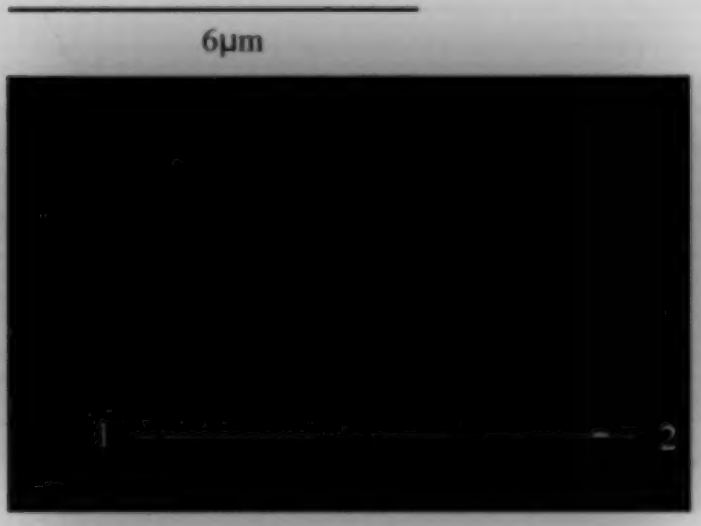


Figure 4-24. EDX Linescan for 430 Rolled 15% Cross Section After 502 h.

Figure 4-25. EDX Linescan for 430 Sandblasted 10 Passes Cross Section After 502 h.

The linescan in Figure 4-22b is slightly more complicated. Again, Fe was depleted in the oxide relative to its level in the bulk; however, a small amount of Fe was present in the oxide. As in Figure 4-22a, Cr was enriched in the oxide layer; however, the Cr level fluctuated throughout the oxide scale. Unlike Figure 4-22a, the Mn distribution has several peaks within the oxide scale. These results support the notion that spalling and subsequent repair of the oxide occurred.

The linescans presented in Figures 4-23 through 4-25 have a similar appearance to that in Figure 4-22a. No significant difference in the distribution of Cr, Fe, Si, Mn, or O in the oxide layer between the different treatment conditions was observed.

### 4.3.4 SIMS Results

#### *4.3.4.1 Native Oxide*

In order to study the native oxide on the 430 specimens prior to oxidation at 800°C, SIMS analysis was carried out. The resulting depth profile is displayed below in Figure 4-26.

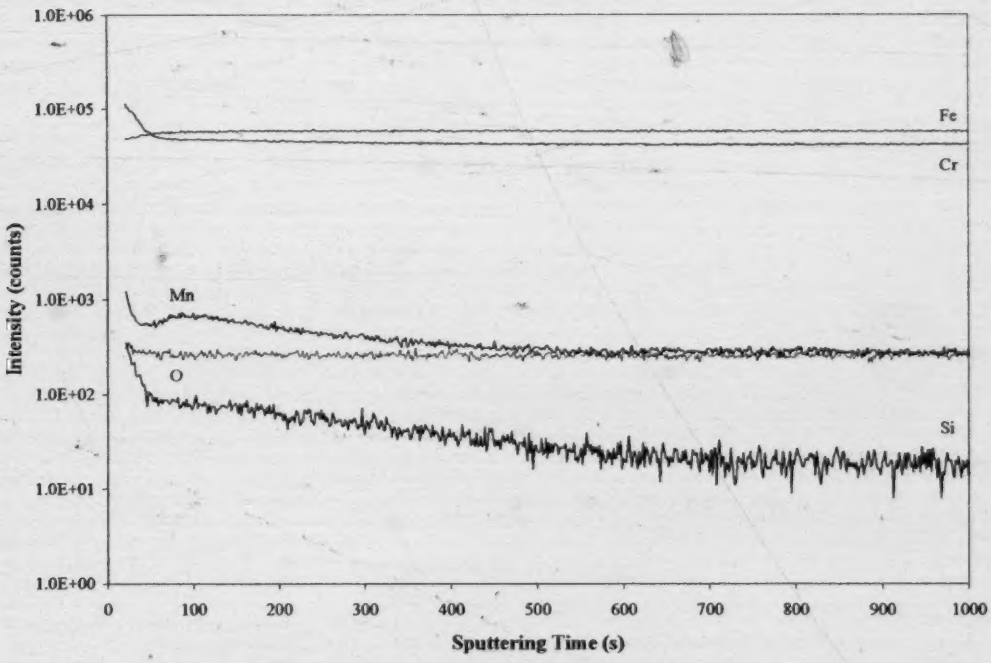


Figure 4-26. SIMS Depth Profile of 430 Native Oxide.

From Figure 4-26, it can be seen that Cr was enriched and Fe was depleted in the native oxide relative to their respective levels in the bulk of the steel. Mn was enriched at the surface of the oxide layer, and also segregated to the metal/oxide interface. Surface enrichment of Si was also present.

#### *4.3.4.2 Oxidized Specimens*

In order to study the early stages of oxide formation, SIMS analysis was carried out on as-is, rolled 15%, and sandblasted 10 passes 430 specimens that were oxidized for 15 minutes at 800°C. The resulting profiles are displayed in Figure 4-27.

From the profiles, it is clear that the same trends are observed for all specimens. Iron was depleted in the oxide layer relative to the amount present in the bulk of the steel, and Cr was enriched throughout the oxide scale. Manganese segregation to the surface of the oxide was observed, with the amount of Mn present decreasing throughout the oxide layer and into the bulk of the steel. Silicon was also present at the surface of the oxide but the majority of the Si was segregated to the metal/oxide interface. For the sandblasted 10 passes specimen, the Al is due to the presence of $Al_2O_3$ particles used in sandblasting that were embedded in the surface of the specimen.

a)

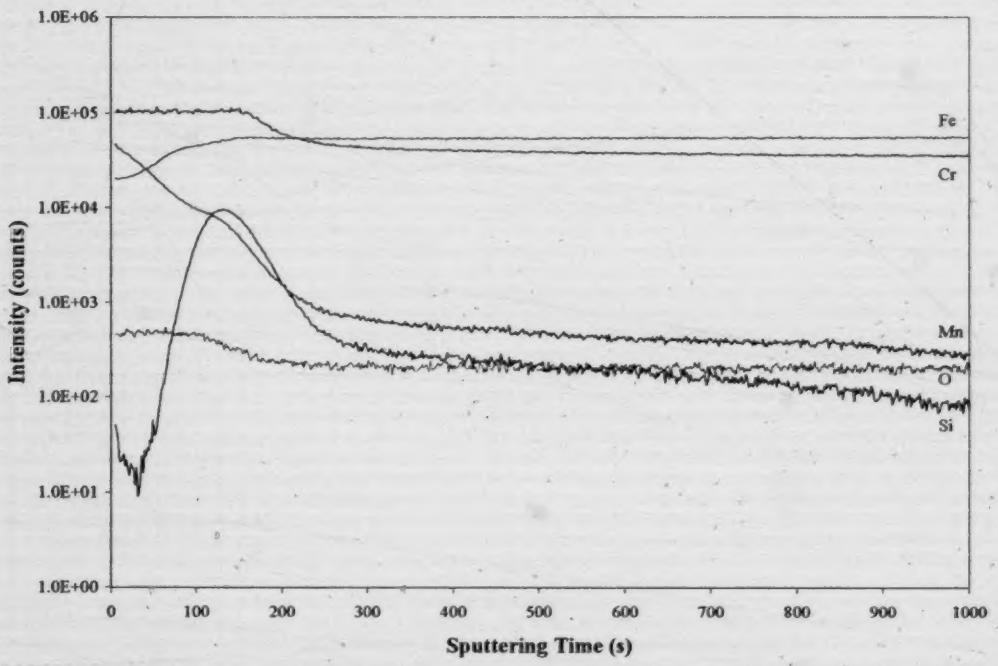

b)

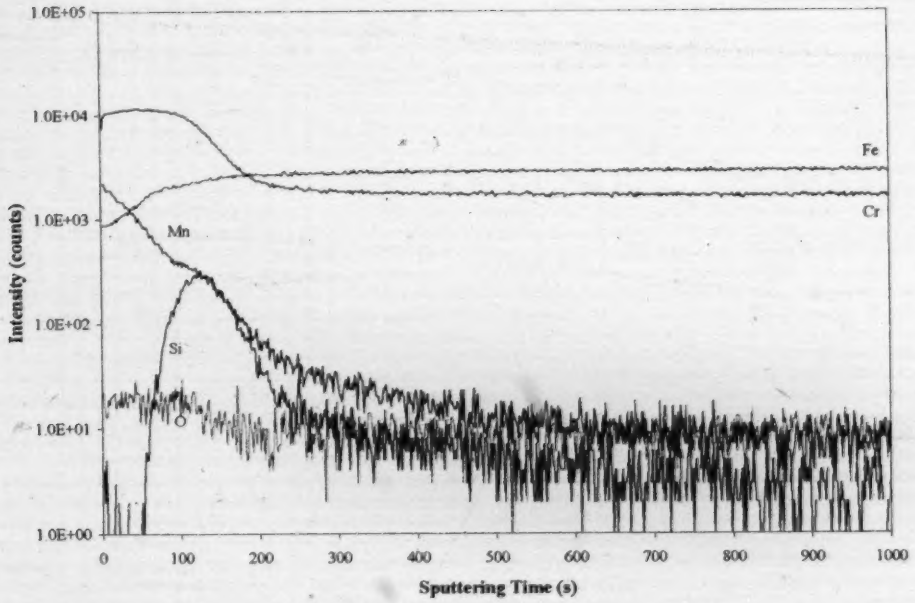


c)

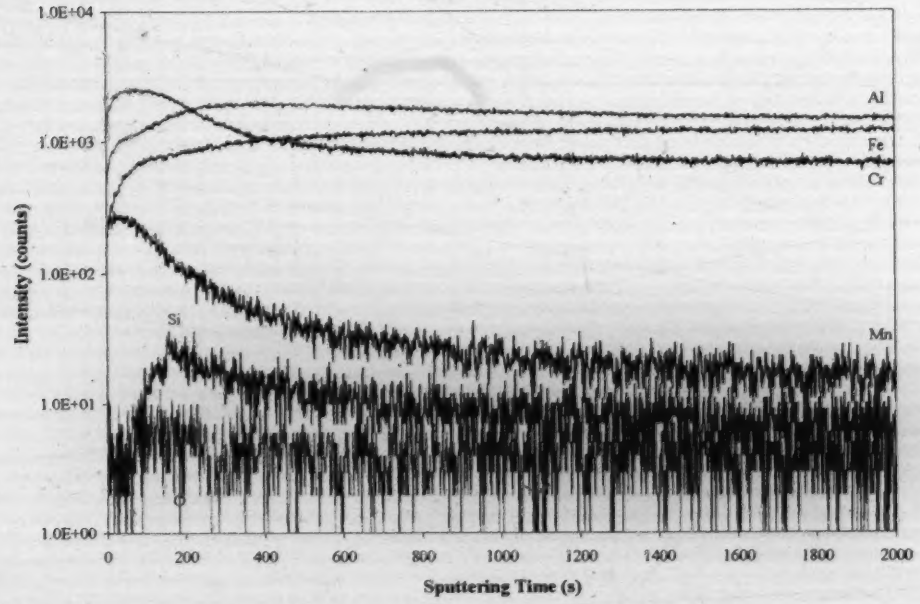


Figure 4-27. SIMS Depth Profiles of 430 Specimens Oxidized for 15 Minutes at 800°C. a) As-Is; b) Rolled 15%; c) Sandblasted 10 Passes

One observation than can be made from Figure 4-27c is that the profile for the sandblasted 10 passes specimen appears more 'rounded' than the other two profiles. This is due to the averaging affect caused by the increased roughness of the sandblasted specimen surface. Because of this, the distribution of the elements is not as well defined as for the other two specimens.

#### *4.3.4.3 Estimated Scale Thickness*

Although the distribution of elements through the oxide layer is similar for all the 430 specimens, the thickness of the oxide scale varies. In order to obtain an estimate for the thickness of the oxide layer, a conversion of 0.2 nm for each second of sputtering time was used. Two methods were used to obtain an approximate oxide layer thickness from the SIMS depth profiles. In the first method, an exponential decay best fit line was determined for the Cr profile, and the end of the oxide layer was defined as the point where the Cr content increased above two standard deviations from the mean, which corresponded to the bulk level reached at the end of the profile. For the second method, an average Cr concentration was determined for the initial plateau, or the Cr concentration in the oxide layer, and an average Cr concentration was calculated for the final plateau, or the Cr concentration in the bulk. The metal/oxide interface was defined as the Cr concentration corresponding to the midpoint between the two values. The results of this analysis are displayed below in Table 4-12.

Table 4-12. Estimated Scale Thicknesses Corresponding to 430 SIMS Depth Profiles.

| Treatment | Oxidation Conditions | Approximate Scale Thickness (nm) | | Si Peak (nm) |
|---|---|---|---|---|
| | | Method 1 | Method 2 | |
| As-is | none | 38 | - | - |
| As-is | 800°C, 0.25 h | 81 | 38 | 26 |
| Rolled 15% | 800°C, 0.25 h | 73 | 27 | 25 |
| Sandblasted 10 passes | 800°C, 0.25 h | 203 | 49 | 32 |

For the native oxide, method 2 was not used as the oxide layer was too thin to be able to determine an average Cr concentration for the oxide layer. From Table 4-12, although the two methods of determining oxide layer thickness give different values, the trend is the same for all specimens. The oxide thickness for the sandblasted specimen is the largest, followed by the as-is specimen and finally the rolled specimen. The position of

the Si peak, which should correspond to the metal/oxide interface, follows the same trend. Table 4-12 also shows that the values for oxide layer thickness determined using method 2 are closer to the Si peak positions than the values determined using method 1. It seems that method 2 gives a more accurate estimate of the oxide layer thickness than method 1. Method 1 seems to overestimate the oxide layer thickness, possibly because it would be more easily affected by the difference in sputtering rates of the different elements. This is particularly evident for the sandblasted specimen for which the averaging effect of the rough surface has already been discussed. For the oxidized specimens, using the Si peak as an indication of the oxide thickness seems to be the best way of determining oxide thickness as it is the easiest method and is not affected as much by sputtering effects as either method 1 or 2, which focus on the Cr profile.

### 4.3.5 XPS Analysis

#### *4.3.5.1 Native Oxide*

In order to determine the chemical state of the elements present in the oxide scale, i.e., whether they were present in the metallic or oxide form, XPS analysis was carried out. Figure 4-28 shows the plots for Cr, Fe, Mn, and Si.

From Figure 4-28a, it can be seen that the Cr at the surface of the oxide was all in the oxide form. As sputtering time increased (i.e., moving through the oxide layer), a small metal Cr peak was observed in addition to the oxide peak. Finally, all the Cr was present in the metal form, indicating that the steel substrate had been reached.

Figure 4-28b shows a slightly different situation for the Fe peak. At the surface of the oxide, the Fe was present in both oxide and metal forms. As sputtering time increased, the oxide peak disappeared and the metal peak increased in height, indicating that the steel substrate had been reached. The presence of the Fe oxide peak at the surface indicates that a small amount of Fe has been incorporated into the oxide scale, while the Fe metal peak indicates the native oxide may not completely cover the steel surface. In comparing the Fe and Cr profiles, the Fe transition to metal form occurs much more rapidly than the Cr transition to metal form. However, this is most likely a sputtering effect resulting from sputtering being carried out at a 45° angle to the specimen surface.

a)

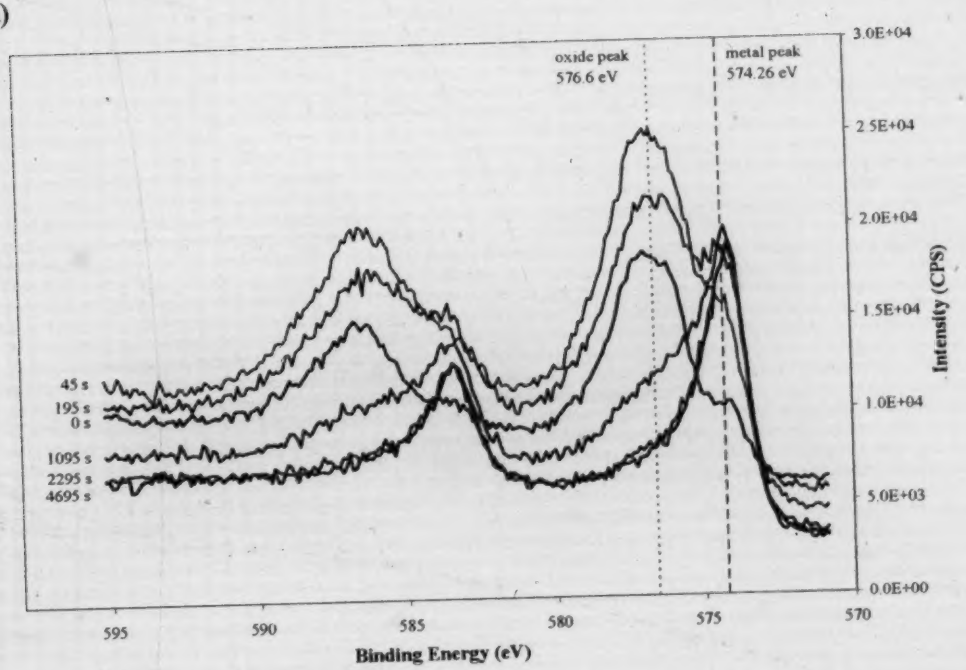
oxide peak
576.6 eV
metal peak
574.26 eV
45 s
195 s
0 s
1095 s
2295 s
4695 s
3.0E+04
2.5E+04
2.0E+04
1.5E+04
1.0E+04
5.0E+03
0.0E+00
Intensity (CPS)
595
590
585
580
575
570
Binding Energy (eV)

b)

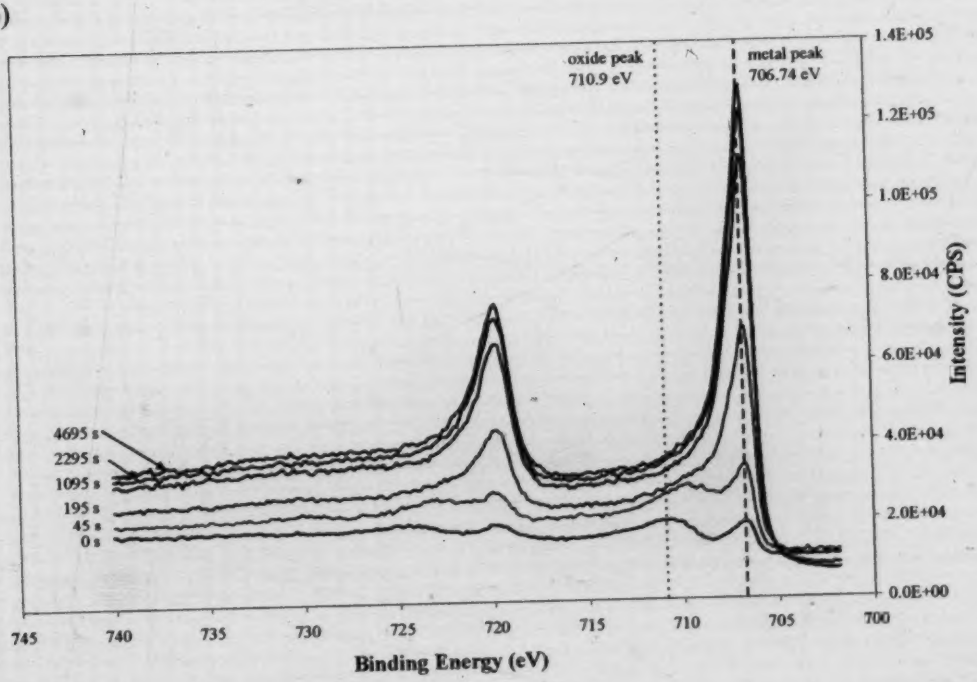
oxide peak
710.9 eV
metal peak
706.74 eV
4695 s
2295 s
1095 s
195 s
45 s
0 s
1.4E+05
1.2E+05
1.0E+05
8.0E+04
6.0E+04
4.0E+04
2.0E+04
0.0E+00
Intensity (CPS)
745
740
735
730
725
720
715
710
705
700
Binding Energy (eV)

c)

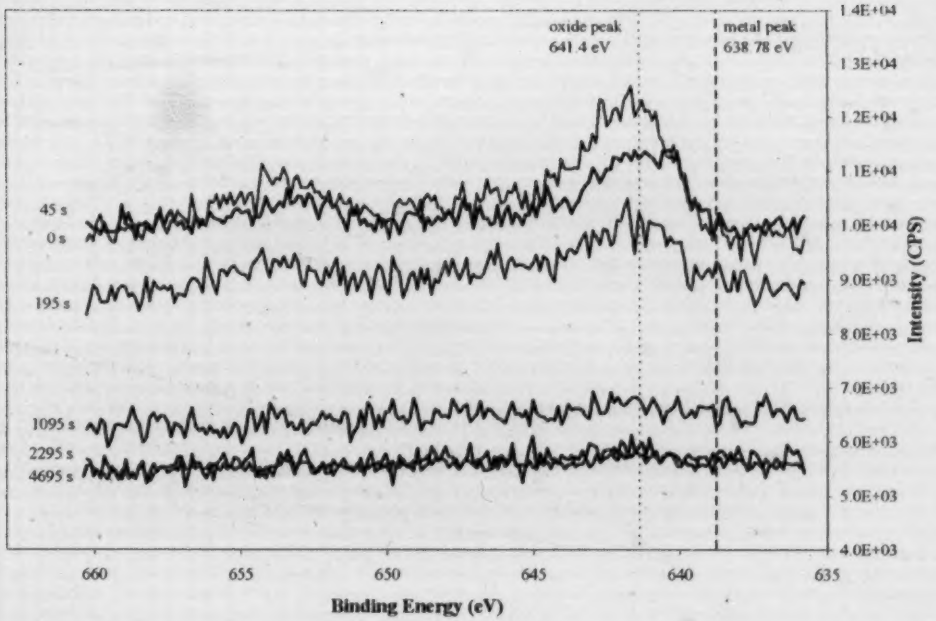


d)

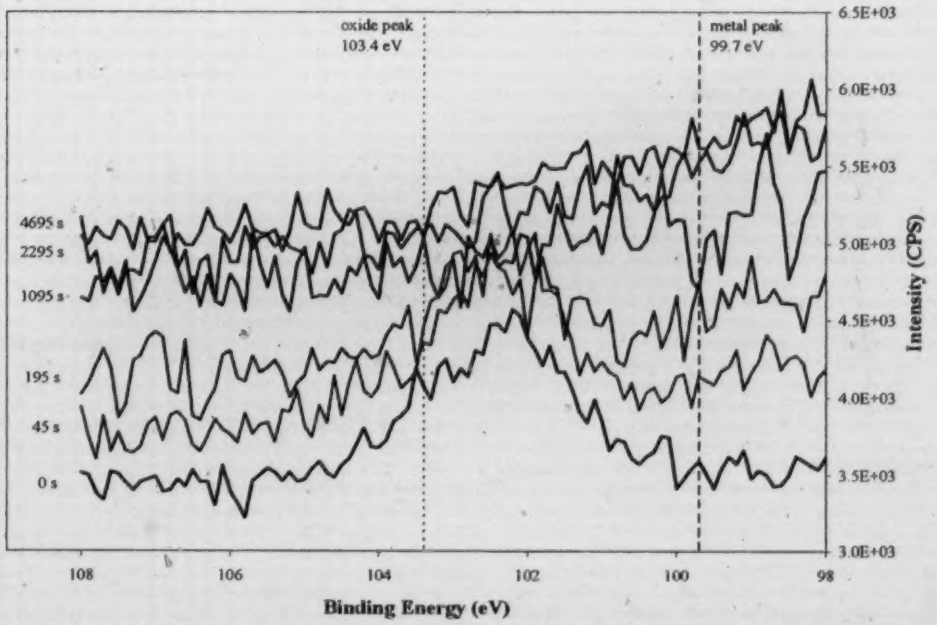


Figure 4-28. XPS 2p Peak Plots for 430 Native Oxide. a) Cr; b) Fe; c) Mn; d) Si.

In Figure 4-28c, it is clear that Mn in the oxide form was segregated to the outer portion of the oxide scale. Although Mn is also present in the steel, the Mn metal peak is not observed. This could be because the level is too small compared to the other elements being analyzed by XPS, or it could be because a Mn depleted zone is present in the steel just below the metal/oxide interface.

Figure 4-28d indicates that, similar to Mn, Si was only present in oxide form, and only in the outer region of the oxide layer.

#### *4.3.5.2 Oxidized Specimens*

Due to the similarites in the SIMS depth profiles between the as-is and rolled specimens as well as the averaging effect that was observed in the profile of the sandblasted specimen, XPS depth profiling was only carried out on the as-is specimen. The 430 as-is specimen was oxidized for 15 minutes at 800°C. The XPS peak plots for Cr, Fe, Mn, and Si are shown in Figure 4-29.

From Figure 4-29a, it can be seen that all the Cr at the surface of the oxide was in the oxide form. The Cr oxide peak remained as sputtering continued through the oxide layer. Then, a small Cr metal peak was observed. The oxide peak decreased in height and the metal peak became stronger, indicating the steel substrate was reached. The transition from oxide to metal is not as clear as for the native oxide. This is because the oxide layer on the oxidized specimen is much thicker than the native oxide. With an increase in the depth of the sputtering crater, it becomes more likely that the analysis includes the sides of the crater, which have not been sputtered as quickly as the crater center and may still contain some oxide.

a)

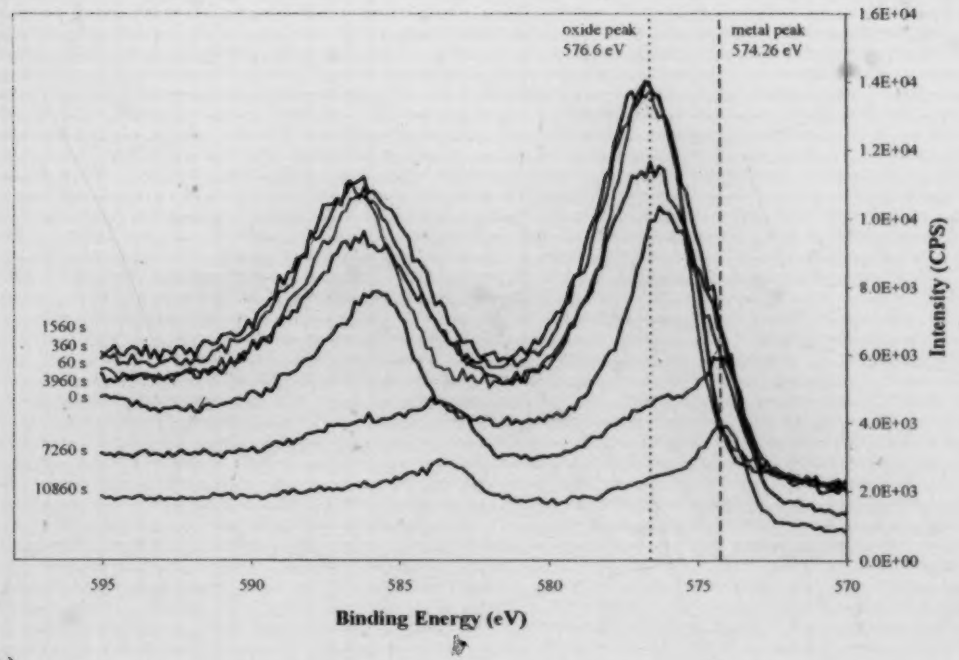
oxide peak
576.6 eV
metal peak
574.26 eV
1560 s
360 s
60 s
3960 s
0 s
7260 s
10860 s
1.6E+04
1.4E+04
1.2E+04
1.0E+04
8.0E+03
6.0E+03
4.0E+03
2.0E+03
0.0E+00
Intensity (CPS)
595
590
585
580
575
570
Binding Energy (eV)

b)

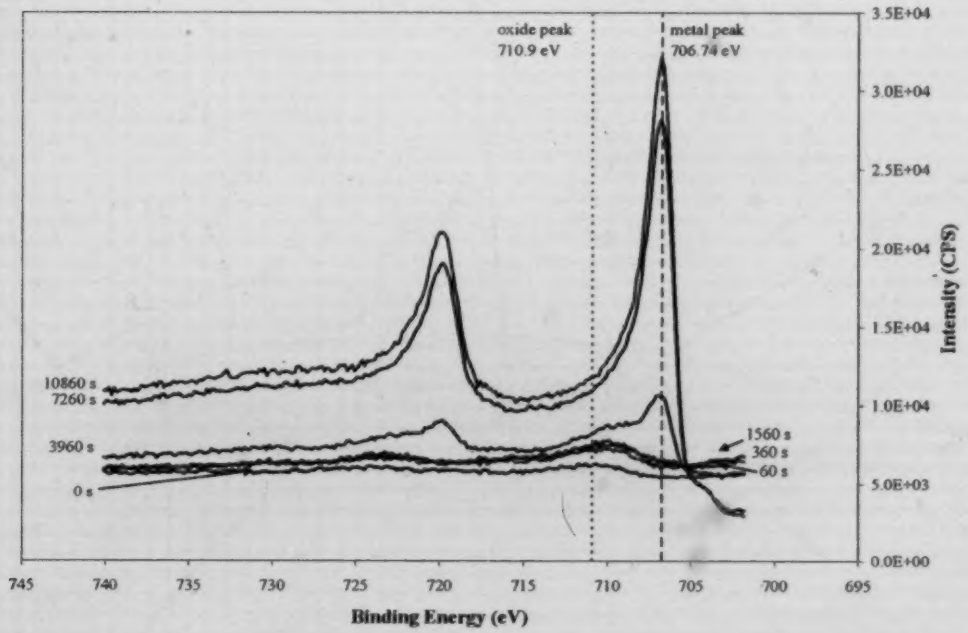
oxide peak
710.9 eV
metal peak
706.74 eV
10860 s
7260 s
3960 s
0 s
1560 s
360 s
60 s
3.5E+04
3.0E+04
2.5E+04
2.0E+04
1.5E+04
1.0E+04
5.0E+03
0.0E+00
Intensity (CPS)
745
740
735
730
725
720
715
710
705
700
695
Binding Energy (eV)

c)

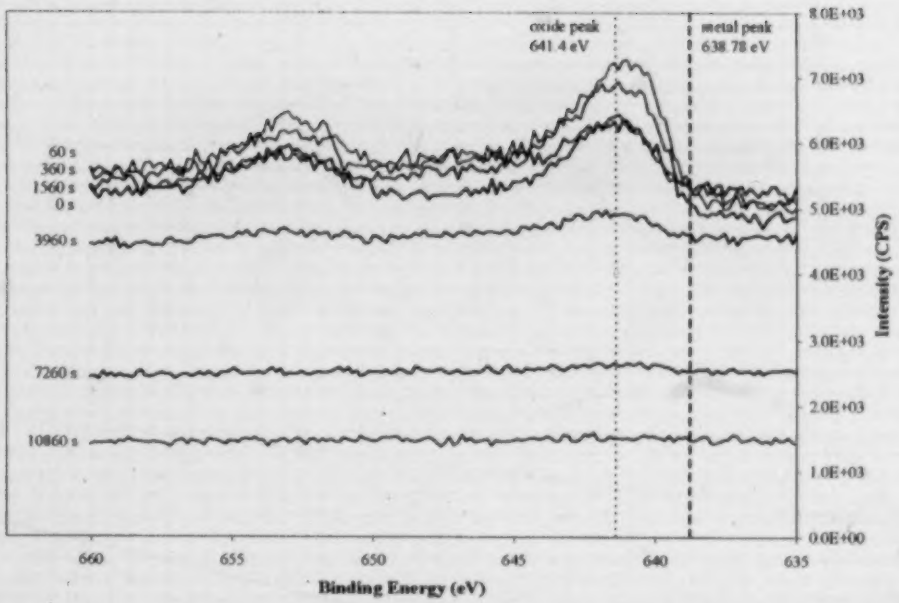


d)

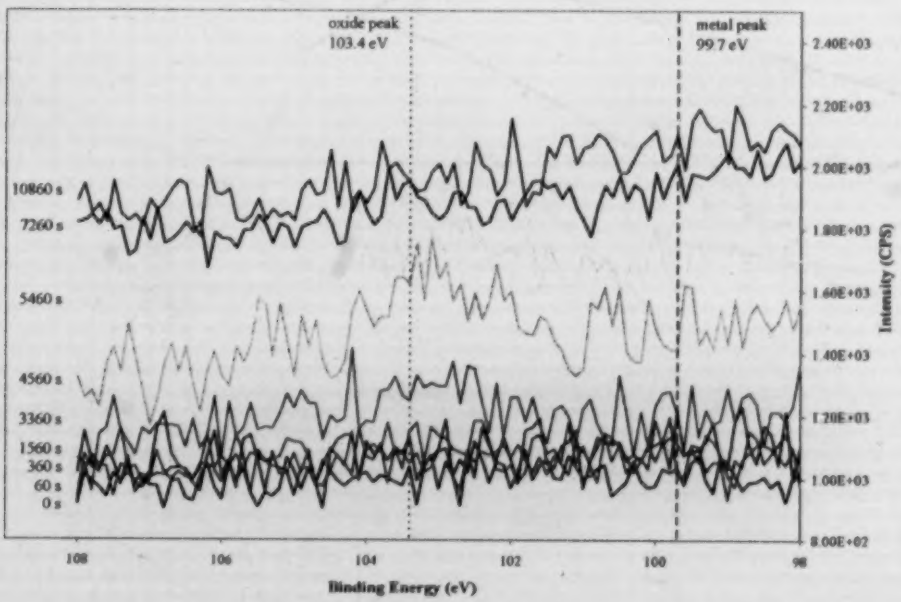


Figure 4-29. XPS 2p Peak Plots for 430 As-Is Specimen Oxidized for 15 Minutes at 800°C. a) Cr; b) Fe; c) Mn; d) Si.

Figure 4-29b shows that initially, an Fe oxide peak was present, indicating that some Fe in oxide form was incorporated in the oxide scale. This peak remained and, after some time, an Fe metal peak also appeared. Then, the oxide peak disappeared and the metal peak became larger. As for the native oxide, the transition of Fe from the oxide to the metal form occured more rapidly than for Cr. Again, this is most likely a sputtering effect. If the Fe peaks in Figure 4-29b are compared with the Si peaks in Figure 4-29d, the Fe oxide peak is present up to and including a sputtering time of 3960 s, and the Si oxide peak indicating the metal/oxide interface appears at a sputtering time of 3360 s. This suggests that the iron in the oxide scale is in oxide form, and the Fe in the bulk of the steel is in the metal form.

Figure 4-29c indicates that Mn was present in its oxide form throughout the oxide; however, the peaks are stronger in the outer region of the oxide scale, indicating that the Mn was segregated to the outer portion of the oxide scale. Manganese was not present in the metal form below the oxide layer, suggesting either a depleted zone or simply that the amount present was relatively small.

For Si, there was a small oxide peak present prior to sputtering, indicating the presence of Si in its oxide form at the surface of the oxide layer. Figure 4-29d also indicates that the Si oxide peak appeared in the middle of the depth profile, indicating that a layer of $SiO_2$ had formed at the metal/oxide interface.

### 4.3.6 Summary of 430 Results

The mass gain data presented in Section 4.1 indicated that the mass gain due to oxidation for the 430 specimens was larger for the treated specimens than for the as-is specimen. The exception was the thin as-is specimen, which had a significantly larger mass gain than any of the other specimens. These results were confirmed by measurements of the oxide thickness from SEM cross section images. For the thin as-is specimen, the cross section images revealed regions in the oxide where cracking and subsequent repair of the oxide scale had occurred. This likely contributed to the higher mass gain for the thin as-is specimen. For the rolled specimens, plan view SEM images revealed the presence of bright clumps of fast growing oxide. EDX analysis identified the presence of impurity elements in the oxide clumps, suggesting they were formed following contamination of

the specimens by the rolling mill. These regions of fast growing oxide may have contributed to the higher mass gain of the rolled specimens.

For all the 430 specimens, the same oxide layer morphology was observed. XRD analysis indicated that two oxide phases were present: $Cr_2O_3$ and $(Mn,Cr)_3O_4$ spinel. EDX linescans of the oxidized cross section specimens revealed that the Mn was segregated to the outer region of the oxide layer and that Cr was present throughout the oxide layer, although more Cr was found in the inner region of the oxide layer. Similar trends were observed by SIMS and XPS analysis, with XPS analysis confirming that the Mn and Cr were both in their oxide form. It is clear that the chromia forms the inner portion of the oxide layer and that spinel particles are present in the outer region of the scale. From the EDX linescans, Fe was depleted in the oxide scale relative to the amount present in the bulk of the steel. However, XPS results suggested that Fe in its oxide form was present throughout the oxide layer. This indicates that Fe is being incorporated into the spinel phase, and that Fe in its oxidized form is outwardly diffusing through the chromia, most likely at the chromia grain boundaries. Additionally, the EDX linescans and SIMS depth profiles revealed that for all specimens, Si had segregated to the metal/oxide interface. XPS analysis indicated that the Si was in its oxide form and had formed a thin layer of $SiO_2$ beneath the oxide scale. The agreement between the short term and long term results for oxidized specimens suggests that there is no change in the oxidation behaviour within the time intervals studied.

Although the same oxide phases were identified for all specimens, the relative amounts of chromia and spinel varied depending on the treatment condition. XRD analysis indicated that for all specimens, the amount of spinel relative to chromia increased with increasing oxidation time. In addition, after 502 h, the as-is specimen had the largest amount of spinel relative to chromia and the specimens that had undergone surface treatment had less spinel relative to chromia. The thin as-is specimen had significantly more spinel relative to chromia than its thick counterpart, which may have contributed to the higher mass gain of the thin specimen. The relatively large amount of spinel compared to chromia for the thin as-is specimen was clearly visible in the SEM cross section image.

EDX analysis of the overall oxide scale composition for the 430 specimens indicated that the amount of Mn relative to Cr increased with increasing oxidation time, which agrees with the XRD results showing an increase in the relative amount of spinel with increasing

oxidation time. The highest amount of Mn relative to Cr was found for the thin as-is specimen, then the as-is specimen, the rolled specimens, and finally the sandblasted specimens. EDX analysis of the spinel region of the oxide scale from the oxidized cross section specimens indicated that the amount of Mn relative to Cr in the spinel was similar for all specimens. Therefore, the EDX results correlate with the XRD results showing that the most spinel was present in the thin as-is specimen, followed by the as-is specimen and then the treated specimens.

EDX analysis of the overall oxide scale composition also indicated that there was a reduced amount of Fe relative to Cr for the as-is and rolled specimens, and that a higher amount of Fe relative to Cr was present in the sandblasted specimens. EDX analysis of the spinel region of the oxide scale showed that the amount of Fe relative to Cr was higher for the sandblasted specimens than the other specimens. This suggests that more Fe had been incorporated into the spinel on the sandblasted specimens. Some of the Fe from the EDX analysis may have come from the steel substrate in areas where the oxide scale was thinner, as the cross section images revealed that the oxide thickness was much less uniform for the sandblasted specimens than for the as-is and rolled specimens. Images of the oxidized cross sections confirm this supposition. Even though the oxide scale was rougher than for the other specimens, there was no obvious evidence of cracking or spalling of the oxide scale, which may have been responsible for the Fe enrichment. The oxide scale on the thin as-is specimen had the highest amount of Fe relative to Cr. However, EDX analysis of select regions of the plan view image indicated that the Fe enrichment appeared to be confined to regions of the scale where spalling had occurred.

Finally, XPS and SIMS analysis of the native oxide on the 430 specimens indicated several differences from the oxide formed at 800°C. The Mn and Fe distributions were similar in the two types of oxide scales; however, the Mn and Si distributions were different. For the native oxide, Mn was present at the surface of the oxide, but also segregated to the metal/oxide interface, whereas for the specimens oxidized at 800°C, the Mn was segregated to the surface of the oxide layer. For the native oxide, Si was segregated to the surface of the oxide; however, the Si had segregated to the metal/oxide interface for the specimens oxidized at 800°C.

## 4.4 434 Results

### 4.4.1 XRD Results

#### *4.4.1.1 XRD Spectra*

XRD analysis was used to identify the phases present in the oxide layers that formed on the 434 specimens after 502 h of oxidation at 800°C. Figure 4-30 is a comparison of the XRD spectra obtained for the different treatments. From Figure 4-30, it can be seen that the same oxide phases, $Cr_2O_3$ and $(Cr,Mn)_3O_4$, were present in the oxide layer formed on all the 434 specimens. However, the relative heights of the chromia and spinel peaks vary depending on the treatment condition, indicating that the type of surface treatment has had an effect on the relative amounts of spinel and chromia formed during oxidation at 800°C.

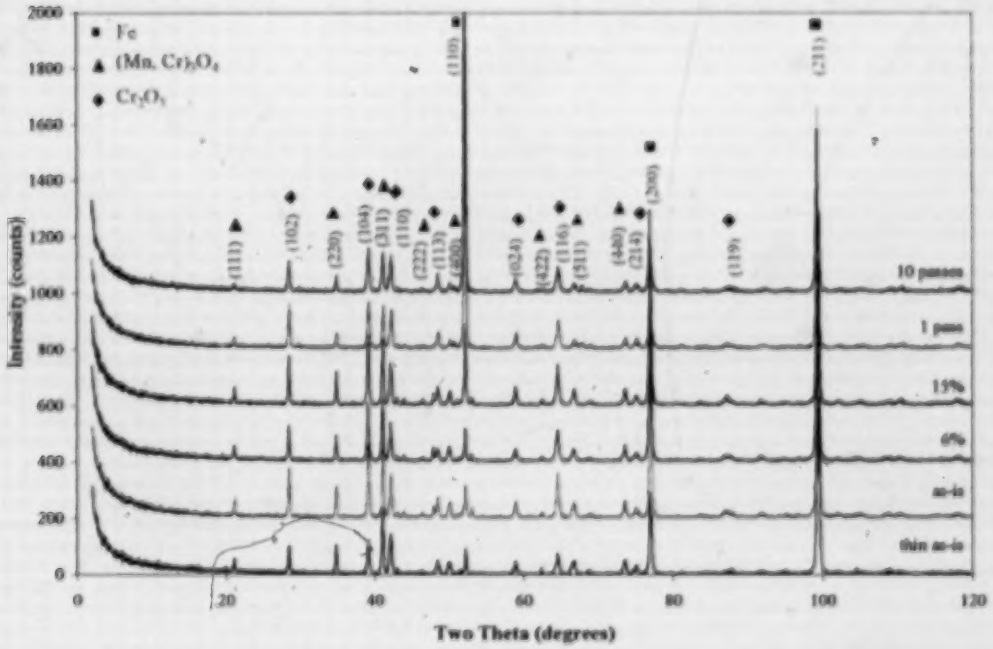


Figure 4-30. Comparison of the 434 XRD Spectra After 502 h of Oxidation.

### *4.4.1.2 Relative Peak Intensities*

In order to analyze the XRD spectra presented in Figure 4-30, the relative peak heights of the five most intense peaks for each oxide phase were determined and the values were compared with the expected peak intensity values from the JCPDS diffraction cards. The results of this analysis are presented in Tables 4-13 and 4-14.

Table 4-13 indicates that for the chromia, a slight (012) preferred orientation was present for all specimens after 50 h. After 502 h of oxidation, for all specimens except for the thin as-is specimen, the (012) preferred orientation was still present. For the thin as-is specimen, a (104) preferred orientation was observed after 502 h. For the spinel phase, the as-is and rolled specimens, after 50 h, exhibited (111) preferred orientation. After 502 h, the preferred orientation no longer existed. For the sandblasted specimens, after 50 h the spinel peaks were not very clear. However, after 502 h, all the spinel peaks were observed with no preferred orientation. No preferred orientation was observed for the thin as-is specimen after 502 h.

Table 4-13. Relative Intensities of Chromia X-Ray Peaks for 434 Specimens.

| | | $Cr_2O_3$ (PDF#38-1479) | | | | | | | | | |
|---|---|---|---|---|---|---|---|---|---|---|---|
| | | 50 h | | | | | 502 h | | | | |
| | **Peak Order** | 1 | 2 | 3 | 4 | 5 | 1 | 2 | 3 | 4 | 5 |
| | **(hkl) Index** | (104) | (110) | (116) | (012) | (024) | (104) | (110) | (116) | (012) | (024) |
| | **Card Intensity (%)** | 100 | 93 | 87 | 73 | 38 | 100 | 93 | 87 | 73 | 38 |
| **Treatment** | As-is (thin) | - | - | - | - | - | 87 (2) | 100 (1) | 53 (4) | 72 (3) | 32 (5) |
| | As-is | 100 (1) | 38 (4) | 47 (3) | 62 (2) | 21 (5) | 100 (1) | 56 (4) | 62 (3) | 68 (2) | 22 (5) |
| | Rolled 6% | 100 (1) | 30 (4) | 31 (3) | 48 (2) | 18 (5) | 100 (1) | 63 (2) | 53 (4) | 60 (3) | 21 (5) |
| | Rolled 15% | 100 (1) | 27 (4) | 27 (3) | 50 (2) | 15 (5) | 100 (1) | 59 (3) | 57 (4) | 68 (2) | 26 (5) |
| | Sandblasted 1 pass | 100 (1) | 53 (3) | 49 (4) | 78 (2) | 25 (5) | 100 (1) | 80 (3) | 61 (4) | 93 (2) | 34 (5) |
| | Sandblasted 10 passes | 100 (1) | 54 (3) | 39 (4) | 66 (2) | 26 (5) | 100 (1) | 79 (2) | 56 (4) | 69 (3) | 31 (5) |

Table 4-14. Relative Intensities of Spinel X-Ray Peaks for 434 Specimens.

| | | $(Cr, Mn)_3O_4$ (PDF#33-0892) | | | | | | | | | |
|---|---|---|---|---|---|---|---|---|---|---|---|
| | | 50 h | | | | | 502 h | | | | |
| | **Peak Order** | 1 | 2 | 3 | 4 | 5 | 1 | 2 | 3 | 4 | 5 |
| | **(hkl) Index** | (311) | (220) | (440) | (511) | (111) | (311) | (220) | (440) | (511) | (111) |
| | **Card Intensity (%)** | 100 | 50 | 45 | 30 | 25 | 100 | 50 | 45 | 30 | 25 |
| **Treatment** | As-is (thin) | - | - | - | - | - | 100 (1) | 46 (2) | 21 (3) | 20 (4) | 20 (4) |
| | As-is | 100 (1) | 47 (3) | 41 (4) | 19 (5) | 52 (2) | 100 (1) | 41 (2) | 23 (4) | 19 (5) | 25 (3) |
| | Rolled 6% | 100 (1) | 49 (3) | 56 (2) | 31 (5) | 49 (3) | 100 (1) | 41 (2) | 27 (3) | 20 (5) | 22 (4) |
| | Rolled 15% | 100 (1) | 47 (2) | 27 (4) | 25 (5) | 42 (3) | 100 (1) | 52 (2) | 24 (5) | 25 (3) | 25 (3) |
| | Sandblasted 1 pass | 100 (1) | 32 (2) | - | - | - | 100 (1) | 35 (2) | 25 (3) | 18 (5) | 22 (4) |
| | Sandblasted 10 passes | 100 (1) | 82 (2) | - | - | - | 100 (1) | 43 (2) | 26 (3) | 20 (4) | 16 (5) |

#### *4.4.1.3 Peak Area Ratios*

In order to determine the relative amounts of chromia and spinel phases present in the oxide layer of the 434 specimens, spinel to chromia peak area ratios were calculated. The results of this calculation are displayed in Table 4-15. As for the 430 specimens, the (311):(104) ratio was not calculated for the sandblasted specimens after 50 h due to overlap of the (311) spinel peak with the (104) alumina peak.

Table 4-14. Spinel to Chromia Peak Area Ratios for 434 Specimens.

| | Spinel to Chromia Peak Area Ratio | | | |
|---|---|---|---|---|
| | 50 h | | 502 h | |
| **Treatment** | (311):(104) | (220):(104) | (311):(104) | (220):(104) |
| As-is (thin) | - | - | 1.9 | 0.6 |
| As-is | 0.5 | 0.3 | 1.0 | 0.3 |
| Rolled 6% | 0.5 | 0.2 | 1.1 | 0.3 |
| Rolled 15% | 0.4 | 0.2 | 1.0 | 0.3 |
| Sandblasted 1 pass | - | 0.1 | 0.7 | 0.2 |
| Sandblasted 10 passes | - | 0.2 | 0.9 | 0.3 |

From Table 4-15, it can be seen that after 50 h of oxidation, the relative amounts of chromia and spinel were similar for all the different treatment conditions. After 502 h,

the (311):(104) ratios indicated that the amount of spinel present relative to chromia had increased for all specimens; however, there was still no significant difference between the different treatment conditions. The exception was the thin as-is specimen, which had significantly more spinel relative to chromia than any of the other specimens.

### 4.4.2 SEM Plan View Results

#### *4.4.2.1 SEM Plan View Images*

After 50 h and 502 h of oxidation, plan view SEM images were taken of the 434 specimens. These images are displayed in Figure 4-31.

After 50 h of oxidation at 800°C, the surfaces of all the specimens was covered by a continuous oxide layer. The general appearance of the oxide scale formed on the as-is and rolled specimens was similar. For these three specimens, the scale was fairly smooth and continuous with the exception of small bright clumps of fast growing oxide. The number of these clumps was approximately the same for each specimen. EDX analysis of the oxide compositon forming the bright clumps was carried out. For the as-is specimen, a few of the clumps were enriched in Fe compared to the surrounding oxide, but most of them had the same composition as the surrounding oxide. These results imply that most of the rapid growing oxide clumps were formed due to the presence of surface defects or flaws; however, a few may have formed due to cracking and spalling of the protective oxide scale. In contrast, for the rolled specimens, the majority of the bright clumps of fast growing oxide were found to be Fe-rich compared to the surrounding scale. For the sandblasted specimens, the appearance of the 1 pass and 10 passes specimens is similar after 50 h. The oxide scale on the sandblasted specimens was much rougher than on the as-is and rolled specimens due to the surface roughness produced by the sandblasting treatment prior to oxidation.

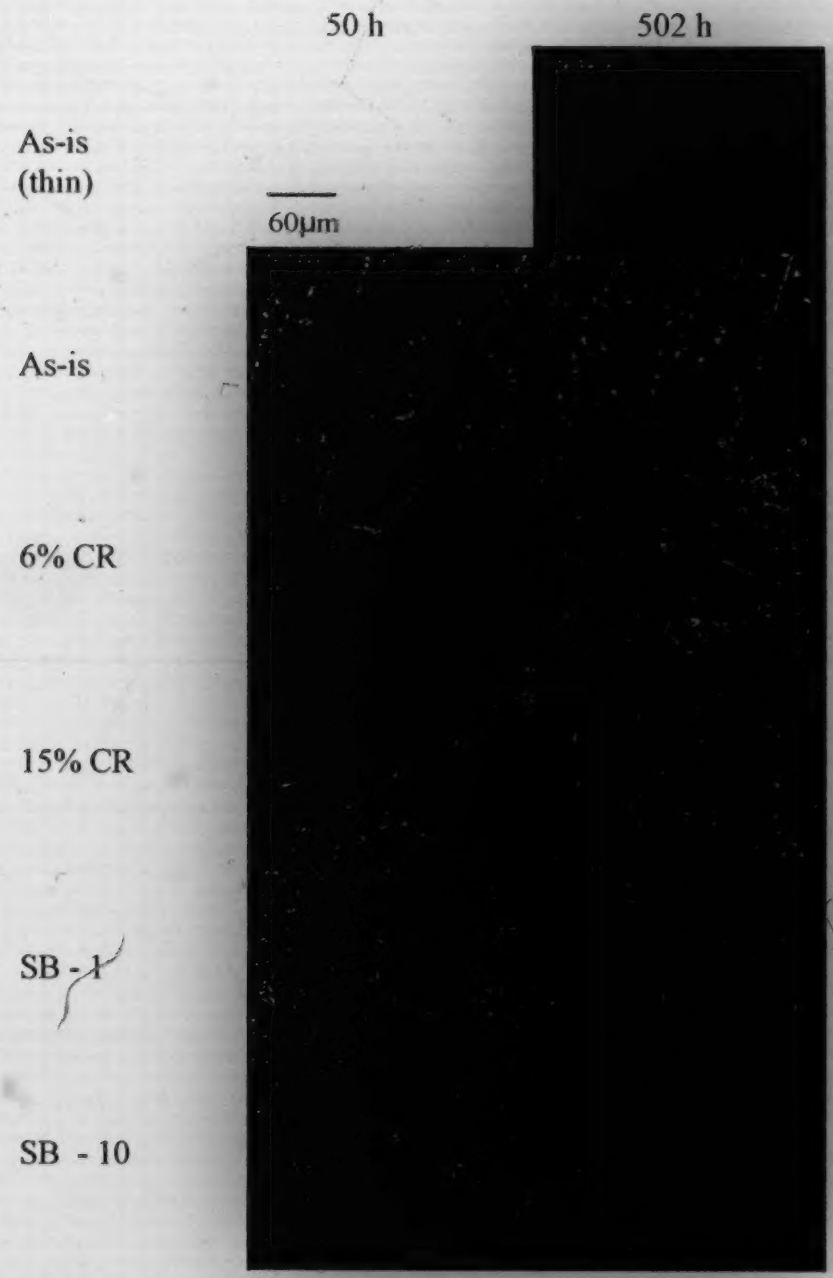


Figure 4-31. SEM Plan View Images of 434 Specimens After 50 h and 502 h of Oxidation.

After 502 h of oxidation, Figure 4-31 indicates that the thickness of the oxide scale increased for all specimens. The appearance of the oxide scale formed on the as-is and rolled specimens was again similar. The oxide scale on these three specimens was fairly smooth and continuous with bright clumps of fast growing oxide. For all the specimens, the number of oxide clumps increased from 50 h to 502 h of oxidation. After 502 h of oxidation, for the as-is and rolled specimens, EDX analysis indicated that a few of the clumps were enriched in Fe compared to the surrounding oxide; however, the majority of the clumps were enriched in Mn compared to other regions of the oxide scale. For the 15% cold rolled specimen, impurities such as Sn and Cu were also detected in some of the oxide clumps, indicating that contamination by the rolling mill may have been responsible for the rapid oxide growth in some locations. The appearance of the thin as-is specimen after 502 h of oxidation was similar to its thick conterpart, except no bright oxide clumps were present for the thin specimen. For the sandblasted specimens, the roughness of the oxide layer was reduced due to an increase in the thickness of the oxide. The original surface morphology produced by the sandblasting treatment was much less evident after 502 h.

#### *4.4.2.2 EDX Analysis*

The overall composition of the oxide scale for all the 434 specimens was analyzed by EDX spectroscopy of a fairly large area (~200μm x ~200μm). Quantitiative analysis of the resulting EDX spectra was carried out and the Cr to Mn and Cr to Fe ratios were determined for each of the treatment conditions. The results are shown in Table 4-16.

For all specimens, an increase in the amount of Mn relative to Cr and an increase in the amount of Cr relative to Fe occurred from 50 h to 502 h of oxidation. After 502 h, the thin as-is specimen had the largest amount of Mn relative to Cr in the oxide scale. For the as-is and rolled specimens, the amount of Mn relative to Cr was similar, while the sandblasted specimens had the lowest amount of Mn enrichment. After 502 h of oxidation, the as-is specimen had the highest amount of Cr relative to Fe, followed by the rolled 15%, rolled 6%, thin as-is, sandblasted 1 pass, and finally the sandblasted 10 passes specimen. After 502 h of oxidation, the oxide scales on all specimens were approximately 2μm thick, and thus the Fe was mostly coming from the oxide layer and not from the underlying steel substrate. The images in Figure 4-31 show that no significant spalling or cracking of the oxide layer occurred for any of the specimens,

indicating that more Fe was likely incorporated in the oxide scale of the sandblasted specimens.

Table 4-16. Cr:Mn and Cr:Fe Ratios from Quantitative EDX Analysis of the Oxide Scale for 434 Specimens.

| Surface Treatment | Cr:Mn | | Cr:Fe | |
|---|---|---|---|---|
| | 50 h | 502 h | 50 h | 502 h |
| As-Is (Thin) | - | 3.7 | - | 10.6 |
| As-Is | 9.6 | 4.8 | 0.6 | 17.4 |
| Rolled 6% | 9.3 | 5.0 | 0.8 | 15.0 |
| Rolled 15% | 8.3 | 4.9 | 0.7 | 12.4 |
| Sandblasted 1 Pass | 12.1 | 6.1 | 0.9 | 5.9 |
| Sandblasted 10 Passes | 11.8 | 5.9 | 0.8 | 3.9 |

### 4.4.3 SEM Cross Section Results

#### *4.4.3.1 SEM Cross Section Images*

SEM cross section images of the 434 specimens after 502 h of oxidation are displayed in Figure 4-32.

In Figure 4-32, the cross section images of all the specimens are similar in appearance except for the 1 pass sandblasted specimen, which has an oxide layer that is much less uniform in thickness than the other specimens. The amount of spinel relative to chromia does not appear to change much with the different surface treatments, except that there appears to be a slightly higher relative amount of spinel for the thin as-is specimen.

From the SEM images of the oxidized cross sections presented in Figure 4-32, the thickness of the oxide scale for each specimen was determined as described in section 4.3.3.1. The values of oxide layer thickness determined in this manner are listed in Table 4-17 and are compared with the values determined from the mass gain measurements.

Figure 4-32. SEM Cross Section Images of 434 Specimens After 502 h of Oxidation.

Table 4-17 shows that, in general, the thickness of the oxide scale on the treated specimens was larger than that for the as-is specimens. Both the SEM and mass gain results indicate that the oxide layer on the 15% cold rolled specimen was thicker than the 6% cold rolled specimen. The oxide layer on the thin as-is specimen was thinner than that on any of the other specimens with the exception of the 10 passes sandblasted specimen. In general, the oxide layer thickness values determined from the SEM images

were larger than those determined from the mass gain measurements by a factor of close to 3.

Table 4-17. Oxide Layer Thickness for 434 Specimens.

| Surface Treatment | Oxide Layer Thickness (μm) | |
|---|---|---|
| | Mass Gain | SEM Image |
| As-is (thin) | 0.47 | 1.69 ± 0.20 |
| As-is | 0.55 | 1.83 ± 0.22 |
| Rolled 6% | 0.57 | 2.03 ± 0.18 |
| Rolled 15% | 0.65 | 2.18 ± 0.24 |
| Sandblasted 1 pass | 0.61 | 1.86 ± 0.73 |
| Sandblasted 10 passes | 0.60 | 1.42 ± 0.32 |

#### *4.4.3.2 EDX Analysis*

In order to analyze the composition of the spinel phase formed on the 434 specimens, EDX spectra were collected from the outer region of the oxide scale. Following quantitative analysis of the spectra, the Cr:Mn and Cr:Fe ratios were determined for each treatment condition. The results are presented in Table 4-18.

Table 4-18. Cr:Mn and Cr:Fe Ratios From Quantitative EDX Analysis of the Spinel for 434 Specimens.

| Surface Treatment | Cr:Mn | Cr:Fe |
|---|---|---|
| As-Is (Thin) | 2.1 | 10.6 |
| As-Is | 1.9 | 4.4 |
| Rolled 6% | 2.4 | 13.1 |
| Rolled 15% | 3.9 | 18.6 |
| Sandblasted 1 Pass | 1.9 | 10.5 |
| Sandblasted 10 Passes | 1.9 | 6.4 |

From Table 4-18, it can be seen that the amount of Cr relative to Mn in the spinel phase was higher for the rolled specimens than for the as-is specimen, and the relative amount of Cr increased with the degree of rolling reduction. The Cr:Mn ratio was the same for the sandblasted specimens as for the as-is specimen. The thin as-is specimen had more

Cr relative to Mn in the spinel phase than its thick counterpart. The amount of Fe relative to Cr in the spinel phase was highest for the as-is specimen. There was a significant decrease in the amount of Fe relative to Cr for the thin as-is specimen when compared to its thick counterpart. The Cr enrichment relative to Fe was higher for the rolled specimens than the sandblasted specimens, and the degree of Cr enrichment increased with the degree of rolling reduction.

#### *4.4.3.3 EDX Linescans*

EDX linescans were collected for the thin as-is, as-is, 15% cold rolled, and 10 passes sandblasted specimens. The linescans for the as-is and rolled 15% specimens were similar to one another, and as a result, only the linescan for the rolled specimen is shown. The EDX linescans for the thin as-is, 15% cold rolled, and 10 passes sandblasted specimens are displayed in Figures 4-33, 4-34, and 4-35, respectively.

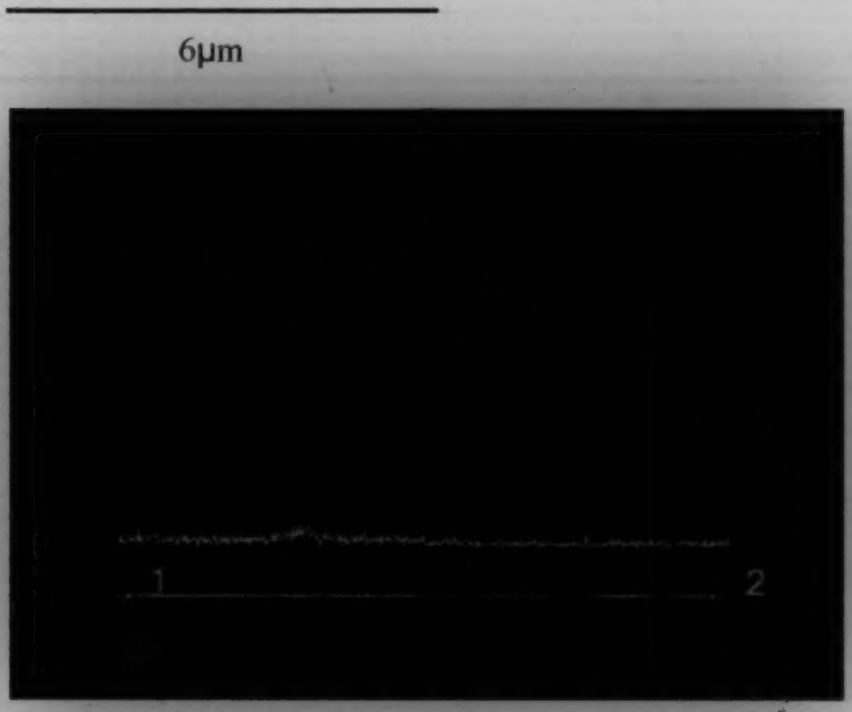


Figure 4-33. EDX Linescan for 434 Thin As-Is Cross Section After 502 h.

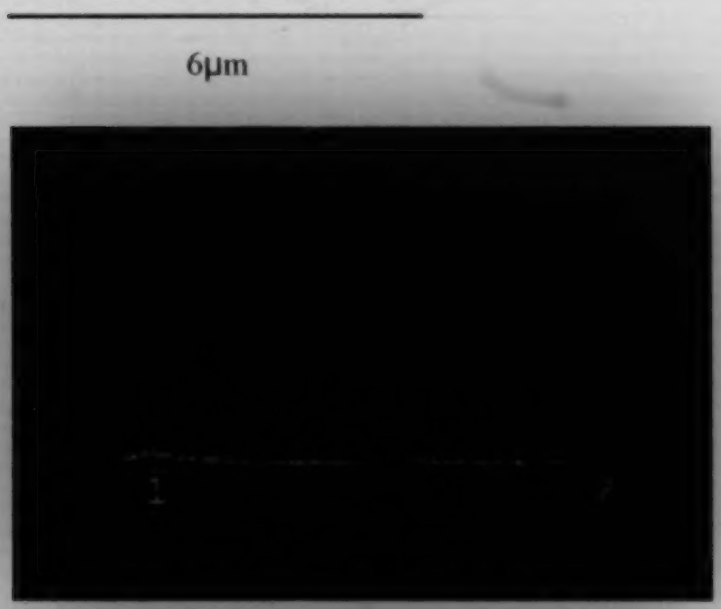


Figure 4-34. EDX Linescan for 434 Rolled 15% Cross Section After 502 h.

Figure 4-35. EDX Linescan for 434 Sandblasted 10 Passes Cross Section After 502 h.

Similar trends were observed for all three specimens. Iron was present in the bulk of the steel and the amount of Fe present in the oxide scale was significantly lower. Chromium was enriched in the oxide scale compared to its level in the steel substrate and Mn was segregated to the outer region of the oxide scale. The Si distruibtion was not as clear; however, there did appear to be a slight segregation of Si to the metal/oxide interface. The exception was the thin as-is specimen (Figure 4-33), where the Si appeared to be enriched throughout the oxide scale. It is not clear whether this was a real effect or as a result of contamination from the grinding media used to prepare the cross section specimen. The profiles for Mo and Nb were fairly flat throughout the oxide layers and these elements did not appear to be concentrated in the protective scale. In Figure 4-33, the Mo and Nb peaks in the steel substrate indicate the presence of a carbide containing these two elements. For the sandblasted specimen (Figure 4-35), Al appeared to only be present at the metal/oxide interface, corresponding to the original metal surface where some $Al_2O_3$ particles were embedded during the sandblasting process. In all cases, O was enriched throughout the oxide scale.

### 4.4.4 SIMS Results

#### *4.4.4.1 Native Oxide*

SIMS analysis was used to study the distribution of elements in the oxide scale present on the 434 specimens prior to oxidation at 800°C. The Mn, Si, Mo, and Nb profiles were found to overlap, and therefore the Mn and Si profiles are presented separately from the Mo and Nb profiles. The resulting depth profiles are displayed in Figure 4-36a and 4-36b. From Figure 4-36a, it is clear that Cr was enriched in the native oxide compared to its level in the bulk of the steel. Iron appeared to be enriched in the outer portion of the native oxide compared to the level of Fe in the bulk, but the level of Fe in the remainder of the oxide was lower than the bulk level. The signals for Mn and Si were both fairly noisy; however, it appeared that Si had segregated to the surface of the oxide layer. Mn may also have been enriched at the surface of the native oxide, but this was not clear. Figure 4-36b shows that Mo was not present in the oxide scale; however, Nb was slightly enriched at the surface of the native oxide. As with the Mn and Si, the signals for the Mo and Nb were quite noisy. The O profile was also very noisy; however, O appeared to be enriched in the native oxide.

a)

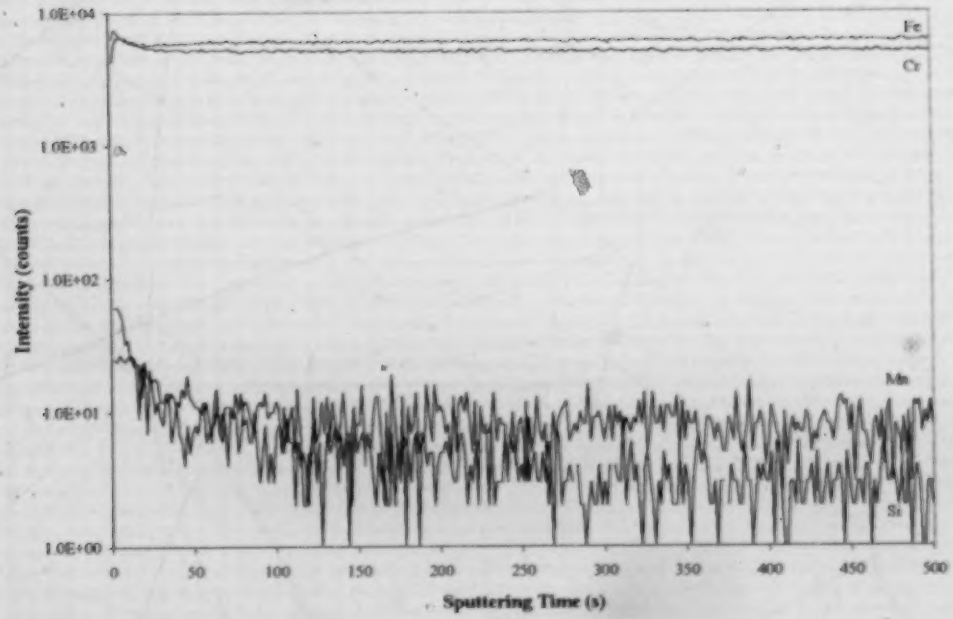


b)

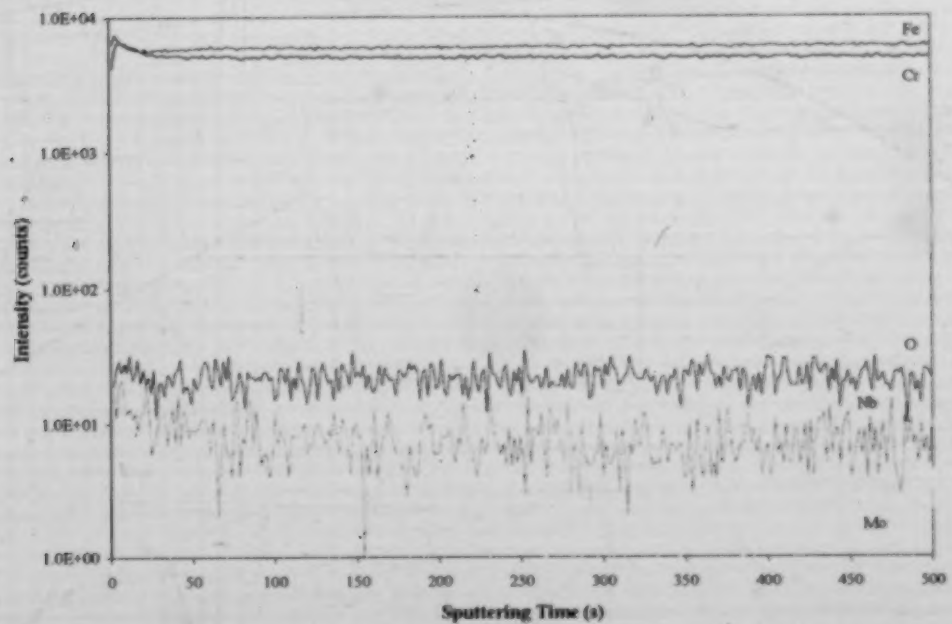


Figure 4-36. SIMS Depth Profile of 434 Native Oxide. a) Si and Mn; b) Mo and Nb.

#### *4.4.4.2 Oxidized Specimens*

In order to study the early stages of oxide formation in the 434 specimens, SIMS analysis of as-is, rolled 15%, and sandblasted 10 passes specimens that were oxidized for 15 minutes at 800°C was carried out. The SIMS profiles for the three specimens are displayed in Figure 4-37.

From Figure 4-37, it can be seen that the trends for Cr, Fe, Mn, Si, O, Nb, and Mo were similar for all three specimens. Chromium was enriched in the oxide scale compared to its level in the steel substrate. Iron was depleted in the oxide compared to its level in the bulk, with the exception of a slight enrichment in the middle of the oxide for the as-is specimen (Figure 4-37a). Manganese was segregated to the surface of the oxide scale, and also appeared to be slightly enriched at the metal/oxide interface. Silicon and Nb were present at the surface of the oxide scale and were segregated at the metal/oxide interface. Oxygen was enriched throughout the oxide layer. Molybdenum was depleted in the oxide compared to its level in the bulk of the steel. For the sandblasted specimen (Figure 4-37c), Al appeared at the surface of the original steel substrate due to the presence of alumina particles that were embedded in the steel surface during sandblasting. As for the 430 specimens, the sandblasted specimen profile was not as well defined as the other two profiles due to the averaging effect caused by the roughness of the original steel surface following sandblasting.

a)

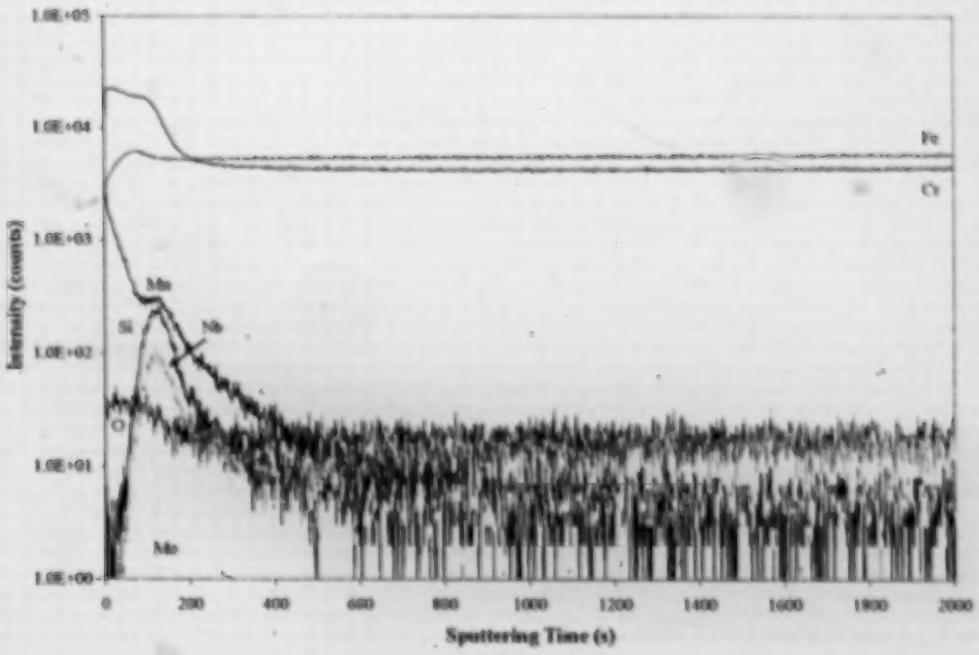
Intensity (counts)
Sputtering Time (s)
Fe
Cr
Mn
Si
Nb
O
Mo

b)

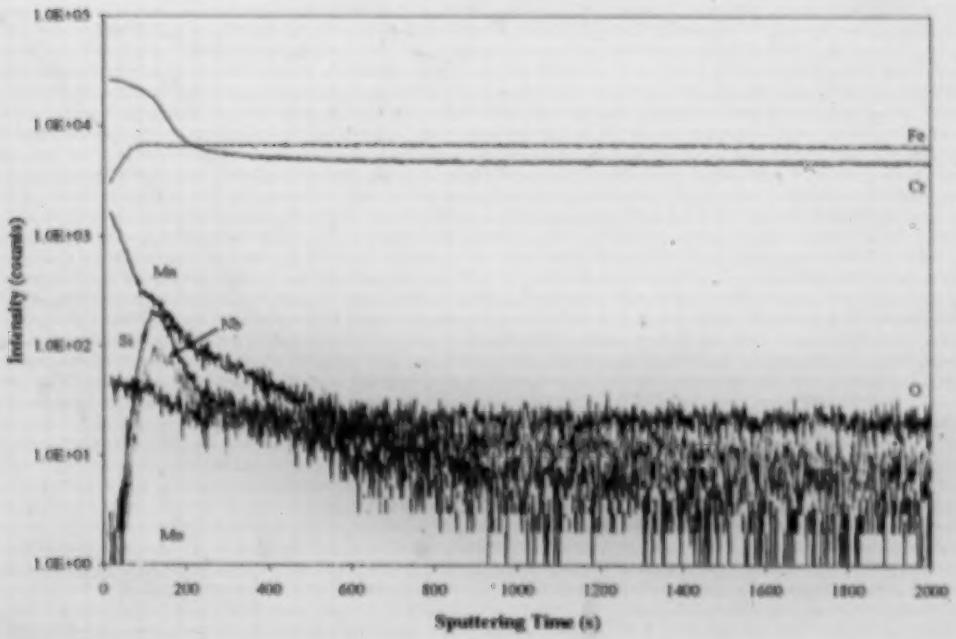
Intensity (counts)
Sputtering Time (s)
Fe
Cr
Mn
Si
Nb
O
Mo

c)

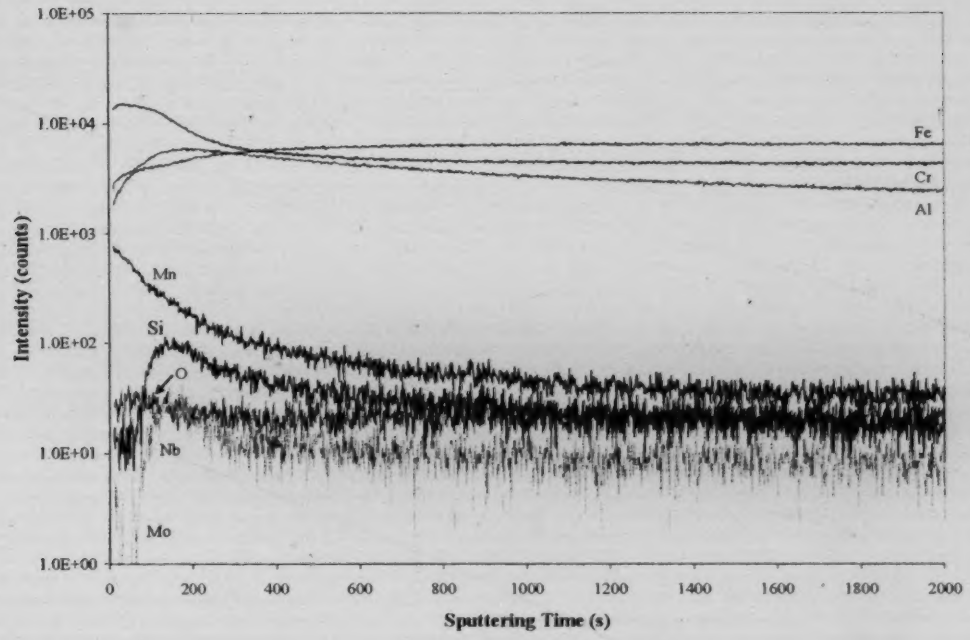


Figure 4-37. SIMS Depth Profile of 434 Specimens Oxidized for 15 Minutes at 800°C. a) As-Is; b) Rolled 15%; c) Sandblasted 10 Passes.

#### *4.4.4.3 Estimated Scale Thickness*

From the SIMS depth profiles in Figure 4-37, it is clear that although the distribution of elements through the oxide scale is similar for the as-is, rolled, and sandblasted specimens, the thickness of the oxide layer on each of the specimens differs. Approximate thickness values for each profile were determined using the procedure described in section 4.3.4.3. The resulting scale thickness values are shown in Table 4-19.

Table 4-19. Estimated Scale Thicknesses Corresponding to 434 SIMS Depth Profiles.

| Treatment | Oxidation Conditions | Approximate Scale Thickness (nm) | | Si Peak (nm) |
|---|---|---|---|---|
| | | Method 1 | Method 2 | |
| As-is | none | 4 | - | - |
| As-is | 800°C, 0.25 h | 50 | 28 | 26 |
| Rolled 21% | 800°C, 0.25 h | 71 | 29 | 23 |
| Sandblasted 10 passes | 800°C, 0.25 h | 168 | 38 | 46 |

From Table 4-19, it can be seen that the native oxide on the 434 steel is extremely thin. For the oxidized specimens, the thickness of the oxide scale on the as-is specimen is the smallest, followed by the rolled specimen, while the oxide layer on the sandblasted specimen is the thickest. The position of the Si peak, which corresponds to the metal/oxide interface, is the deepest for the sandblasted specimen, and similar for the other two specimens.

### 4.4.5 XPS Analysis

#### *4.4.5.1 Native Oxide*

XPS analysis was carried out in order to determine whether the elements present in the oxide scale exist in the metal or oxide form. Figure 4-38 shows the XPS plots for Cr, Fe, Mn, Si, Mo, and Nb.

From Figure 4-38a, it can be seen that, initially, all the Cr was present in oxide form. After a short interval of sputtering, the metal peak for Cr appeared. Then, a transition was seen as the height of the oxide peak decreased and the height of the metal peak increased. Finally, all the Cr was present in the metal form, indicating that the steel substrate had been reached.

For Fe, Figure 4-38b shows that, initially, most of the Fe was present in oxide form, but a small metal peak was also present. The metallic Fe most likely originates from the steel and not from the native oxide. The native oxide was estimated from the SIMS profile to be approximately 4 nm (Table 4-19), which is close to the depth resolution of XPS. As sputtering continued, the height of the metal peak increased and the height of the oxide

peak decreased, indicating a transition from the native oxide to the underlying steel substrate. Finally, all the Fe was present in metal form.

Figure 4-38c does not show the presence of Mn clearly at any sputtering interval in either the oxide or the metal form. This could mean that the Mn enrichment in the native oxide is not significant compared to the other elements.

Prior to sputtering, Figure 4-38d confirms that Si is present at the surface of the native oxide. There appears to be a small metal peak in addition to an oxide peak. The Si oxide peak occurs at approximately 101 eV, which does not correspond to the oxide peak for $SiO_2$ at 103.4 eV. This indicates that the Si may be present as $SiO_x$ at the surface, where x is less than 2. Silicon appears in the outer region of the native oxide, but the Si peak disappears very quickly, suggesting that Si is segregated at the surface of the native oxide scale.

a)

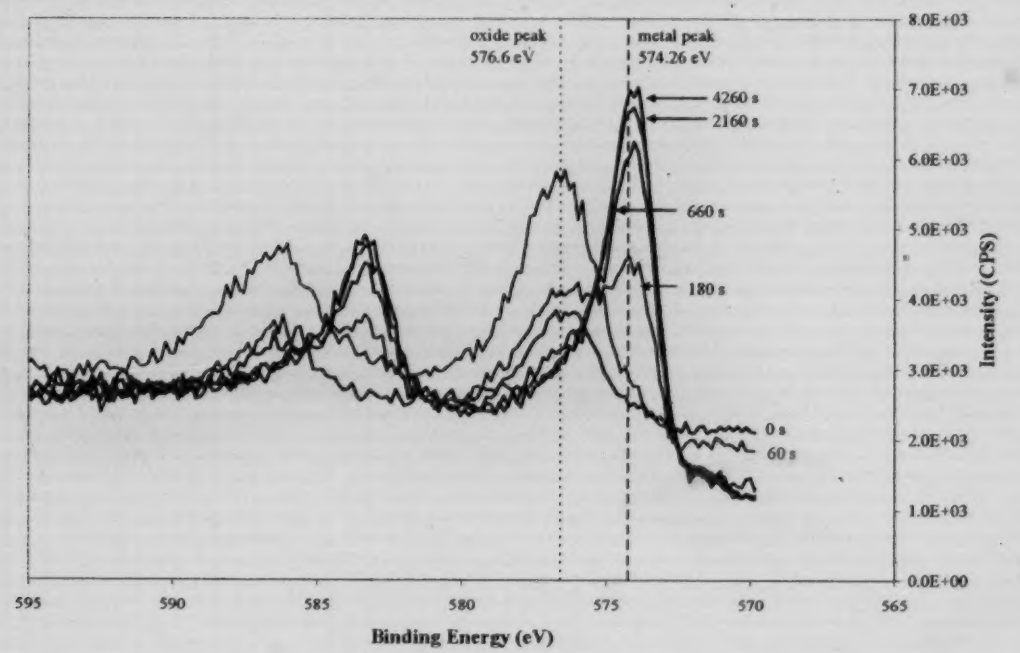

b)

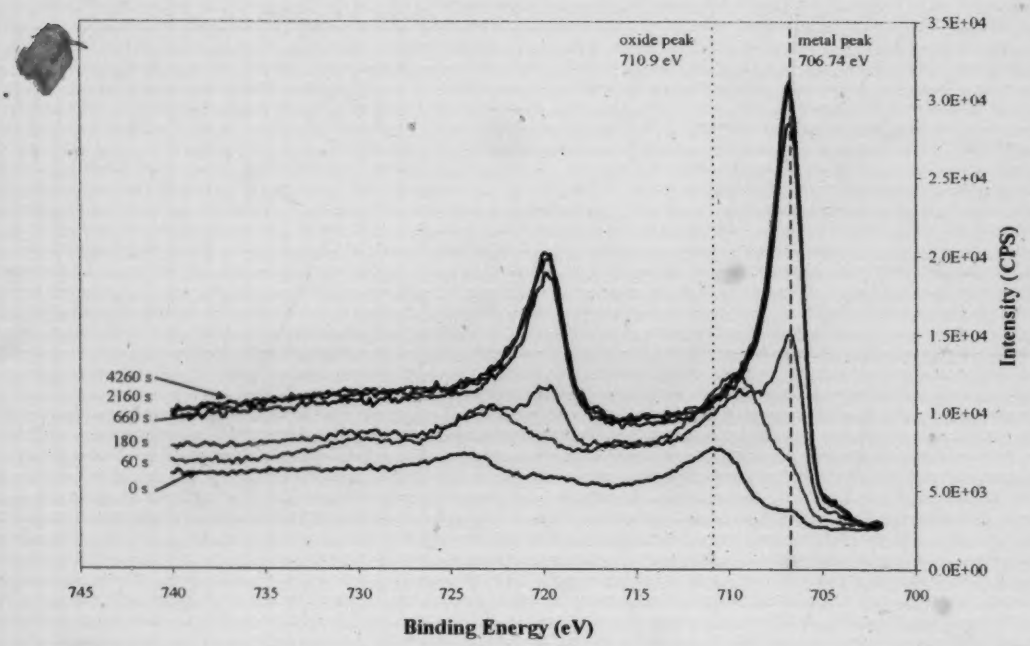
oxide peak
710.9 eV
metal peak
706.74 eV
4260 s
2160 s
660 s
180 s
60 s
0 s
3.5E+04
3.0E+04
2.5E+04
2.0E+04
1.5E+04
1.0E+04
5.0E+03
0.0E+00
Intensity (CPS)
745
740
735
730
725
720
715
710
705
700
Binding Energy (eV)

c)

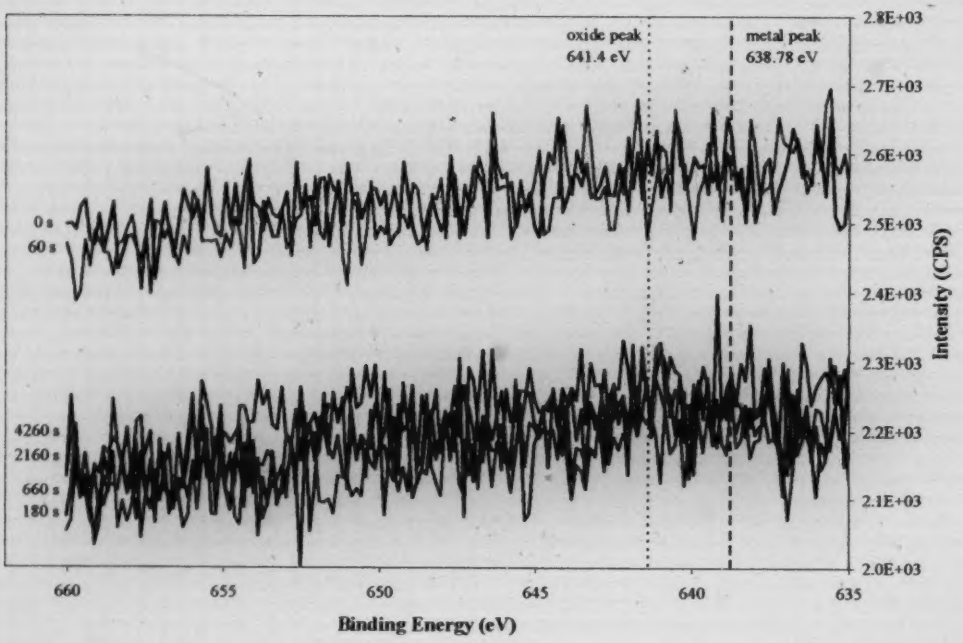
oxide peak
641.4 eV
metal peak
638.78 eV
0 s
60 s
4260 s
2160 s
660 s
180 s
2.8E+03
2.7E+03
2.6E+03
2.5E+03
2.4E+03
2.3E+03
2.2E+03
2.1E+03
2.0E+03
Intensity (CPS)
660
655
650
645
640
635
Binding Energy (eV)

d)

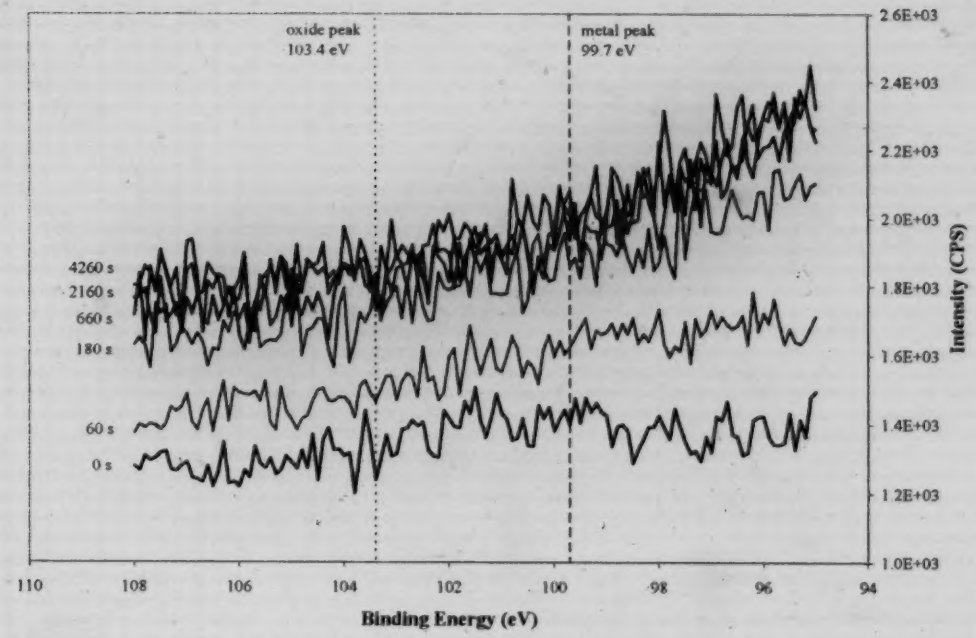
oxide peak
103.4 eV
metal peak
99.7 eV
4260 s
2160 s
660 s
180 s
60 s
0 s
2.6E+03
2.4E+03
2.2E+03
2.0E+03
1.8E+03
1.6E+03
1.4E+03
1.2E+03
1.0E+03
Intensity (CPS)
110
108
106
104
102
100
98
96
94
Binding Energy (eV)

e)

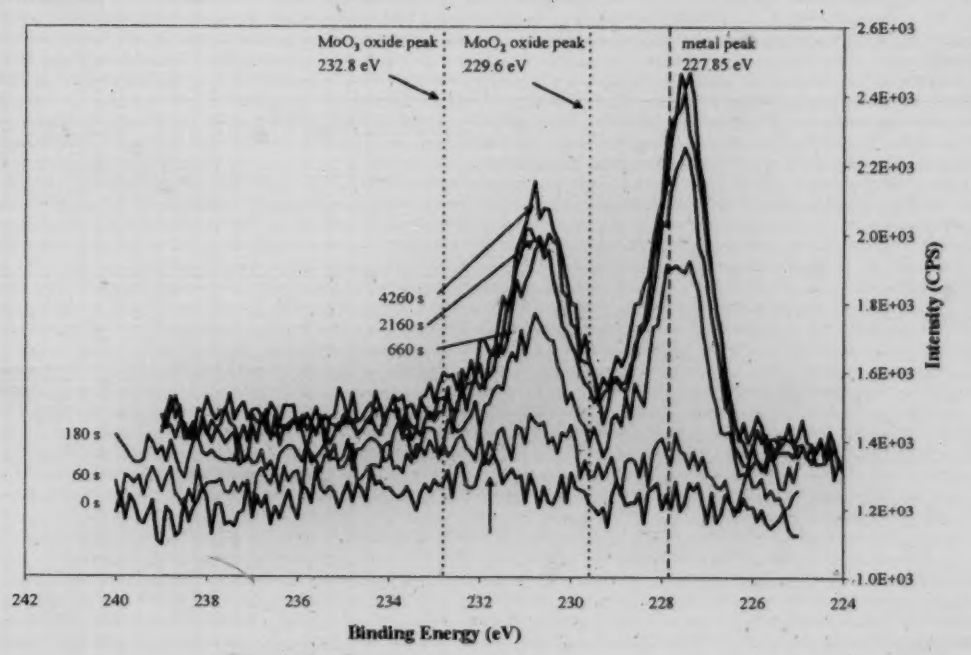
MoO3 oxide peak
232.8 eV
MoO3 oxide peak
229.6 eV
metal peak
227.85 eV
4260 s
2160 s
660 s
180 s
60 s
0 s
2.6E+03
2.4E+03
2.2E+03
2.0E+03
1.8E+03
1.6E+03
1.4E+03
1.2E+03
1.0E+03
Intensity (CPS)
242
240
238
236
234
232
230
228
226
224
Binding Energy (eV)

f)

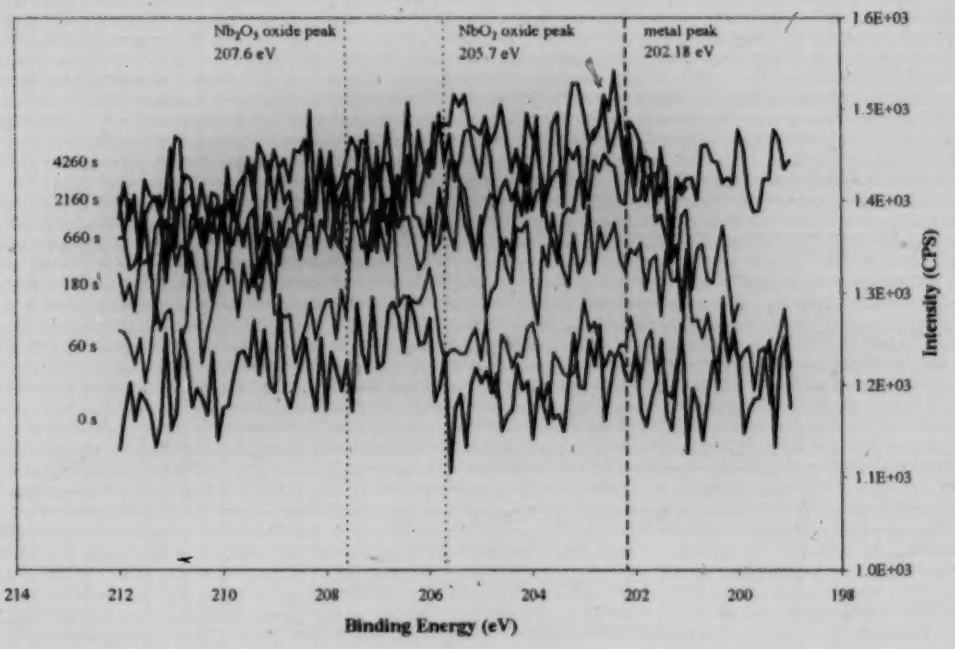


Figure 4-38. XPS Peak Plots for 434 Native Oxide. a) Cr 2p; b) Fe 2p; c) Mn 2p; d) Si 2p; e) Mo 3d; f) Nb 3d.

Figure 4-38e reveals the presence of weak oxide (indicated by the vertical arrow) and metal peaks for Mo at the native oxide surface. As sputtering continues, the oxide peak disappears and the height of the metal peak increases. This is similar to the trend observed in Figure 4-38b for Fe. The oxide peak for Mo is between that for $MoO_2$ and that for $MoO_3$, indicating that a mixture of the two oxides may be present.

According to Figure 4-38f, Nb is present at the surface of the native oxide in oxide form. The Nb oxide peak is still present after a short sputtering interval, and then disappears. The Nb metal peak appears after longer sputtering times, indicating that the steel substrate has been reached. As with Mo, the Nb oxide peak is between that for $NbO_2$ and $Nb_2O_5$, indicating that the Nb has a charge between +4 and +5. It is likely that either a mixture of the two oxides is present, or that the Nb has been incorporated into a mixed oxide.

### *4.4.5.2 Oxidized Specimens*

XPS depth profiling was carried out for the as-is and rolled 15% specimens oxidized for 15 minutes at 800°C, but in both cases, similar peak profiles were obtained. Therefore, only the results for the as-is specimen are shown. The XPS peak plots for Cr, Fe, Mn, Si, Mo, and Nb are displayed in Figure 4-39.

From Figure 4-39a, initially, all the Cr was present in oxide form. As sputtering continued through the oxide layer, the Cr peak remained relatively unchanged. A small metal peak appeared, indicating a transition from the oxide layer to the underlying steel. Finally, the oxide peak disappeared and all the Cr was present in the metal form, indicating that the steel substrate had been reached.

a)

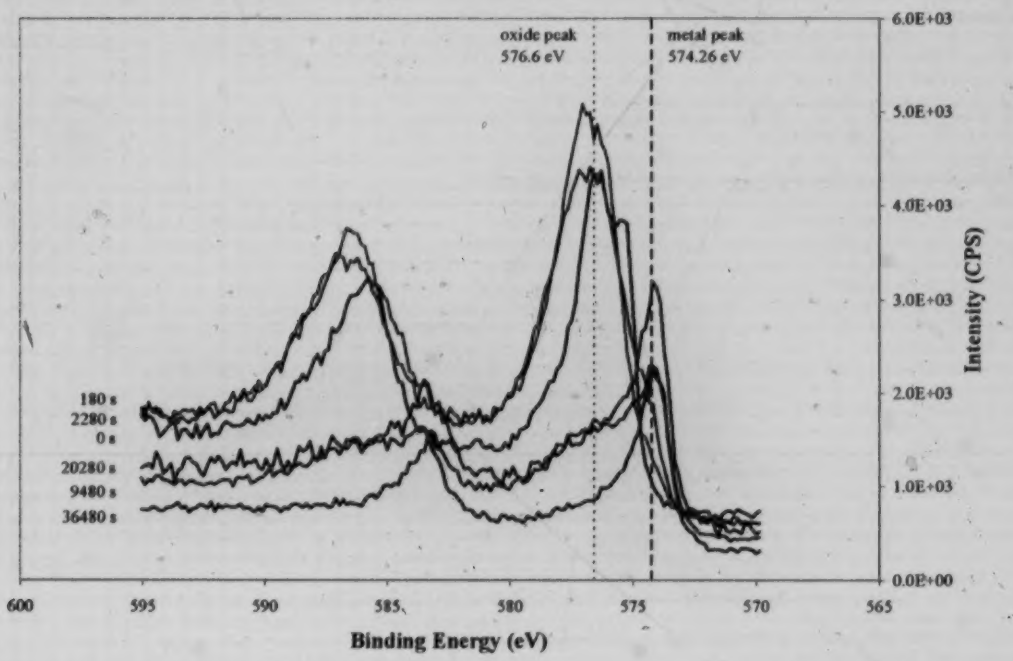

b)

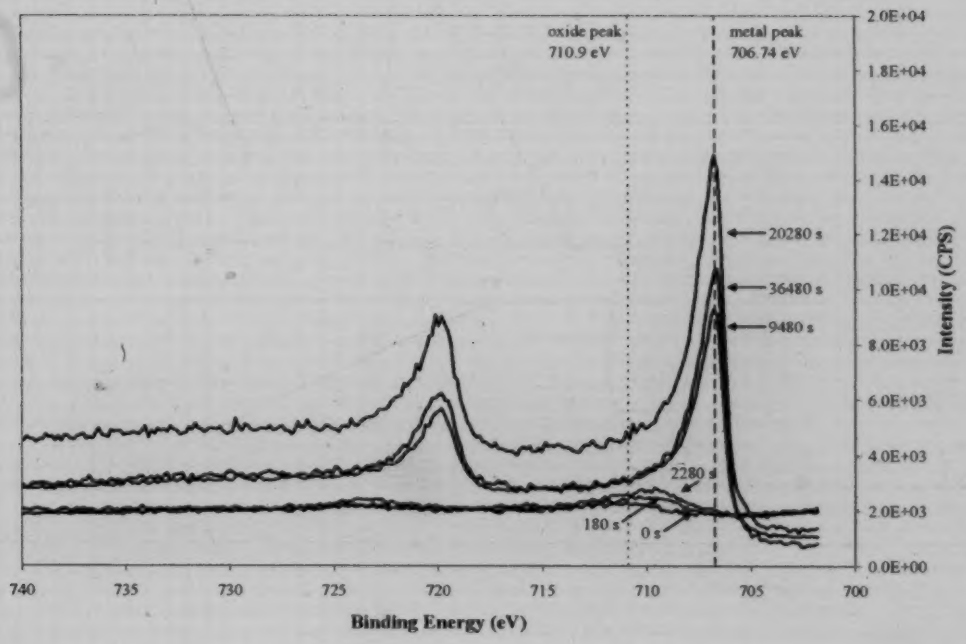
oxide peak
710.9 eV
metal peak
706.74 eV
20280 s
36480 s
9480 s
2280 s
180 s
0 s
Intensity (CPS)
Binding Energy (eV)

c)

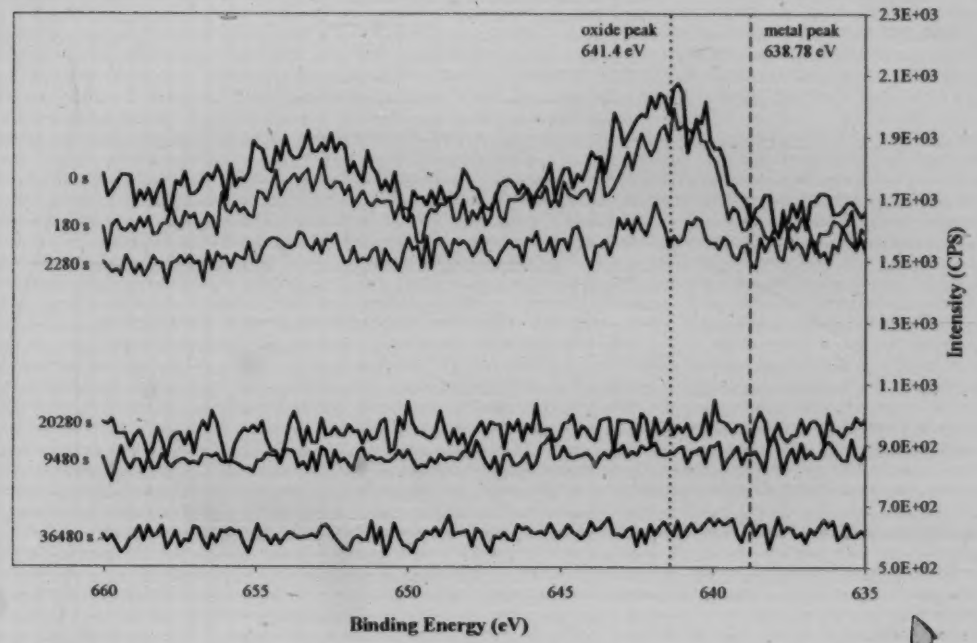
oxide peak
641.4 eV
metal peak
638.78 eV
0 s
180 s
2280 s
20280 s
9480 s
36480 s
Intensity (CPS)
Binding Energy (eV)

d)

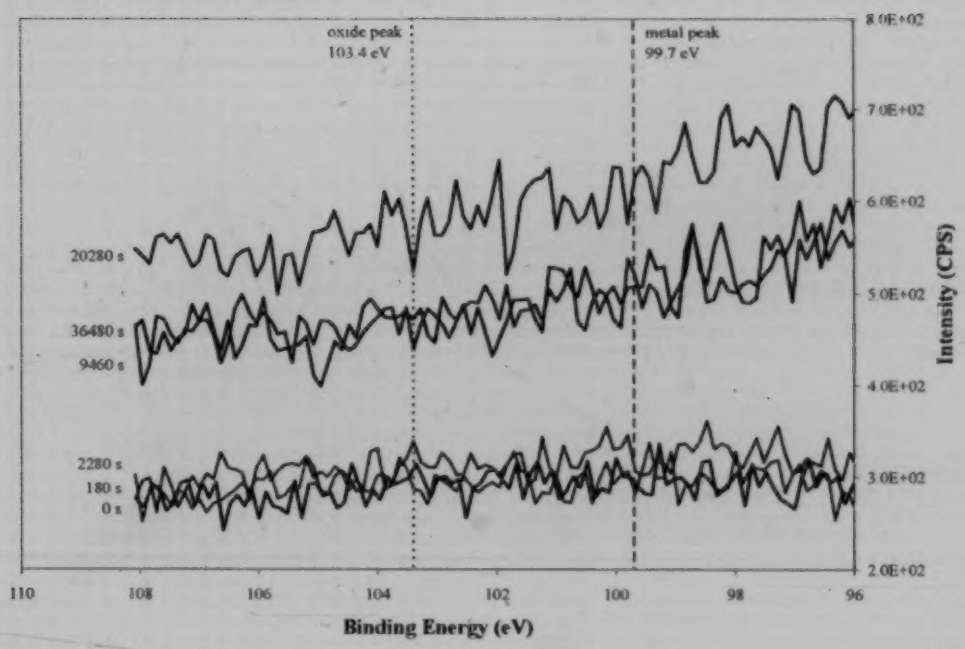
oxide peak
103.4 eV
metal peak
99.7 eV
20280 s
36480 s
9460 s
2280 s
180 s
0 s
8.0E+02
7.0E+02
6.0E+02
5.0E+02
4.0E+02
3.0E+02
2.0E+02
Intensity (CPS)
110
108
106
104
102
100
98
96
Binding Energy (eV)

e)

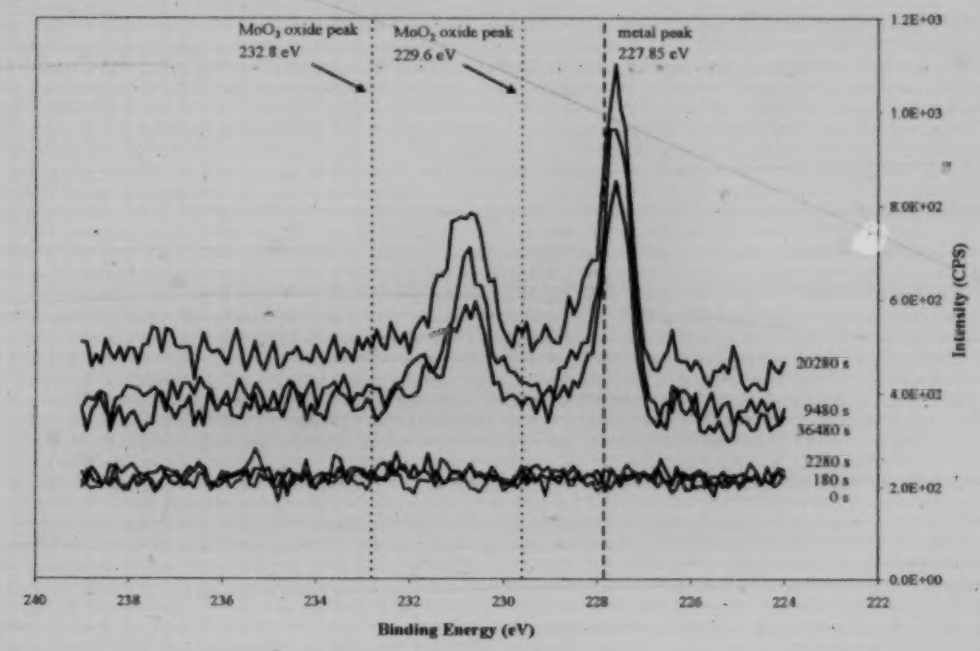
MoO3 oxide peak
232.8 eV
MoO2 oxide peak
229.6 eV
metal peak
227.85 eV
20280 s
9480 s
36480 s
2280 s
180 s
0 s
1.2E+03
1.0E+03
8.0E+02
6.0E+02
4.0E+02
2.0E+02
0.0E+00
Intensity (CPS)
240
238
236
234
232
230
228
226
224
222
Binding Energy (eV)

f)

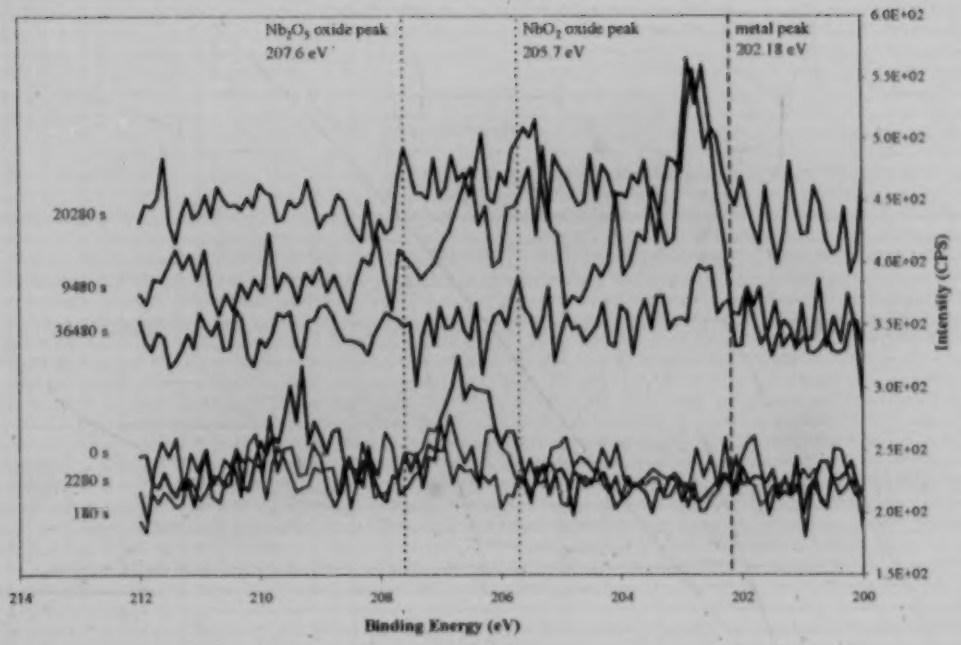


Figure 4-39. XPS Peak Plots for 434 As-Is Specimens Oxidized for 15 Minutes at 800°C. a) Cr 2p; b) Fe 2p; c) Mn 2p; d) Si 2p; e) Mo 3d; f) Nb 3d.

For Fe, Figure 4-39b indicates that as with Cr, all the Fe was initially in the oxide form. After a relatively short sputtering time compared to the Cr, the Fe oxide peak disappeared. As sputtering continued, the Fe metal peak increased in height. As mentioned in Section 4.3.5.1, this is most likely a sputtering effect.

From Figure 4-39c, it can be seen that the Mn was present in oxide form, but only in the outer region of the oxide scale.

For Si, Figure 4-39d shows that no Si oxide or metal peaks were clearly present, although the Si signal was quite noisy. From the XPS results, there was no evidence of Si segregation in the oxide scale.

For Mo, no peaks were present during the initial sputtering. Mo metal peaks appeared in Figure 4-39e only after very long sputtering times, indicating that Mo was not present in the oxide scale but remained in the steel substrate.

Figure 4-39f indicates that on the surface of the oxide layer, Nb was present in the oxide form. As with the native oxide, the Nb oxide peak is between the location of the $NbO_2$ and that of the $NbO_5$ peak. Although the Nb signal is quite noisy, Nb appears to be present in the oxide form at the metal/oxide interface. After long sputtering times, the Nb metal peak appeared, indicating the presence of Nb in the steel.

### 4.4.6 Summary of 434 Results

From both the mass gain data presented in Section 4.1 and the measurements of oxide scale thickness from the 434 SEM cross section images, the treated 434 specimens had a larger mass gain, due to oxidation, than the as-is 434 specimen. Also, the mass gain, due to oxidation, for the thin as-is specimen was slightly less than its thick counterpart. For both the as-is and rolled specimens, the plan view SEM images revealed the presence of bright clumps of fast-growing oxide. For the as-is specimen, many of these clumps were found by EDX analysis to be enriched in Mn compared to the overall composition of the oxide; however, for the rolled specimens, in addition to Mn enrichment, the presence of impurities such as Sn and Cu in the bright oxide clumps was also noted. This suggests that the rolled specimens were contaminated by the rolling mill, and that the fast oxide growth that occurred at the impurity sites could have contributed to the increase in mass gain of the rolled specimens compared with the untreated specimens.

For all the 434 specimens, the same oxide layer morphology was observed. XRD analysis indicated that the oxide layer was composed of two oxide phases: an inner layer of $Cr_2O_3$ and outer $(Mn,Cr)_3O_4$ spinel particles. EDX linescans of the oxidized cross section specimens confirmed that the Mn was segregated to the outer region of the oxide scale and that Cr was present throughout the oxide scale. Similar trends were observed by SIMS and XPS analysis, with XPS analysis confirming that the Mn and Cr were both in the oxide form. The distribution of Si in the oxide scale was not entirely clear from the EDX linescans, although slight enrichment of Si at the metal/oxide interface was possible. SIMS depth profiles revealed that, for all specimens, Si had segregated to the metal/oxide interface after 15 min of oxidation at 800°C; however, no Si peaks were

present in the XPS analysis. This may be a result of the low Si signal compared to other elements in the oxide scale. Also, XPS depth profiling is a discontinuous process and if the Si segregation occurred over a very small region, the Si-rich portion of the oxide scale may have been sputtered away without being analyzed. Overall, it seems likely that a thin layer of $SiO_2$ would exist at the metal/oxide interface after 502 h of oxidation. For the Nb and Mo, the carbide forming elements, the EDX linescans clearly reveal their presence only where a carbide in the steel is encountered by the linescan. However, XPS results indicate that a small amount of Mo in oxide form is present at the surface of the oxide scale. For Nb, the SIMS results indicate that a small amount of Nb is present at the surface of the oxide and there is segregation of Nb to the metal/oxide interface. XPS results confirm the presence of Nb at the surface of the oxide scale as well as at the metal/oxide interface in oxide form. In both cases, the oxide peaks do not exactly correspond to either $NbO_2$ or $Nb_2O_5$, indicating that a mixture of the two oxides may be present. The formation of Nb oxides is not surprising as the free energy of formation of both $NbO_2$ and $Nb_2O_5$ is large. Nb in metal form was detected once the steel substrate had been reached. The reason that the EDX linescan failed to detect the presence of either Mo or Nb in the oxide scale after 502 h could be simply because the amount of these elements present was too small. With the exception of Nb and Mo, the distribution of elements in the oxide scale was similar after both short term and long term oxidation.

As mentioned above, both XRD and SEM cross section analysis indicated that the same oxide phases were identified for all the treatment conditions. XRD analysis indicated that, for all specimens, the amount of spinel relative to chromia increased with increasing oxidation time. However, no significant difference between the relative amounts of chromia and spinel were found between the different treatments after either 50 h or 502 h of oxidation. The exception was the thin as-is specimen, which had significantly more spinel relative to chromia than any of the thick specimens. The relatively large amount of spinel compared to chromia for the thin as-is specimen was clearly visible in the SEM cross section image.

EDX analysis of the overall oxide scale composition indicated that the amount of Mn relative to Cr increased with increasing oxidation time, which agrees with the XRD results indicating an increase in the relative amount of spinel with increasing oxidation time. The highest amount of Mn relative to Cr was found for the thin as-is specimen, then the as-is specimen and finally the rolled specimens. The smallest amount of Mn

relative to Cr was found for the sandblasted specimens. EDX analysis of the spinel region of the oxide scale from the oxidized cross section specimens indicated that the amount of Mn relative to Cr in the spinel was significantly larger for the thin as-is, as-is, and sandblasted specimens than for the rolled specimens. These results indicate that although the relative amount of spinel is similar for all the specimens, cold rolling does appear to have produced a change in the composition of the spinel phase, namely Cr enrichment. The degree of Cr enrichment in the spinel is larger for the 15% cold rolled specimen than for the 6% cold rolled specimen.

EDX analysis of the overall oxide scale composition also indicated that there was a reduced amount of Fe relative to Cr for the as-is specimen, followed by the rolled specimens; the highest amount of Fe relative to Cr was present in the thin as-is and sandblasted specimens. EDX analysis of the spinel region of the oxide scale showed that the amount of Fe relative to Cr was significantly lower for the rolled specimens than the other specimens, followed by the sandblasted and thin as-is specimens; the highest amount of Fe relative to Cr occurred in the as-is specimen. These results also suggest that more Cr has been incorporated into the oxide scale of the rolled specimens than for any of the other specimens.

Finally, XPS and SIMS analysis of the native oxide on the 434 specimens indicated several differences from the oxide formed at 800°C. The Cr, Fe, and Mo distributions were similar in the two types of oxide scales; however, the Mn, Si, and Nb distributions were different. For the native oxide, no clear evidence of Mn segregation to the surface of the oxide scale was observed in either the SIMS or XPS results, whereas for the specimens oxidized at 800°C, the Mn was segregated to the surface of the oxide layer. For the native oxide, Si was found to be segregated at the surface of the oxide; however, the SIMS results indicated that Si segregated to the metal/oxide interface for the specimens oxidized for 15 min at 800°C. In the native oxide, Nb was present at the surface of the oxide in oxide form; however, for the specimens oxidized for 15 minutes, both the SIMS and XPS results indicated that the Nb had segregated to the metal/oxide interface.

TEM analysis of the precipitates found in the 434 steel indicated that, in addition to the expected NbC precipitates, Nb/Fe-rich carbides of the form $M_7C_3$ were also present. In addition to Nb, these carbides contained Mo and Cr. It is difficult to calculate whether or

not the amount of Nb and Mo added to the 430 steel would be more than enough to tie up all the C present in the steel. However, the presence of Cr and Fe in the $M_7C_3$ precipitates suggests that all the Mo and Nb are tied up in carbide form, since Cr and Fe are not as strong carbide forming elements as Mo and Nb. This would in turn suggest that it is unlikely that a large amount of either Mo or Nb would be available for oxide formation. No information was found in literature pertaining to a Nb-rich carbide of the form $M_7C_3$, and it is not clear how stable this type of carbide would be at 800°C. Therefore, even if all the carbide forming elements were initially present in carbide form, dissolution of the precipitates could occur, allowing some Mo or Nb to be incorporated into the oxide scale. Since no evidence of these elements was detected in the EDX linescans after 502 h of oxidation, it appears that their level of incorporation into the oxide scale after long oxidation times is minimal.

## 4.5 ZMG 232 Results

### 4.5.1 XRD Results

#### *4.5.1.1 XRD Spectra*

XRD analysis was carried out on each of the ZMG 232 specimens in order to identify the phases present in the oxide scale. Figure 4-40 shows the XRD spectra obtained from each treatment condition after 502 h of oxidation. Figure 4-40 indicates that, for all specimens, both chromia and spinel phases are present in the oxide scale. However, the relative heights of the chromia and spinel peaks differ between the surface treatments, indicating that the relative amount of the chromia and spinel phases in the oxide layer depends on the surface treatment condition of the specimen.

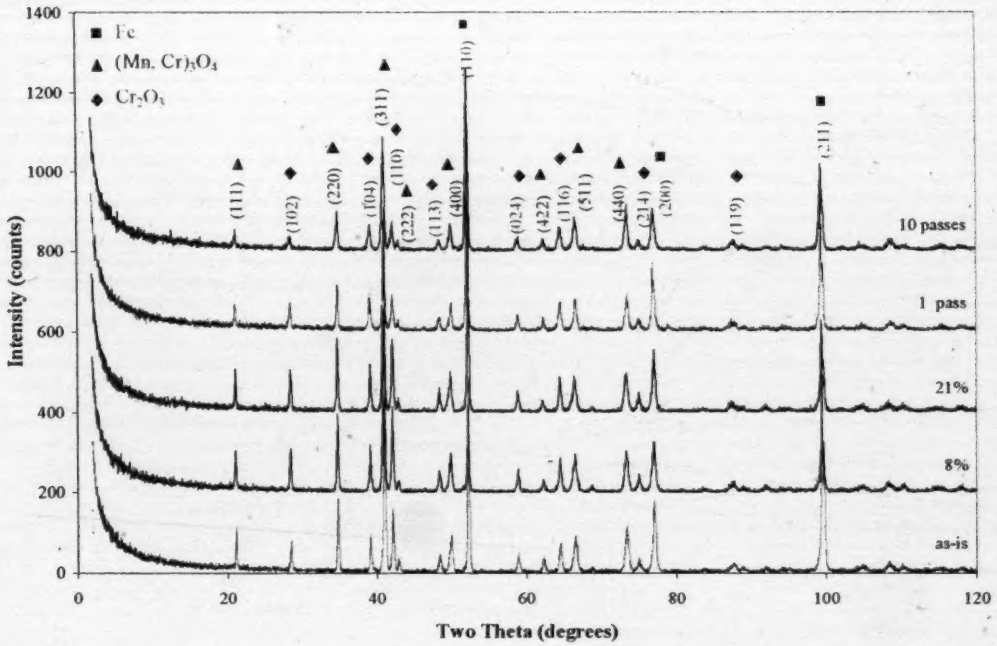


Figure 4-40. Comparison of the ZMG 232 XRD Spectra After 502 h of Oxidation.

#### *4.5.1.2 Relative Peak Intensities*

In order to analyze the XRD results, the first step was to determine if preferred orientation was present for either the chromia or spinel phase on any of the specimens. To determine this, the relative peak intensities of the 5 most intense peaks were compared with the theoretical peak intensities from the JCPDS diffraction cards (International Center for Diffraction Data. 1996). The results of this comparison are presented in Table 4-20 for chromia and Table 4-21 for spinel.

From Table 4-20, after 50 h of oxidation, a slight (012) preferred orientation of the chromia phase exists for all specimens. After 502 h, the (012) preferred orientation has been reduced for all specimens, but is still present for the as-is and rolled specimens. For the as-is and rolled specimens, after 502 h, a (110) preferred orientation is present. A slight (110) preferred orientation is also present in the sandblasted 10 passes specimen.

Table 4-20. Relative Intensities of Chromia X-Ray Peaks for ZMG 232 Specimens.

| | | $Cr_2O_3$ (PDF#38-1479) | | | | | | | | | |
|---|---|---|---|---|---|---|---|---|---|---|---|
| | | 50 h | | | | | 502 h | | | | |
| | **Peak Order** | 1 | 2 | 3 | 4 | 5 | 1 | 2 | 3 | 4 | 5 |
| | **(hkl) Index** | (104) | (110) | (116) | (012) | (024) | (104) | (110) | (116) | (012) | (024) |
| | **Card Intensity (%)** | 100 | 93 | 87 | 73 | 38 | 100 | 93 | 87 | 73 | 38 |
| **Treatment** | As-is | 100 (1) | 67 (3) | 54 (4) | 77 (2) | 24 (5) | 63 (2) | 100 (1) | 45 (4) | 49 (3) | 26 (5) |
| | Rolled 8% | 100 (1) | 44 (4) | 49 (3) | 65 (2) | 21 (5) | 56 (2) | 100 (1) | 41 (4) | 50 (3) | 26 (5) |
| | Rolled 21% | 100 (1) | 47 (4) | 54 (3) | 80 (2) | 23 (5) | 65 (2) | 100 (1) | 49 (4) | 58 (3) | 25 (5) |
| | Sandblasted 1 pass | 100 (1) | 59 (3) | 57 (4) | 80 (2) | 26 (5) | 100 (1) | 92 (2) | 87 (3) | 72 (4) | 45 (5) |
| | Sandblasted 10 passes | 100 (1) | 60 (4) | 63 (3) | 77 (2) | 23 (5) | 97 (2) | 100 (1) | 84 (3) | 48 (5) | 52 (4) |

For the spinel phase, Table 4-21 indicates that a (111) preferred orientation exists after 50 h of oxidation and is slightly stronger for the as-is and rolled specimens than the sandblasted specimens. After 502 h of oxidation, the (111) preferred orientation has been reduced for the as-is and rolled specimens and is no longer present for the sandblasted specimens.

Table 4-21. Relative Intensities of Spinel X-Ray Peaks for ZMG 232 Specimens.

| | | $(Cr, Mn)_3O_4$ (PDF#33-0892) | | | | | | | | | |
|---|---|---|---|---|---|---|---|---|---|---|---|
| | | 50 h | | | | | 502 h | | | | |
| | **Peak Order** | 1 | 2 | 3 | 4 | 5 | 1 | 2 | 3 | 4 | 5 |
| | **(hkl) Index** | (311) | (220) | (440) | (511) | (111) | (311) | (220) | (440) | (511) | (111) |
| | **Card Intensity (%)** | 100 | 50 | 45 | 30 | 25 | 100 | 50 | 45 | 30 | 25 |
| **Treatment** | As-is | 100 (1) | 47 (2) | 24 (4) | 17 (5) | 29 (3) | 100 (1) | 41 (2) | 26 (3) | 20 (5) | 21 (4) |
| | Rolled 8% | 100 (1) | 46 (2) | 19 (5) | 19 (5) | 23 (3) | 100 (1) | 43 (2) | 22 (3) | 21 (4) | 20 (5) |
| | Rolled 21% | 100 (1) | 41 (2) | 20 (4) | 15 (5) | 23 (3) | 100 (1) | 41 (2) | 20 (4) | 18 (5) | 21 (3) |
| | Sandblasted 1 pass | 100 (1) | 33 (2) | 21 (3) | 20 (4) | 20 (4) | 100 (1) | 36 (2) | 30 (3) | 25 (4) | 17 (5) |
| | Sandblasted 10 passes | 100 (1) | 40 (2) | 23 (3) | 17 (5) | 18 (4) | 100 (1) | 34 (3) | 40 (2) | 25 (4) | 16 (5) |

#### *4.5.1.3 Peak Area Ratios*

In order to compare the relative amount of chromia and spinel present in the oxide scale for the different surface treatments, the peak areas were determined using Jade software and the spinel to chromia peak area ratios were determined for each specimen. These ratios are displayed in Table 4-22.

Table 4-22. Spinel to Chromia Peak Area Ratios for ZMG 232 Specimens.

| | **Spinel to Chromia Peak Area Ratio** | | | |
|---|---|---|---|---|
| | **50 h** | | **502 h** | |
| **Treatment** | (311):(104) | (220):(104) | (311):(104) | (220):(104) |
| As-is | 3.0 | 1.2 | 6.8 | 2.1 |
| Rolled 6% | 2.1 | 0.8 | 5.1 | 1.7 |
| Rolled 15% | 2.3 | 0.8 | 4.4 | 1.5 |
| Sandblasted 1 pass | 2.5 | 0.8 | 3.8 | 1.0 |
| Sandblasted 10 passes | 2.2 | 0.5 | 5.1 | 1.5 |

From Table 4-22, it can be seen that after both 50 h and 502 h of oxidation, the spinel to chromia peak area ratio is higher for the as-is specimen than for either the rolled or sandblasted specimens, indicating that the relative amount of spinel is higher for the as-is specimen than for the surface treated specimens. It is also evident that the relative amount of spinel increases with increasing oxidation time for all the specimens.

### 4.5.2 SEM Plan View Results

#### *4.5.2.1 SEM Images*

SEM plan view images of the ZMG 232 specimens after 50 h and 502 h of oxidation are displayed in Figure 4-41.

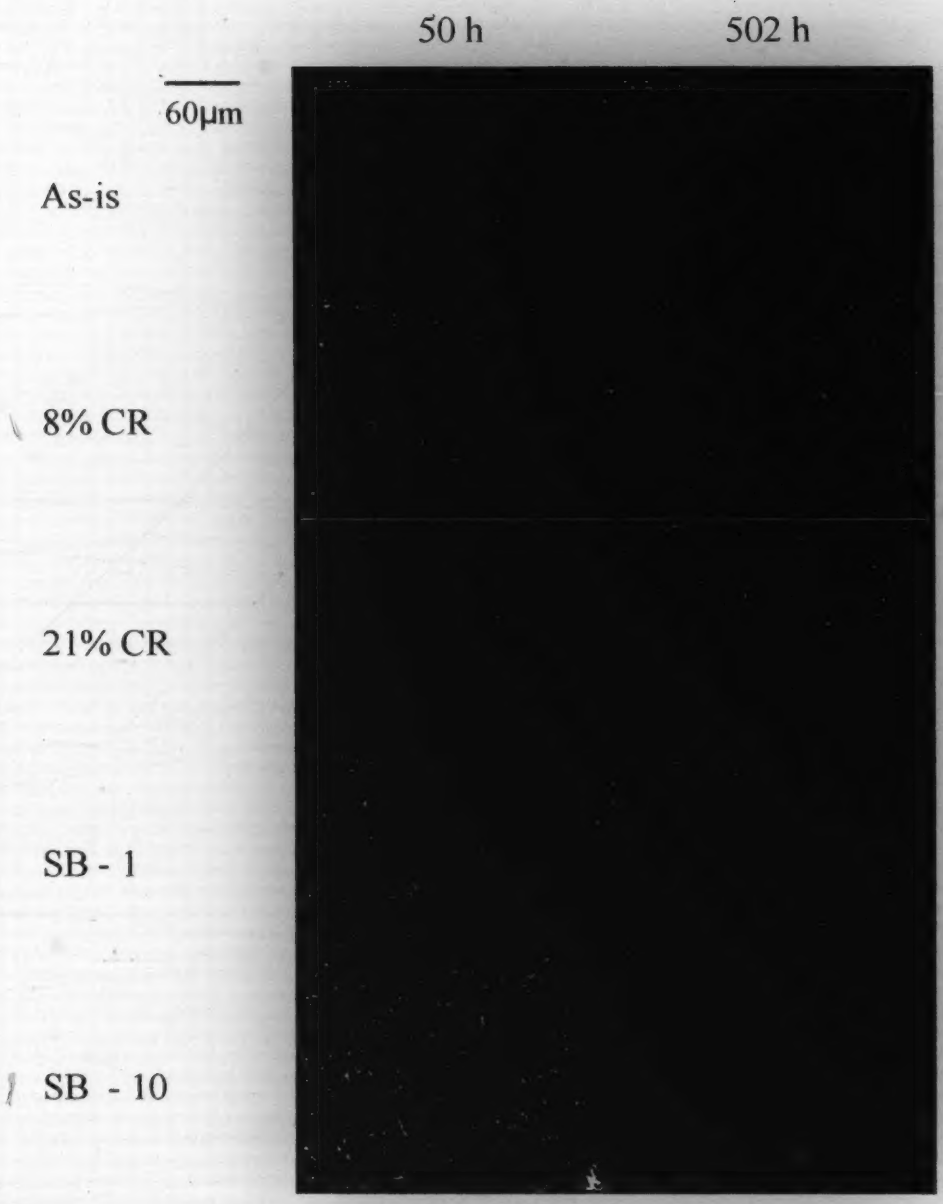


Figure 4-41. SEM Plan View Images of ZMG 232 Specimens After 50 h and 502 h of Oxidation.

After 50 h, it can be seen that a continuous oxide scale has formed on the surface on all the specimens. The appearance of the oxide scale on the as-is and rolled specimens is similar: the oxide is relatively even and smooth. For the sandblasted specimens, the surface roughness produced by the sandblasting treatment is still visible and the oxide scale is much rougher than for the as-is and rolled specimens.

After 502 h of oxidation, the oxide scale is much thicker than after 50 h for all the specimens. For the as-is specimens, the roughness of the oxide scale has increased. For the sandblasted specimens, oxide growth has caused the roughness of the initial sandblasting treatment to become less evident. It appears that the oxide scale on the sandblasted specimens is thicker than the oxide on the as-is or rolled specimens.

#### *4.5.2.2 EDX Analysis*

In order to compare the composition of the oxide scale on the ZMG 232 specimens, EDX analysis of a fairly large area (~200μm x ~200μm) was performed for each of the specimens. Quanitiative analysis of the EDX spectra was done and the Cr:Mn and Cr:Fe ratios were calculated for each specimen after 50 h and 502 h of oxidation. The results of this analysis are presented in Table 4-23.

Table 4-23. Cr:Mn and Cr:Fe Ratios from Quantitative EDX Analysis of the Oxide Scale for ZMG 232 Specimens.

| Surface Treatment | Cr:Mn | | Cr:Fe | |
|---|---|---|---|---|
| | 50 h | 502 h | 50 h | 502 h |
| As-Is | 2.7 | 1.2 | 2.4 | 8.2 |
| Rolled 8% | 3.1 | 1.3 | 3.1 | 6.9 |
| Rolled 21% | 2.7 | 1.2 | 2.2 | 6.4 |
| Sandblasted 1 Pass | 2.7 | 1.6 | 1.3 | 8.2 |
| Sandblasted 10 Passes | 2.9 | 1.7 | 1.3 | 8.3 |

Table 4-23 indicates two general trends for all specimens: an increase in the amount of Mn relative to Cr and an increase in the amount of Cr relative to Fe from 50 h to 502 h. However, after 50 h, since the oxide scale is much thinner, it is likely that the EDX

analysis is including information from the steel substrate. Therefore, a comparison of the Cr:Mn and Cr:Fe ratios after 502 h would provide more valuable information.

For the Cr:Mn ratios, the amount of Mn relative to Cr is larger for the as-is and rolled specimens than for the sandblasted specimens. For the Cr:Fe ratios, Table 4-23 shows that the relative amount of Cr enrichment is higher for the as-is and sandblasted specimens than the rolled specimens. This indicates that there is a greater amount of Fe present in the oxide scale of the rolled specimens than for the as-is or sandblasted specimens.

### 4.5.3 SEM Cross Section Results

#### *4.5.3.1 SEM Cross Section Images*

SEM cross section images of the ZMG 232 specimens are shown in Figure 4-42. The oxide scales for all specimens have a similar morphology with an inner, continuous chromia layer and outer spinel particles. In general, the relative amount of spinel compared to chromia appears to be largest for the as-is specimen, which confirms the XRD and EDX results. The relative amount of spinel on the sandblasted 10 passes specimen is larger than for any of the other treated specimens; however, the thickness of the spinel layer is much less uniform than for any of the other specimens. Figure 4-42 also indicates that the thickness of the oxide layer is more uniform for the as-is and rolled specimens than for the sandblasted specimens. For all the specimens, rounded dark regions, some of which are enclosed by a rectangle, are visible towards the inner portion of the oxide scale. EDX point analysis revealed that these areas show significant Si enrichment but also some Al enrichment. All the specimens have dark regions in the steel below the oxide scale, either circular areas or thin "lines". Some of these areas are indicated with arrows. The most obvious example is the large dark circular region for the 10 passes specimen. EDX analysis of these regions revealed the presence of significant Al enrichment as well as some Si enrichment. It is likely that these regions are areas where internal oxidation has occurred.

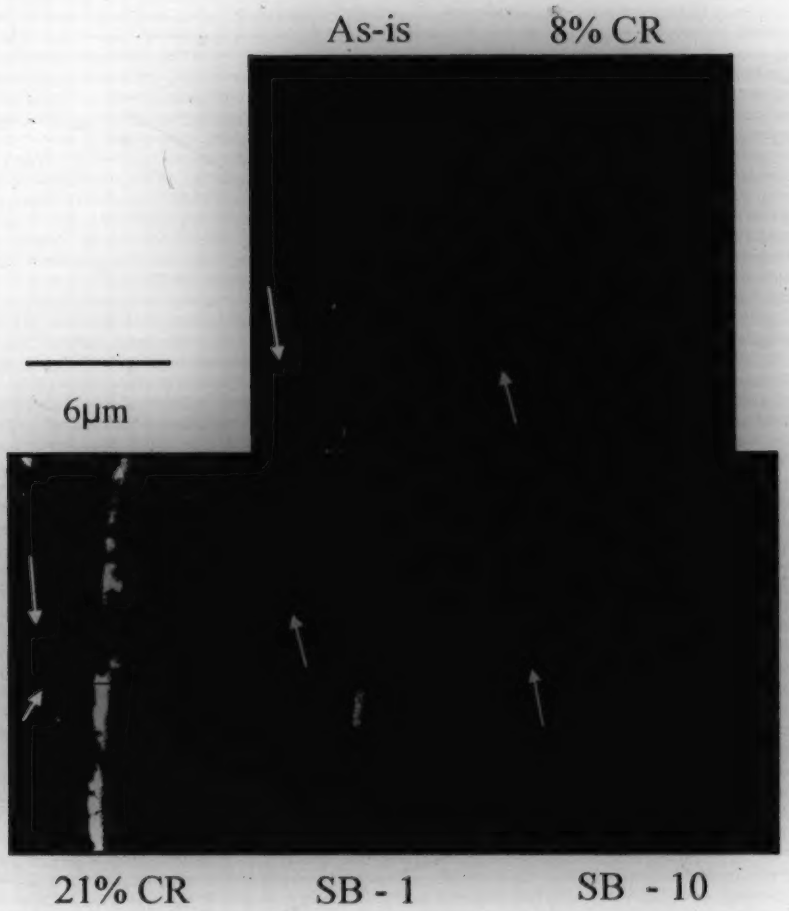


Figure 4-42. SEM Cross Section Images of ZMG 232 Specimens After 502 h of Oxidation.

From the images presented in Figure 4-42, the oxide thickness for each specimen was determined as described in section 4.3.3.1. The results of this analysis are listed in Table 4-24.

Table 4-24. Oxide Layer Thickness for ZMG 232 Specimens.

| Surface Treatment | Oxide Layer Thickness (μm) | |
|---|---|---|
| | Mass Gain | SEM Image |
| As-is | 1.17 | 3.91 ± 0.65 |
| Rolled 8% | 1.33 | 3.69 ± 0.71 |
| Rolled 21% | 1.39 | 3.70 ± 0.54 |
| Sandblasted 1 pass | 1.26 | 3.28 ± 1.26 |
| Sandblasted 10 passes | 1.30 | 4.34 ± 0.83 |

Table 4-24 indicates that the cross section thickness measurements do not follow the same trend as the mass gain data. However, considering the variable thickness of the oxide scales, the correlation between the thicknesses calculated from the mass gain data using the bulk density value for chromia and the measured cross section thicknesses is not too bad. Since the measurements were taken from a very small region of the oxide scale, the area selected for the measurement may not have been representative of the overall oxide scale thickness. This was particularly likely for the sandblasted specimens, for which the oxide scale thickness was much less uniform than for the other specimens. The reason for taking oxide scale thickness measurements at such a high magnification is that at lower magnifications, although the measured area was more representative, it was more difficult to accurately identify the metal/oxide interface. Table 4-24 also indicates that the measured values of oxide scale thickness were larger than the oxide thicknesses based on mass gain measurements by a factor of 2.5 to 3.

#### *4.5.3.2 EDX Analysis*

In order to compare the spinel composition of the ZMG 232 specimens, EDX spectra were taken from the outer region of the oxide scale in the cross section samples. From quantitative analysis of these spectra, the Cr:Mn and Cr:Fe ratios were determined for each specimen. The results of this analysis are displayed in Table 4-25.

Table 4-25. Cr:Mn and Cr:Fe Ratios From Quantitative EDX Analysis of the Spinel for ZMG 232 Specimens.

| Surface Treatment | Cr:Mn | Cr:Fe |
|---|---|---|
| As-Is | 0.8 | 4.6 |
| Rolled 8% | 1.5 | 6.4 |
| Rolled 21% | 0.8 | 3.7 |
| Sandblasted 1 Pass | 1.2 | 4.9 |
| Sandblasted 10 Passes | 1.2 | 5.4 |

From Table 4-25, it is clear that the Cr:Mn ratio in the spinel is higher in general for the treated specimens than for the as-is specimen. This indicates that the relative amount of Mn in the spinel is lower for the treated specimens than for the as-is specimen. The Cr:Fe ratio for the as-is specimen is also higher in general for the treated specimens than for the as-is specimen, indicating that the relative amount of Fe in the spinel phase is higher for the as-is specimen than for the treated specimens. The exception is the rolled 21% specimen, for which the relative amount of Fe is higher than the as-is specimen.

#### *4.5.3.3 EDX Linescans*

EDX Linescans were collected for the as-is, rolled 21%, and sandblasted 10 passes specimen. These linescans are displayed in Figures 4-43 through 4-45.

In Figure 4-43, the linescan indicates that Fe is depleted in the oxide relative to the steel. A small increase in the Fe trace is seen towards the outer portion of the oxide scale, indicating that some Fe is most likely present in the spinel phase. Chromium is enriched in the oxide scale compared to the level in the steel, in particular in the inner portion of the oxide scale. Manganese is segregated to the outer region of the oxide scale. Silicon has segregated to the metal/oxide interface to form a silica layer. Aluminum appears to have also segregated to the metal/oxide interface, forming a layer of alumina below the silica layer. Zirconium does not appear to be present in the oxide scale. This is not surprising considering that Zr is a carbide former and thus should be present in carbide form in the bulk of the steel. The signal for La is not very strong and it is difficult to determine from the EDX linescan if it is present in the oxide scale. Although Ni is

present in ZMG 232 steel, it does not appear to be present in the oxide scale as the only significant Ni signal is from the Ni plated layer.

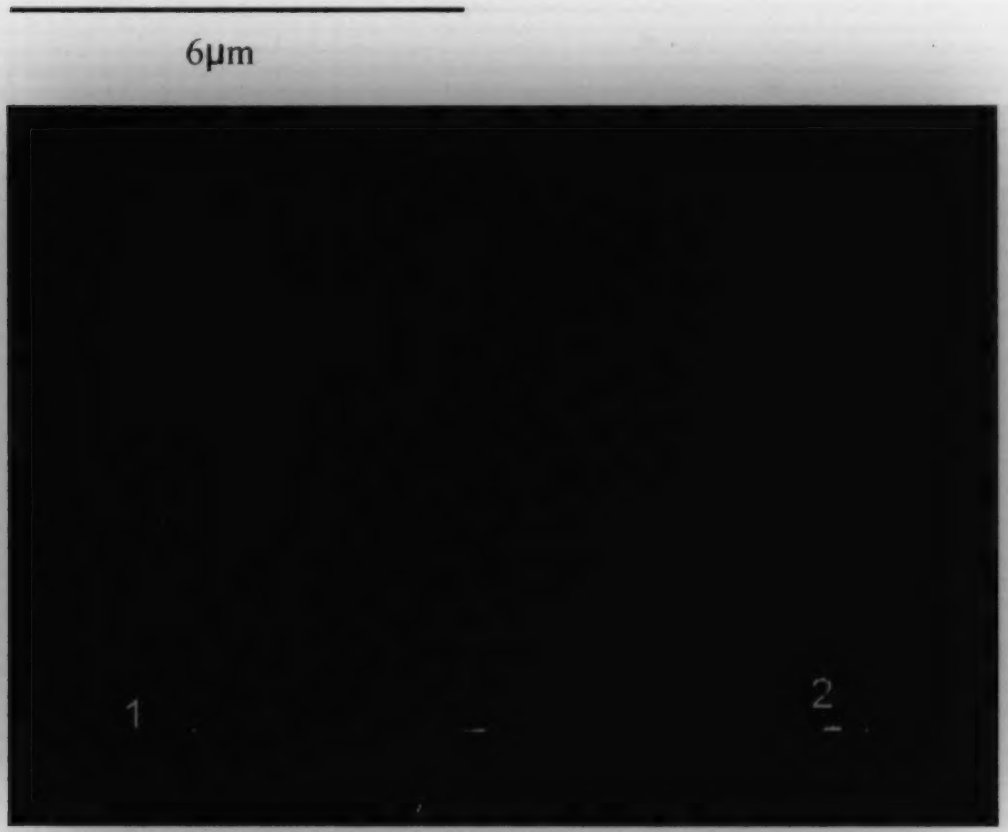


Figure 4-43. EDX Linescan for ZMG 232 As-Is Cross Section After 502 h.

The linescan presented in Figure 4-44 for the rolled 21% specimen is similar to that presented in Figure 4-43. The only significant difference between the two linescans is that for the rolled specimen, the linescan crosses over a region of internal oxidation. In this area, which appears dark in the SEM image, both Al and O are present, indicating that internal alumina formation has occurred.

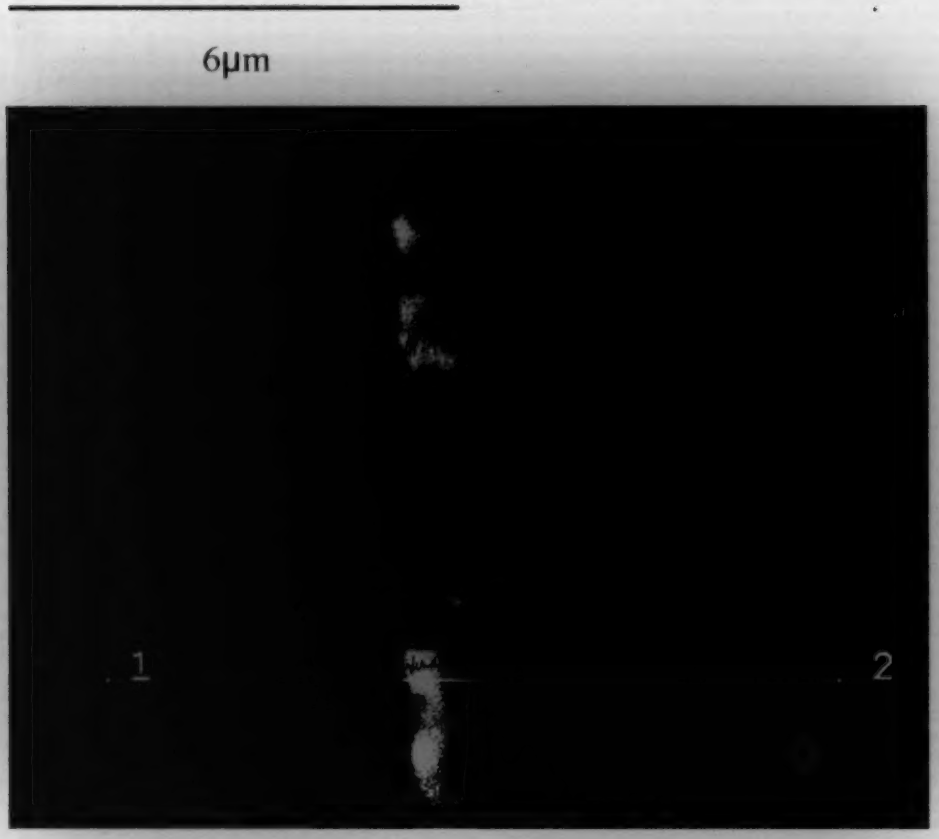


Figure 4-44. EDX Linescan for ZMG 232 Rolled 21% Cross Section After 502 h.

The linescan presented in Figure 4-45 is slightly more complicated than the other two linescans. Well below the metal/oxide interface, an increase in the Al and O traces are seen. This could be evidence of internal oxidation. As the linescan approaches the metal/oxide interface, the Al and O levels again increase. However, the Cr and Mn levels are also high at this location, suggesting that spinel formation has occurred at the interface between the steel substrate and alumina. The alumina could either have formed by internal oxidation or been introduced as a particle by the sandblasting treatment. Closer to the metal/oxide interface, an Al peak followed by a Si peak is observed, indicating the formation of alumina and silica layers at the metal/oxide interface as in the other ZMG 232 specimens. After this point, the distribution of the elements in the oxide scale is similar to the other two linescans.

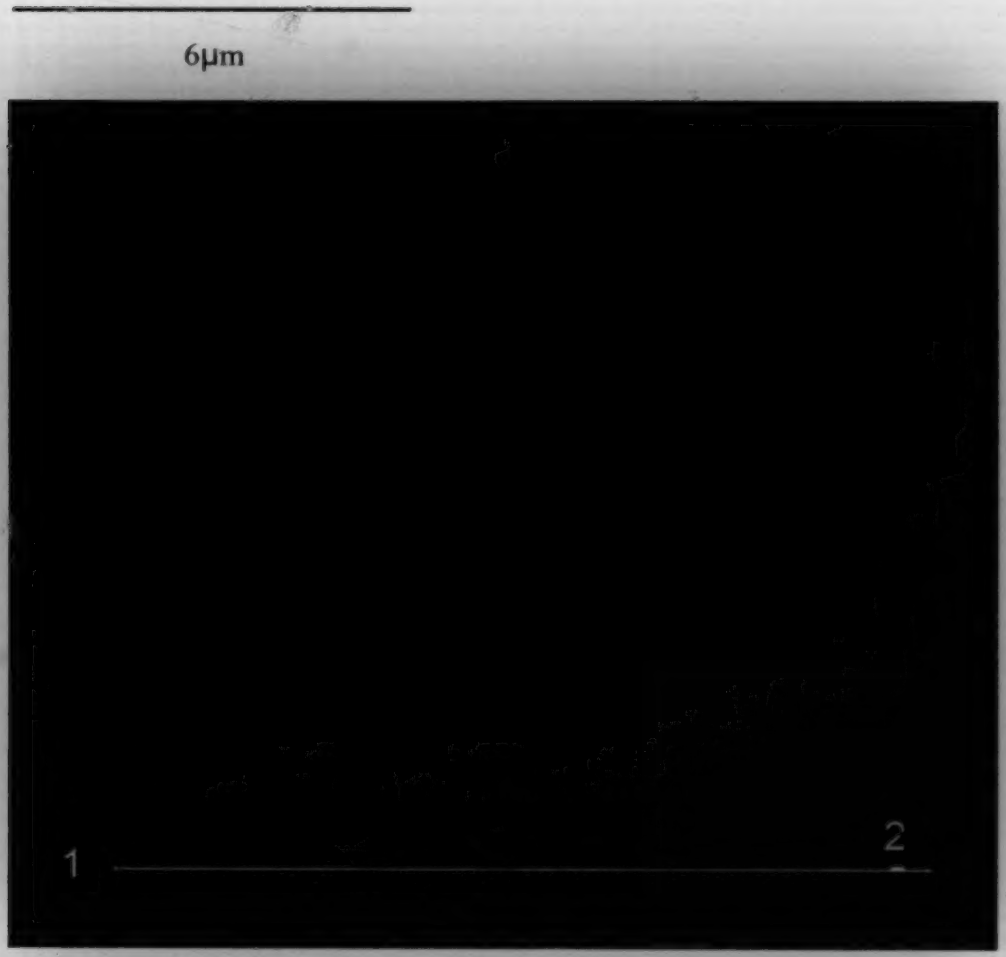


Figure 4-45. EDX Linescan for ZMG 232 Sandblasted 10 Passes Cross Section After 502 h.

### 4.5.4 SIMS Results

#### *4.5.4.1 Native Oxide*

In order to study the distribution of elements present in the oxide scale of the ZMG 232 specimens prior to oxidation at 800°C, SIMS analysis was carried out. The depth profile that was obtained is displayed in Figure 4-46.

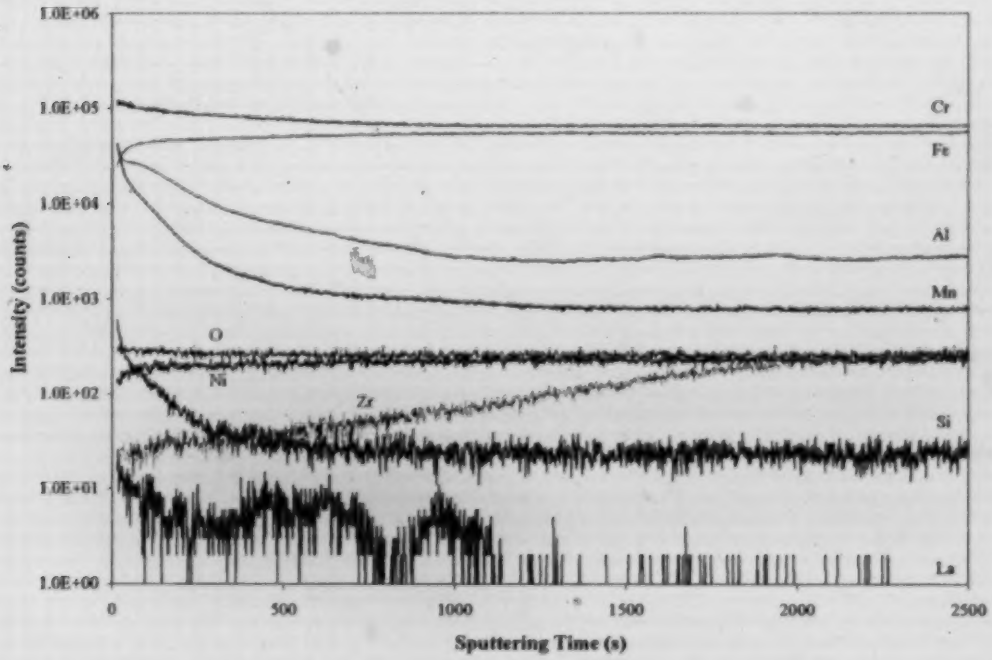


Figure 4-46. SIMS Depth Profile of ZMG 232 Native Oxide.

From Figure 4-46, it can be seen that there is a reduced amount of Fe compared to the bulk level in the ZMG 232 native oxide. Chromium is enriched in the native oxide with respect to its level in the bulk of the steel. Silicon, Al, and Mn are all segregated to the surface of the native oxide. The Al signal shows a plateau at the metal/oxide interface, indicating that some Al may also be present in this location. Neither Ni nor Zr appear to be present in the oxide scale. Although the La signal is quite noisy, it appears that La has segregated to the oxide scale and could be depleted in the bulk of the steel.

#### *4.5.4.2 Oxidized Specimens*

In order to study the early stages of oxide formation, SIMS depth profiling was carried out on ZMG 232 as-is, rolled 21%, and sandblasted 10 passes specimens that were oxidized for 15 minutes at 800°C. The resulting profiles are shown in Figure 4-47.

a)

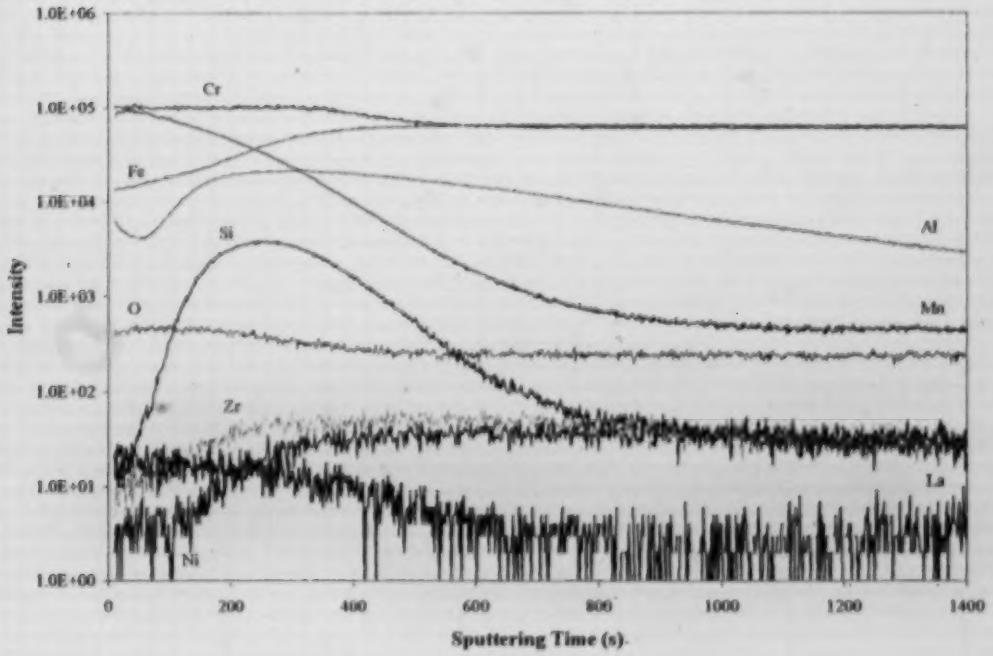

b)

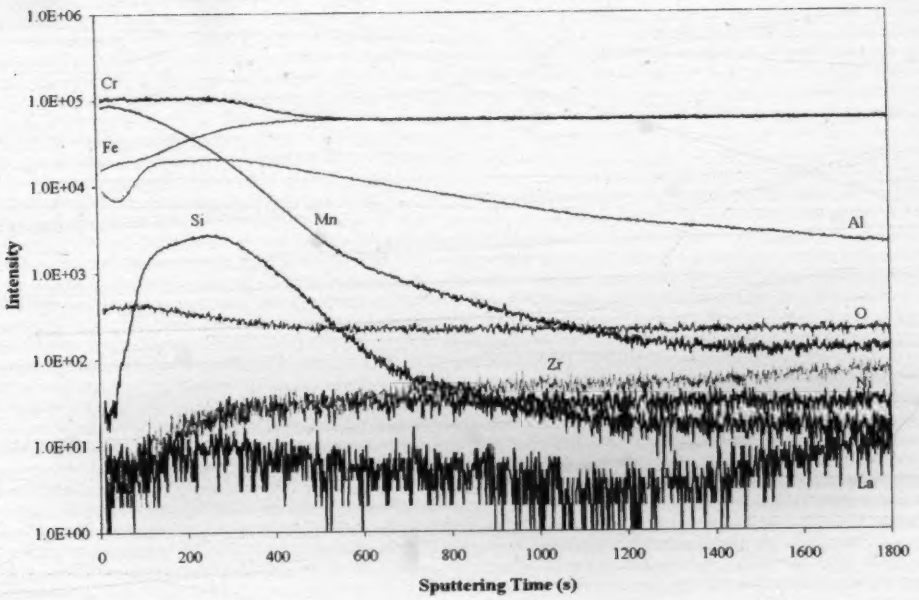


c)

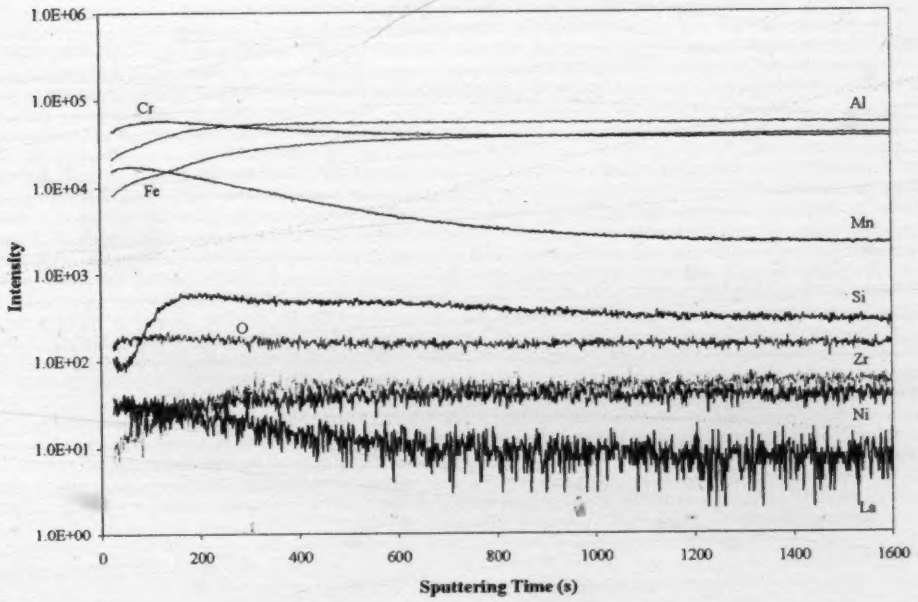


Figure 4-47. SIMS Depth Profile of ZMG 232 Specimens Oxidized for 15 Minutes at 800°C. a) As-Is; b) Rolled 15%; c) Sandblasted 10 Passes.

The same trends are observed for all the profiles. Iron is depleted in the oxide layer relative to the amount present in the bulk of the steel. Chromium is enriched throughout the oxide layer relative to the amount present in the steel. Manganese is concentrated at the surface of the oxide scale. There appears to be a small amount of Si present at the surface of the oxide layer; however, most of the Si has segregated to the metal/oxide interface. As for the native oxide, Zr and Ni are present in the oxide scale. Lanthanum is enriched in the oxide scale compared to the amount present in the bulk of the steel. For the as-is and rolled specimens, Al is present at the surface of the oxide scale as well as at the metal/oxide interface. For the sandblasted specimen, the Al level is relatively constant through the steel and decreases through the oxide. The segregation of Al to either the oxide surface or the metal/oxide interface is not observed for the sandblasted specimen, most likely because of the averaging effect of the rough sandblasted surface. The SIMS depth profile for the sandblasted specimen appears more "rounded" than for the other two specimens, likely a result of an averaging effect due to the surface roughness resulting from the sandblasting treatment.

#### *4.5.4.3 Estimated Scale Thickness*

By examining the SIMS depth profiles presented in Figure 4-47, it can be seen that, although the distribution of the elements in the oxide scale is similar for all three profiles, the scale thickness varies depending on the surface treatment. Estimates of scale thickness values for the ZMG specimens were determined using the procedure described in section 4.3.4.3. The estimated scale thickness values are presented in Table 4-26.

Table 4-26. Estimated Scale Thicknesses Corresponding to ZMG 232 SIMS Depth Profiles.

| Treatment | Oxidation Conditions | Approximate Scale Thickness (nm) | | Si Peak (nm) | Al Peak (nm) |
|---|---|---|---|---|---|
| | | Method 1 | Method 2 | | |
| As-is | none | 151 | - | - | - |
| As-is | 800°C, 0.25 h | 133 | 89 | 49 | 65 |
| Rolled 21% | 800°C, 0.25 h | 125 | 76 | 50 | 58 |
| Sandblasted 10 passes | 800°C, 0.25 h | 201 | 67 | 40 | - |

From Table 4-26, it appears that the native oxide is quite thick on the ZMG 232 specimen. However, according to method 1 (best fit exponential decay curve) of

determining the scale thickness, the native oxide is thicker than the oxide scale that formed on both the as-is and rolled specimens after 15 minutes of oxidation at 800°C. This obviously is not likely. It is likely that the estimated thickness value for the native oxide is larger than the true value due to the difficulty in defining the metal/oxide interface when the Cr profile shows a gradual decline. Both methods indicate that the thickness of the oxide scale on the as-is specimen is larger than that for the rolled specimen. However, method 1 indicates that the scale thickness is largest for the sandblasted specimen, whereas method 2 (midpoint of Cr profile) concludes that the sandblasted specimen has the thinnest oxide scale. The position of the Si peak, which should correspond to the metal/oxide interface, is in agreement with method 2. A distinct Al peak at the metal/oxide interface could not be identified for the sandblasted specimen However, the position of the Al peak indicates that the oxide scale on the rolled specimen is thinner than that on the as-is specimen, which was also found by both methods of determining the approximate scale thickness. In general, the scale thickness values obtained using method 2 are closer to the Si and Al peak locations, indicating that method 2 is a more accurate way of determining estimated scale thickness values than method 1.

### 4.5.5 XPS Analysis

#### *4.5.5.1 Native Oxide*

XPS depth profiling was used to determine how the chemical state of the elements present in the native oxide varied through the depth of the oxide scale. Figure 4-48 shows the XPS peak plots for Cr, Fe, Mn, Si, and Al. Nickel and La were not analyzed as they were found to overlap with the Fe peaks. Zirconium was analyzed; however, the signal was very noisy and no clear peaks were observed.

Figure 4-48a shows that Cr is initially present entirely in the oxide form. The Cr oxide peak remains as sputtering continues with a Cr metal peak also appearing and increasing in intensity. The oxide peak finally disappears, indicating that the steel substrate has been reached.

a)

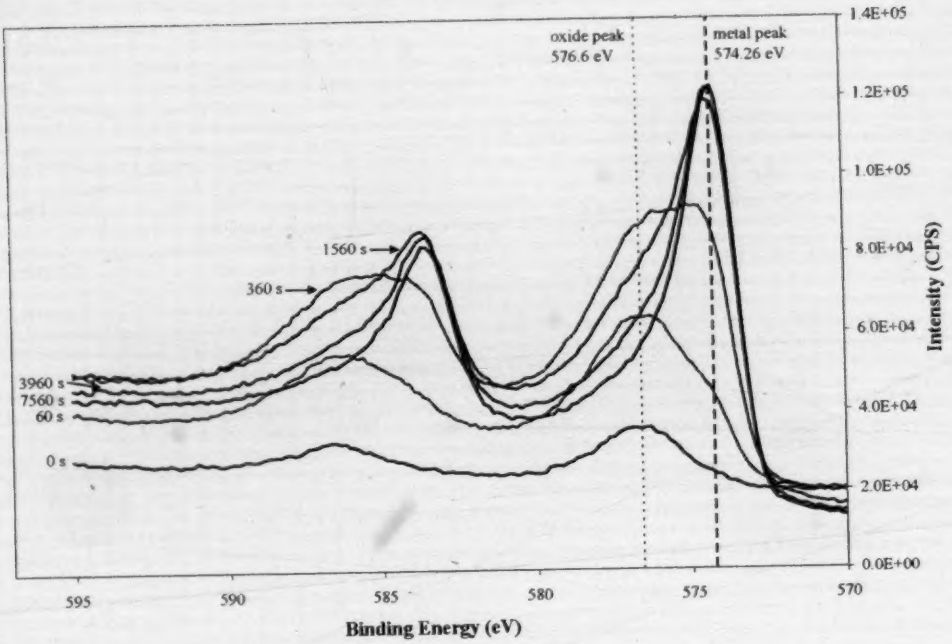
oxide peak
576.6 eV
metal peak
574.26 eV
1560 s
360 s
3960 s
7560 s
60 s
0 s
1.4E+05
1.2E+05
1.0E+05
8.0E+04
6.0E+04
4.0E+04
2.0E+04
0.0E+00
Intensity (CPS)
595
590
585
580
575
570
Binding Energy (eV)

b)

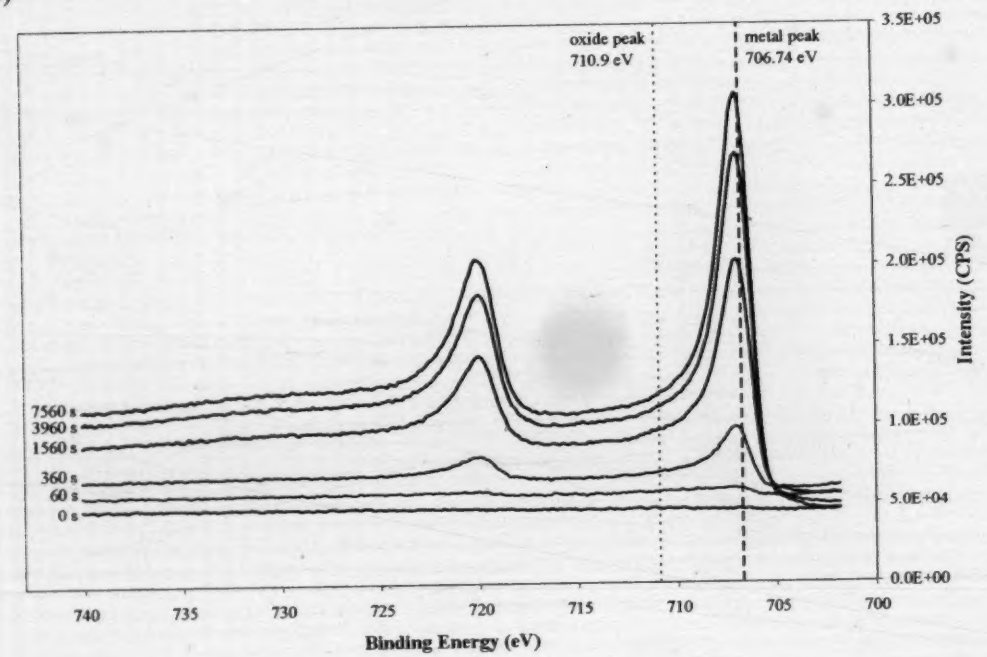
oxide peak
710.9 eV
metal peak
706.74 eV
7560 s
3960 s
1560 s
360 s
60 s
0 s
3.5E+05
3.0E+05
2.5E+05
2.0E+05
1.5E+05
1.0E+05
5.0E+04
0.0E+00
Intensity (CPS)
740
735
730
725
720
715
710
705
700
Binding Energy (eV)

c)

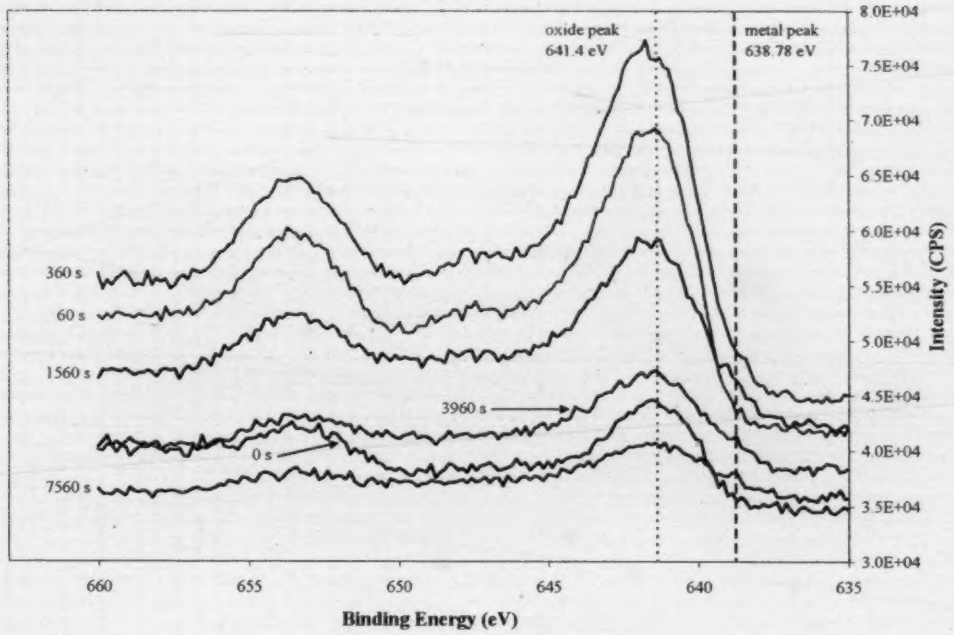
oxide peak
641.4 eV
metal peak
638.78 eV
360 s
60 s
1560 s
3960 s
0 s
7560 s
8.0E+04
7.5E+04
7.0E+04
6.5E+04
6.0E+04
5.5E+04
5.0E+04
4.5E+04
4.0E+04
3.5E+04
3.0E+04
Intensity (CPS)
660
655
650
645
640
635
Binding Energy (eV)

d)

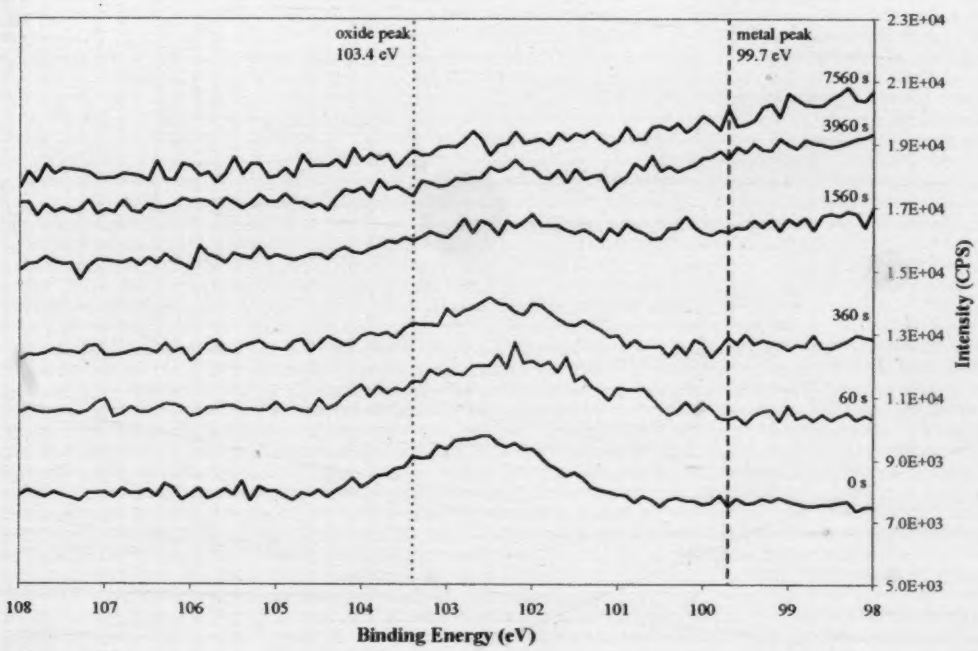
oxide peak
103.4 eV
metal peak
99.7 eV
7560 s
3960 s
1560 s
360 s
60 s
0 s
2.3E+04
2.1E+04
1.9E+04
1.7E+04
1.5E+04
1.3E+04
1.1E+04
9.0E+03
7.0E+03
5.0E+03
Intensity (CPS)
108
107
106
105
104
103
102
101
100
99
98
Binding Energy (eV)

e)

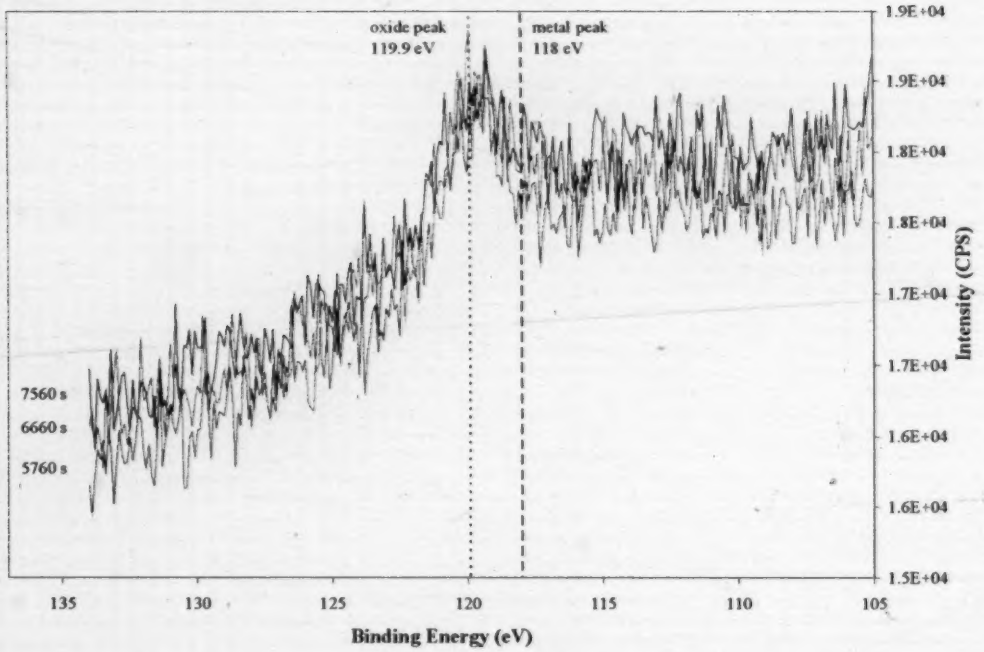


Figure 4-48. XPS Peak Plots for ZMG 232 Native Oxide. a) Cr 2p; b) Fe 2p; c) Mn 2p; d) Si 2p; e) Al 2s.

For Fe, Figure 4-48b shows that, initially, no Fe peaks are seen. After some sputtering, a small Fe metal peak is present. As sputtering continues, the Fe metal peak increases in intensity. These results suggest that very little Fe in oxide form is incorporated in the ZMG 232 native oxide.

Figure 4-48c shows the presence of Mn in oxide form throughout the oxide scale. The Mn oxide peak intensity is larger in the outer region of the native oxide, indicating that the majority of the Mn is segregated to the surface of the native oxide.

For Si, Figure 4-48d indicates that Si is present in the oxide form and has segregated to the surface of the native oxide. No metal Si peak is observed despite the fact that 0.4 wt% Si is present in the bulk of the steel. This may be due to the presence of a depleted zone

in the steel below the metal/oxide interface, or simply because the amount of Si is too low relative to the other elements (Cr and Fe) to be detected.

Figure 4-48e indicates that Al is present at the metal/oxide interface in oxide form. An Al 2p oxide peak was also detected at the surface of the oxide scale, indicating that Al in oxide form has also segregated to the surface of the oxide scale.

#### *4.5.5.2 Oxidized Specimens*

Due to the similarities in the SIMS depth profiles between the three ZMG 232 specimens, as well as the averaging effect present in the profile of the sandblasted specimen, XPS depth profiling was only carried out on the as-is specimen oxidized at 800°C for 15 minutes. The XPS peak plots for Cr, Fe, Mn, Si, and Al, are shown in Figure 4-49. Again, Ni and La were not analyzed. No clear peaks were present for Zr as the signal was noisy.

From Figure 4-49a, it can be seen that, initially, all the Cr is in the oxide form. The Cr oxide peak persists for a long time. After sputtering for more than 3000 s, a metal peak appears. The Cr metal peak increases in intensity while the oxide peak decreases in intensity with further sputtering, indicating a transition from the oxide scale to the steel substrate.

Initially, a small amount of Fe is present in the oxide form. The peak countinues throughout the top portion of the oxide scale; then, a small metal peak appears. The metal peak increases in height and the oxide peak disappears, indicating a transition to the steel substrate. The transition from oxide peak to metal peak occurs at around the same time as the Si oxide peak appears, indicating the presence of the metal/oxide interface. This suggests that Fe in the oxide form is present throughout the oxide scale.

From Figure 4-49c, it can be seen that, initially, a strong Mn oxide peak is present. This peak remains intense throughout the outer portion of the oxide scale. As sputtering continues, the intensity of the Mn oxide peak decreases. No Mn metal peak is observed and the Mn oxide peak does not completely disappear, which indicates that the oxide scale may not have been completely sputtered through.

a)

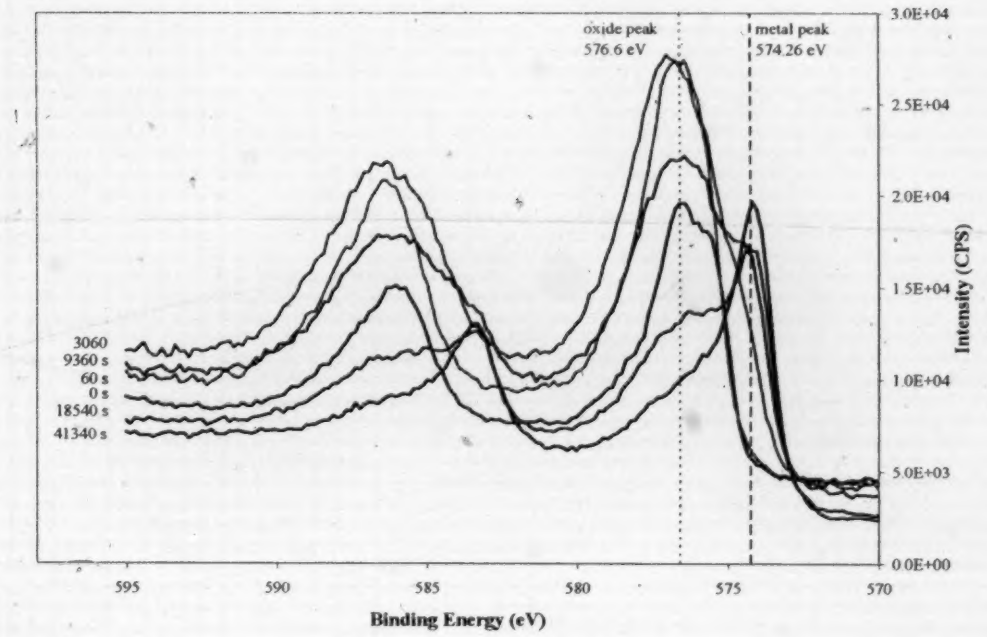
oxide peak
576.6 eV
metal peak
574.26 eV
3060
9360 s
60 s
0 s
18540 s
41340 s
3.0E+04
2.5E+04
2.0E+04
1.5E+04
1.0E+04
5.0E+03
0.0E+00
Intensity (CPS)
595
590
585
580
575
570
Binding Energy (eV)

b)

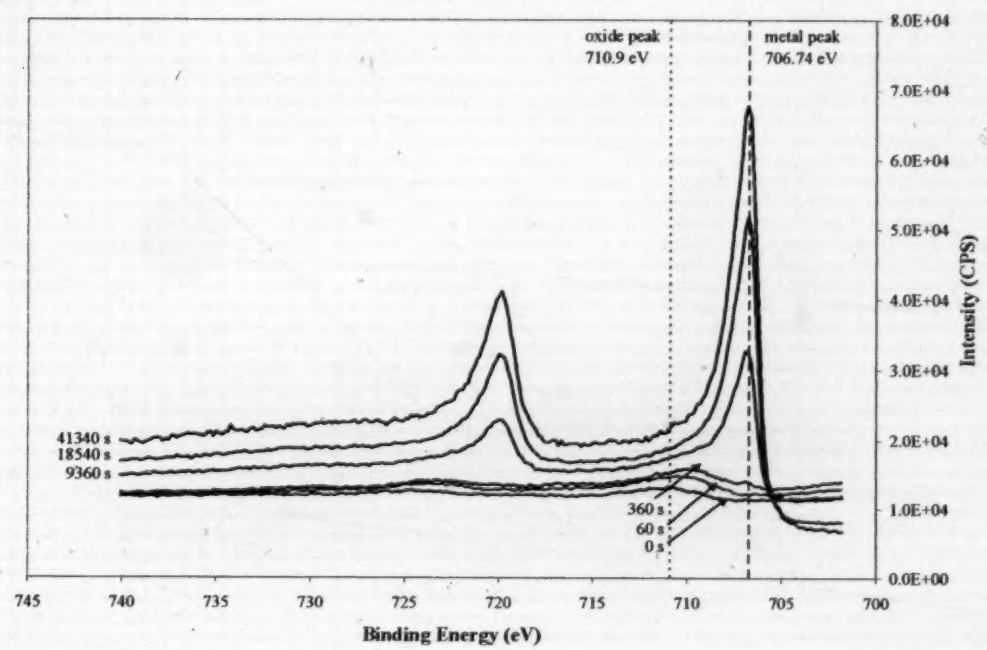
oxide peak
710.9 eV
metal peak
706.74 eV
41340 s
18540 s
9360 s
360 s
60 s
0 s
8.0E+04
7.0E+04
6.0E+04
5.0E+04
4.0E+04
3.0E+04
2.0E+04
1.0E+04
0.0E+00
Intensity (CPS)
745
740
735
730
725
720
715
710
705
700
Binding Energy (eV)

c)

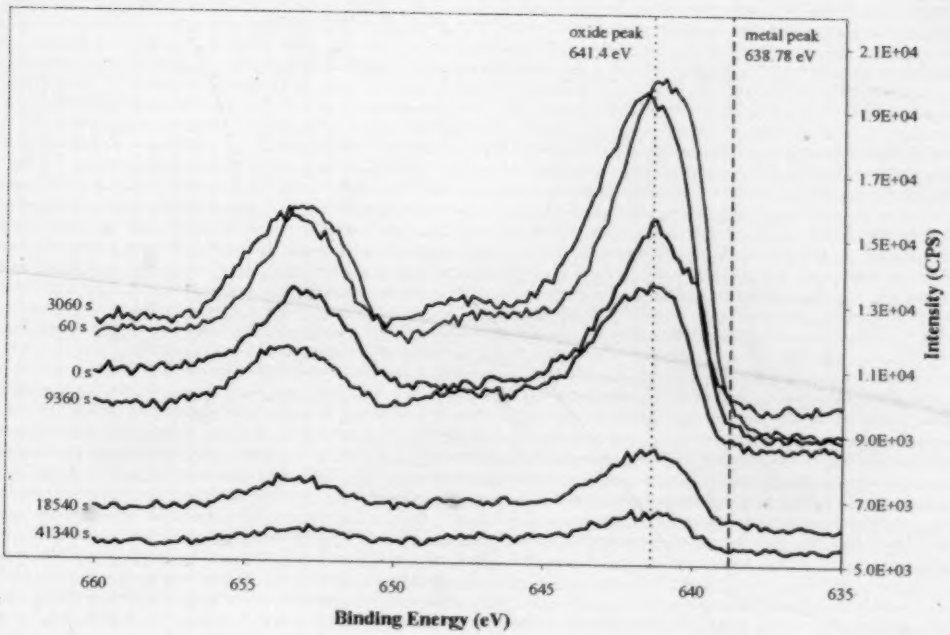
oxide peak
641.4 eV
metal peak
638.78 eV
3060 s
60 s
0 s
9360 s
18540 s
41340 s
2.1E+04
1.9E+04
1.7E+04
1.5E+04
1.3E+04
1.1E+04
9.0E+03
7.0E+03
5.0E+03
Intensity (CPS)
660
655
650
645
640
635
Binding Energy (eV)

d)

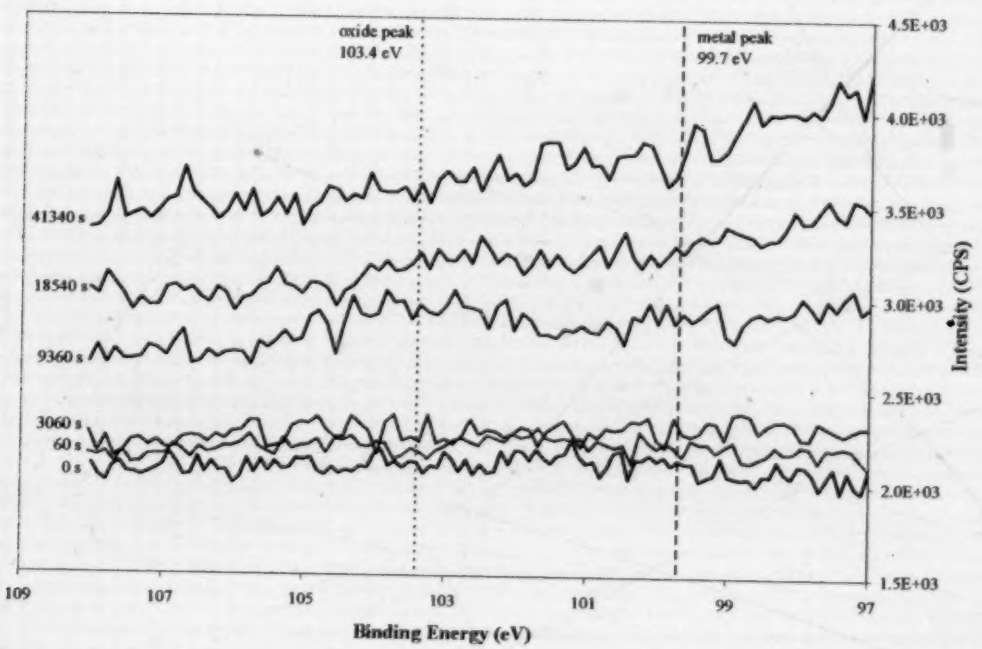
oxide peak
103.4 eV
metal peak
99.7 eV
41340 s
18540 s
9360 s
3060 s
60 s
0 s
4.5E+03
4.0E+03
3.5E+03
3.0E+03
2.5E+03
2.0E+03
1.5E+03
Intensity (CPS)
109
107
105
103
101
99
97
Binding Energy (eV)

e)

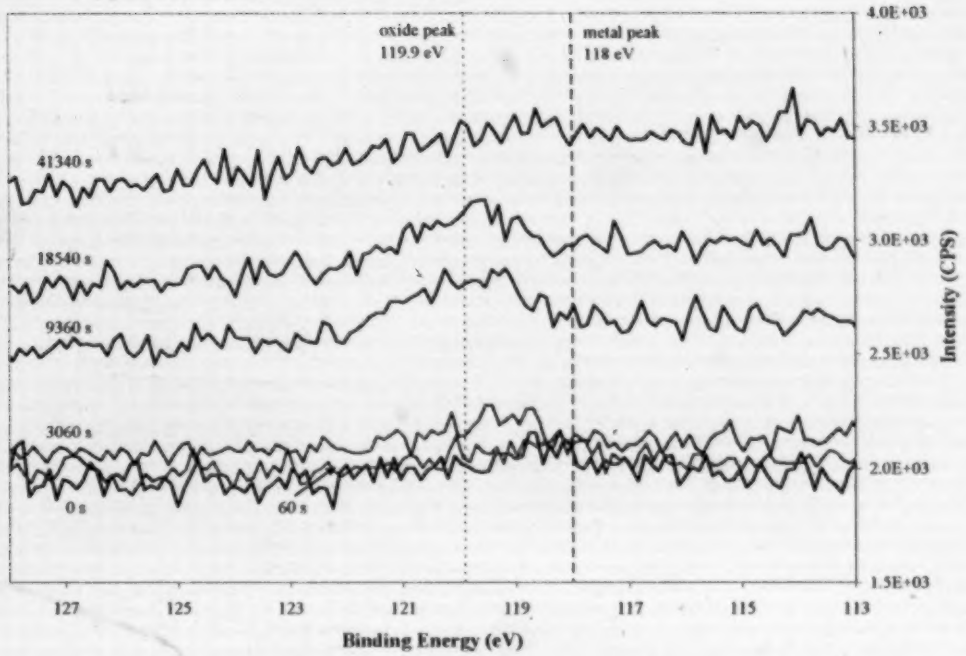


Figure 4-49. XPS Peak Plots for ZMG 232 As-Is Specimen Oxidized for 15 Minutes at 800°C. a) Cr 2p; b) Fe 2p; c) Mn 2p; d) Si 2p; e) Al 2s.

For Si, Figure 4-49d indicates that a Si oxide peak is present only at the metal/oxide interface, indicating the segregation of Si to from a layer of silica at the metal/oxide interface.

The Al peak plot is similar to that for Si. A strong Al oxide peak is present at the metal/oxide interface, indicating the segregation of Al to the metal/oxide interface where an alumina layer forms.

### 4.5.6 Summary of ZMG 232 Results

The mass gain results presented in Section 4.1 indicated that the treated specimens had a higher mass gain during oxidation than the as-is ZMG 232 specimen. The SEM cross section thicknesses did not clearly show the same trend. However, the difference in the oxide thicknesses calculated from the mass gain results was not very large between the different samples, and the agreement was not too bad considering the variability of the oxide thickness measurements. In addition, a limited area was used for the thickness measurements and may not have been representative of the cross section as a whole. This is particularly true for the sandblasted specimens, for which the SEM cross section images revealed that the oxide section thickness was much less uniform than for the as-is and rolled specimens.

XRD analysis of the ZMG 232 specimens, following 502 h of oxidation at 800°C, revealed that, for all specimens, the oxide layer consisted of two oxide phases: $Cr_2O_3$ and $(Mn,Cr)_3O_4$ spinel. EDX linescans of the SEM cross sections indicated that Cr was present throughout the oxide but at a higher amount in the inner chromia layer, and that Mn was predominately present in the outer spinel particles. SIMS analysis revealed a similar trend after short term oxidation, and XPS analysis confirmed that both Cr and Mn were in the oxide form. Iron was found by both EDX and SIMS to be depleted in the oxide scale relative to the Fe level in the bulk of the steel; however, XPS analysis showed that some Fe in oxide form was present in the oxide scale. Silicon and Al were found by both EDX and SIMS analysis to be segregated to the metal/oxide interface, and XPS confirmed that these elements were in oxide form. This points to the formation of insulating silica and alumina layers at the metal/oxide interface during oxidation of ZMG 232 at 800°C. Nickel and Zr were shown, by a combination of EDX linescans and depth profiling, to be absent from the oxide scale. Although the amount of La in the steel was too small to be detected in the EDX linescans, SIMS analysis showed La to be segregated to the oxide scale. The oxidation state of the La was not determined by XPS due to interference with both the Fe and Ni signals.

Although the same oxide phases, chromia and spinel, were present in the oxide scale on all the specimens, the relative amount of spinel was found to vary depending on the treatment condition. XRD analysis indicated that the as-is specimen formed relatively more spinel compared to the treated specimens, and that the rolled specimens had slightly

more spinel than the sandblasted specimens. The SEM cross section images confirmed the presence of more spinel on the as-is specimen compared to the other specimens. For all specimens, XRD analysis indicated that the relative amount of spinel increased with oxidation time. This was confirmed by EDX analysis of the plan view specimens, which revealed that the amount of Mn relative to Cr increased for all specimens, from 50 h to 502 h of oxidation at 800°C. Plan view EDX analysis also indicated that the amount of Cr relative to Fe increased from 50 h to 502 h of oxidation. This is most likely because the thickness of the oxide scale increased during oxidation, and thus the EDX analysis after 50 h incorporated some information from the steel substrate, whereas the analysis after 502 h did not.

EDX analysis of the plan view specimens, after 502 h of oxidation time, indicated that the amount of Mn relative to Cr was highest for the as-is and rolled specimens and lower for the sandblasted specimens. These results confirm the XRD analysis indicating that the relative amount of spinel was lowest for the sandblasted specimens. EDX analysis of the oxidized cross sections revealed that the amount of Mn relative to Cr in the spinel was greater for the as-is than for the treated specimens.

EDX analysis of the oxidized plan view specimens also found that the relative amount of Cr compared to Fe was higher for the as-is and sandblasted specimens than for the rolled specimens. However, EDX analysis of the spinel phase from the oxidized cross sections indicated that the relative amount of Cr compared to Fe in the spinel phase was lowest for the as-is specimen and higher for the treated specimens. This suggests that, although more Fe is present in the oxide scale of the rolled specimens, it is not incorporated in the spinel phase.

SIMS and XPS analysis were also carried out on the ZMG 232 native oxide. The distribution of the majority of the elements in the native oxide was similar to the distribution seen after oxidation at 800°C. However, differences were seen in both the Si and Al profiles. In the native oxide, both Si and Al were segregated to the surface of the oxide scale in oxide form, whereas after oxidation at 800°C, these two elements were segregated to the metal/oxide interface where they formed insulating silica and alumina layers.

# 5 Discussion

## 5.1 Specific Mass Gain

For SOFC interconnect applications, it is important to reduce the overall scale thickness that forms on the interconnect during fuel cell operation (Quadakkers, et al. 2003). This is because thick scales result in interconnect dimensionsal changes which can reduce the load bearing ability of the interconnect (Quadakkers, et al. 2003). Also, thick oxide scales can block air and fuel channels, reducing fuel cell performance. Therefore, it is important for any candidate interconnect material that specific mass gain due to oxidation be as low as possible. In the long term oxidation experiments carried out under simulated SOFC cathode operating conditions (air, 800°C), it was found that the specific mass gain of ZMG 232 was significantly higher (by a factor of approximately 2, see Figures 4-11 through 4-13) than that for both 430 and 434. The 430 and 434 steels had similar specific mass gains with that of 434 being slightly smaller.

One reason for the difference in specific mass gain between the three steels is the amount of Cr available for oxide formation. 430 nominally contains 16-18% Cr, while 434 contains 19% Cr and ZMG 232 contains 22% Cr. 434 and ZMG 232 contain carbide forming elements that preferentially form carbides, allowing more Cr to be available for protective oxide formation. 430 does not contain additional carbide formers, meaning that the amount of Cr available for oxidation is reduced due to the formation of Cr carbides. First of all, it is important to determine whether or not enough carbide forming elements are added to 434 and ZMG 232 to tie up all the C. For 434, both Nb and Mo are added. As discussed in section 4.1.3, it is difficult to do an accurate calculation since two types of carbides, $M_7C_3$ and (Nb,Ti)C are formed and it is not known how much of each type of carbide is present. Also, the $M_7C_3$ type carbide contains some Cr and Fe in addition to Mo and Nb. An approximate calculation can be carried out by assuming that no Cr or Fe is involved in carbide formation, that all the Nb forms NbC, and that the Mo forms $Mo_2C$ (Smith. 1993). First, the steel composition (accounting for C, Cr, Fe, Mo, and Nb only) is converted to atomic percent assuming that the maximum allowable amount of C is present. This means that 0.55 at% C, 20.23 at% Cr, 0.21 at% Nb, and 1.15 at% Mo are present in the steel. Since Nb is the strongest carbide forming element, it is assumed that all the Nb will form NbC. This leaves 0.34 at% C available for carbide formation with Mo. Assuming that $Mo_2C$ will form, 0.69 wt% Mo is used to tie up the

remaining C, leaving 0.47 at% Mo in the bulk of the steel. This means that based on the amount of carbide formers added, all the C could be tied up in Nb and Mo carbides, leaving all the Cr in 434 available for oxide formation. In reality, both Cr and Fe are present in the $M_7C_3$ type carbides as shown in Figure 4-9b; therefore, not all the Cr will be available for oxide formation. Figure 4-9b also indicates that Nb does not account for more than half of the metal elements in $M_7C_3$; therefore, assuming that all the Nb forms NbC is not a bad assumption, from a compositional point of view. However, only a small amount of Mo is present in the $M_7C_3$ type carbides. Therefore, much more than the 0.47 at% Mo (the value that was calculated assuming that all the Mo forms $Mo_2C$) will be remaining in the bulk of the steel. Figure 5-1 is an isothermal section of the Fe-Mo-Nb phase diagram at 900°C. With 2 wt% Mo and 0.35 wt% Nb, Figure 5-1 indicates that a solid solution is formed. Therefore, it seems reasonable that at 800°C, any remaining Mo and Nb not used in oxide formation would exist in solid solution in the α-Fe matrix.

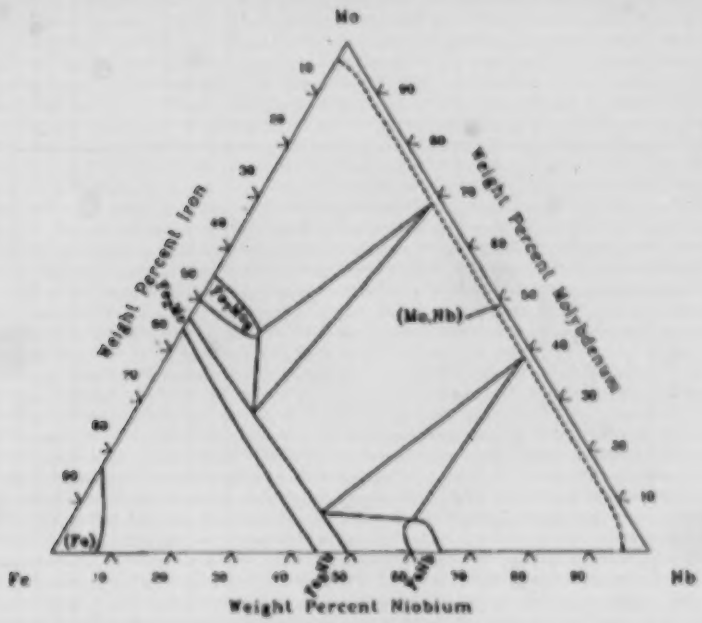


Figure 5-1. Isothermal Section of the Fe-Mo-Nb Phase Diagram at 900°C (ASM International. 2002b).

For ZMG 232, Zr is added to form ZrC. By converting the steel composition to atomic percent, it is found that 0.09 at% C and 0.13 at% Zr is present, meaning that all of the C will form ZrC, leaving 0.04 at% Zr in the bulk of the steel.

In order to determine the amount of Cr available for oxide formation in 430, the amount of Cr tied up in carbide formation must be calculated. By converting the steel composition (accounting only for C, Cr, and Fe) into atomic percent assuming the maximum allowable amount of C and the mimumum allowable amount of Cr, it is found that 0.55 at% C and 16.91 at% Cr are present in 430 steel. Assuming that all the C forms $Cr_{23}C_6$ (Jian, et al. 2003), it is found that 2.1 at% Cr is used up in carbide formation. This leaves 14.8 at% Cr, or 14.0 wt% Cr available for oxide formation in 430. Therefore, as a best case estimate, 434 has up to 5 wt% more Cr available for protective scale formation than 430, and ZMG 232 has up to 8 wt% more Cr.

According to the above order of magnitude calculation, since no significant spalling was found on any of the specimens except for the 430 thin specimen, it would seem that the higher specific mass gain for the ZMG 232 specimens can be correlated with the fact that this steel has more Cr available for protective oxide formation than either ZMG 232 or 434. However, since 434 has more Cr available for oxide formation than 430, it would be expected that the specific mass gain of the 434 specimens would be higher than for the 430 specimens, which was not the case.

It is possible that the specific mass gain findings would have been different under more severe oxidation conditions. In this study, no significant evidence of spalling was found for any of the specimens with the exception of the 430 thin as-is specimen. Because of this, it does not seem like the ability of the steels to repair their protective oxide scales following cracking or spalling was tested. In situations where cracking and spalling of the protective oxide occurs, such as under thermal cycling conditions, the specific mass gain of the 434 and ZMG 232 specimens may be reduced compared to the 430 specimens, since having more Cr available for oxide formaiton would allow the protective oxide to be more easily repaired. In addition, a number of studies have found that the addition of reactive elements (RE), such as La, can reduce the oxidation rate and improve protective oxide adhesion, especially under themal cycling conditions (Huang, et al. 2001, Riffard, et al. 2002, Zhu et Deevi. 2003b). Therefore, it is possible that the specific mass gain of ZMG 232 would be reduced compared to either 430 or 434 under

thermal cycling conditions. Thermal cycling conditions would also more closely ressemble the actual SOFC operating conditions, where the stack is subjected to thermal cycles during startup and shutdown.

From the specific mass gain results, it was determined that for all the specimens, the parabolic oxidation model was the best fit for the measured data. The parabolic oxidation model assumes that the oxidation process is diffusion limited, meaning that the rate of oxidation is limited by the rate of diffusion of either oxygen or metal ions across the oxide scale (Kofstad. 1998). This result is not surprising as parabolic oxidation is known to describe the oxidation of most metals at high temperatures (Kofstad. 1998). In this study, the parabolic rate constants were found to vary between 5 and 13 $x10^{-14}$ $g^2/cm^4 \cdot s$ for the 430 specimens, between 3 and 7 $x10^{-14}$ $g^2/cm^4 \cdot s$ for the 434 specimens, and between 20 and 29 $x10^{-14}$ $g^2/cm^4 \cdot s$ for the ZMG 232 specimens (Table 4-4). In order for ferritic stainless steels to be suitable for SOFC interconnect applications, a parabolic rate constant below $10^{-14}$ $g^2/cm^4 \cdot s$ is required, and a value below $10^{-15}$ $g^2/cm^4 \cdot s$ would be ideal (Antepara, et al. 2005). This value is based on a calculation of the oxide layer thickness at the target SOFC lifetime of 40 000 h assuming fully dense chromia forms (De Jonghe, et al. 2004). As none of the steels or treatment conditions resulted in a parabolic rate constant within the required range, it seems that further modifications are required in order for the steels tested to be suitable for SOFC interconnect applications.

In general, it was found that the specific mass gain for the treated specimens was higher than for the as-is specimens. The thickness of the specimens may have had an effect on the difference in mass gain between the treated and as-is specimens. This is because for a thinner specimen, a greater proportion of the overall specimen thickness would be affected by the surface treatment than for a thicker specimen. Since the thickness of the ZMG 232 specimens was 0.25 mm and that for the 430 and 434 specimens was approximately 1 mm, it would be expected that surface treatment would have a greater effect for the ZMG 232 specimens than for either the 430 or 434 specimens. By examining the parabolic rate constants listed in Table 4-4, it can be seen that, in general, the difference between the parabolic rate constants for the as-is and treated specimens was slightly larger for the ZMG 232 specimens than for the other 2 steels; however, the difference is not very large.

The effect of surface treatment on oxidation has been described previously in the literature. A major effect of surface treatment is that energy is stored in the surface region of a metal in the form of dislocations (Ostwald & Grabke. 2004, Rakowski, et al. 1996). In the early stages of oxidation, these dislocations act as fast diffusion paths, increasing the rate of transport of protective scale-forming elements to the metal surface. Assuming the oxidation temperature is higher than the recrystallization temperature, recovery and recrystallization then occur, resulting in the formation of a fine-grained surface microstructure. In the later stages of oxidation, following the annihilation of dislocations by recovery and recrystallization, it is these grain boundaries and subgrain boundaries that act as fast diffusion paths for scale-forming elements (Grabke, et al. 1998, Ostwald & Grabke. 2004, Rakowski, et al. 1996, Stokes, et al. 1989). Therefore, preferential oxidation of these scale-forming elements can result in easier formation of a protective oxide layer for a surface treated metal. Also, the increased transport of scale-forming elements from the bulk of the metal results in reduced depletion of scale-forming elements in the region directly below the metal/oxide interface. Therefore, the specific mass gain results may have been different if the specimens had been tested under thermal cycling conditions since repair of the protective oxide scale could be easier for the treated specimens than for the as-is specimens (Quadakkers, et al. 1994). It has also been reported that specimens that have undergone surface treatment form oxide scales with a reduced amount of porosity than those formed on untreated specimens (Leistikow, et al. 1987, Caplan & Cohen. 1966). A reduced amount of porosity would result in an increase in scale conductivity. Therefore, even though the scales formed on treated specimens were thicker than those on the as-is specimens, the resistivity may not have been higher. In order to confirm this, the conductivity of the oxide scales of both the treated and as-is specimens should be measured. Also, under SOFC operating conditions, one side of the interconnect is also exposed to the fuel environment. It is possible that the effect of surface treatment could be different in this environment where the formation of a protective oxide scale may not be as easy as in air.

In this study, oxidation was carried out at 800°C for 502 h. For 430 and 434, annealing treatments are typically carried out between 705 and 790°C (Douthett. 2002). Since the oxidation in this experiment was performed at a temperature above the typical anneal temperature range and for an extended period of time, it can be assumed that recovery and recrystallization did occur. It is known that it is easier to form a continuous protective oxide layer for a fine grained material than a large grained material (Leistikow,

et al. 1987, Grabke, et al. 1998). This is because, initially, oxide nuclei form at locations where grain boundaries intersect with the metal surface. These nuclei will be more closely spaced for a fine grained material, reducing the lateral diffusion distance required for the formation of a continuous protective layer. Therefore, a reduction in the grain size at the surface of the steel following recrystallization would have increased the rate of protective scale formation in the treated specimens.

The melting temperature range for the 430 and 434 steels is 1425 – 1510°C (1698 – 1783 K) (Washco & Aggen. 2002). In this work, oxidation of the stainless steel specimens was carried out at 800°C, which corresponds to 0.60 to 0.63 $T_m$, where $T_m$ is the melting temperature in K. In general, bulk diffusion becomes dominant at temperatures higher than 0.75-0.8 $T_m$, which for the ferritic stainless steels tested corresponds to a temperature range of 1000°C to 1150°C (Porter & Easterling. 1981). The oxidation experiments were carried out at a temperature that was lower than that where bulk diffusion would be expected to dominate; however, the temperature was still fairly high. Therefore, although the treated specimens would be expected to have increased grain boundary diffusion compared to the as-is specimens, at 800°C bulk diffusion would be fairly high in all specimens. In principle, the difference between the as-is and treated specimens could potentially be higher if the oxidation was performed at a lower temperature, where the contribution of bulk diffusion would be reduced and grain boundary diffusion would be more significant.

In order to quantitatively estimate the relative importance of bulk and grain boundary diffusion at 800°C, an order of magnitude diffusion calculation was carried out. The diffusion coefficients for bulk and grain boundary diffusion are represented by $D_l$ and $D_b$, respectively (Porter & Easterling. 1981). The change in diffusion coefficient with temperature is expressed in Equation 5-1 for bulk diffusion and Equation 5-2 for grain boundary diffusion (Porter & Easterling. 1981).

$$D_l = D_{l0} \exp\left(\frac{-Q_l}{RT}\right) \quad (5\text{-}1)$$

$$D_b = D_{b0} \exp\left(\frac{-Q_b}{RT}\right) \quad (5\text{-}2)$$

In Equations 5-1 and 5-2, $D_{l0}$ and $D_{b0}$ are the frequency factors for bulk and grain boundary diffusion, respectively, $Q_l$ and $Q_b$ are the activation energies for bulk and grain boundary diffusion, respectively, $R$ is the gas constant (8.314 J/mol·K), and $T$ is the absolute temperature in K.

In order to determine the relative importance of grain boundary diffusion, the case of steady-state diffusion through a sheet of material in which the grain boundaries are perpendicular to the sheet is considered. The geometry of one repeating unit is shown in Figure 5-2.

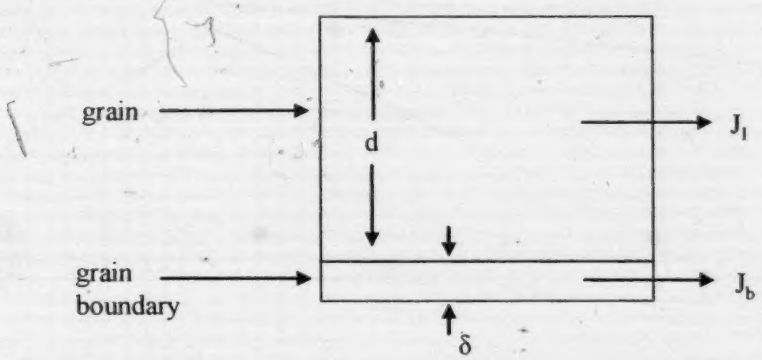


Figure 5-2. Geometry for Combining Grain Boundary and Lattice Diffusion.

In Figure 5-2, $J_l$ and $J_b$ are the fluxes of atoms diffusing through the lattice and grain boundary, respectively. If it is assumed that the concentration gradients in the lattice and along the grain boundary are equal, then the expressions for $J_l$ and $J_b$ are as follows (Porter & Easterling. 1981):

$$J_l = -D_l \frac{dC}{dx} \quad (5\text{-}3)$$

$$J_b = -D_b \frac{dC}{dx} \quad (5\text{-}4)$$

The actual contribution of grain boundary diffusion relative to the total amount of diffusion occurring at a given temperature depends on the ratio of the effective grain

boundary thickness $\delta$ to the grain size $d$ (Porter & Easterling. 1981). A typical value for $\delta$ is 0.5 nm (Porter & Easterling. 1981).

From Figure 5-2, the total flux of atoms through the metal sheet is equal to the sum of the flux of atoms through the grain and the flus of atoms through the grain boundary. The total flux $J$ can be written as follows (Porter & Easterling. 1981):

$$J = \frac{(J_b\delta + J_l d)}{d} = -\left(\frac{D_b\delta + D_l d}{d}\right)\frac{dC}{dx} \qquad (5\text{-}5)$$

From Equation 5-5, the apparent diffusion coefficient $D_{app}$ taking into account both bulk and grain boundary diffusion is as follows: (Porter & Easterling. 1981):

$$D_{app} = D_l + \left(\frac{\delta}{d}\right)D_b \qquad (5\text{-}6)$$

Using Equation 5-6, the relative contributions of grain boundary and bulk diffusion can be determined as a function of temperature. Two methods were used for this calculation. The first method used $D_0$ and $Q$ values for bulk and grain boundary diffusion that were found in a paper for Fe-10.18Cr and Fe-8.03Cr-0.17C in the temperature range of 743-1043 K (470-770°C) (Cermak, et al. 1996). The data used for this calculation is presented in Table 5-1.

Table 5-1. Data Used In First Diffusion Calculation (Cermak, et al. 1996).

| $D_{l0}$ ($m^2/s$) | $Q_l$ (J/mol) | $D_{b0}$ ($m^2/s$) | $Q_b$ (J/mol) |
|---|---|---|---|
| 2.6E-05 | 204000 | 6.8 | 244000 |

The relative contributions of bulk and grain boundary diffusion as a function of temperature were also calculated using bulk diffusion data from the Smithells Metals Reference Book for diffusion in a Fe-Cr binary alloy valid in the temperature range of 1073-1673 K (800-1400°C) (Brandes & Brook. 1998). As no diffusion data for grain

boundary diffusion was available in this reference, the calculation was carried out by assuming that $D_{b0} = D_{l0}$ and that $Q_b = 0.5Q_l$. The data used for this calculation is listed in Table 5-2.

Table 5-2. Data Used in Second Diffusion Calculation *(Brandes & Brook. 1998).

| Cr (wt%) | $D_{l0}$ ($m^2/s$)* | $Q_l$ (J/mol)* | $Q_b$ (J/mol) |
|---|---|---|---|
| 17 | 1.9E-05 | 218100 | 109050 |
| 20 | 1.8E-05 | 216900 | 108450 |

For both 430 and ZMG 232, the grain size was found to be in the range of 10 to 20μm, and that for 434 was between 25 and 35μm (Section 4.1.2). For the purposes of the two diffusion calculations, values in the middle of this range were used. Thus, for 430 and ZMG 232, $d$ was 15μm and for 434, the value of $d$ was 30μm.

The plots for 430 and 434 obtained using the first diffusion calculation based on the data in Table 5-1 are displayed in Figure 5-3. The result for ZMG 232 was the same as that for 430 since the two steels had approximately the same grain size.

Figure 5-3 indicates that for both 430 and 434, bulk diffusion dominates at the oxidation temperature of 800°C. Since surface treatment affects the grain boundary diffusion rate, Figure 5-3 suggests that the effect of surface treatment at 800°C should be relatively insignificant. In addition, the fact that the grain size for 434 is larger than that for either 430 or ZMG 232 should not have a large effect on the oxidation behaviour. However, contrary to what is generally accepted, Figure 5-3 indicates that for both 430 and 434, grain boundary diffusion is insignificant at lower temperatures and becomes more important as the oxidation temperature increases. This is a result of the data used in this calculation (Table 5-1). The activation energy for grain boundary diffusion determined by the authors of the paper was higher than that for bulk diffusion (Cermak, et al. 1996).

a)

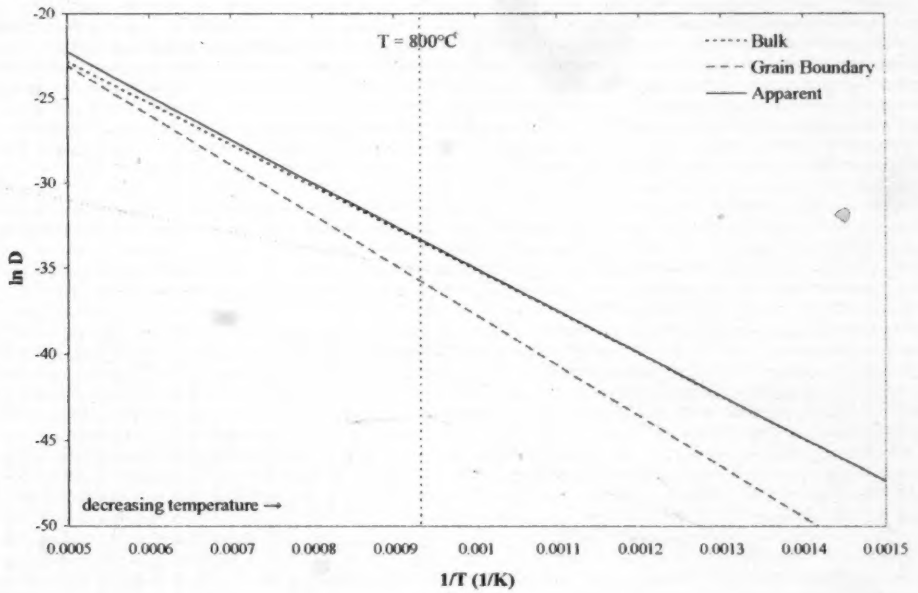


b)

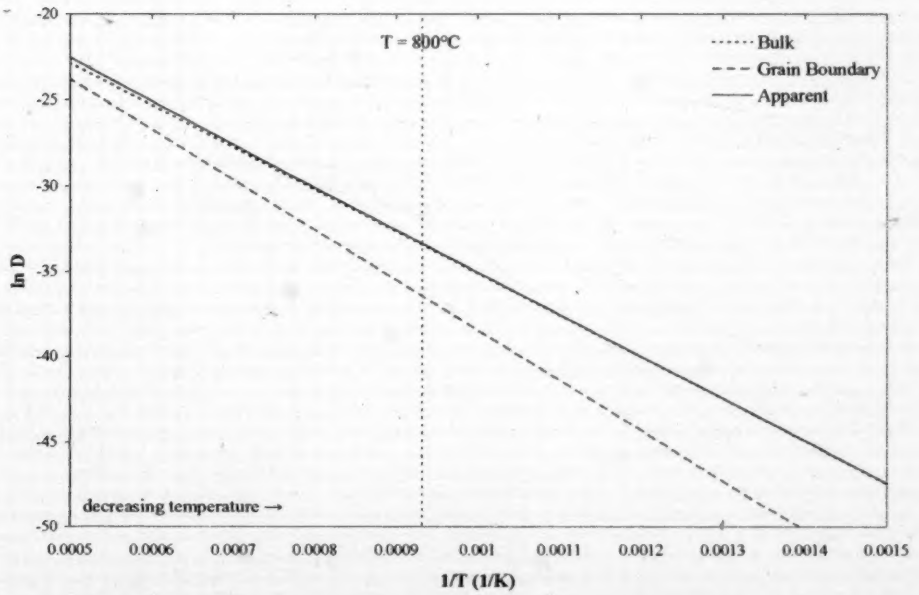


Figure 5-3. Relative Contributions of Bulk and Grain Boundary Diffusion as a Function of Temperature Based on Data in Table 5-1. a) 430; b) 434.

The justification given was that C atoms that had segregated to the grain boundaries interacted with diffusing Cr atoms (Cermak, et al. 1996). As a result, additional activation energy would be required in order to break the attraction between the Cr and C atoms (Cermak, et al. 1996). However, the Cr content of the steels used in the paper was lower than those used in this research (10.18% and 8.03% compared to 16-18% for 430, 19% for 434 and 22% for ZMG 232). With higher Cr contents, and particularly for 434 and ZMG 232 where additional carbide formers are added, it is much less likely that a significant amount of C would be segregated to the grain boundaries.

The plots for 430 and 434 obtained using the second diffusion calculation based on the data in Table 5-2 are displayed in Figure 5-4. Again, the plot for ZMG 232 is not shown as it was similar to that for 430.

a)

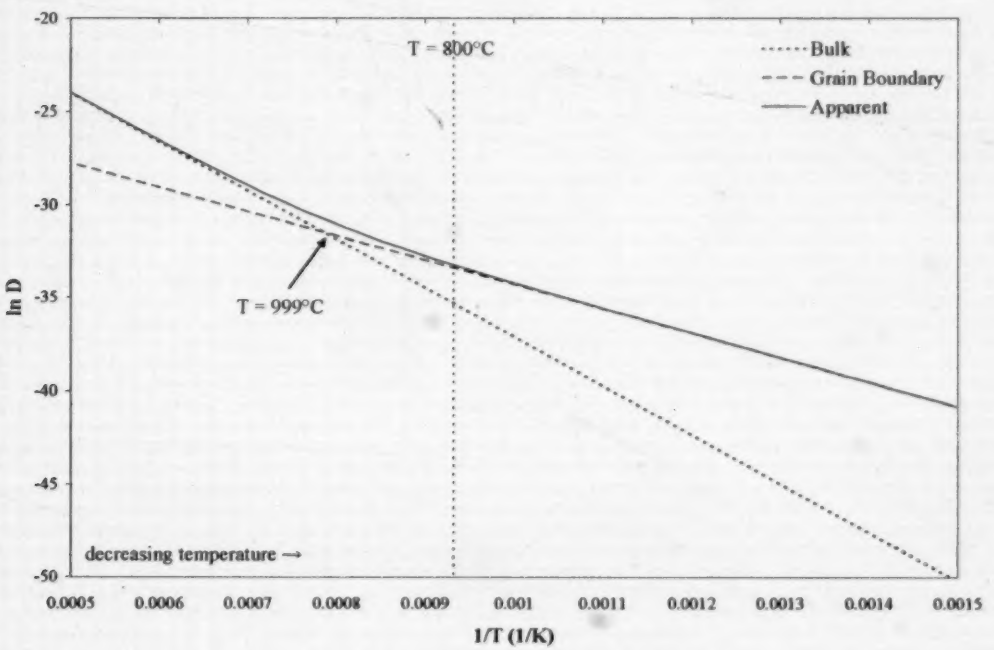

b)

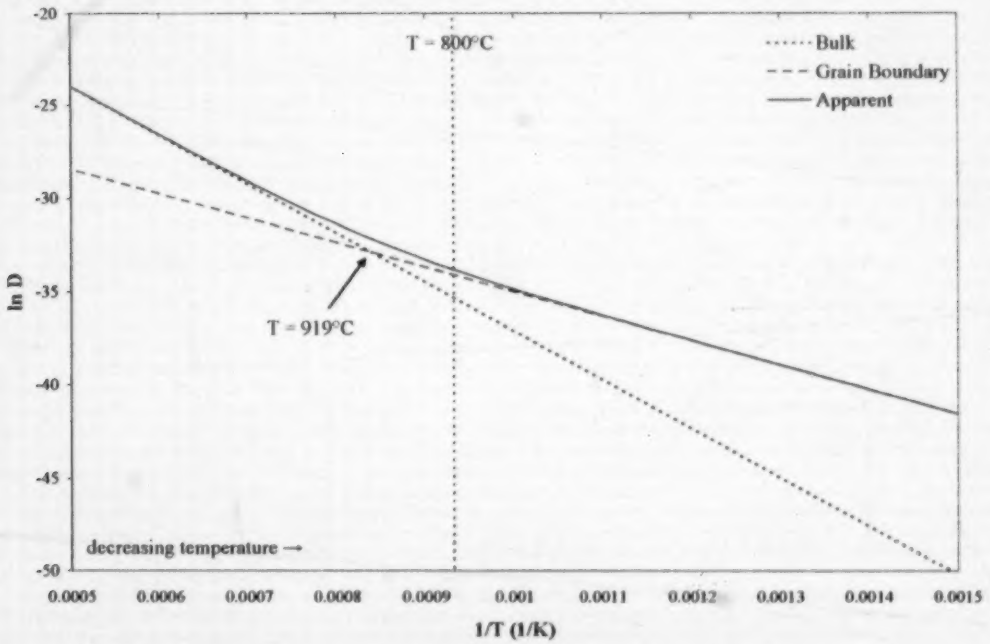


Figure 5-4. Relative Contributions of Bulk and Grain Boundary Diffusion as a Function of Temperature Based on Data in Table 5-2. a) 430; b) 434.

In this case, Figure 5-4 indicates for both 430 and 434 that at the oxidation temperature of 800°C, grain boundary diffusion is more significant than bulk diffusion. In both a) and b), the temperature at which $D_l = \left(\frac{\delta}{d}\right) D_b$ is shown. This temperature is lower for 434 because of the larger grain size of this steel. Figure 5-4 also indicates that at lower temperatures, grain boundary diffusion should be expected to dominate, whereas at high temperatures, bulk diffusion is more important. This trend is more in line with what is commonly expected and occurs because the activation energy for diffusion was assumed to be less for grain boundary diffusion than for bulk diffusion. However, this is the opposite of the trend observed in Figure 5-3. At this time, it is not clear which model is a better approximation for the steels used in this research.

According to the literature, the effect of surface treatment on oxidation rate is due to the fact that surface treatment introduces additional dislocations into the surface region of the

metal. Prior to recrystallization, these dislocations are supposed to increase the supply of scale-forming elements to the surface of the metal by acting as fast diffusion paths. Following recrystallization, the grain size of the metal in the surface region is reduced, and the increased number of grain boundaries results in more rapid transport of scale forming elements to the surface of the metal. In order to comfirm whether or not recrystallization significantly reduced the grain size of the treated specimens, etched cross sections of the 434 as-is and rolled 15% specimens that were oxidized for 15 minutes at 800°C were examined in the SEM. 434 was chosen because the initial grain size was larger, and therefore any change in grain size would be easier to see. The images are displayed in Figure 5-5.

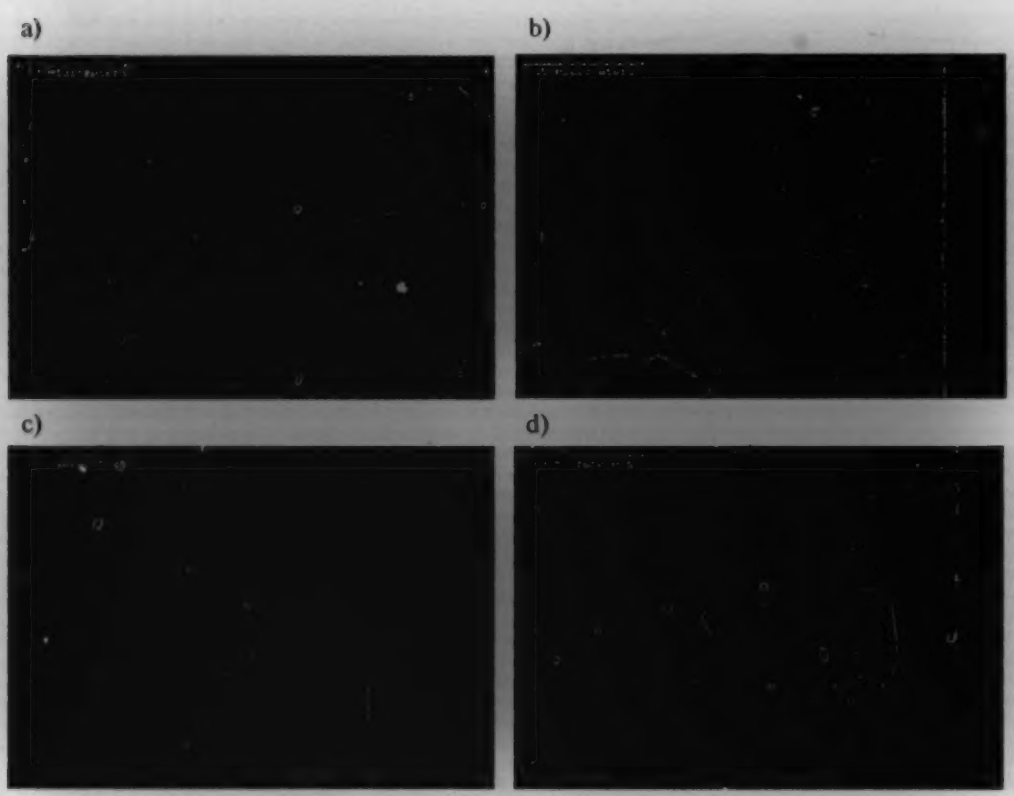


Figure 5-5. Grain Structure of 434 Specimens Oxidized for 15 Minutes at 800°C. As-Is Centre (a) and Surface (b) of Specimen; Rolled 15% Centre (c) and Surface (d) of Specimen.

Several differences between the as-is and rolled specimens are evident from Figure 5-5. First, in comparing Figure 5-5a and 5-5b, it can be seen that the grains are equiaxed and the grain size does not change significantly from the middle to the surface of the specimen. For the rolled specimen, the elongation of the grains due to the rolling treatment is seen clearly. In comparing Figure 5-5c and 5-5d, it can be seen that at the surface of the rolled specimen, the grains are slightly smaller and more equiaxed than in the centre of the specimen, indicating that at least some recrystallization of the surface region has occurred, resulting in an increased number of grain boundaries at the metal surface. Therefore, it seems reasonable that grain boundary diffusion could make a contribution to the oxidation behaviour of the treated specimens as seen in Figure 5-4. However, the SIMS results in Tables 4-12 (430), 4-19 (434) and 4-26 (ZMG 232) indicate that the location of the Si peak is not significantly different for the rolled specimens compared to the as-is specimens after 15 min of oxidation at 800°C, indicating that grain boundary diffusion has not observably affected the oxidation behaviour of the rolled specimens at this oxidation time.

It has been reported in the literature that the minimum amount of Cr required for protective scale formation is reduced as alloy grain size is reduced because of the increase in the grain boundary density which allows for more rapid transport of scale-forming elements to the surface of the alloy (Danielewski, et al. 2005). In section 4.1.2, it was found that the grain size of the 434 steel was approximately twice as large as for the other two steels. The resulting reduced rate of transport of Cr to the surface for the 434 steel could explain why the specific weight gain for 434 was lower than that for 430, despite 434 having more Cr available for protective oxide formation.

In the long term oxidation experiments, although it was seen that in general, the treated specimens had a higher specific mass gain than the untreated specimens, the difference between the treated and untreated specimens was not large. In the literature, it is stated that the effect of surface treatment on oxidation depends on the oxidation temperature (Dudala, et al. 2005, Leistikow, et al. 1987). At lower temperatures, the effect of surface treatment would be expected to be significant, as bulk diffusion rates are fairly low and the contribution of grain boundary diffusion is relatively high. However, the effect of surface treatment would not be as large since overall oxidation rates are fairly low at low temperatures because oxidation reaction rates are lower at lower temperatures. In intermediate temperature ranges, the effect of surface treatment would be the largest,

since oxidation rates are higher than at lower temperatures and because bulk diffusion rates are still fairly low, thus the contribution of grain boundary diffusion would still be significant. At high oxidation temperatures, surface treatment would not be expected to have a large effect on oxidation behaviour because bulk diffusion rates are quite high and factors such as grain boundary and dislocation density, both of which are influenced by surface treatment, would not have a significant effect on the overall diffusion rate. Based on the results of the diffusion calculation presented in Figure 5-3, the accepted trend may not apply under the conditions of this research. In order to be able to fully understand the relative contribution of grain boundary diffusion as a function of temperature for the steels studied in this work, experiments need to be carried out at other temperatures to determine whether or not a measureable change in specific mass gain occurs for treated specimens.

In the literature, studies have been carried out on pure iron in air and Incoloy 800 in superheated steam to determine the effect of oxidation temperature on whether or not surface treatment is beneficial, detrimental, or has no effect (Caplan & Cohen. 1966, Leistikow. 1981, Tomlinson & Blick. 1990). In this context, beneficial means that protective oxide formation is enhanced by surface treatment, resulting in a reduction in overall mass gain due to oxidation because the formation of non-protective, fast growing oxides is reduced or prevented. Detrimental means that mass gain due to oxidation is increased by surface treatment. In the study of Incoloy 800 (a Ni-Fe-Cr alloy containing 30-35% Ni, a minimum of 39.5% Fe, and 19-23% Cr) in superheated steam, it was found that surface treatment was beneficial for oxidation temperatures between 0.53 and 0.66 $T_m$. Surface treatment was detrimental for temperatures above 0.71 $T_m$, where the melting point range of Incoloy 800 is between 1357 and 1385°C (1630 and 1658 K) (Leistikow. 1981). Translating these results to ferritic stainless steels, surface treatment would be beneficial in the temperature range of 627 – 904°C, and detrimental at temperatures above 933°C. For pure iron in air, surface treatment was found to be beneficial for oxidation temperatures between 0.26 and 0.48 $T_m$, and to have no effect at temperatures above 0.51 $T_m$, where the melting temperature of pure iron is 1538°C (1811 °K). Translating these results to ferritic stainless steels, surface treatment would be beneficial in the temperature range of 168 - 583°C, and would have no effect at temperatures greater than 636°C. For this work, surface treatment was found to be slightly detrimental at an oxidation temperature of 800°C, which is not in agreement with the findings of either Incoloy 800 in superheated steam or iron in air. A comparison between this work and the

oxidation of iron in air may not be valid since the oxide scale formed on pure iron is not protective and thus a different mechanism is most likely involved. A comparison between this research and the oxidation behaviour of Incoloy 800 is more meaningful since this alloy forms a protective $Cr_2O_3$ scale. In this case, either the difference in material or in environment may account for the disagreement between the Incoloy 800 findings and those of this research.

Another factor to consider is the effect of oxidation time. Following recovery and recrystallization, grain growth should occur, which could cause the effect of surface treatment to disappear after long oxidation times. Since the target SOFC lifetime is 40 000 h, longer term oxidation experiments should be carried out to see if the increase in specific mass gain of the treated specimens relative to as-is specimens is maintained after longer periods of oxidation.

In this study, for all three steels, a higher specific mass gain corresponded to specimens that had undergone a higher rolling reduction. One reason for this is that the depth of the deformed region in a cold rolled metal increases with an increase in the percentage reduction in thickness (Sun, et al. 2004). This would mean that the recrystallized region would extend deeper into the metal, allowing for faster transport of scale-forming elements to the surface. Also, an increase in the amount of deformation would mean an increase in the number of dislocations in the surface region of the metal, producing a finer surface microstructure following recrystallization. In the literature, several studies have been done on the effect of the degree of cold rolling on oxidation behaviour. In a study of the oxidation of Inconel 625 (58Ni-1Co-21.5Cr-9Mo-5Fe) in air at 1000°C for up to 36 h, it was found that the mass gain due to oxidation decreased as the cold rolling reduction was increased from 10% to 30% (Khalid & Benjamin. 2000). A study of the oxidation of Incoloy 800 in superheated steam at 600°C for 1000 h also found that the weight gain due to oxidation decreased as the amount of cold work increased from 10% to 90% (Leistikow, et al. 1987). The latter study also found that the oxidation kinetics changed from parabolic to cubic to logarithmic as the rolling reduction was increased (Leistikow, et al. 1987). In the current study, the amount of rolling reduction did not change the oxidation kinetics. It is not clear why the current study showed an opposite trend to the two other studies in the literature (an increase instead of a decrease in the mass gain due to oxidation with an increase in the cold rolling reduction). The difference

in material or oxidation conditions may account for the discrepancy. In order to confirm the trend observed in this study, specimens with larger rolling reductions could be tested.

In general, the sandblasted specimens in this study had a higher mass gain than the as-is specimens. In the literature, several studies have also reported an increase in the mass gain due to oxidation following a sandblasting treatment. One study of several stainless steels containing between 9 and 20% Cr at 600°C for 100 h, in both air and reducing environments, found that the oxide scale thickness was larger for sandblasted specimens than for electropolished, polished, or ground specimens (Ostwald & Grabke. 2004). Similar results were reported in a study of 9% Cr steels containing Mo and 12% Cr steels containing Mo and V in air and reducing environments at 600°C for 100 h (Grabke, et al. 2004). However, a study of an iron based oxide-dispersion strengthened (ODS) FeCrAl alloy, annealed at 1000°C for up to 100 h, found that the oxide scale thickness formed on specimens that were sandblasted with alumina for 30 min was smaller than that on specimens that were polished with 1μm alumina paste (García-Alonso, et al. 2001). In theory, the increase in surface roughness produced by the sandblasting treatment would result in an increased oxide nucleation rate, not only because of the increased surface area of the rougher surface, but also because the sandblasted surface has more sharp edges and points which act as preferred nucleation sites (Taylor, et al. 1998). Although in this work, the difference in surface area between the sandblasted specimens and the other specimens was not found to be significant, the SEM images of the sandblasted specimens prior to oxidation confirmed the presence of sharp edges and points.

In this study, two different sandblasting processes were studied: 1 pass and 10 passes. The intention was that the 10 passes specimen would have increased surface deformation and roughness compared to the 1 pass specimen. However, for the 434 and ZMG 232 steels, the specific mass gains for the two sandblasting treatements were similar, while for the 430 steel, the sandblasted 1 pass specimen had a higher mass gain (Figures 4-11 through 4-13). The difference in the amount of deformation between the two sandblasting treatments may not have been significant enough to have a large effect on the specific mass gain. The depth of the surface layer that was deformed by the sandblasting treatment may have been the same for both the 1 pass and 10 passes treatment. In other studies, increasing the deformation from a sandblasting process has been accomplished by increasing the sand grain size. This was not done in this work in

order to replicate the conditions in industry, where only one size of alumina particle was used.

One criterion of a surface treatment is that it should uniformly deform the surface of a material so that an oxide scale of uniform thickness is produced (Van der Biest, et al. 1979, Zhu & Deevi. 2003b). For the sandblasted specimens, cross sections of the oxide layer revealed that this was not the case; the oxide thickness was found to vary significantly along the specimen surface. It is also important that a surface treatment does not introduce contaminant species to the surface of the alloy as this can result in an increase in the oxidation rate of the alloy (Leistikow. 1981). The impurities could either act as nucleation sites for oxide formation, or could themselves oxidize. For the 430 and 434 rolled specimens, rapidly growing clumps of oxide enriched with impurities (Ni, Sn, Cu, P, Si, and Al) were observed after 502 h of oxidation. In this case, impurities introduced during the rolling treatment may have acted as nucleation sites for oxide formation. This type of contamination could be prevented by using a rolling mill only used for steel; however, this may not be practical in an industrial setting. For the sandblasted specimens, alumina particles containing a small amount of Ti were found to be imbedded in the surface of the steel prior to oxidation. This type of contaminant may also have acted as a preferred nucleation site for oxide formation. It is unlikely that a cleaning process such as ultrasonic cleaning would be able to remove the alumina particles from the stainless steel substrate. In any case, an extensive cleaning process would be impractical in industry as it would be expensive and time consuming.

In this work, the effect of specimen thickness on oxidation behaviour was not clear. For the 434 thin specimen, the specific mass gain was slightly lower than for its thick counterpart while for the 430 thin specimen, the specific mass gain was significantly higher than for the 430 thick specimen (Figures 4-11 and 4-12). Additionally, for the 430 thin specimen, evidence of oxide spalling and subsequent repair was observed in the cross section specimen (Figure 4-21b).

Physical cracking of the oxide scale may have been responsible for the spallation of the oxide on the 430 thin specimen. In comparing the cross section images of the 430 thick and thin specimens (Figure 4-20), the amount of spinel is significantly larger for the thin specimen and the spinel is much more continuous. The increased amount of spinel in the oxide scale of the 430 thin specimen may have made the oxide layer more susceptible to

physical cracking. The thermal expansion coefficient (TEC) of 430 stainless steel is 11.4 x $10^{-6}$/°C, while that of $Cr_2O_3$ is 9.6 x $10^{-6}$/°C and that of $MnCr_2O_4$ is 7.2 x $10^{-6}$/°C (Wei. 2004). Because the TEC of both of the oxide phases is less than that of the stainless steel substrate, compressive stresses will develop in the oxide scale upon cooling (Bradford. 2002). Because of the difference in TEC between the two oxide phases, stresses will also be present at the interface between the chromia and spinel (Bradford. 2002). The ratio of the TEC of the stainless steel substrate to that of chromia is 1.2, while the ratio of the TEC of stainless steel to that of spinel is 1.6. Since the difference in TEC is larger between the steel and the spinel than between the steel and the chromia, larger thermal stresses will develop in scales that have a higher relative amount of spinel. However, the cracking of the oxide scale could also be due to the overall thickness of the oxide scale on the 430 thin specimen. The thickness of the oxide scale on the 430 thin specimen was much larger than any of the other 430 specimens (Table 4-10), and thicker oxides are more susceptible to cracking than thinner ones.

Because the 430 and 434 thin specimens did not exhibit the same behaviour, it is not clear whether the thickness of the ZMG 232 specimens affected the oxidation behaviour of the steel. Therefore, in order to determine whether the trends observed in this work are a result of the difference in steel and not in specimen thickness, 430, 434, and ZMG 232 specimens of the same thickness should be tested. It would also be interesting to see if the effect of surface treatment would remain the same if thin 430 and 434 specimens were used.

## 5.2 Chromium Depletion

In order to determine whether there was significant Cr depletion in the steels below the oxide layer, an approximate diffusion distance for Cr after 502 h of oxidation was calculated using Equation 5-7:

$$x = \sqrt{D_{app} t} \qquad (5\text{-}7)$$

where $x$ is the diffusion distance, $D$ is the apparent diffusion coefficient, and $t$ is the oxidation time (in this case 502 h). The value of the apparent diffusion coefficient at the oxidation temperature was determined from Equations 5-1, 5-2, and 5-6 using the data in

both Table 5-1 and Table 5-2. A summary of the results of this calculation is presented in Table 5-3.

Table 5-3. Order of Magnitude Diffusion Distance Calculation.

| Steel | $D_{app}$ ($m^2/s$)* | $D_{app}$ ($m^2/s$)** | x (m)* | x (m)** | x (mm)* | x (mm)** |
|---|---|---|---|---|---|---|
| 430 | 3.3E-15 | 3.6E-15 | 7.8E-05 | 8.0E-05 | 0.078 | 0.080 |
| 434 | 3.2E-15 | 3.2E-15 | 7.6E-05 | 7.6E-05 | 0.076 | 0.076 |
| ZMG 232 | 3.3E-15 | 3.6E-15 | 7.8E-05 | 8.1E-05 | 0.078 | 0.081 |

* (Cermak, et al. 1996)

**(Brandes & Brook. 1998)

The thickness of the thin and thick specimens was 0.25 mm and 1 mm, respectively. Therefore, the distance from the middle of the specimen to the metal/oxide interface was 0.125 mm for the thin specimens and 0.5 mm for the thick specimens. From Table 5-3, it is clear that, regardless of the source of the diffusion data, bulk diffusion alone could not have been responsible for Cr depletion in the thick specimens. However, the x values calculated in Table 5-3 are of the same order of magnitude as the distance from the middle of the specimen to the metal/oxide interface for the thin specimens. Therefore, it is possible that Cr depletion was present in the thin specimens.

In order to confirm whether significant Cr depletion occurred in the thin 430 specimen, EDX analysis was used. First, a baseline Cr level was determined by measuring the Cr concentration at three equally spaced points from the middle of the thin 430 specimen to the outer edge prior to oxidation. Then, the Cr concentration was measured at 10 equally spaced points from the middle to the outer edge for both the 430 thin and thick specimens after 502 h of oxidation at 800°C. The results are displayed in Figure 5-6.

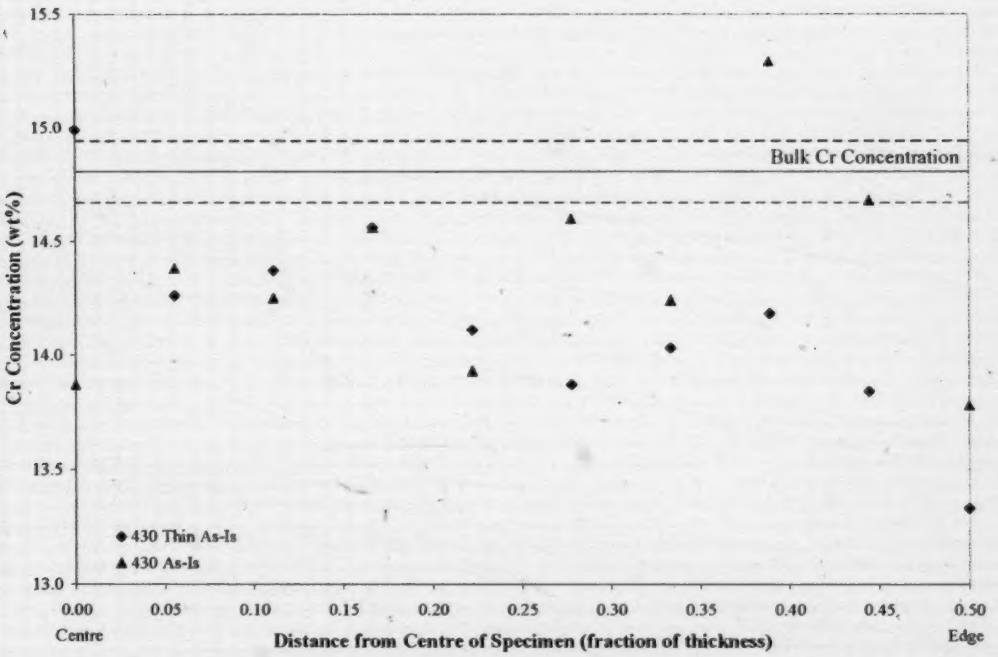


Figure 5-6. Cr Concentration Profile Through the Steel for 430 As-Is Thick and Thin Specimens After 502 h of Oxidation at 800°C.

The bulk Cr concentration was determined by taking the average of the three measured Cr concentration values. The dotted lines above and below the black line indicate one standard deviation above and below the average value. From Figure 5-6, it is clear that although there may be slightly more depletion in the thin specimen, the amount of depletion is not significant, particularily close to the centre of the specimen. In Figure 5-6, the distance from the centre of the specimen is plotted as a fraction of specimen thickness. Since the thin specimen has a thickness approximately ¼ that of the thick specimen, the 10 equally spaced points are not separated by the same absolute distance in the thin and thick specimens (for the thin specimen, the points are much closer to one another).

Although bulk Cr depletion has not occurred in the 430 thin specimen, local Cr depletion could exist directly below the spalled regions. In order to determine whether this was indeed the case, EDX analysis was again used. First, the Cr concentration at a distance of

approximately 3.34μm below the oxide scale was determined at 10 locations where spalling was not observed, and the average of the 10 values was calculated. Then, the Cr concentration was measured at the same distance below the oxide scale for 10 regions where spalling was observed. The resulting Cr concentration values were plotted and are displayed in Figure 5-7.

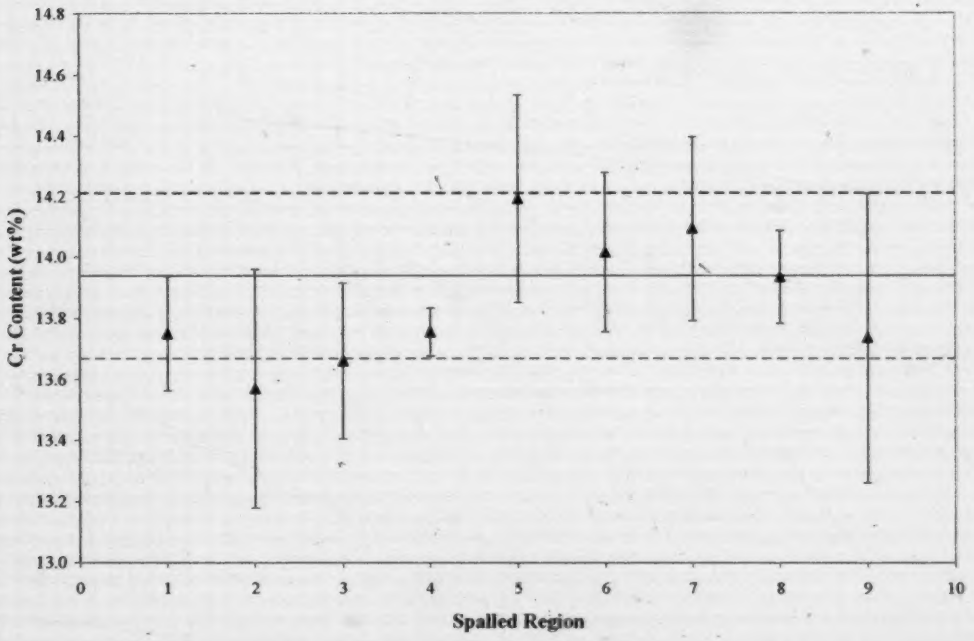


Figure 5-7. Cr Concentration Below The Oxide Scale at Regions Where Spalling Was Observed.

In Figure 5-7, the solid line represents the average Cr concentration at a distance of approximately 3.34μm below the oxide scale in regions where spalling did not occur. The dotted lines represent one standard deviation above and below the average value. From Figure 5-7, it is seen that the Cr concentration directly below the oxide scale in regions where spalling occurred is within one standard deviation of the average Cr concentration below the oxide scale at regions where spalling did not occur. Therefore, it seems that local Cr depletion was not present in regions where spalling of the oxide scale on the thin 430 specimen occurred.

## 5.3 Oxide Thickness

In this work, both specific mass gain and oxide scale thickness were used to characterize the effect of surface treatment on oxidation behaviour. In theory, there should be a linear relationship between the two quantities. In order to determine whether this was the case, a plot of oxide scale thickness measured from SEM cross section images vs. specific mass gain was constructed. The plot is presented in Figure 5-8.

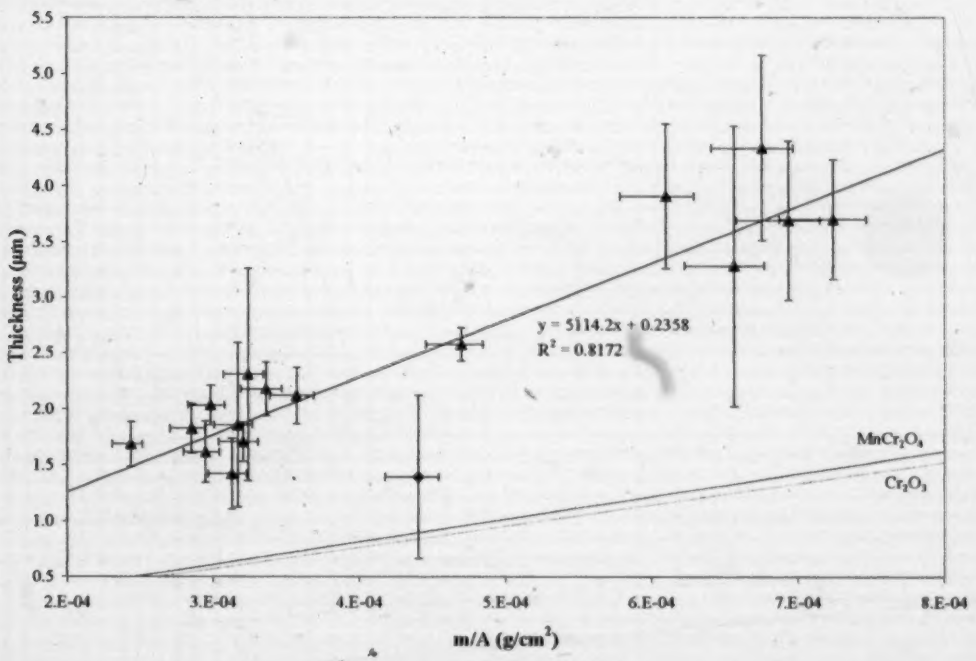


Figure 5-8. Comparison of Oxide Scale Thickness and Specific Mass Gain.

From the plot, it can be seen that all the data points fall reasonably well along a straight line, with the exception of the 430 sandblasted 1 pass specimen. However, for this and all the other sandblasted specimens, the oxide scale thickness was not uniform. Therefore, measuring the thickness over a limited region of the specimen could have resulted in larger errors than for the as-is or rolled specimens, which had a much more uniform oxide thickness.

Figure 5-8 also displays straight lines representing the relationship between specific mass gain and oxide scale thickness assuming that the scale consists entirely of either chromia or spinel. The specific mass gain values were determined for various scale thicknesses using the bulk densities of chromia and spinel. For the chromia, a density value of 5.231 $g/cm^3$ was used. This value was listed on the JCPDS Diffraction Card for $Cr_2O_3$ (#38-1479) (International Center for Diffraction Data. 1996). For the spinel, a value of 4.925 $g/cm^3$ from the JCPDS Diffraction Card for $MnCr_2O_4$ (#54-0876) was used (International Center for Diffraction Data. 1996). It is clear that the thickness of the oxide scales of all of the specimens was significantly higher than the values predicted using the bulk density of either chromia or spinel. This makes sense, as it is common for the density of oxides to be lower than the theorectical bulk density value since oxides are not usually fully dense.

In addition to determining total steel oxide scale thickness, the chromia layer thickness was also measured from the SEM cross section images for the 430, 434, and ZMG 232 as-is specimens as well as for the 430 and 434 thin as-is specimens. The chromia thicknesses were determined as described in Section 4.3.3.1 for the overall oxide scale thickness. The results of this analysis are presented in Table 5-4.

Table 5-4. Chromia Thickness Comparison.

| Specimen | Chromia Thickness (μm) |
|---|---|
| 430 As-is | 1.00 ± 0.20 |
| 434 As-is | 1.32 ± 0.19 |
| ZMG 232 As-is | 2.71 ± 0.30 |
| 430 As-is (thin) | 0.74 ± 0.21 |
| 434 As-is (thin) | 1.17 ± 0.17 |

From Table 5-4, it is clear that the chromia scale thickness is highest for ZMG 232, followed by 434 and then 430. For both 430 and 434, the chromia layer is reduced for the thin specimens compared to their thick counterparts. The reduction in chromia thickness is more significant for the 430 thin specimen.

## 5.4 Oxide Scale

### 5.4.1 Spinel

For all three steels, the relative amount of spinel compared to chromia in the oxide scale increased with increasing oxidation time (Table 4-8 for 430, Table 4-14 for 434, and Table 4-22 for ZMG 232). Therefore, after 502 h the bulk of the steel had not yet been depleted of Mn, even for the ZMG 232 specimens, which were much thinner than either the 430 or 434 specimens. In addition, the ZMG 232 specimens had the highest relative amount of spinel, followed by the 430 specimens, and the 434 specimens had the least relative amount of spinel. This was consistent with the overall oxide composition from EDX analysis of a relatively large area (~4 $mm^2$), which showed that the amount of Mn relative to Cr in the oxide scale was highest for ZMG 232, followed by 430, and then 434 (Table 4-9 for 430, Table 4-16 for 434, and Table 4-23 for ZMG 232). It is known that steels with more Mn form more spinel than steels of a similar composition with less Mn (Honneger, et al. 2001). According to the specifications (Table 3-1), ZMG 232 has 0.5% Mn while for 430 and 434, the maximum amount of Mn is 1%. Therefore, it is unlikely that there is more Mn present in ZMG 232 than in the other two steels. In comparing the chromia thickness between the three steels, Table 5-4 indicates that the chromia thickness for ZMG 232 is much larger than for the other two steels (by a factor between 2 and 3). The chromia thickness for 434 was larger than for 430. A thinner layer of chromia would result in a reduced diffusion distance for Mn to travel from the metal/oxide interface to the outer region of the oxide scale, and thus could explain an increase in the relative amount of spinel present. However, this explanation does not apply to ZMG 232 since the chromia thickness for this steel was higher than for the other two steels, which formed less spinel. The chromia that formed on the ZMG 232 specimens may have been less protective than for the 430 or 434 specimens and, thus, diffusion of Mn through the oxide scale was faster for ZMG 232. The reason for the chromia being less protective for ZMG 232 is not clear at this time, especially since ZMG 232 contains La, which is supposed to improve the protective ability of the chromia. The formation of a thicker chromia layer for 434 is most likely due to the increased amount of Cr available for oxide formation compared to 430. It is also possible that the chromia formed on the 434 specimens was more protective and thus diffusion of Mn through the oxide scale was more difficult for 434. Again, the reason for this is not understood at this time.

For 430 and ZMG 232, surface treatment was found to have an effect on the relative amount of spinel that formed. Relatively more spinel compared to chromia formed on the as-is specimens in comparison to the treated specimens. This can be explained by the effect of surface treatment on the supply of Cr from the bulk. An increased supply of Cr for oxide formation would result in the formation of a thicker chromia layer for the treated specimens. The resulting decreased diffusion rate for Mn travelling through the oxide layer would in turn reduce the amount of spinel formed compared to a specimen that did not undergo surface treatment. Presumably, the effect of surface treatment on the supply of Cr from the bulk and subsequent chromia formation would be more significant than the increased supply of Mn from the bulk as a result of the surface treatment. For 434, a similar amount of spinel was found to form on all specimens. The reason for this is not clear at this time.

The effect of specimen thickness on the amount of spinel formation was fairly clear. Both 430 and 434 thin specimens formed significantly more spinel than their thick counterparts, and the 430 thin specimen formed more spinel relative to chromia than the ZMG 232 specimens. Therefore, part of the reason why the ZMG 232 specimens formed the highest relative amount of spinel could be due to the thin specimens that were used. In comparing the chromia thickness between the 430 and 434 thin and thick specimens, for both steels the thickness of chromia was reduced for the thin specimens (Table 5-4). The thinner chromia layer and resulting reduced diffusion distance for Mn may be responsible for the increased spinel formation in the thin specimens.

The relative amounts of spinel and chromia in the oxide scale are significant for SOFC interconnect applications. It is known that the resistance of the oxide scale is proportional to its thickness; therefore, interconnects should not form thick oxide scales (Quadakkers, et al. 2003, Zhu & Deevi. 2003b). However, the conductivity of the spinel phase is much higher than that of chromia. The values reported in the literature for the resistivity of chromia and various (Cr,Mn) spinels vary significantly. For $Cr_2O_3$, the resistivity has been reported as $1.8 \times 10^4$ Ω·cm (Virkar & England. 2000) and 200 Ω·cm (Wei. 2004) at 750°C. For $MnCr_2O_4$, the resistivity at 750°C has been measured as 7.2 Ω·cm (Virkar & England. 2000) and as 1900 Ω·cm at 800°C (England. 2003). As the relative amount of Mn in the spinel increases, the resistivity decreases. For $Mn_{1.5}Cr_{1.5}O_4$, the resistivity at 750°C is 4 Ω·cm (Virkar & England. 2000). For $Mn_2CrO_4$, the resistivity at 800°C is 3.5 Ω·cm (England. 2003). Because of the large difference in the

conductivity of the chromia and spinel phases, the overall conductivity of a thicker oxide scale containing a large relative amount of spinel may in fact be higher than that of a thinner oxide scale consisting mainly of chromia. It has been reported that even though oxides that form on Mn-containing steels are thicker, they tend to have a lower electrical resistance due to the high conductivity of the spinel (Zhu & Deevi. 2003a). In order to verify this, conductivity measurements need to be carried out on the steel specimens. In comparing the 430 and 434 specimens, this research found that although the overall scale thicknesses on the 430 steel were similar to that of 434, more spinel was present in the case of 430. Conductivity measurements could be used in this case to further examine the suitability of these two steels for SOFC interconnect applications. It is theoretically possible to calculate the resistivity of the oxide scales formed on the specimens in this work using the weighted average of the resistivities of the chromia and spinel phases (rule of mixtures). However, the value of such a calculation is questionable since it would rely on the accuracy of the oxide thickness measurements and the relative amounts of the two oxide phases.

A second advantage of spinel formation in terms of SOFC interconnect applications is that spinel reduces the formation of volatile Cr species, because it reduces the activity of Cr in the oxide scale (Quadakkers, et al. 2003). A continuous layer of spinel would be much better for this. The spinel layer on the 430 thin specimen was found to be much more continuous and uniform in thickness than that on any of the other specimens (Figure 4-20). In this work, the spinel that formed on the sandblasted specimens was much less continuous than for either the as-is or rolled specimens. Because of this, sandblasting may not be a good method of surface treatment.

The composition of the spinel phase was found to vary depending on the steel. For the 430 and 434 specimens, EDX point analysis of the spinel phase in cross section indicated that the ratio of Cr to Mn in the spinel was close to 2:1 (Table 4-11 for 430 and 4-18 for 434). However, for ZMG 232, this ratio was closer to 1:1 (Table 4-25). The ZMG 232 specimens were also found to have significantly more Fe relative to Cr in the spinel than for either the 430 or 434 specimens. It has been reported that the presence of Fe can increase the conductivity of the spinel phase (Sakai, et al. 2005). In comparing 430 and ZMG 232, it was found that the conductivity of the oxide scale that formed on the ZMG 232 specimens was higher than that for the 430 specimens, and this was attributed to the higher relative amount of Fe present in the spinel on the ZMG 232 specimens (Sakai, et

al. 2005). The higher relative amounts of Fe and Mn in the spinel on the ZMG 232 specimens also suggests that the chromia layer may be less protective for this steel.

### 5.4.2 Insulating Oxides

In the native oxide, Si segregation to the outer surface was observed by SIMS and XPS for all three steels. No evidence of $SiO_2$ formation at the metal/oxide interface of the native oxide was found for any of the three steels. For ZMG 232, SIMS indicated that, in the native oxide, the majority of the Al was segregated to the outer surface; however, some Al also appeared at the metal/oxide interface, implying that a thin layer of alumina may be present in the native oxide of ZMG 232. Segregation of Si and Al (in the case of ZMG 232) to form insulating oxides at the metal/oxide interface appears to begin in the early stages of oxidation at 800°C. For 430 and ZMG 232, evidence of Si segregation to the metal/oxide interface to form $SiO_2$ after both short and long oxidation times was found by SIMS, XPS, and EDX analysis. For 434, Si segregation to the metal/oxide interface was observed by SIMS; however, it was not detected by either XPS or EDX analysis. For ZMG 232, Al was also present in the steel and evidence of $Al_2O_3$ formation at the metal/oxide interface was seen after both short and long oxidation times. Internal oxidation involving both Al and Si was also observed in SEM cross section images for all ZMG 232 specimens. This type of internal oxidation was not observed for either the 430 or 434 speicmens.

From the Ellingham Diagram presented in Figure 2-4, it can be seen that both $SiO_2$ and $Al_2O_3$ are more stable than $Cr_2O_3$ at 800°C; therefore, their formation is thermodynamically favoured (Shifler, 2003). The fact that these oxides form at or below the metal/oxide interface indicates that the rate of outward diffusion of Si and Al ions is slower than the rate of inward diffusion of oxygen ions. One problem with the formation of alumina and silica is that they are both insulating oxides and thus they increase the electrical resistance of the interconnect (Yang, et al. 2004a). For ZMG 232, this may be especially true since both alumina and silica form. In fact, it is thought that the addition of REs such as La promote the accumulation of Si at the metal/oxide interface (Riffard, et al. 2002). For 434, the silica underlayer is not as evident as for 430; therefore, the conductivity of 434 oxides may be higher than for 430. However, the formation of insulating oxides at the metal/oxide interface may not be entirely detrimental as it is

thought that alumina and silica can both act as a diffusion barrier for other scale-forming elements and improve the adhesion of the oxide scale (Yang, et al. 2004a).

It has also been speculated that surface treatment can have an effect on the adhesion of the oxide scale. In a study of 99.7% pure Cr containing Fe, it was found that although a higher average compressive residual stress existed in oxide scales formed on smooth surfaces, the distribution of the residual stress was relatively uniform throughout the oxide layer. For rough surfaces, the oxide scales had a non-uniform distribution of residual stresses, with tensile residual stresses in 'crests' or higher regions and compressive residual stresses in 'troughs' or lower regions (Mougin, et al. 2001). Because of this, oxide scales formed on specimens with rough surfaces tended to spall while those formed on smooth surfaces did not. However, other studies have found that surface treatment can increase the resistance of the oxide scale to spalling. In order to determine the effect of surface treatment on the adhesion of the oxide scales under SOFC operating conditions, specimens should be tested under thermal cycling conditions.

## 5.5 Oxidation Model

The general process of oxidation has been previously described and is summarized as follows. First, oxygen from the environment adsorbs on the surface of the metal (Kofstad. 1998). Adsorption of oxygen continues until a 2-D layer of adsorbed oxygen completely covers the metal surface (Bradford. 2002). At this point, a thin oxide film rapidly forms on the metal surface (Wasielewski & Rapp. 1972). This process is referred to as "transient oxidation", as the film contains oxides of every scale-forming element in the metal in an amount proportional to the amount of the element in the bulk of the metal (Ostwald & Grabke. 2004). The majority of these oxides have a lower thermodynamic stability than the protective oxide (Ostwald & Grabke. 2004). Once a continuous film has formed, the formation of 3-D oxide nuclei occurs at defect sites such as grain boundaries, impurities, dislocations, and surface flaws (Kofstad. 1998). These oxide nuclei have the same composition as the protective oxide, which is chromia in this study. Then, the oxide nuclei grow laterally until a continuous protective oxide film covers the surface (Kofstad. 1998). The growth of the transient oxides, which are less thermodynamically stable, stops (Leistikow, et al. 1987). Some of these oxides will eventually decompose, while others will be incorporated into the outer portion of the

protective oxide (Leistikow, et al. 1987). Once a continuous film of chromia is formed, the metal that is directly below the oxide film will be depleted in Cr. In order for oxide formation to continue, Cr must be supplied through diffusion from the bulk of the alloy (Ostwald & Grabke. 2004). Subsequent growth of the protective oxide relies on the transport of metal and oxygen ions across the scale in accordance with parabolic oxidation kinetics (Wasielewski & Rapp. 1972). For stainless steels, chromia grows predominately through the outward diffusion of metal ions, namely $Cr^{3+}$ (Kofstad. 1992, Quadakkers, et al. 2003). Typically, the formation of metal ions occurs at the metal/oxide interface while the formation of oxygen ions occurs at the oxide/gas interface (Kofstad. 1998).

For the ferritic stainless steels studied in this work, (Cr,Mn) spinel containing some Fe forms in addition to chromia. The reason for the formation of a separate spinel layer is that Mn has a low solubility in chromia (Quadakkers, et al. 2003). Spinel formation occurs in the outer portion of the oxide scale because the diffusion of Mn ions through chromia is rapid (Brylewski, et al. 2004). The diffusion rates of metal ions through chromia, assuming substitution in cation lattice sites, is as follows: $D_{Mn} > D_{Fe} > D_{Ni} > D_{Cr}$ (Kurokawa, et al. 2004). Because of this, it is likely that spinel formation occurs predominately through the reaction of Mn ions with chromia and not through the reaction of Mn and Cr ions with oxygen ions. Further evidence for the formation of spinel by Mn ions reacting with chromia is seen in Table 5-4. Both the 430 and 434 thin specimens had a thinner chromia layer than their thick counterparts, and both formed relatively more spinel. The reduction in chromia thickness was greater for the 430 thin specimen, which formed relatively more spinel than the 434 thin specimen. In the early stages of oxidation, the spinel is not continuous (Yang, et al. 2006b).

From both XPS and SIMS analysis, Mn in the oxide form was found at the surface of the oxide even after only 15 min of oxidation. When 430 and 434 specimens that were oxidized for 15 min were examined in the SEM, faceted spinel crystals were not clearly visible; however, for the ZMG 232 specimens, many spinel crystals were visible all over the surface of the oxide. For 430, specimens that were oxidized for 30 min were also examined in the SEM. In this case, spinel crystals were clearly visible. Therefore, it seems reasonable to assume that at 800°C, the formation of spinel begins almost immediately.

A model of oxidation of 430 steel at 750°C has previously been proposed (Wei. 2004). The model claims that at 750°C, spinel formation is not evident until after 50 h, which was certainly not the case at 800°C. Aside from this, the model proposed in this work is in agreement with the model previously proposed and is displayed below in Figure 5-9.

a)

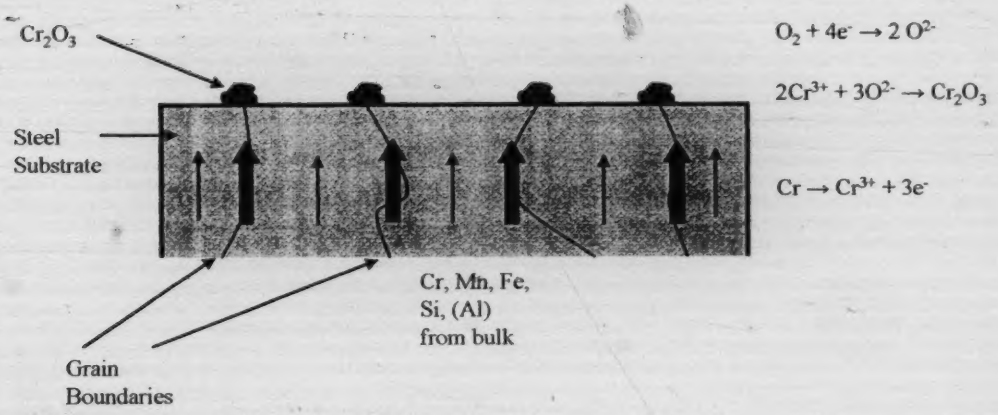


b)

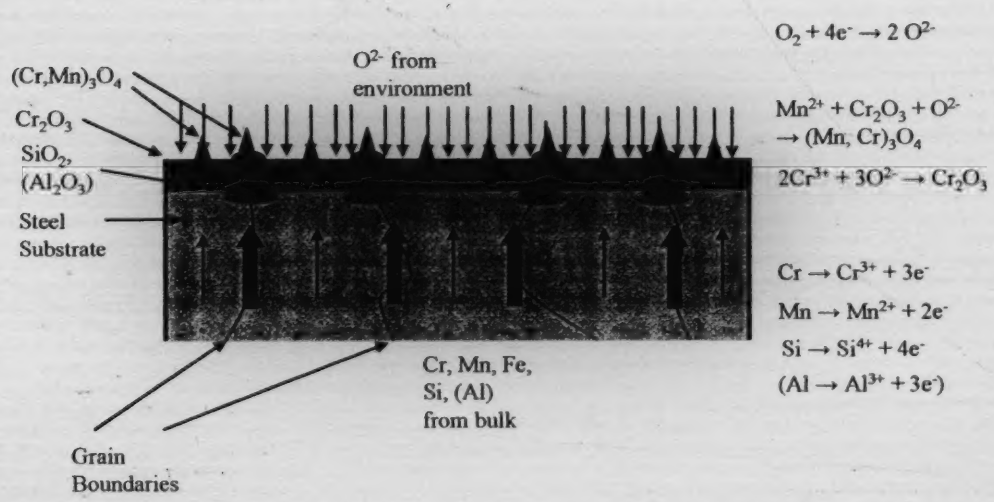
$(Cr,Mn)_3O_4$
$Cr_2O_3$
$SiO_2$, $(Al_2O_3)$
Steel Substrate
Grain Boundaries
$O^{2-}$ from environment
Cr, Mn, Fe, Si, (Al) from bulk
$O_2 + 4e^- \rightarrow 2\,O^{2-}$
$Mn^{2+} + Cr_2O_3 + O^{2-} \rightarrow (Mn, Cr)_3O_4$
$2Cr^{3+} + 3O^{2-} \rightarrow Cr_2O_3$
$Cr \rightarrow Cr^{3+} + 3e^-$
$Mn \rightarrow Mn^{2+} + 2e^-$
$Si \rightarrow Si^{4+} + 4e^-$
$(Al \rightarrow Al^{3+} + 3e^-)$

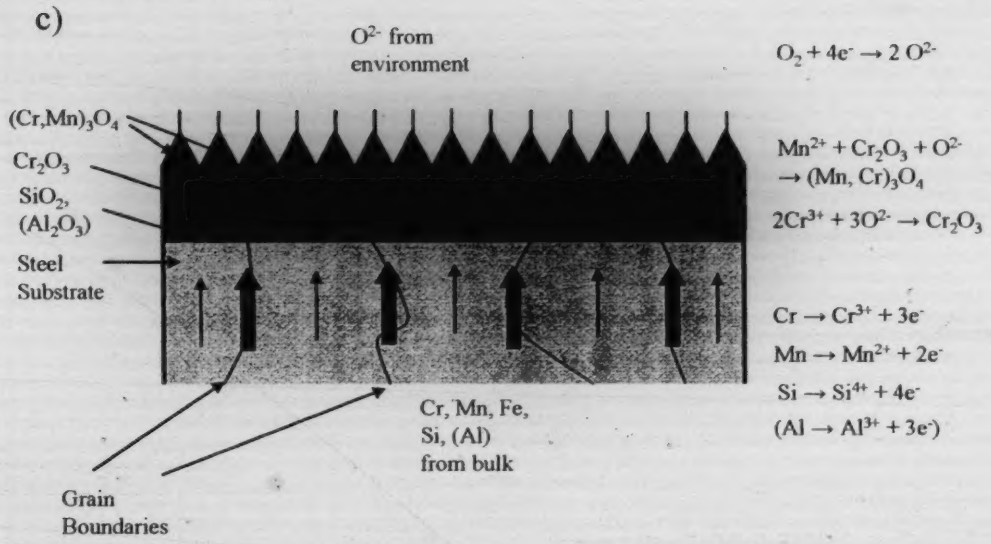


Figure 5-9. Model of Oxidation for 430, 434, and ZMG 232 at 800°C in Air. a) Formation of Chromia Nuclei; b) Continuous Chromia Layer and Formation of Spinel and Insulating Oxides; c) Inner Chromia, Outer Spinel, and Insulating Oxides at Metal/Oxide Interface.

Figure 5-9a shows the initial formation of chromia nuclei at the ferrite grain boundaries. In Figure 5-9b, the chromia layer is thicker above the ferrite grain boundaries because transport of Cr from the bulk of the steel is faster through the grain boundaries than through the grains. $SiO_2$ and $Al_2O_3$ form as individual oxide nuclei in Figure 5-9b. This is because the rate of transport of Si and Al to the metal/oxide interface will be faster at grain boundaries than through the ferrite. However, the growth of these oxides is limited by the rate of inward diffusion of oxygen ions through chromia grain boundaries. Because the chromia grain size is much smaller than that of the steel, oxygen ions are in effect distributed evenly along the metal/oxide interface. Therefore, it is also possible that the insulating oxides could initially form as a thin, continuous layer along the oxide/metal interface. In Figure 5-9b, Fe ions are not shown. In reality, these ions likely behave the same as the Mn. As for the Mn, they are incorporated in the spinel by reacting with the $Cr_2O_3$ layer. Figure 5-9c shows the case where spinel crystals cover the surface of the oxide scale. The chromia layer is thicker and a continuous layer of insulating oxide is shown below the metal/oxide interface.

In summary, the oxidation model shown in Figure 5-9 helps to explain some of the differences observed between the steels in this research. For ZMG 232, the significantly higher specific mass gain, due to oxidation, than the other two steels can be attributed to the larger amount of Cr available for oxide formation. For the 430 and 434, although 434 has more Cr available for oxide formation, this did not translate into a larger specific mass gain. This could be due to the larger grain size of 434, which reduced the contribution of grain boundary diffusion of Cr to the metal/oxide interface.

The relative amount of spinel formed on the oxide scales of the three steels is seen from the model in Figure 5-9 to depend on two different factors: the supply of Mn from the bulk of the steel and the rate of transport of Mn though the chromia to the outer portion of the oxide scale. The rate of transport of Mn through the oxide scale could depend on the thickness of the chromia scale or on how protective the chromia scale is. If the chromia scale had a finer grain size or increased porosity, transport of metal ions through the chromia would be faster. For ZMG 232, the thickness of the chromia scale was greater than the other two steels, which should not contribute to increased spinel formation. Therefore, it seems that the increased spinel formation could be due to faster transport of Mn ions through the chromia. ZMG 232 was found to have more Mn relative to Cr in the spinel than either 430 and 434, and assuming that the spinel forms primarily by Mn ions reacting with chromia, it is clear that the transport of Mn ions across the oxide scale influences the Mn enrichment of the spinel. Further evidence to support the fast transport of ions through the chromia scale in ZMG 232 is that the spinel for this steel was enriched in Fe compared to the other steels, indicating that the transport of Fe through the chromia was also faster. For 434, the chromia scale was thicker than for 430, and the resulting decrease in the rate of diffusion of Mn across the thicker chromia could explain the reduced spinel formation. For both 430 and 434 thin specimens, a thinner chromia scale leads to increased spinel formation compared to the corresponding thick specimens.

The oxidation model in Figure 5-9 can also help explain the observed effect of the surface treatments on oxidation. The specimens that experienced surface treatment would have been able to supply Cr more rapidly to the surface of the metal, resulting in an increase in mass gain due to oxidation. The increased rate of transport of Cr from the bulk, from an increased amount of surface dislocations and a reduced grain size, would have resulted in the rapid formation of a thick chromia scale. The thickness of the chromia scale would have reduced the rate of transport of Mn ions across the scale,

resulting in reduced formation of spinel. The transport of Mn could have been slowed by a reduction in porosity of the oxide scale as this phenomenon has been reported to occur as a result of surface treatment.

# 6 Conclusions

In this study, the effect of sandblasting and cold rolling on the oxidation behaviour of three ferritic stainless steels (430, 434, and ZMG 232) in air at 800°C was studied. Specific mass gain measurements after 502 h of oxidation indicated that the mass gain of ZMG 232 was significantly higher than either 430 or 434, which had similar specific mass gains with those for 434 being slightly lower. For all three steels, the specimens subjected to surface treatment (both cold rolling and sandblasting) had a higher specific mass gain than the as-is specimens. The thickness of the ZMG specimens was 0.25 mm while that for the 430 and 434 specimens was approximately 1 mm; therefore, thin as-is 430 and 434 specimens were also tested. The specific mass gain of the 430 thin specimen was significantly higher than that for its thick counterpart, and evidence of spalling and subsequent repair of the oxide scale was present. For the 434 specimen, no spalling was observed and the specific mass gain was similar to, although slightly lower than, its thick counterpart.

XRD analysis of the oxide scales formed on all specimens indicated that two oxide phases were present in the protective oxide layer: chromia and (Cr,Mn) spinel. The relative amount of chromia and spinel phases varied with the type of steel: the ZMG 232 specimens had the highest relative amount of spinel, followed by the 430 specimens, and the 434 specimens had the least spinel compared to chromia. For 430 and ZMG 232, surface treatment decreased the relative amount of spinel compared to the as-is specimens. For 434, all specimens had similar relative amounts of spinel. Specimen thickness affected the relative amount of spinel in the oxide scale. For both 430 and 434, an increase in the relative amount of spinel was found for the thin as-is specimens in comparison to their thick counterparts. The relative amount of spinel compared to chromia is important for SOFC interconnect applications as spinel is more electrically conductive than chromia. For ZMG 232, the spinel was enriched in Fe compared to that for either 430 or 434. The presence of Fe in the spinel phase has been reported to further increase its electronic conductivity.

The formation of insulating oxides at the metal/oxide interface was also observed. For 430, surface science analysis indicated the formation of $SiO_2$ at the metal/oxide interface after only 15 minutes of oxidation at 800°C. EDX analysis of oxidized cross section specimens after 502 h of oxidation confirmed the presence of this insulating oxide layer

at the metal/oxide interface after 502 h of oxidation. For 434, the presence of $SiO_2$ and Nb-containing oxides at the metal/oxide interface was detected after 15 minutes of oxidation; however, the Si and Nb segregation was not clearly visible after 502 h of oxidation. For ZMG 232, owing to the presence of both Al and Si in the bulk, the formation of a silica and an underlying alumina layer was noted after both short and long oxidation times. The formation of insulating oxide layers at the metal/oxide interface is not particularly beneficial for SOFC interconnect applications since these oxides further increase the electrical resistance of the interconnect.

TEM analysis was used to characterize the carbides present in 434 steel. Contrary to expectations, two types of carbides were found: (Nb,Ti)C precipitates similar to those found in microalloyed steels, and carbides of the type $M_7C_3$, containing mainly Nb, Fe, and Cr with some Mo.

# 7 Recommendations

In this study, the effect of surface treatment on oxidation behaviour was studied at 800°C in air. However, this testing condition does not completely simulate the environment that a SOFC interconnect would be exposed to during typical operation. In order to fully evaluate the effect of surface treatment under SOFC operating conditions, other tests should be performed. The effect of surface treatment on oxidation should be evaluated under thermal cycling conditions which would be encountered during startup and shutdown. In this situation, cracking and spalling of the oxide scale on the interconnect would be likely, and surface treatment may offer some benefits in repairing the protective oxide that were not encountered under the isothermal conditions of this study. The relative performance of the three steels may be different under these conditions. The additional Cr available for oxide formation in ZMG 232 could result in reduced specific mass gain under thermal cycling conditions if faster repair of the protective oxide scale occurred. The SOFC interconnect is also exposed to a fuel environment during operation. The effect of surface treatment may be different under these conditions. In the fuel cell stack, there are many other variables that are difficult to replicate uner laboratory testing conditions. It would be useful to test the effect of surface treatment on oxidation during operation of the fuel cell stack.

Another important factor that was not considered in this study was the conductivity of the oxide scale. In this study, the total thickness of the oxide scale was considered to be a measure of the oxidation behaviour of the specimen. However, because of the difference in the electrical conductivity of the spinel and chromia phases, some of the specimens with thicker oxide scales, that contained a higher relative amount of spinel, may have been more conductive, and thus would have better performance as a SOFC interconnect. Also, surface treatment has been reported to reduce the porosity of the oxide scale which in turn improves its electrical conductivity. The oxide scales that formed on some of the treated specimens, although thicker, may have been more conductive than those on the as-is specimens.

Finally, although oxidation tests were carried out for 502 h in this study, compared to the target SOFC lifetime of 40 000 h, this is a fairly short time. Looking at the effect of surface treatment over longer oxidation times to determine whether or not there is a change from what was observed in this study would be beneficial.

# References


Alman DE, Jablonski PD. 2004. Low Coefficient of Thermal Expansion (CTE) Nickel Base Superalloys for Interconnect Applications in Intermediate Temperature Solid Oxide Fuel Cells. In *Superalloys 2004*, eds. KA Green, TM Pollock, H Harada, TE Howson, RC Reed, et al, 617-22. Warrendale, PA: TMS (The Minerals, Metals & Materials Society)

Althaus PG. 1985. *Residual Stresses in Internal Grinding.* Industrial Diamond Review. 45 : 124-7

Amin KE, Ganesh S. 1981. *Residual Stresses in Copper-2% Beryllium Alloy Strips.* Experimental Mechanics. 21 : 473-6

Antepara I, Villarreal I, Rodríguez-Martínez LM, Lecanda N, Castro U, Laresgoiti A. 2005. *Evaluation of Ferritic Steels for Use as Interconnects and Porous Metal Supports in IT-SOFCs.* Journal of Power Sources. 151 : 103-7

ASM International. 2002a. Elevated Temperature Properties of Stainless Steels. In *ASM Handbooks Online*, 1 : ASM International

ASM International. 2002b. Ternary Alloy Phase Diagrams. In *Alloy Phase Diagrams*, 3 : Materials Park, Ohio: ASM International

Bačová V, Draganovská D. 2004. *Analyses of the Quality of Blasted Surfaces.* Materials Science. 40 : 125-31

Badawi K, Bielle J, Castex L, Giraudeau A. 1986. *Influence of Sand Blasting Parameters on the Geometrical and Mechanical Characteristics of 1010 Steel Sand Blasted Surfaces.* Advances in Surface Treatments: Technology, Applications, Effects. 3 : 229-41

Batawi E, Glatz W, Kraussler W, Janousek M, Doggwiler B, Diethelm R. 1999. *Oxidation Resistance & Performance in Stack Tests of Near-Net-Shaped Chromium-Based Interconnects. Presented at Solid Oxide Fuel Cells (SOFC VI): Proceedings of the Sixth International Symposium, Honolulu, Hawaii, 1999,* 99-19 : 731. Pennington, N.J.: The Electrochemical Society

Beeston BEP, Horne RW, Markham R. 1972. *Electron Diffraction and Optical Diffraction Techniques*, ed. AM Glauert, Vol. 1. Amsterdam: North-Holland. 435pp

Boudghene Stambouli A, Traversa E. 2002. *Fuel Cells, An Alternative to Standard Sources of Energy*. Renewable and Sustainable Energy Reviews. 6 : 297-306

Bradford SA. 2002. *Corrosion Control*, Edmonton, Alberta: CASTI Publishing. 491pp. 2nd ed.

Brandes EA, Brook GB, eds. 1998. *Smithells Metal Reference Book*, Oxford: Butterworth Hermann. 13-1 - 13-119 pp. 7th ed.

Brinksmeier E. 1987. *A Model for the Development of Residual Stresses in Grinding. Presented at Proceedings of the AST World Converence: Advances in Surface Treatments and Surface Finishing, 1987*, 5 : 173

Brylewski T, Dąbek J, Przybylski K. 2004. *Oxidation Kinetics Study of the Iron-Based Steel for Solid Oxide Fuel Cell Application*. Journal of Thermal Analysis and Calorimetry. 77 : 207-16

Brylewski T, Maruyama T, Nanko M, Przybylski K. 1999. *TG Measurements of the Oxidation Kinetics of Fe-Cr Alloy With Regard to its Application as a Separator in SOFC*. Journal of Thermal Analysis and Calorimetry. 55 : 681-90

Brylewski T, Nanko M, Maruyama T, Przybylski K. 2001. *Application of Fe-16Cr Ferritic Alloy to Interconnector for a Solid Oxide Fuel Cell*. Solid State Ionics. 143 : 131-50

Burakowski T, Wierzchon T. 1999. *Surface Engineering of Metals: Principles, Equipment, Technologies*, New York: CRC Press. 586pp

Callister Jr., WD. 2000. *Materials Science and Engineering: An Introduction*, New York: John Wiley and Sons. 842pp. 5th ed.

Caplan D, Cohen M. 1966. *Effect of Cold Work on the Oxidation of Iron from 400-650°C*. Corrosion Science. 6 : 321-35

Ceram Research. 2006. *Solid Oxide Fuel Cells*. http://www.azom.com/details.asp?ArticleID=919&head=Solid+Oxide+Fuel+Cells

Cermak J, Ruzickova J, Pokorna A. 1996. *Low-Temperature Tracer Diffusion of Chromium in Fe-Cr Ferritic Alloys.* Scripta Mater. 35 : 411-6

Chen L, Jha B, Yang Z, Xia G, Stevenson JW, Singh P. 2006. *Clad Metals by Roll Bonding for SOFC Interconnects.* Journal of Materials Engineering and Performance. 15 : 399-403

Danielewski M, Filipek R, Kucharska B. 2005. *Prediction of the Depletion Zone due to Selective Oxidation of P91 steel.* Defect and Diffusion Forum. 137-240 : 965-70

De Jonghe LC, Jacobson CP, Visco SJ. 2004. *Alloy Supported Thin-Film SOFCs. Presented at 6$^{Th}$ European Solid Oxide Fuel Cell Forum, Lucerne, Switzerland, 2004,* 1 : 91

De Souza S, Visco SJ, De Jonghe, LC. 1997. *Thin-film Solid Oxide Fuel Cell with High Performance at Low Temperature.* Solid State Ionics. 98 : 57-61

Deng X, Wei P, Bateni MR, Petric A. 2006. *Cobalt Plating of High Temperature Stainless Steel Interconnects.* Journal of Power Sources. 160 : 1225-9

Douthett J. 2002. Heat Treating of Stainless Steels. In *Heat Treating,* 4 : ASM International

Dudala J, Gilewicz-Wolter J, Wolter M, Hetmanczyk M. 2005. *The Comparison of the Diffusion Rates of Chromium, Manganese, and Iron in Cr-Mn Steels of Austenitic, Austenitic-Ferritic, and Ferritic Structure. Presented at Proceedings of the 1$^{St}$ International Conference on Diffusion in Solids and Liquids (DSL-2005), University of Aveiro, Aveiro, Portugal, 2005*

Ebenau A, Vöhringer O, Macherauch E. 1987. Influence of the Shot Peening Angle on the Condition of Near Surface Layers in Materials. In *Shot Peening: Science, Technology, Application,* eds. H Wohlfahrt, R Kopp, O Vöhringer, 253-60. Germany: Deutsche Gesellschaft für Metallkunde

EG&G Services, Parsons Inc., Science Applications International Corporation. 2000. *Fuel Cell Handbook.* U.S. Department of Energy

Elangovan S, Balagopal S, Hartvigsen J, Bay I, Larsen D, .et al. 2006. *Selection and Surface Treatment of Alloys in Solid Oxide Fuel Cell Systems.* Journal of Materials Engineering and Performance. 15 : 445-52

Elangovan S, Balagopal S, Timper M, Bay I, Larsen D, Hartvigsen J. 2004. *Evaluation of Ferritic Stainless Steel Interconnects for Use as Metal Interconnects for Solid Oxide Fuel Cells.* Journal of Materials Engineering and Performance. 13 : 265-73

Elangovan S, Hartvigsen R, Lashway R, Balagopal S, Bay I. 2003. *Metal Interconnect Development: Design and Long-Term Stability. Presented at Solid Oxide Fuel Cells VIII (SOFC VIII): Proceedings of the Eigth International Symposium on Solid Oxide Fuel Cells, 2003,* 2003-07 : 851. Pennington, N.J.: The Electrochemical Society

England DM. 2003. *A Metallic Interconnect For a Solid Oxide Fuel Cell Stack.* Ph.D. University of Utah, Salt Lake City, Utah.

England DM, Virkar AV. 2001. *Oxidation Kinetics of Some Nickel-Based Superalloy Foils in Humidified Hydrogen and Electronic Resistance of the Oxide Scale Formed.* Journal of The Electrochemical Society. 148 : A330-8

England DM, Virkar AV. 1999. *Oxidation Kinetics of Some Nickel-Based Superalloy Foils and Electronic Resistance of the Oxide Scale Formed in Air: Part 1.* Journal of The Electrochemical Society. 146 : 3196-202

Franco T, Henne R, Lang M, Metzger P, Schiller G, et al. 2003. *Metallic Components for a Plasma Sprayed Thin-Film SOFC Concept. Presented at Solid Oxide Fuel Cells VIII (SOFC VIII): Proceedings of the International Symposium on Solid Oxide Fuel Cells, Paris, France, 2003,* 2003-07 : 923. Pennington, N.J.: The Electrochemical Society

Fuel Cells 2000. 2006. *Fuel cells 2000: The Online Fuel Cell Information Resource.* http://www.fuelcells.org/

García-Alonso MC, Escudero ML, González-Carrasco JL, Chao J. 2001. *Effect of Sandblasting on the Oxidation and Corrosion Behaviour of an Oxide-Dispersed Strengthened (ODS) FeCrAl alloy.* ISIJ International. 41 : 56-62

Garcia-Vargas MJ, Lelait L, Kolarik V, Fietzek H, Juez-Lornzo, Maria del Mar. 2005a. *Oxidation of Potential SOFC Interconnect Materials, Crofer 22 APU and Avesta 353 MA, in Dry and Humid Air Studied In Situ by X-ray Diffraction.* Materials at High Temperatures. 22 : 245-51

Garcia-Vargas MJ, Lelait L, Kolarik V, Fietzek H, Juez-Lorenzo M. 2005b. *Study of the Oxide Layer Formed on Potential SOFC Interconnect Materials in Dry and Humid Air. Presented at Meeting Abstracts: 207$^{Th}$ Meeting of the Electrochemical Society, Quebec, 2005,* 244. The Electrochemical Society

Geyer B. 2001. *A Fuel Cell Primer.* IAEI News. 10-4

Giggins CS, Petit FS. 1969. *Oxidation of Ni-Cr Alloys Between 800 and 1200°C.* Transactions of The Metallurgical Society of AIME. 245 : 2495-507

Government of Canada. 2001. *Canada and the Kyoto Protocol.* http://www.climatechange.gc.ca/cop/cop6_hague/english/overview_e.html

Government of Canada, Fuel Cells Canada, PricewaterhouseCoopers. 2003. *Canadian Fuel Cell Commercialization Roadmap.*

Grabke HJ, Müller-Lorenz EM. 1998. *Protection of High Alloy Steels Against Metal Dusting by Oxide Scales.* Materials and Corrosion. 49 : 317-20

Grabke HJ, Müller-Lorenz EM, Eltester B, Lucas M, Monceau D. 1997. *Resistance of 9-20% Cr-Steels Against Metal Dusting.* Steel Research. 68 : 179-85

Grabke HJ, Müller-Lorenz EM, Strauss S, Pippel E, Woltersdorf J. 1998. *Effects of Grain Size, Cold Working, and Surface Finish on the Metal-Dusting Resistance of Steels.* Oxidation of Metals. 50 : 241-54

Grabke HJ, Tökei Z, Ostwald C. 2004. *Initial Oxidation of a 9%CrMo- and a 12%CrMoV-Steel.* Steel Research International. 75 : 38-46

Hamdi H, Zahouani H, Bergheau J. 2004. *Residual Stress Computation in a Grinding Process.* Journal of Materials Processing Technology. 147 : 277-85

Hammersly GJ. 1993. Surface Prestressing by Controlled Shot Peening to Improve Resistance to Stress Corrosion Cracking. In *Surface Engineering Volume II: Engineering Applications*, eds. PK Datta, JS Gray, 181-96. Cambridge: The Royal Society of Chemistry

Hänsel M, Boddington CA, Young DJ. 2003. *Internal Oxidation and Carburisation of Heat-Resistant Alloys*. Corrosion Science. 45 : 967-81

Holcomb GR, Alman DE. 2006. *Effect of Manganese Addition on Reactive Evaporation of Chromium in Ni-Cr Alloys*. Journal of Materials Engineering and Performance. 15 : 394-8

Holcomb GR, Ziomek-Moroz M, Cramer SD, Covino, Jr., Bernard S., Bullard SJ. 2006. *Dual-Environment Effects on the Oxidation of Metallic Interconnects*. Journal of Materials Engineering and Performance. 15 : 404-9

Honneger K, Plas A, Diethelm R, Glatz W. 2001. *Evaluation of Rerritic Steel Interconnects for SOFC Stacks. Presented at Solid Oxide Fuel Cells VII: Proceedings of the Seventh International Symposium, Ibaraki-shi, Japan, 2001*. 2001-16 : 803. Pennington, N.J.: The Electrochemical Society

Horita T, Xiong Y, Kishimoto H, Yamaji K, Sakai N, Yokokawa H. 2004. *Application of Fe-Cr Alloys to Solid Oxide Fuel Cells for Cost Reduction: Oxidation Behaviour of Alloys in Methane Fuel*. Journal of Power Sources. 131 : 293-8

Horita T, Xiong Y, Yamaji K, Sakai N, Yokokawa H. 2003. *Stability of Fe-Cr Alloy Interconnects Under $CH_4$-$H_2O$ Atmosphere for SOFCs*. Journal of Power Sources. 118 : 35-43

Huang K, Hou PY, Goodenough JB. 2001. *Reduced Area Specific Resistance for Iron-Based Metallic Interconnects by Surface Oxide Coatings*. Materials Research Bulletin. 36 : 81-95

Huang K, Hou PY, Goodenough JB. 2000. *Characterization of Iron-Based Alloy Interconnects for Reduced Temperature Solid Oxide Fuel Cells*. Solid State Ionics. 129 : 237-50

International Center for Diffraction Data. 1996.

Ivey DG. 2003. *ZMG 232 -Potential IC Material.*

Jablonski PD, Alman DE, Kung SC. 2005. *Surface Modification of Ferritic and Ni Based Alloys for Improved Oxidation Resistance in SOFC Applications. Presented at Advances in Solid Oxide Fuel Cells: A Collection of Papers Presented at the 29th International Conference on Advanced Ceramics and Composites, Cocoa Beach, Florida, USA, 2005,* 26 : 193. American Ceramic Society

Jacobus K, DeVor RE, Kapoor SG. 2000. *Machining-Induced Residual Stress: Experimentation and Modelling.* Journal of Manufacturing Science and Engineering. 122 : 20-31

Jian L, Huezo J, Ivey DG. 2003. *Carburisation of Interconnect Materials in Solid Oxide Fuel Cells.* Journal of Power Sources. 123 : 151-62

Jian L, Jian P, Jianzhong X, Xiaoliang Q. 2005. *Oxidation of Haynes 230 Alloy in Reduced Temperature Solid Oxide Fuel Cell Environment.* Journal of Power Sources. 139 : 182-7

Johnson Matthey. 2006. *Fuel Cell Today.* http://www.fuelcelltoday.com/FuelCellToday/EducationCentre/EducationCentreExternal/EduCentreDisplay/0,3995,PressKitHome,00.html

Kadowaki T, Shiomitsu T, Matsudu E, Nakagawa H, Tsuneizumi H, Maruyama T. 1993. *Applicability of Heat Resisting Alloys to the Separator of Planar Type Solid Oxide Fuel Cell.* Solid State Ionics. 67 : 65-9

Kane RD. 2003. High Temperature Gaseous Corrosion. In *Corrosion: Fundamentals, Testing and Protection, Vol. 13A, ASM Handbook,* 228-35. ASM International

Karabelchtchikova O, Rivero IV. 2005. *Variability of Residual Stresses and Superposition Effect in Multipass Grinding of High-Carbon High-Chromium Steel.* Journal of Materials Engineering and Performance. 14 : 50-60

Kee RJ, Goodwin DG. 2004. *Solid-Oxide Fuel Cells (SOFC) with Hydrocarbon and Hydrocarbon-Derived Fuels.* http://www.uic.edu/eng/ems/Combustion/Kee_Goodwin_Zhu_VG.pdf.

Kendall K. 2005. *Progress in Solid Oxide Fuel Cell Materials.* International Materials Reviews. 50 : 257-64

Khalid FA, Benjamin SE. 2000. *The Effect of Deformation Substructure on the High-Temperature Oxidation of Inconel 625.* Oxidation of Metals. 54 : 63-71

Khanna AS. 2002. *Introduction to High Temperature Oxidation and Corrosion,* Materials Park, Ohio: ASM International. 320pp

Köck W, Martinz H, Greiner H, Janousek M. 1995. *Development and Processing of Metallic Cr Based Materials for SOFC Parts. Presented at Proceedings of the 4th International Symposium on Solid Oxide Fuel Cells (SOFC-IV), 1995,* 841. Pennington, NJ: The Electrochemical Society

Kofstad P. 1998. *High Temperature Corrosion,* New York: Elsevier Applied Science. 534pp

Kofstad P. 1992. *High Temperature Corrosion in SOFC Environments.* Solid State Ionics. 52 : 69-75

Kofstad PK, Hed AZ. 1969. *High-Temperature Oxidation of Co-10 w/o Cr Alloys: I. Microstructure of Oxide Scales.* Solid State Science. 116 : 224-9

Kruger SE, Bouesnard O, Charlier J, Rebello JMA, Segers L. 2000. *Shot Peening Treatment Characterization by Surface Acoustic Waves. Presented at AIP Conference Proceedings: Review of Progress in Quantitative Nondestructive Evaluation, 2000,* 509 : 1479. American Institute of Physics

Kung SC, Morris TA, Barringer EA. 2000. *Performance of Metallic Interconnect in Solid-Oxide Fuel Cells. Presented at Proceedings of the 2000 Fuel Cell Seminar, Portland, Oregon, 2000,* 585.

Kurokawa H, Kawamura K, Maruyama T. 2004. *Oxidation Behaviour of Fe-16Cr Alloy Interconnect for SOFC Under Hydrogen Potential Gradient.* Solid State Ionics. 168 : 13-21

Leistikow S. 1981. *Chances and Limitations of Improved Corrosion Resistance in Oxidising Gases by Cold Working Pre-Treatment of Austenitic CrNi-Steels. Presented at Behaviour of High Temperature Alloys in Aggressive Environments: Proceedings of the Petten International Conference, JRC Petten Establishment, The Netherlands, 1981,* 197. London: Metals Society

Leistikow S, Wolf I, Grabke HJ. 1987. *Effects of Cold Work on the Oxidation Behaviour and Carburization Resistance of Alloy 800.* Werkstoffe und Korrosion. 38 : 556-62

Linderoth S, Hendriksen PV, Mogensen M, Langvad N. 1996. *Investigations of Metallic Alloys for Use as Interconnects in Solid Oxide Fuel Cell Stacks.* Journal of Materials Science. 31 : 5077-82

Mankins WL, Lamb S. 2002. Nickel and Nickel Alloys. In *ASM Handbooks Online,* 2 : ASM International

Meadowcroft DB. 1969. *Some Properties of Strontium-Doped Lanthanum Chromite.* Brittish Journal of Applied Physics. 2 : 1225-33

Menig R, Pintschovius L, Schulze V, Vöhringer O. 2001. *Depth Profiles of Macro Residual Stresses in Thin Shot Peened Steel Plates Determined by X-ray and Neutron Diffraction.* Scripta Materialia. 45 : 977-83

Metal Suppliers Online. 2006. *Metal Suppliers Online: Material Property Data.* http://www.suppliersonline.com

Meulenberg WA, Uhlenbruck S, Wessel E, Buchkremer HP, Stöver D. 2003. *Oxidation Behaviour of Ferrous Alloys Used as Interconnecting Material in Solid Oxide Fuel Cells.* Journal of Materials Science. 38 : 507-13

Mikkelsen L, Linderoth S. 2003. *High Temperature Oxidation of Fe-Cr Alloy in $O_2$-$H_2$-$H_2O$ atmospheres; Microstructure and Kinetics.* Materials Science and Engineering A. 361 : 198-212

Minh NQ, Takahashi T. 1995. *Science and Technology of Ceramic Fuel Cells,* Amsterdam, The Netherlands: Elsevier. 347pp

Mougin J, Lucazeau G, Galerie A, Dupeux M. 2001. *Influence of Cooling Rate and Initial Surface Roughness on the Residual Stresses in Chromia Scales Thermally Grown on Pure Chromium.* Materials Science and Engineering A. 308 : 118-23

Mũnoz-Escalona P, Cassier Z, Payares MC, Zurita O. 2001. *Empirical Model of Grinding for the Prediction of Roughness on Stainless Steels. Presented at Proceedings of the 2001 ASME Pressure Vessels and Piping Conference, Atlanta, 2001,* 427 : 133. American Society of Mechanical Engineers

Murphy JA, ed. 1971. *Surface Preparation and Finishes for Metals,* New York: McGraw-Hill. 484 pp

National Energy Technology Laboratory. 2006. *Fuel Cells.* http://www.netl.doe.gov/technologies/coalpower/fuelcells/seca.html

Notoya H, Yonetani S, Takatsuji Y. 1986. *Influence of Grinding Conditions on Residual Stress and Distortion in the Ground Layer.* Transaction of the Japan Institute of Metals. 27 : 534-45

Ostwald C, Grabke HJ. 2004. *Initial Oxidation and Chromium Diffusion. I. Effects of Surface Working on 9-20%Cr Steels.* Corrosion Science. 46 : 1113-27

Parent Simonin S, Flavenot JF. 1987. Shot Peening of Nodular Cast Iron. In *Shot Peening: Science, Technology, Application,* eds. H Wohlfahrt, R Kopp, O Vöhringer, 133-40. Germany: Deutsche Gesellschaft für Metallkunde

Park E, Speigel M. 2005. *Effects of Heat Treatments on Near Surface Elemental Profiles of Fe-15Cr Polycrystalline Alloy.* Corrosion Engineering, Science and Technology. 40 : 217-25

Paulik SW, Baskaran S, Armstrong TR. 1998. *Mechanical Properties of Calcium- and Strontium- Substituted Lanthanum Chromite.* Journal of Materials Science. 33 : 2397-404

Piehl C, Toeki Z, Grabke HJ. 2000. *Influence of Chromium Diffusion and Different Surface Finishes on the Oxidation Behaviour of Chromium Steels.* Materials at High Temperatures. 17 : 243-6

Porter DA, Easterling KE. 1981. High Diffusivity Paths. In *Phase Transformations in Metals and Alloys*. 98-103. Toronto: Van Nostrand Reinhold

Quadakkers WJ, Greiner H, Hänsel M, Pattanaik A, Khanna AS, Malléner W. 1996. *Compatibility of Perovskite Contact Layers Between Cathode and Metallic Interconnector Plates of SOFCs*. Solid State Ionics. 91 : 55-67

Quadakkers WJ, Greiner H, Köck W. 1994. *Metals and Alloys for High Temperature SOFC Application. Presented at Proceedings of the 1st European SOFC Forum, Lucerne, Switzerland, 1994*, 525

Quadakkers WJ, Piron-Abellan J, Shemet V, Singheiser L. 2003. *Metallic Interconnectors for Solid Oxide Fuel Cells*. Materials at High Temperatures. 20 : 115-27

Rakowski JM, Meier GH, Pettit FS. 1996. *The Effect of Surface Preparation on the Oxidation Behaviour of Gamma TiAl-Base Intermetallic Alloys*. Scripta Materialia. 35 : 1417-22

Rao TV, Vook RW, Meyer W, Joshi A. 1986. *Effect of Surface Treatments on Near Surface Composition of 316 Nuclear Grade Stainless Steel*. J. Vac. Sci. Technol. A. 4 : 1604-7

Rhouma AB, Braham C, Fitzpatrick ME, Lédion J, Sidhom H. 2001. *Effects of Surface Preparation on Pitting Resistance, Residual Stress, and Stress Corrosion Cracking in Austenitic Stainless Steels*. Journal of Materials Engineering and Performance. 10 : 507-14

Riffard F, Buscail H, Caudron E, Cueff R, Issartel C, Perrier S. 2002. *In-Situ Characterization of the Oxide Scale Formed on Yttrium-Coated 304 Stainless Steel at 1000°C*. Materials Characterization. 49 : 55-65

Ross RB. 1988. *Handbook of Metal Treatments and Testing*, New York: Chapman and Hall. 568pp. 2nd ed.

Rowe WB, McCormack DF, Jin T. 2001. *Controlling the Surface Integrity of Ground Components*. Grinding and Abrasives Magazine. October : 24-30

Roy M, Ray KK, Sundararajin G. 1999. *The Influence of Erosion-Induced Roughness on the Oxidation Kinetics of Ni and Ni-20Cr alloys.* Oxidation of Metals. 51 : 251-72

Sakai N, Horita T, Xiong YP, Yamaji K, Kishimoto H, et al. 2005. *Structure and Transport Property of Manganese-Chromium-Iron Oxide as a Main Compound in Oxide Scales of Alloy Interconnects for SOFCs.* Solid State Ionics. 176 : 681-6

Scholtes B, Vöhringer O. 2001. Mechanical Surface Treatment. In *The Encyclopedia of Materials: Science and Technology,* eds. KHJ Buschow, RW Cahn, MC Flemings, B Ilschner, EJ Kramer, S Mahajan, 5253-62. Elsevier Science

Shackelford JF, Alexander W, eds. 2001. *CRC Materials Science and Engineering Handbook,* New York: CRC Press. 3rd ed.

Shifler D. 2003. High Temperature Gaseous Corrosion Testing. In *Corrosion: Fundamentals, Testing and Protection,* 13A : 650-81. ASM International

Simner SP, Anderson MD, Xia G-, Yang Z, Pederson LR, Stevenson JW. 2005. *SOFC Performance with Fe-Cr-Mn Alloy Interconnect.* Journal of The Electrochemical Society. 152 : A740-5

Smith WF. 1993. Stainless Steels. In *Structure and Properties of Engineering Alloys,* eds. BJ Clark, J Maisel, 288-334. Toronto: McGraw-Hill

Smithstonian Institution. 2005. *Collecting the History of Fuel Cells.* http://americanhistory.si.edu/fuelcells/

Steele BCH. 2000. *Materials for IT-SOFC Stacks.* Solid State Ionics. 134 : 3-20

Stokes PSN, Stott FH, Wood GC. 1989. *The Influence of Laser Surface Treatment on the High Temperature Oxidation of $Cr_2O_3$-Forming Alloys.* Materials Science and Engineering. A121 : 549-54

Sun WX, Nishida S, Hattori N, Usui I. 2004. *Fatigue Properties of Cold-Rolled Notched Eutectiod Steel.* International Journal of Fatigue. 26 : 1139-45

Taylor P, McEachern RJ, Doern DC, Wood DD. 1998. *The Influence of Specimen Roughness on the Rate of Formation of $U_3O_8$ on $UO_2$ in Air at 250°C.* Journal of Nuclear Materials. 256 : 213-7

Thomas S, Zalbowitz M. 2000. *Fuel Cells - Green Power.* Los Alamos National Laboratory, U.S. Department of Energy, Los Alamos, New Mexico. http://education.lanl.gov/resources/fuelcells/fuelcells.pdf

Tolpygo VK, Clarke DR, Murphy KS. 2001. *The Effect of Grit Blasting on the Oxidation Behaviour of a Platinum-Modified Nickel-Aluminide Coating.* Metallurgical and Materials Transactions A. 32A : 1467-78

Tomlinson WJ, Blick K. 1990. *Substrate Roughness, Cold Work, and the Oxidation of Pure Iron at 200 to 600°C.* Journal of Materials Science Letters. 9 : 1005-10

U.S. Department of Energy. 2006. *Fuel cells.* http://www.eere.energy.gov/hydrogenandfuelcells/fuelcells/

Uehara T, Toji A, Inoue K, Yamaguchi M, Ohno T. 2003. *Total Solution of Metallic Materials for SOFC. Presented at SOFC VIII: Proceedings of the Eighth International Symposium on Solid Oxide Fuel Cells, Paris, France, 2003,* 2003-07 : 914. Pennington, N.J.: The Electrochemical Society

Uran S, Veal B, Grimsditch M, Pearson J, Berger A. 2000. *Effect of Surface Roughness on Oxidation.* Oxidation of Metals. 54 : 73-85

Van der Biest, O., Harrison JM, Norton JF. 1979. *Characterization of Protective Layers Formed in Carburizing Environment. Presented at Behaviour of High Temperature Alloys in Aggressive Environments: Proceedings of the Petten International Conference, JRC Petten Establishment, Petten, The Netherlands, 1979,* 681. London: The Metals Society

Vázquez-Navarro MD, McAleese J, Kilner JA. 1999. *Candidate Interconnect Materials: Oxidation study of a Ni-Based Superalloy in Pure Oxygen at 800°C. Presented at Solid Oxide Fuel Cells (SOFC VI): Proceedings of the Sixth International Symposium, 1999,* 99-19 : 749. Pennington, N.J.: The Electrochemical Society

Virkar AV, England DM. 2000. *Patent No. US 6,054,231*

Vöhringer O. 1987. Changes in the State of the Material by Shot Peening. In *Proceedings of the Third International Conference on Shot-Peening, Shot-Peening: Science, Technology, Applications*, eds. H Wohlfahrt, R Kopp, O Vöhringer, 185-204. Germany: Deutsche Gesellschaft für Metallkunde

Was GS, Pelloux RM, Frabolot MC. 1981. *Effect of Shot Peening Methods on the Fatigue Behaviour of Alloy 7075-T6. Presented at First International Conference on Shot Peening, 1981*, 445. Toronto: Pergamon Press

Washco SD, Aggen G. 2002. Wrought Stainless Steels: Physical Properties. In *Properties and Selection: Irons, Steels, and High Performance Alloys*, 1 : ASM International

Wasielewski GE, Rapp RA. 1972. Chapter 10: High-Temperature Oxidation. In *The Superalloys*, eds. CT Sims, WC Hagel, 287-316. New York: John Wiley and Sons

Wei Q. 2004. *Interconnect Coatings for Solid Oxide Fuel Cell Applications*. M. Eng. in Chemical Engineering. University of Calgary, Calgary, Alberta. 119 pp.

Werner C. 2000. *Fuel Cell Fact Sheet*. Environmental and Energy Study Institute, Washington, D.C.

Whittle DP, Wood GC. 1968. *Chromium Oxide Scale Growth on Iron-Chromium Alloys: II. Influence of Alloy Composition*. Journal of The Electrochemical Society. 115 : 133-42

Wikimedia Foundation. 2006a. *Solid-Oxide Fuel Cell*. http://en.wikipedia.org/wiki/Solid-oxide_fuel_cell

Wikimedia Foundation. 2006b. *Alkaline Earth Metal*. http://en.wikipedia.org/wiki/Alkaline_earth_metal

Williams MC, Strakey JP, Surdoval WA. 2005. *The U.S. Department of Energy, Office of Fossil Energy Stationary Fuel Cell Program*. Journal of Power Sources. 143 : 191-6

Wincewicz KC, Cooper JS. 2005. *Taxonomies of SOFC Material and Manufacturing Alternatives*. Journal of Power Sources. 140 : 280-96

Woelfel MM. 1987. Maximization of Flexural Fatigue Strength of Heat-Treated Steel Specimens Using Multiple Peening Techniques. In *Shot Peening: Science, Technology, Application*, eds. H Wohlfart, R Kopp, O Vöhringer, 125-32. Germany: Deutsche Gesellschaft für Metallkunde

Xia G, Yang Z, Walker MS, Singh P, Stevenson JW. 2004. *Effects of Thermal History on the Anomalous Oxidation behaviour of Stainless Steels Under SOFC Interconnect Exposure Conditions. Presented at High Temperature Corrosion and Materials Chemistry V: Proceedings of the International Symposium, Honolulu, Hawaii, 2004*, 81. The Electrochemical Society

Yamamoto A, Yamada T, Nakahigashi S, Lu L, Terasawa M, Tsubakino H. 2004. *Effects of Surface Grinding on Hardness Distribution and Residual Stress in Low Carbon Austenitic Stainless Steel SUS316L.* ISIJ International. 44 : 1780-2

Yamamoto R, Kadoya Y, Kawai H, Magoshi R, Noda T, et al. 2002. *New Wrought Ni-Based Superalloys with Low Thermal Expansion for 700C Steam Turbines.* Materials for Advanced Power Engineering. 21 : 1351-60

Yang Z, Hardy JS, Walker MS, Xia G, Simner SP, Stevenson JW. 2004a. *Structure and Conductivity of Thermally Grown Scales on Ferritic Fe-Cr-Mn Steel for SOFC Interconnect Application.* Journal of The Electrochemcial Society. 151 : A1825-31

Yang Z, Singh P, Stevenson JW, Xia G. 2006a. *Investigation of Modified Ni–Cr–Mn Base Alloys for SOFC Interconnect Applications.* Journal of The Electrochemical Society. 153 : A1873-9

Yang Z, Walker MS, Singh P, Stevenson JW. 2003a. *Anomalous Corrosion Behaviour of Stainless Steels Under SOFC Interconnect Exposure Conditions.* Electrochemical and Solid State Letters. 6 : B35-7

Yang Z, Walker MS, Singh P, Stevenson JW, Norby T. 2004b. *Oxidation Behaviour of Ferritic Stainless Steels Under SOFC Interconnect Exposure Conditions.* Journal of The Electrochemical Society. 151 : B669-78

Yang Z, Weil KS, Paxton DM, Stevenson JW. 2003b. *Selection and Evaluation of Heat-Resistant Alloys for SOFC Interconnect Applications.* Journal of The Electrochemical Society. 150 : A1188-201

Yang Z, Xia G, Maupin GD, Stevenson JW. 2006b. *Evaluation of Perovskite Overlay Coatings on Ferritic Stainless Steels for SOFC interconnect applications.* Journal of The Electrochemical Society. 153 : A1852-8

Yang Z, Xia G, Singh P, Stevenson JW. 2005. *Effects of Water Vapour on Oxidation Behaviour of Ferritic Stainless Steels Under Solid Oxide Fuel Cell Interconnect Exposure Conditions.* Solid State Ionics. 176 : 1495-503

Yang Z, Xia G, Stevenson JW. 2006c. *Evaluation of Ni–Cr-base Alloys for SOFC Interconnect Applications.* Journal of Power Sources. 160 : 1104-10

Yang ZG, Stevenson JW, Singh P. 2003c. *Solid Oxide Fuel Cells.* Advanced Materials & Processes. 161 : 34-7

Zheng XG, Young DJ. 1998. *Influence of Yttrium on the High Temperature Corrosion of Chromium and Fe-28Cr in CO-$CO_2$-$N_2$(-$SO_2$) Atmospheres.* Corrosion Science. 40 : 741-56

Zhu WZ, Deevi SC. 2003a. *Development of Interconnect Materials for Solid Oxide Fuel Cells.* Materials Science and Engineering A. 348 : 227-43

Zhu WZ, Deevi SC. 2003b. *Opportunity of Metallic Interconnects for Solid Oxide Fuel Cells: A Status on Contact Resistance.* Materials Research Bulletin. 38 : 957-72

Zurek J, Wessel E, Niewolak L, Schmitz F, Kern T, et al. 2004. *Anomalous Temperature Dependence of Oxidation Kinetics During Steam Oxidation of Ferritic Steels in the Temperature Range 550-650°C.* Corrosion Science. 46 : 2301-17